ESTIMATION OF TIME-LAPSE VELOCITY CHANGES FROM TIME-LAPSE SEISMIC DATA

Nguyen Thi Kim Phung

Thesis presented for the degree of Doctor of Philosophy

Institute of Petroleum Engineering
School of Energy, Geoscience, Infrastructure and Society
Heriot-Watt University, Edinburgh, UK

July 2018

Abstract

Time-lapse velocity changes represent changes in pore-fluid and rock properties within the reservoir, reflect the geomechanical effects and provide input to an imaging correction for enhanced time-lapse interpretation. Here I present three different time-lapse velocity change estimation methods that can be applied to time-shifts from both post-stack data and also partial-stacked data. The aim of this research is to calculate robust yet stable and efficient algorithms for velocity change estimation by analytical development. Starting with the post-stack domain, I firstly develop a new method of Gaussian reconstruction that allows stable recovery of the time-lapse velocity changes despite varying levels of noise in the post-stack time-shifts. I then extend to partial-stack time-shift domain where the dependency of time-shift versus offset is explored via an extensive revision together with numerical examples before presenting the development of another robust method to extract the time-lapse velocity changes from partial-stack time-shifts. Here, I simplify tomographic inversion by using a straight-ray assumption and specialised re-gridding technique. In addition to time-shifts, in the post-stack seismic domain, amplitude changes are taken into account together with time-shifts and are inverted simultaneously by incorporating the Gaussian reconstruction method into a trace-warping algorithm. Overall, the algorithms developed in this work perform well when applied to data from the high-pressure high-temperature Shearwater field. Time-lapse velocity changes are shown to be inverted in a robust and efficient manner, without the need of a prior model or over-regularisation. The techniques are sufficiently versatile that they can be applied to different data types: post-stack time-shifts, partial-stack time-shifts or post-stack seismic traces.

Kính tặng Tía và anh Khoa!

To my inner child Chappi and our little baby(ies).

Acknowledgments

I would like to share my deepest gratitude for my supervisor, Professor Colin MacBeth, who brought me here and has been constantly supporting me with such incredible patience. You are my Zen teacher in doing research and the Professor that I have been looking for throughout my career and also life path. I would like to share my endless thankfulness for my co-supervisor, Dr. Maria Daphne Mangriotis, who helped me ground the research topics in this research thesis. I am amazed at her kindness and good nature. I have been very lucky to have you both as my supervisors! I also would like to thank Dr. Asghar Shams for showing me the big picture when I started my PhD. To Dr. David Iacopini and Prof. Hamed Amini, I thank you for being my external and internal examiners !

I am thankful to the Edinburgh Time Lapse Project (ETLP) sponsors of Phase V and VI, for their support and for providing the datasets used in my research (Aker BP, BG, BP, Chevron, CGG, ConocoPhillips, ENI, ExxonMobil, Hess, Ikon Science, Landmark, Maersk, Nexen, Norsar, RSI, OMV, Petoro, Petrobras, Shell, Statoil, Suncor, TAQA, TGS and Total). I would especially like to thank John Brain, Henning Hoeber, David Grey, Shaji Mathews, Sean Ferris and John Edgar for their practical discussions and communications. I am also grateful to Gualtiero Böhm of National Institute of Oceanography and Experimental Geophysics for your prompt and constant support in providing the free license of CAT3D– tomography package for my numerical examples in Chapter 3. To my greatest team ever, ETLP, thank you very much for all being such great individuals– Angel Briceno, Ricardo Rangel, David Yin, Dennis Obidegwu, Sean Tian, Niki Obiwulu, Ming Yi Wong, Veronica Omofoma, Justin Geng, Lee Jean, Romain Chassagne, Miguel, Anders Matheson, Hamed Amini, Alejandro Jaramillo, Gustavo Corte and Qi Zhang– and especially to Dr. Lu Ji for providing the time-shift codes and to Dr. Ilya Fursov for your help in enhancing my mathematical and programming skills.

I am also grateful to such beautiful Zen communities I have been practicing with– Wild Geese Sangha, Heart Sangha and Wake Up Edinburgh– for the spiritual support, and to my Viet gangs for all the friendship and sharing, especially to co Nhung, Tina, for always fulfilling my empty stomach with Viet home food. And of course,

I could never reach this point without the unconditional support from each single member of my family. *Con cam on ca nha nhieu lam! Con cam on Ba, Me, anh, chi va tui nho rat nhieu.*

Finally, my heartfelt gratitude to my husband, Keith Smith, the cutest and most gentle, adorable yet grounded and spacious person I have ever known. Thank you so very much for always being there for me patiently and loving me. This is also for to his wonderful family who has warmly welcomed me as a new family member.

Entirely, a huge gratitude to the whole cosmos, either bad or good, noise or signal, that have came together, brought me here and made this PhD journey enrich my life!

Contents

List of Tables

List of Figures

Abbreviations

GMM	:	Gaussian Mixture Model
NMO	:	normal move-out
TVO	:	Time-shift versus offset
$\mathbf{TVO_x}$	:	Time-shift versus offset at offset before NMO correction
$\mathbf{aTVO_x}$	:	Absolute time-shift versus offset before NMO correction
$\mathbf{rTVO_x}$	:	Relative time-shift versus offset before NMO correction
$\mathbf{TVO_0}$	:	Time-shift versus offset after NMO correction
$\mathbf{aTVO_0}$	:	Absolute time-shift versus offset after NMO correction
$\mathbf{rTVO_0}$	:	Relative time-shift versus offset after NMO correction
OB	:	overburden
OF	:	objective function
NLI	:	non-linear inversion
CLM	:	correlated leakage method
DHF	:	Dave-Hale Fast Cross-correlation

Chapter 1

The role of velocity change estimation in time-lapse seismic

ABSTRACT

Time-lapse changes in velocity can imprint both traveltime and amplitude of time-lapse seismic data. In this opening chapter, I introduce the first important attribute of time-lapse seismic, which is time-shifts and its values in understanding the reservoir and surrounding intervals. Different from the static time-shifts due to seismic processing procedure, this time-lapse time-shift attribute is due to the hydrocarbon production and has been observed in many different field examples. From here, I explain the role of time-lapse velocity changes and the current methods for estimating this quantity from time-shifts. Then, the main challenges relating to the time-lapse velocity change estimation topic are addressed together with the objectives of this thesis. Finally, the chapter finishes with the outline of the subsequent chapters.

1.1 Time-lapse seismic

Time-lapse seismic, also known as 4D seismic, has been proved to be an effective tool in reservoir monitoring and management even though its fundamental base in geophysics. By repeatedly acquiring the seismic surveys over the same area of the field at various production time, the geophysicists can monitor the production-related changes in the reservoir and surrounding areas. Well data provides a high vertical resolution but not horizontal. Conversely, seismic data has much broader horizontal coverage (Figure 1.1). The integration of these two 4D seismic and well-based data closes the loops and provides insight about the reservoir. This is an essential application in reservoir monitoring and management.

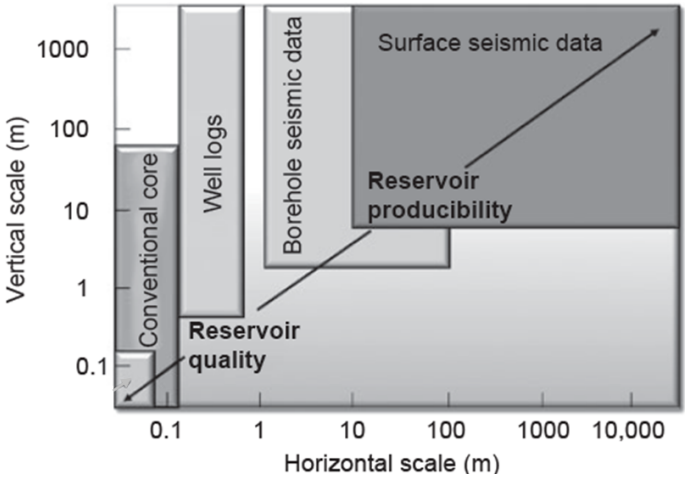

Figure 1.1: Various resolutions of different data types. The left side of each box is the horizontal-resolution limit; the right side is its horizontal coverage; the bottom gives the vertical-resolution limit; and the top is the vertical coverage. Further information of the heterogeneity that controls reservoir quality and production are visible. After Johnston (2013).

First introduced about 40 years ago by Nur (1982), Nur et al. (1984) and Nur and Wang (1987) with the rock-physics models to monitor the enhanced oil recovery process, the application of 4D seismic has spread from North Sea to Gulf of Mexico, West Africa, Brazil, Asia, Australia with various geological reservoir settings and under different production mechanisms as detailed in Rangel (2016). Figure 1.2 shows the growth of CO_2 plume being injected into a major sandstone aquifer via time-lapse seismic data acquired at various years from 1994 to 2008 (Chadwick et al., 2010). Figure 1.3 shows another successful story of 4D seismic in detecting of contact movement in a carbonate field Sarawak, Malaysia. The gas production

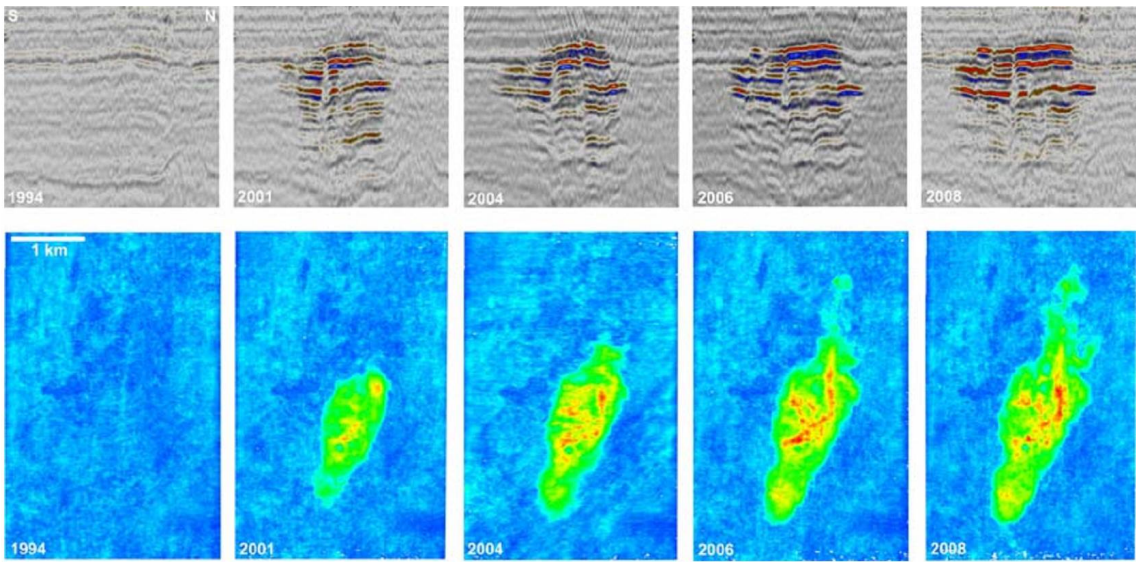

Figure 1.2: An example of 4D seismic technology applied at a Norwegian North Sea field with CO_2 storage operation. Seismic images of the CO_2 plume growing over the years through (top) seismic profiles and (bottom) plan view of total reflection amplitude. The rock is gradually saturated by CO_2 which causes a large velocity pushdown, observed by slower seismic traveltime over the years. After Chadwick et al. (2010).

from this field driven by a strong aquifer mechanism causes a 4D signature between baseline (1990) and monitor (2001) surveys, in which the original and present gas-water contacts are clearly revealed (Waal and Calvert, 2003). Figure 1.4 provides a 4D field example in the North Sea where the injectors cause delays in the travel-time in the reservoir, which are called time-shifts and will be further discussed in the next section.

Success of 4D seismic analysis and interpretation rely a lot on the 4D seismic repeatability, so that the true differences can be brought out. To measure the repeatability of 4D seismic, Kragh and Christie (2002) defined normalized root-mean-square (NRMS) difference between two monitor m_t and baseline b_t traces with a given time window $(t_1 - t_2)$ as following:

$$NRMS = 200\frac{RMS(m_t - b_t)}{RMS(m_t) + RMS(b_t)} \tag{1.1}$$

where

$$RMS(x_t) = \sqrt{\frac{\sum_{t_1}^{t_2} x_t^2}{N}} \tag{1.2}$$

where N is the sample numbers in the interval $t_1 - t_2$. It should be noted that the value of NRMS does not range between $0 - 100\%$. When both of traces contain

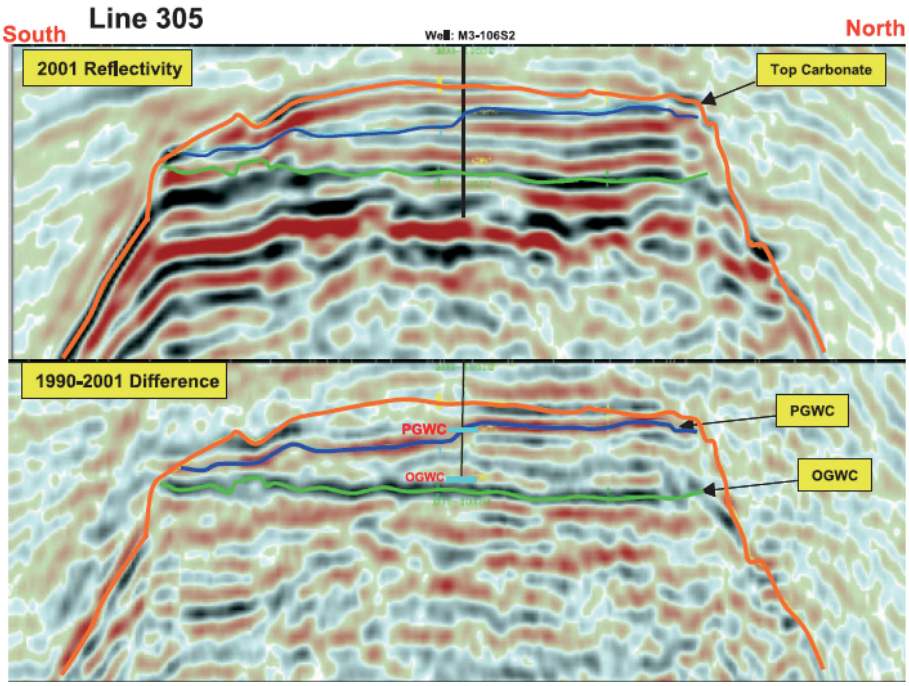

Figure 1.3: An 4D seismic signature driven by a strong aquifer in a gas carbonate field Sarawak, Malaysia. The 4D seismic differences (bottom) reveal the original and present gas-water contact (OGWC and PGWC, respectively) after the gas production. After Waal and Calvert (2003).

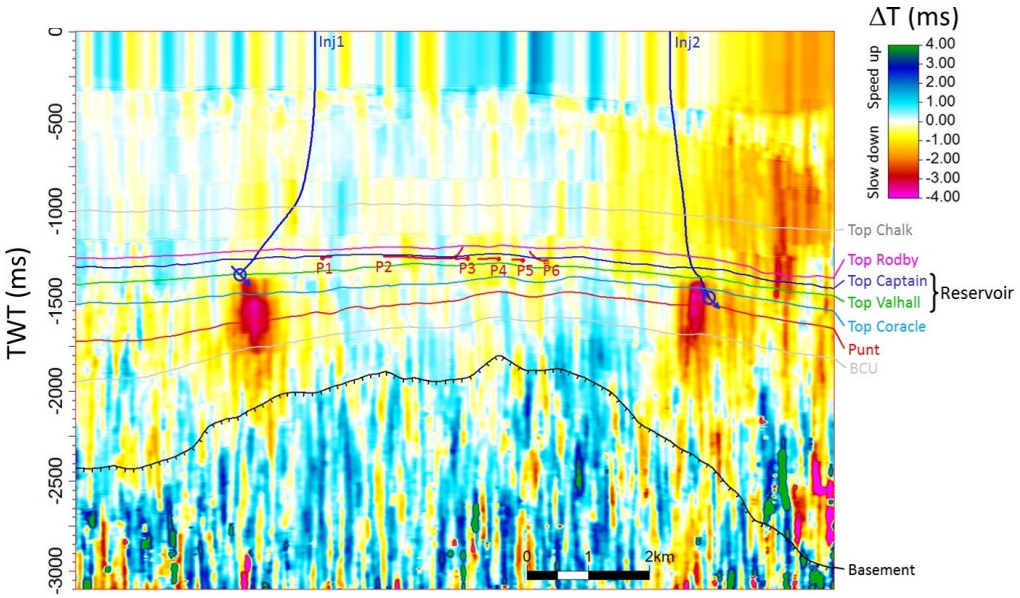

Figure 1.4: A time-lapse seismic field example in the North Sea with about 4ms time-shifts caused by the injectors into the aquifer. Courtesy of Amini and Marsden, 2017.

random noise, the value of NRMS is 141%. If the traces have anti-correlation (180^0 out of phase), the value is 200% (which is theoretically the maximum value). Typical value of NRMS is 60-80% for early time-lapse seismic studies with legacy data, which are not acquired in the purpose of 4D seismic. In Vedanti et al. (2009), the NRMS value was reported 10-30% as "good" value in some cases thanks to the advance of

4D survey technology like a steerable streamer technology. Most recently, with the innovation of seismic acquisition of permanent reservoir monitoring, the 4D seismic data are even much better. This NRMS value will be quoted in the next sections to access the quality of time-lapse seismic data.

1.2 Post-stack time-shifts

As mentioned above in Figure 1.4, time-shifts are caused by changes in two-way traveltime between datasets due to changes in subsurface seismic properties over elapsed period between time-lapse seismic data. As a measurement, time-shifts are of cumulative nature, they reflect the sum of changes of two-way traveltime at each reflector and the overburden above it. In this chapter, we will discuss time-shifts observed and measured from post-stack seismic data.

1.2.1 Time-shift observations in field data

There are observed time-shifts from 4D seismic data which relate to the production and injection. These time-shifts are opposed to being artefacts of acquisition or processing non-repeatability. For example, in Figure 1.5, Alsos et al. (2009) observed up to about 10ms in time-shifts (Figure 1.5c) in the Svale Field due to large pressure changes over the field. This time-shift causes a significant differences between the time-lapse differences before and after time-shifts correction (Figure 1.5b and c, respectively).

Time-shifts can be present throughtout the subsurface in 4D seismic data. In some highly compacting chalk reservoir (e.g. Ekofisk), we can observe reflector movements related to expansion in the overburden and consequent compression caused by reservoir production (Hawkins et al., 2007; Hatchell et al., 2003). In the reservoir, time-shift behaviour becomes more complex because of overlapping effects between geo-mechanics and fluid saturations. In the under-burden, the effect is even harder to understand due to the accumulation of all the phenomenon occur above, and are captured within the cumulative nature of time-shifts. Figure 1.6 shows two typical time-shift examples because of draw-down pressure and geo-mechanics from the production activities.

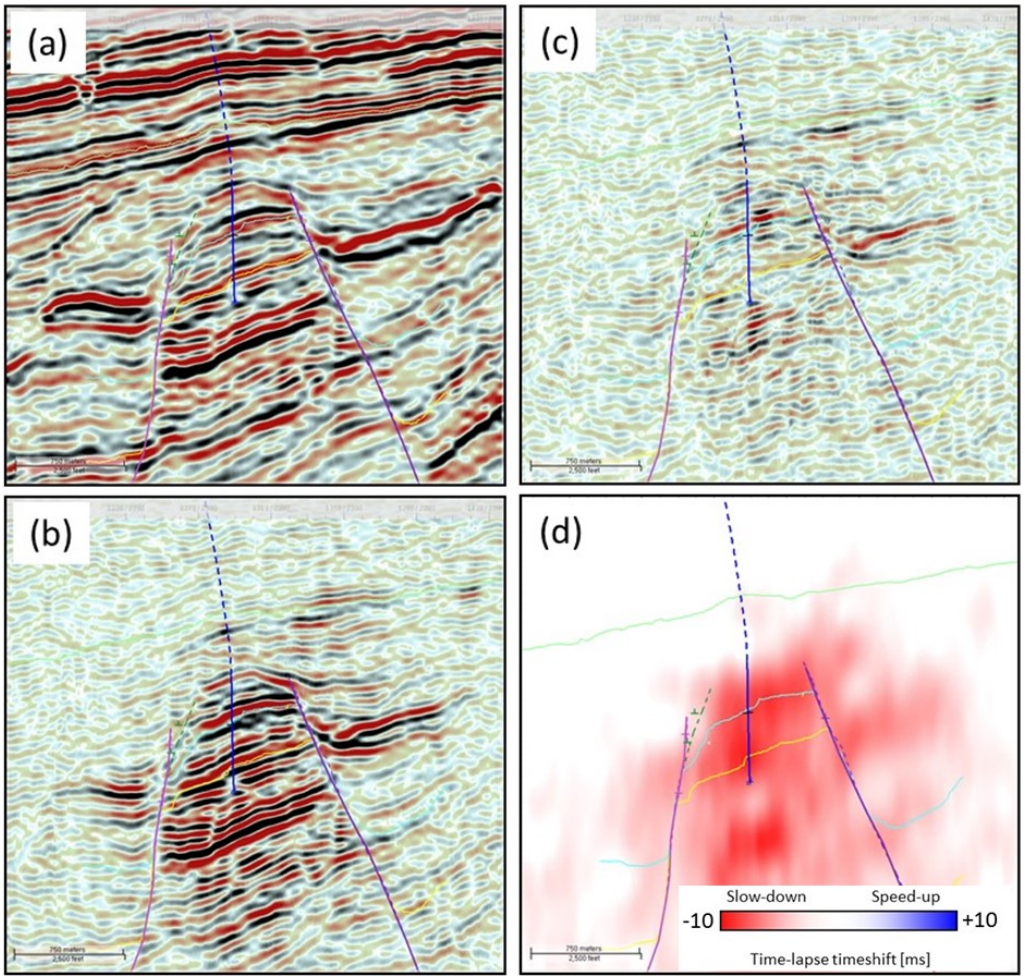

Figure 1.5: An example of observed time-shifts in Svale field. (a)Baseline survey, (b) Time-lapse seismic differences, (c) Time-lapse seismic differences after applying time-shift correction and (d) Measured time-shifts. Modified after Alsos et al. (2009).

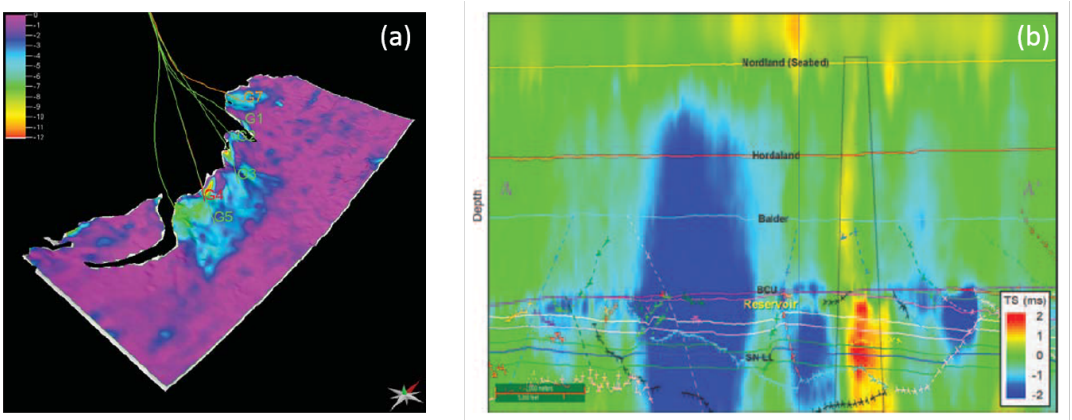

Figure 1.6: Another time-shift examples at (a) Genesis stacked turbidite field in the Gulf of Mexico, there is a good correlation with pressure drawdown at the production wells (after (Hodgson et al., 2007) and (b) Snorre sandstone field due to strong geomechanical effects with a blue "bar", starting right beneath the seabed and increasing toward the reservoir. After (Røste et al., 2015).

1.2.2 Time-shift magnitude and physical expression

Obviously, magnitude of time-shifts depend on the reservoir, production mechanism and the period of time-lapsed monitoring. Table 1.7 from MacBeth et al. (2017b) shows a collection of time-shifts measured over 50 different fields. The showing ranges between 2 to $24ms$. There are more time-shifts associated with slowdown $(+)$ than speedup $(-)$ in the overburden. Generally, slowdown time-shifts are large, on average about $5-20ms$ in cases of extension overburden, gas out of solution due to production pressure depletion or gas injection. Time-shifts related directly to changes in pore pressure are smaller, about $2-5ms$. Speedup time-shifts in the overburden do exist but seldom reported. They might come from an extension in the reservoir due to the injectors or complex deformation due to stress-arching effects (Røste and Ke, 2017).

As time-shift is a measure of 4D changes in the kinematic component of seismic data, it depends on the changes of subsurface layer thickness and velocity. Its physical expression at zero-offset is derived by Landrø and Stammeijer (2004) as:

$$\frac{\Delta t}{t} \approx \frac{\Delta z}{z} - \frac{\Delta V}{V}. \tag{1.3}$$

where t, V, z are traveltime, velocity and thickness of baseline survey. ΔV and Δz represent the time-lapsed velocity and thickness changes, respectively. The thickness changes are related to geo-mechanic effects where the reflectors are either moved up or down. Meanwhile, the velocity changes are usually dominated by fluid saturation, even though there is also contribution from deformation. This aspect will be further discussed in the next section 1.3. Please note that this fundamental equation will be explored in various scenarios hence will be often recalled throughout this work.

1.2.3 Time shift measurements

So far, we have observed the presence of time-shifts in 4D seismic data and have also understood the physical meaning of time-shifts. In theory, time-shifts can be measured very accurately in discrete and regularly sampled data. The accuracy are quoted at 0.1ms even at 4ms sampling rate (MacBeth et al., 2017b). Nevertheless, *"it is difficult to measure them accurately at fine enough scale to impact reservoir*

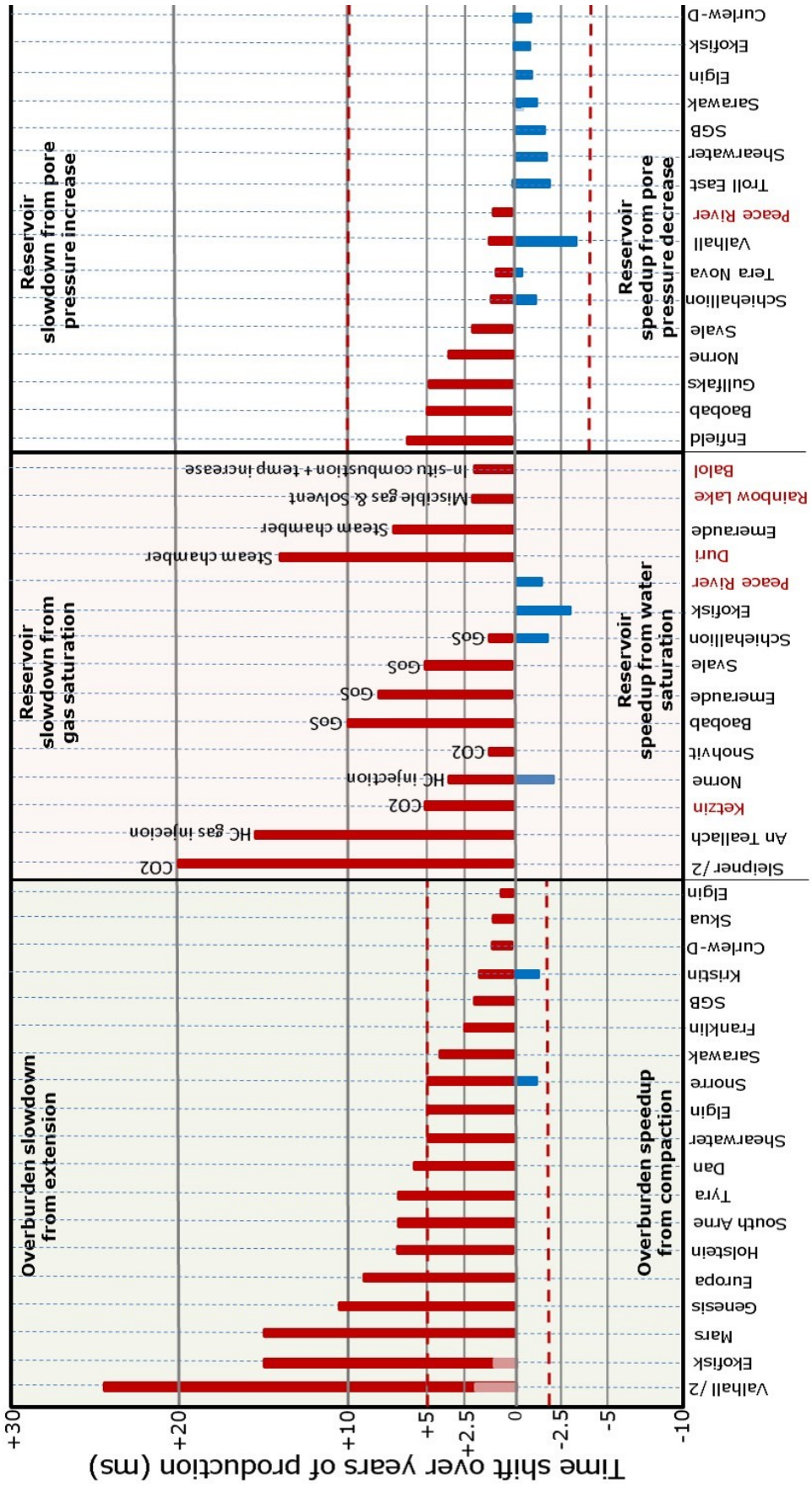

Figure 1.7: The magnitude of post-stack time-shifts collected and summarized from various reservoir and production mechanism in the literature by MacBeth et al. (2017b). Field names in red are for land data. More time-shifts associated with slowdown (+) than speedup (-). In cases of overburden extension, pressure up or gas, time-shifts are particularly strong.

management. Seismic data are inherently noisy, and we are always pushing the limits of the data we have available" as pointed by (Rickett et al., 2007). This has been an active topic and there are more than a handful of different methods developed to measure the time-shifts. However, measuring time-shifts correctly is challenging as it depends on noise level of data, robustness of the algorithm, and desired results' accuracy and resolution (Kanu et al., 2016). Here are a few specific reasons:

(i) Time-shift involves measuring traveltime (kinematic) changes through comparison of baseline-monitor seismic traces. As such they depend on all changes between two traces both kinematic and dynamic aspects. Because the wave interference phenomena seems to be different between baseline and monitor, the waveform of baseline and monitor are slightly varied as well. This waveform variation is picked up in some time-shift measurement algorithms which would usually not be able to distinguish a waveform change from a time-shift. Dynamic time-shift algorithm, on the other hand, would attempt to do so.

(ii) Another interesting phenomenon that may arise in time-shift analysis is the creation of spurious time-shift as pointed in MacBeth et al. (2016), whereby 4D tunning may create time-shift if opposite polarity to the polarity dictation by the sign of velocity changes.

(iii) Beyond that, there are also the effects from seismic processing including migration (Chen et al., 2014) or multiple removal.

(iv) Finally, as seen below, most time-shift algorithms rely on analysis of a window around each time of interest, hence dependence on window selection's parameters. Other algorithms may require analysis over the entire trace which entails non-local information impacting time-shift estimation at location of interest (for example: NLI time-shift measurement method).

Revision of various time-shift measurement methods can be found in Kanu et al. (2016); Ji (2017) with descriptions and comparisons on both synthetic and field examples. Often used methods are local cross-correlation, such as local fast cross-correlation (Rickett et al., 2006), Dave Hale's fast (DHF) cross-correlation (Hale, 2009) which are fast but usually suffer from the choice of window size and *" are accurate only where shifts are more slowly varying"* (Hale, 2013). The other non-

cross-correlation based methods such as non-linear inversion (NLI) by Rickett et al. (2007), correlated leakage method (CLM) by Whitcombe et al. (2010), Bayesian inversion with constraints for smooth time-shifts by Lie (2011) or dynamic image warping by Hale (2013) try to overcome these localized time-shift extraction by introducing a global solution which takes into account the entire traces (e.g. NLI method) so that in the case of large shifts or rapid changes in space and time, we can still obtain the robust and reliable time-shifts (Hale, 2013). These two studies conclude that CLM provides the best resolution and NLI turns out as the most stable method as shown in Figure 1.8. However, DHF still works well for some geologically simple models.

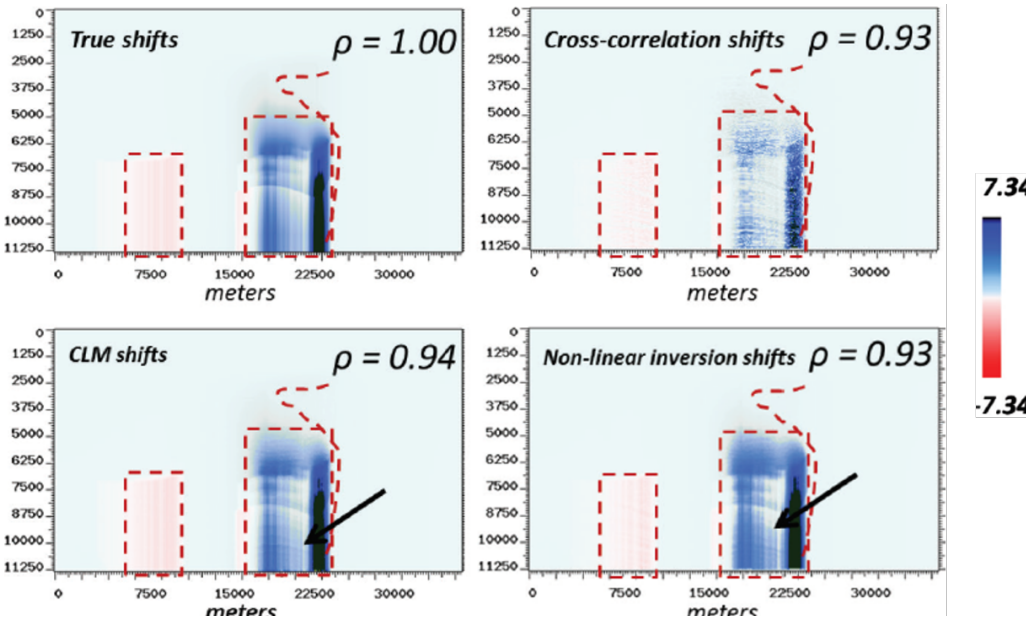

Figure 1.8: Comparison of measured time-shifts with the true zero-offset shift imposed in the zero-offset case. The red dashed outlines indicate the edge of the salt and the sections of the model with dominant time-shifts. ρ is the spearman rank correlation what compares the similarity of the estimated shifts with the true shifts. CLM and NLI provide the nearly identical results to the true time-shifts, except the additional banding marked with the black arrows. After Kanu et al. (2016).

Recently, Khalil and Hoeber (2016) presents another method to measure time-shifts unlike the traditional methods by relying on the physics of seismic imaging which is governed by the wave equation. For the work in this thesis, I need to measure time-shift for the velocity changes estimation. I select the three most common used methods described by Ji (2017), which are DHF, CLM and NLI as mentioned above. The codes are compiled and written in MATLAB by Hale (2009) (CLM – originally in JAVA), Ji (2017) and Chamberfort (2013) (CLM), and Hodgson (2009) (NLI).

Detailed formulae and descriptions on measuring time-shifts using these three methods are fully provided in Appendix B. In principle, DHF and CLM are window-based methods which depend on the choice of window size. The smoothness of solutions hence rely on how large the window size is. CLM overcomes the shortcoming of based-cross-correlation DHF by employing Taylor series expansion so that the time-shifts is found uniquely. Meanwhile NLI does not. NLI minimizes the objective function of differences between two traces to find out the time-shift function after being regularized by the global smooth functions.

1.3 Time-lapse velocity changes

So far, we have observed the imprints of production and injection activities on time-shifts. Interpreting this attribute helps to monitor the changes in the subsurface. Apart from using time-shifts as correction term to obtain a "clean" 4D amplitude seismic responses in conventional 4D seismic interpretation, this attribute has been further explored through the inversion scheme to recover for reservoir fluid saturation, pressure and geo-mechanic parameters (Kenter et al., 2004). These factors are implicitly expressed through two quantities of velocity and thickness changes in Equation 1.3. However, the effect of $\Delta z/z$ is often very small, especially in non-compacting reservoirs or pressure is well maintained (Chu et al., 2012) as compared to the impact from velocity changes. In this section, I will focus only on investigating the physical meaning and essential role of velocity changes $\Delta V/V$ in 4D seismic. Nevertheless, the effect of $\Delta z/z$ will be studied in Chapter 3.

1.3.1 $\Delta V/V$ as an attribute

Contrary to the time-shift attribute, which is accumulative, velocity change is an interval property. Therefore, it directly reflects changes in the reservoir and well activity. There is also other similar interval attribute to velocity changes, which is time-strain. It is the derivative of time-shifts and has an opposite polarity to the velocity changes as will be shown in Section 2.1.1. Figure 1.9 (left) shows the interval time-strain from the geo-mechanical modelling for a strong compaction chalk field at the North Sea over 20 years of primary depletion. On the right, it is the

accumulatively measured time-shifts.

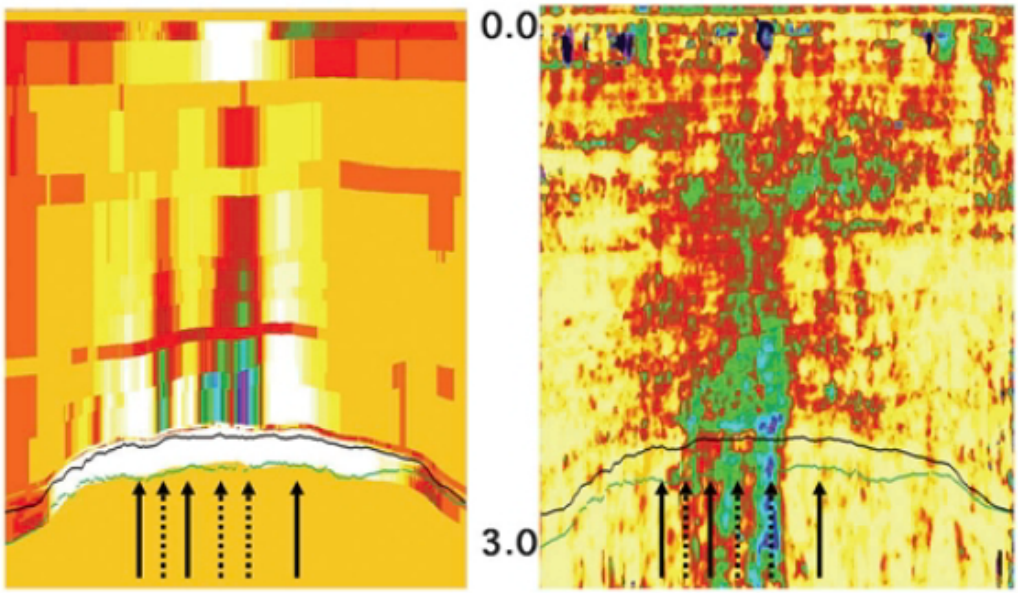

Figure 1.9: The interval time-strain from geo-mechanical modelling (left) versus the accumulative time-shifts (right) at the North Sea chalk field. A strong compaction over 20 years of depletion in the reservoir causes the extension in the overburden with largest time-shift up to 20 ms (blue). Obviously, time-strain (hence velocity changes) reflect the interval properties while the time-shifts are accumulative across over the subsurface. Unfortunately, the colour scales of neither the time-shifts nor the velocity changes are available. After Barkved and Kristiansen (2005).

Moreover, $\Delta V/V$ is now becoming a standard quantity in 4D seismic. It contributes to not only better seismic processing for time-lapse seismic in terms of imaging but also to 4D seismic analysis and interpretation.

Application for imaging

In 4D seismic processing, it is critical to make sure the static issues (for examples: acquisition and processing parameters before the migration steps) are aligned and only dynamic changes relating to the production are kept in the 4D seismic difference. However, in practice, most of the time in 4D seismic, the seismic vintages are migrated with the same baseline velocity model and even though this velocity model is not accurate for monitor. This can cause biases in the stacked 4D seismic amplitude difference, which can not be corrected by time-shift alignment (Chen et al., 2014). Figure 1.10 pointed out the artefacts due to the offset-dependent timing mismatch of seismic reflections. Hence, processors may seek for updating the monitor velocity to improve the seismic image and consequently 4D seismic analysis.

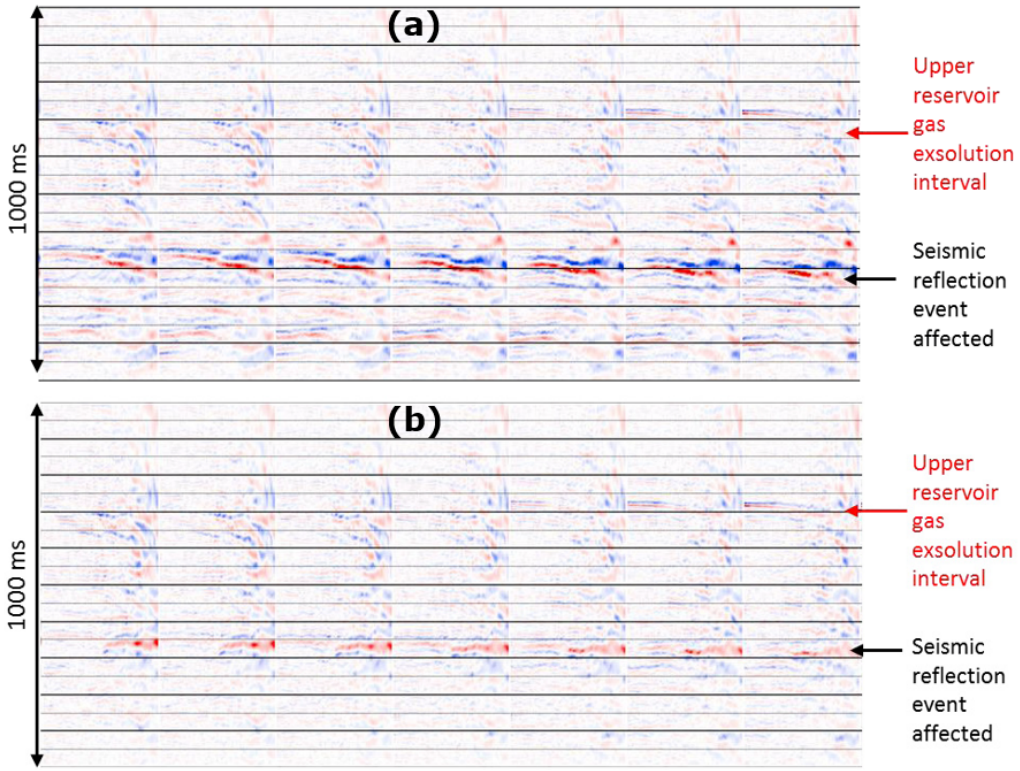

Figure 1.10: 4D seismic difference after (a) migration with V_{baseline} and (b) migration with V_{baseline} and $V_{\text{perturbed}}$. In (a), the seismic reflection event pointed by the black arrow is slightly under-corrected, resulting in the large 4D difference. With the same monitor gathers migrated with the perturbed velocity model (b), the seismic reflection event becomes flatter and the offset-dependent timing mismatch is largely removed. After Chen et al. (2014).

Geo-mechanics

The integration of geo-mechanics into 4D seismic was first studied by Hatchell et al. (2003), who managed to explain the distribution of observed time-shifts in real 4D seismic data. The observed largest time-shifts at the overburden in their study is explained by the compaction phenomenon inside the reservoir due to reservoir depletion. As a result, the other two sides of the reservoir (overburden and underburden) are stretched and consequently their seismic velocity decreases whilst in the reservoir, the velocity increases. These variations in velocity can be defined as related to the strain deformation linearly via the dilation factor R and α by Hatchell and Bourne (2005) and Røste et al. (2005), respectively. These two factors were introduced simultaneously with opposite polarity, $R = -\alpha$ defined as:

$$\frac{\Delta V}{V} = -R\frac{\Delta z}{z} \quad \text{and} \quad \frac{\Delta V}{V} = \alpha\frac{\Delta z}{z}. \tag{1.4}$$

Even though Equation 1.4 has been applied successfully in practice over the last decade, the physical implication of this factor are still a topic under investigation (MacBeth et al., 2017a). Inserting Equation 1.4 into Equation 1.3 and re-arranging provides a simple relationship between time-shift and velocity changes as:

$$\frac{\Delta t}{t} = -\left(1 + \frac{1}{R}\right)\frac{\Delta V}{V}. \tag{1.5}$$

According to Equation 1.5, if $\Delta V/V$ is well-estimated independently, together with the measured $\Delta t/t$, it is possible to obtain an independent measurement for the R or α factor.

Fluid saturation

During production, water replaces oil and gas might be released depending on the pressure reaching bubble point; these phenomena lead to fluid saturation changes with accompanying contact movement, which translate to changes in seismic velocity and consequently seismic responses. Gassmann (1951) described the dependence of seismic velocity as a function of the rock bulk modulus and density, which includes the rock frame, the grains or minerals and effects from fluids saturated inside the pores. There are several physics or petro-elastic models describing the dependence of velocity on fluid saturation as detailed in Nguyen and Nam (2011) and Briceño (2017).

The responses of velocity changes caused by fluid saturation or contact movement in non-compacting reservoirs are usually more localized than in compacting reservoirs due to the pressure depletion, which include extension in overburden. Correspondingly, in the absence of geo-mechanical changes, the observed time-shifts due to fluid saturation should in theory be zero above the top reservoir and constant below the base of the reservoir. Figure 1.11 shows an example of velocity changes decreasing at the production due to gas exsolution (Figure 1.11a) and increasing at the injection well due to water injection (Figure 1.11b) at the turbidities sandstone Dalia field, Angola.

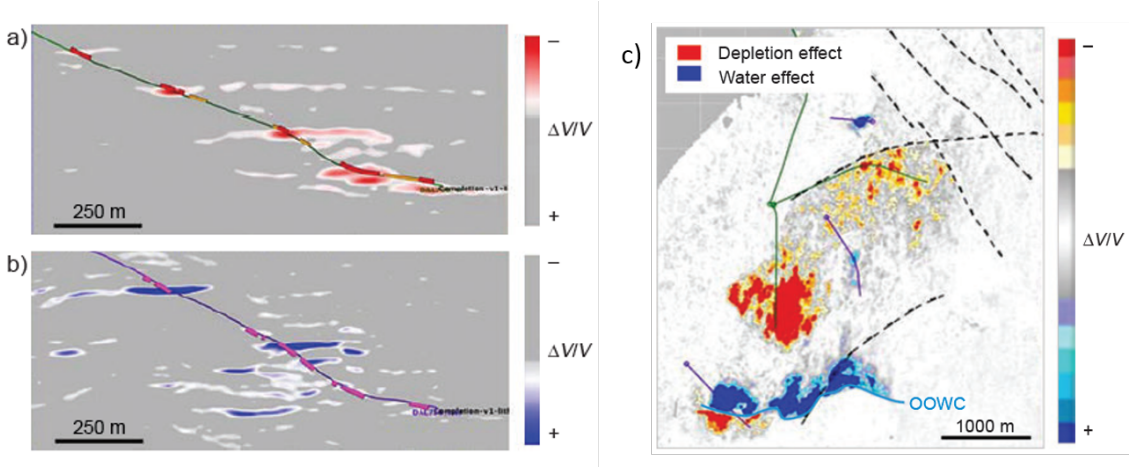

Figure 1.11: Vertical section of relative velocity changes $\Delta V/V$ (about 5% - educated guess) extracted along well paths for (a) a producer well ($\Delta V/V$ decreases due to gas exsolution from depletion) and for (b) a water-injection well ($\Delta V/V$ increases due to water injection into the oil pool) at Dalia field, offshore Angola. (c) shows a map of extracted $\Delta V/V$ attribute along the south water injection well into the oil pool (positive $\Delta V/V$ above the original oil-water contact (OOWC)) and into the water pool (negative $\Delta V/V$ with water leg below OOWC). Coloured sections around well paths correspond to completions. Quantitative colour scale is not accessible. After Johnston (2013) and Brechet et al. (2010).

1.3.2 Current methods for inverting $\Delta V/V$

In the earlier days of 4D seismic, the inversion scheme for $\Delta V/V$ relied on the inversion of a single seismic vintage using the 3D inversion methods, which is extensively reviewed in Barclay et al. (2008); Russell (1988). The velocity changes are then estimated by taking the differences from these inverted products. Sarkar et al. (2003) divided the general workflows for performing 4D seismic inversion into three categories as an uncoupled inversion, coupled inversion and inversion of the difference. I use Figure 1.12 summarized from Tian (2014) to visualize them. For uncoupled inversion, each seismic vintage is inverted separately without any additional effort to time align the vintages before the inversion (Leguijt, 2009; Floricich et al., 2012). Conversely, coupled inversion requires the baseline seismic data time aligned with the monitor survey before carrying out the inversion. The inversion result of baseline survey will be used as the initial model in the inversion of the monitor survey(s) (Tian, 2014). Regarding inversion of the difference, the inversion neither uses the baseline or monitor surveys, but the 4D seismic difference between them to directly invert for the velocity changes. With the current growth of 4D seismic in both acquisition and processing, there are more high quality and dedicated processed 4D

seismic data available. Moving forward to extract the velocity changes directly from the "4D difference domain" is a natural step that helps to save time and effort.

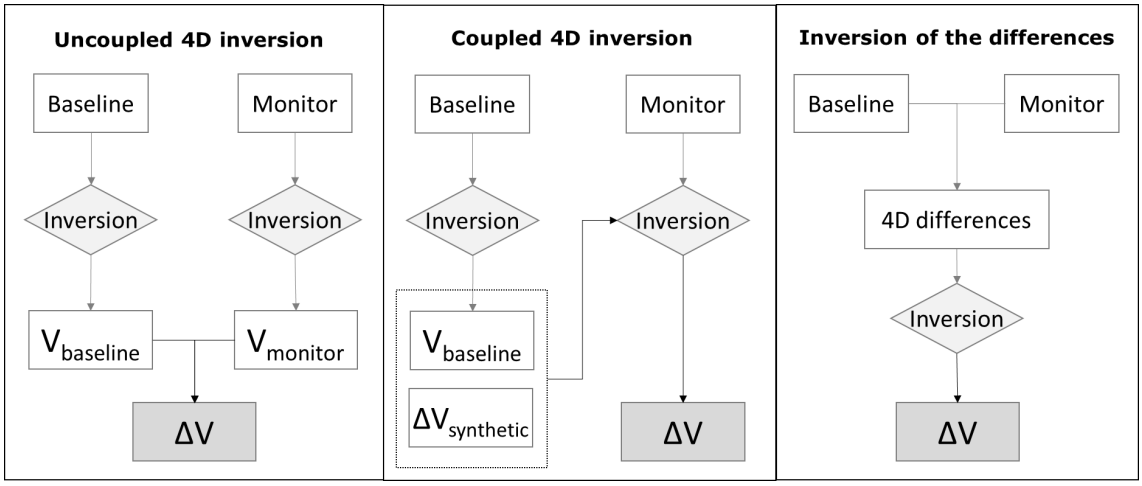

Figure 1.12: Three schematic options in inverting for 4D velocity changes $\Delta V/V$. Uncoupled and coupled inversion sequentially invert for $V_{baseline}$ and $V_{monitor}$ from the single baseline and monitor, respectively and then $\Delta V/V$ is obtained. Inversion of the difference directly uses the 4D seismic difference instead of the baseline and monitor surveys to invert for $\Delta V/V$. Therefore, inversion of the difference focuses on exploring the two important attributes of 4D seismic (time-shifts and amplitude changes) by setting up the new 4D equation derived from the differences between baseline and monitor surveys. Modified after Sarkar et al. (2003) and Tian (2014).

Therefore, in this thesis, I focus on the "inversion of difference" methods which directly input 4D seismic data. The seismic modelling is then formulated using the 4D seismic attributes, which are time-shifts and amplitude changes. The time-shift attribute is used more commonly than amplitude changes in the methods of estimating time-lapse velocity changes since its accumulative nature makes the estimation more stable. Chapter 2 provides a revision of the velocity change estimation methods using the measured time-shift data in the post-stack domain. Other velocity change estimation methods using angle-stack time-shifts, which are measured from offset/angle-stack data or shot gathers, are further investigated in Chapter 3. It should be noted that only vertical measurement of time-shifts are taken account in my study. The lateral effects of time-shift are further explain in Cox and Hatchell (2008) and Hale et al. (2008). In terms of incorporating the amplitude change attribute into the velocity change estimation, Chapter 6 will provide a full investigation.

1.3.3 Ranges of $\Delta V/V$

There are limited publications reporting the magnitude of velocity changes recovered from 4D real dataset with clear colour bars and quoted magnitudes (as experienced in the above Figure 1.11 and 1.9). Nevertheless, I summarise the magnitude of velocity changes $\Delta V/V$ in Table 1.1 together with the synthetic studies and educated guess (noted with the superscript symbol $*$). $\Delta V/V$ ranges from $0.8-10\%$ depending on the underlined mechanism and also elapsed time production, which is not stated clearly in these publications. For the geo-mechanic activities in overburden, the induced-velocity changes $\Delta V/V$ is quite small, only about $1-2\%$ (Vallhall, Shearwater, Field X) whereas in the reservoir, these changes are much larger, up to 10% (West Africa example). Most of these studies use different methods to invert for $\Delta V/V$ and the density contributions are not mentioned.

Field	**Magnitude(%)**	**Mechanisms**	**Publications**
Synthetic modelling for Vallhall	$0.8-1.0$	Extension in the overburden	Hall et al. (2005)
Field X	1^*	Extension in the overburden*	Edgar and Mastio (2017)
Synthetic	1.5^*	Extension in overburden	Edgar and Blanchard (2015)
Shearwater - gas condensate reservoir	$1.5-2^*$	Extension in the overburden	Staples et al. (2007a)
Norne	$2-6$	Water and gas injection	Aarre (2006)
Genesis	2.5	Moderate nature water drive, significant depletion	Rickett et al. (2007)
West Africa	$3-10$	Gas saturation	Chen et al. (2014)
Synthetic - deep water field	5^*	Fluid substitution, pressure is maintained	Routh et al. (2012)
An unconsolidated turbidite sand reservoir	10	Extension in the overburden or saturation	Griffiths et al. (2015)
Synthetic	10	N/A	Angus et al. (2016)

Table 1.1: Magnitude of $\Delta V/V$ from selected publication. Superscript $*$ denotes educated guesses.

1.3.4 The effects of time-lapse seismic processing on interpreting $\Delta V/V$

So far, we have discussed about the post-stack time-shifts (and amplitude change in Chapter 6) and various methods to invert for the time-lapse velocity changes. Before getting into the other developed methods in this thesis, it is important to aware of the effects of time-lapse seismic processing on the time-shifts and amplitude changes prior to interpret this quantity $\Delta V/V$. In Campbell et al. (2011), the authors used Foinaven field to present how the seismic data are improved by being processed in shot-domain (including water-column correction, demultiple), emphasizing the important role of 4D binning procedure in conjunction with regularization, and migration schemes. Figure 1.13 shows that the new precessing was able to bring the NRMS down to a level of 14%.

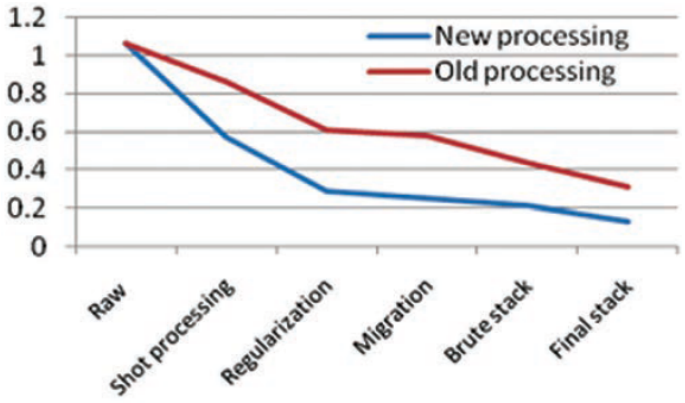

Figure 1.13: Reduction of NRMS throughout the processing sequence for the previous (red) and new (blue) processing. After Campbell et al. (2011).

I here focus on discussing two most important processing steps, which are NMO correction and migration methods. The choice of migration method could also affect the time-lapse time-shifts and amplitude changes. Figure 1.14 shows that the replacement of Kirchhoff depth migration for Kirchhoff time migration revealed better resolution and amplitude preservation.

Most recently, JafarGandomi et al. (2018) introduced specular dip-angle migration which significantly reduces 4D imaging noise. Figure 1.15 shows the comparison of this developed migration with the conventional Kirchhoff pre-stack depth migration. The map view on the left is a sum of negative amplitude around the reservoir horizon. Obviously from top row (conventional method) to the bottom row, the resolution is

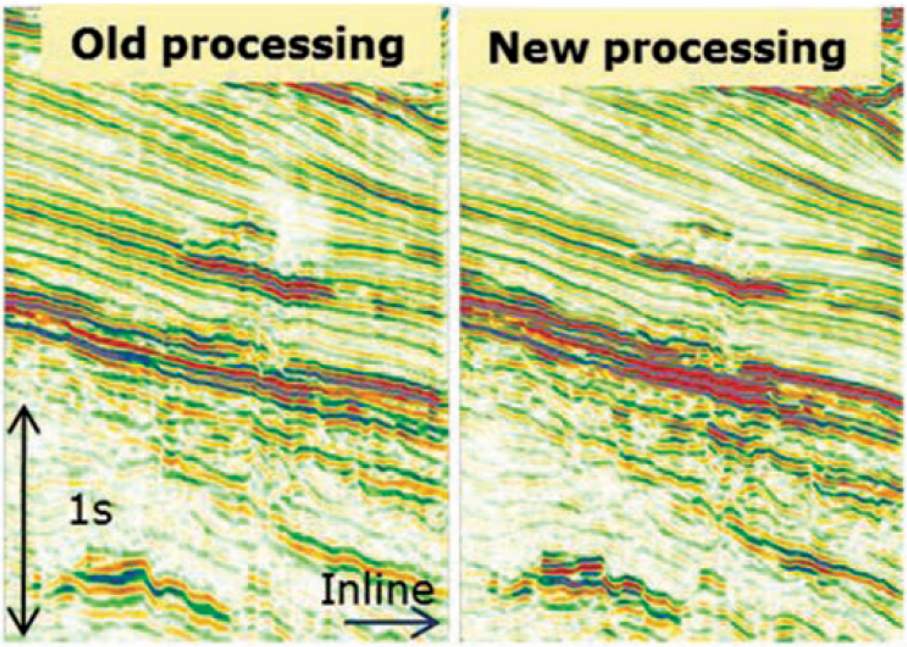

Figure 1.14: 3D section obtained with previous pre-stack time migration (left) and new pre-stack depth migration stretched to time (right). It is observed that the improved resolution and reduced amplitude stripping in the new migration scheme. After Campbell et al. (2011).

much better and the imaging is much clearer.

Beside that, the choice of either baseline or monitor velocity model also affects to the resultant of time-lapse seismic image as mentioned above in Figure 1.10. This choice of velocity is also important in NMO correction step as it might remove the angle dependence effect. If both baseline and monitor are NMO-corrected using the same baseline velocity model, the time-shifts between baseline and monitor traveltime is still observed and the angle dependence should be remained as well. However, if the baseline and monitor are NMO-corrected by their own velocity models (baseline and monitor, correspondingly), there is still time-shifts as each traveltime is shifted by different amounts but the angle dependence will be removed. This NMO correction will be further mentioned in Chapter 3.

1.4 Main challenges and objectives of this thesis

I have pointed out the need of velocity change models along with time-shift attribute. Figure 1.16 summarizes the use of $\Delta V/V$ in 4D seismic work-flow via route 3 and 4. In this thesis, these velocity changes will be inverted using the 4D seismic attributes,

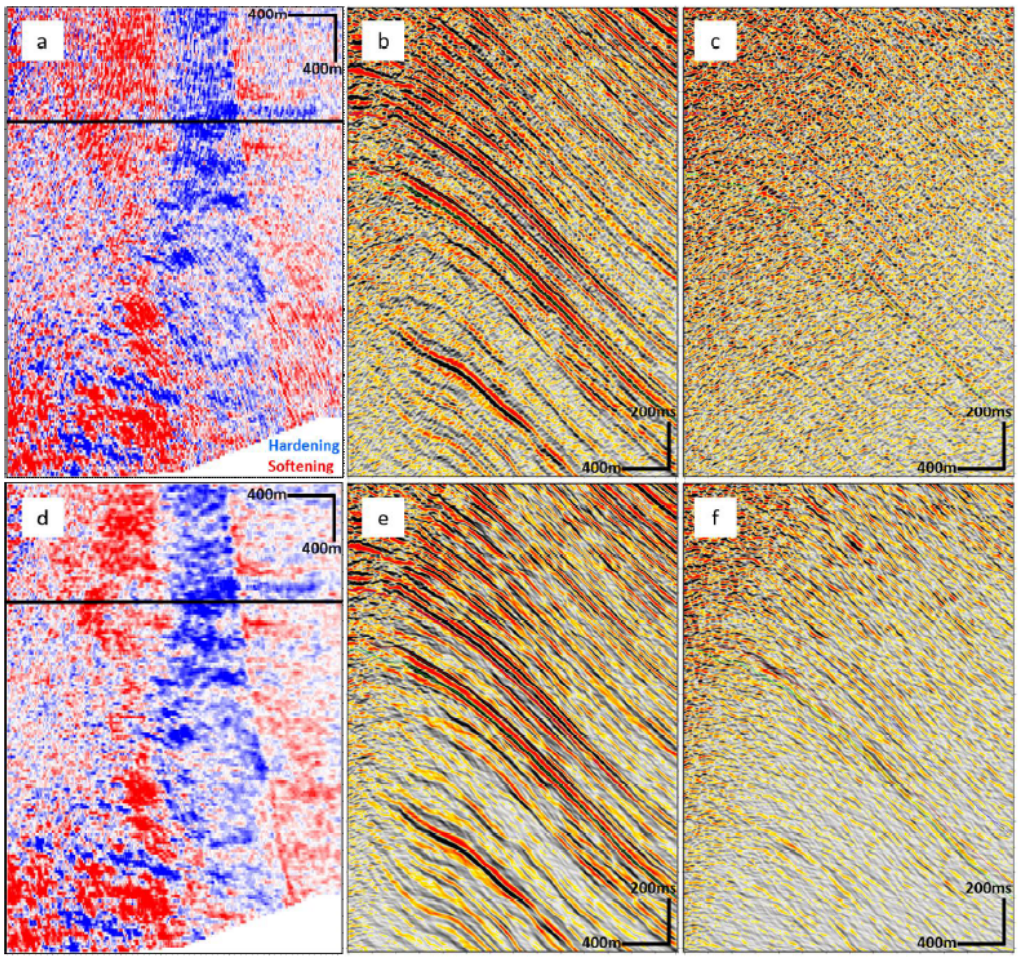

Figure 1.15: Conventional Kirchhoff pre-stack depth migration (a b c) compared to specular Kirchhoff pre-stack depth imaging (d e f) in map view (a d), 3D section (b and e) and in 4D difference section (c anf f). After JafarGandomi et al. (2018).

either via route 2 using the measured time-shifts as revised above or via route 1 using the 4D differences between baseline and monitor, which will be further explored in Chapter 6.

The work in this thesis aims to derive simple and quick yet stable and efficient methods to estimate time-lapse velocity changes. Further, the thesis aims to explore the solutions in such the fashion in different 4D seismic domains. These objectives come from my awareness of following challenges of 4D seismic and the developed methodologies are proposed to tackle them:

- **Computational time**

  Being aware of the fast developments of 4D seismic with many more monitor surveys aquired, I see that finding a fast, direct but stable scheme is essential. Using a full inversion scheme which costs months (Grandi et al., 2009b) might be too slow for the immediate decisions. Therefore, I seek a data-driven

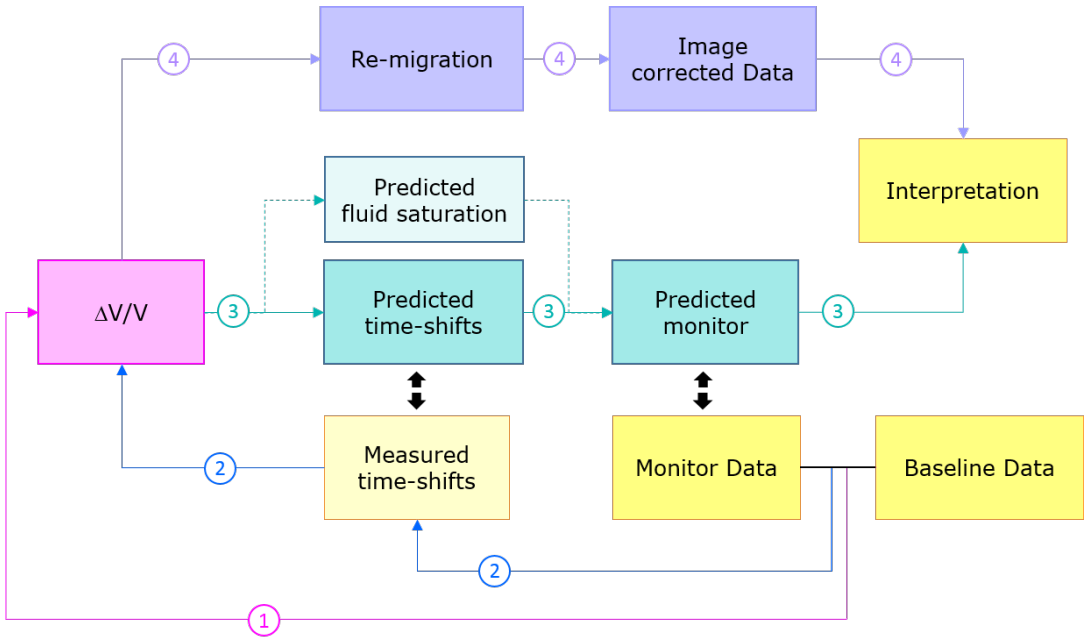

Figure 1.16: The use of $\Delta V/V$ quantity in 4D seismic work-flow. After the quantity is inverted either from (1) Baseline and Monitor seismic data directly or (2) measured time-shifts, $\Delta V/V$ is used for modelling (3) either time-shifts or fluid saturation (hence amplitude changes) or to directly reconstruct the best matched monitor with the monitor data. The quantity is also an essential input for (4) re-migration.

inversion approaches which quickly yet efficiently recovers the relative velocity changes in very few manipulations. I hence avoid almost all the iterative inversion schemes but rather develop a stable and invertible forward operator.

- **Post-stack domain - an angle limited solution**

  It has been a standard routine to work on post-stack seismic data, which has high vertical solution. Meanwhile the inversion inherently carries a certain degree of uncertainty, using post-stack time-shifts or 4D seismic to invert is a safe good choice. However, the post-stack domain is limited in only providing the almost zero-offset solution. Further, there is competition from the contributions of velocity and thickness changes to observed time-shifts as expressed in Equation 1.3. For examples, I pick up here two scenarios, geo-mechanics and gas injection. The time-shift in the overburden from geo-mechanical effects tells us about the changes in both thickness and velocity. Also, for gas injection, it captures the coupled effects of volume and velocity changes. Therefore, we need another independent measurement, either from another angle-stack or from amplitude changes. In this study, in spite of the assumed negligible effect of $\Delta z/z$, my attempts of estimating $\Delta V/V$ in angle-stack domain and

data domain establish the methodologies for further applications/implications. This issue will be well-invested in the last chapter.

- **Complication of angle-stack domain**

  Two main challenges of working in angle-stack domain are signal to noise ratio and computational cost due to multiplication of data volumes. Interestingly, these are two generic issues of any inversion problems. In order to overcome these challenges, in this work I propose a re-gridding to keep the algorithm the same throughout. Further, the inversion is achieved through a modelling operator, which makes this method very robust. The method works well on angle-stack domain of the chosen dataset without a need of constraint or regularisation, under the assumption of straight-raypath.

- **Ignorance of amplitude attributes**

  Many studies ignore the amplitude changes term as it always comes along with the wavelet and the its coupling effects with time-shifts. Also, this attribute is easily damaged during the processing. Therefore, I introduced the Gaussian reconstruction method as mentioned above to stabilize the inversion and the solution is quickly convergent.

1.5 The work of this thesis

I use three different 4D seismic data domains which include post-stack time-shifts, post-stack 4D seismic (time-shifts and amplitude) and angle-stack time-shifts. The work are divided into 4 following packages:

- **First step - Time-shift measurement**

  The input data of this study are time-shifts. I here use code provided by Hale (2009) and my colleagues (Ji, 2017; Hodgson, 2009) to measure the time-shifts for the next inversion step.

- **Second step - Post-stack time-shift inversion**

  Inspired from a quick and simple fashion of the inversion using the modelling operator, I set up the governing equations relating time-shifts and velocity changes through a matrix operator. The matrix describes the velocity changes model corresponding to the understanding of nature of time-shifts data. And

its inversion must be highly invertible and stable. Because of inherent noise in time-shifts data, some smoothing terms are added to stabilize the inverted time-shifts. I then parameterise the velocity changes using basis functions based on a Gaussian Mixture Model (GMM), find the corresponding function for the time-shifts and rewrite the governing equation through the basis functions. By expressing the model and data through the analytical forms, the results are achieved at highly stable level, open a door to angle-stack or 4D seismic domains to overcome the limitation of signal to noise ratio.

- **Third step - Angle-stack tomographic inversion**
  A literature review on time-shifts versus offset (TVO) was first carried out to examine the TVO relationship before doing the inversion. I remain the same inversion fashion of using the modelling operator and establish the tomographic matrix, which links the ray path traveltime through the velocity changes model and angle-stack time-shifts. Here I choose angle-stack domain to describe the dependence of time-shifts to offset.

- **Fourth step - Post-stack 4D seismic inversion**
  Including amplitude effect of 4D seismic data into the govern equation, I invert for the velocity changes by optimisation. The coupling effect of time-shifts and amplitude are complex hence the previous GMM are integrated to possibly extract more precise inverted velocity changes.

1.5.1 Thesis outline

Based on the challenges and the work packages discussed above, I decided to entitle this thesis *"Estimation of time-lapse velocity changes from time-lapse seismic data"*. The remainder of this thesis is divided into six chapters based on the above addressed challenges as follows:

Chapter 2 presents three different methods to invert for velocity changes using post-stack time-shifts. The two former methods of Layer-stripping and Damped-Least square solution are adapted from the literature. I develop a new method, the third one - Gassian reconstruction which provides a quick and stable answer.

Chapter 3 first describes the evolution of offset/angle dependent time-shifts from the literature. Several synthetic examples are then provided to numerically examine

this time-shifts versus offset (TVO) relationship.

Chapter 4 explains my new developed algorithm, *time-lapse tomography*, which uses straight-ray assumption to recover the perturbed velocity changes from angle-stack time-shifts.

Chapter 5 implements the above three post-stack time-shift inversion methods and angle-stack time-lapse tomography for a field dataset in the North Sea. This is a high pressure high temperature (HPHT) reservoir and has dominant geo-mechanical effects in reservoir, overburden and underburden. This study uses three seismic vintages of baseline 2001 and two monitors 2004 and 2013. Time-shift data are measured by three popular methods which are: CLM, DHF and NLI as mentioned above. These methods work well on this dataset with quick and stable solutions as expected.

Chapter 6 goes beyond the time-shift inversion. I here directly input baseline and monitor traces instead of measured time-shifts for velocity changes recovery by employing Gaussian reconstruction method mentioned in Chapter 3. Both time-shifts and amplitude changes are simultaneously taken into account in this inversion. The algorithm quickly converges after 4 to 5 iterations.

Chapter 7 closes the thesis with the conclusions, discussion and put forward for further future research.

1.5.2 Publications

Specific aspects of this thesis have been published and presented in the conferences:

- Nguyen, P. K. T., MacBeth, C., and Mangriotis, M. D. (2017). Estimation of Time-lapse Velocity Changes Using Gaussian Reconstruction. In 79th EAGE Conference and Exhibition 2017, Extended Abstract, B101.
- Nguyen, P. K. T., MacBeth, C., and Mangriotis, M. D. (2018). Applicating time-lapse time-shift inversion using angle-stack tomography. In 'Saint Petersburg 2018. Innovations in geosciences time for breakthrough, Extended Abstract, B101.

Chapter 2

Time-shift inversion at zero-offset

ABSTRACT

This chapter focuses on methods for inverting to time-lapse velocity changes $\Delta V/V$ using measured time-shift data from the baseline and monitor seismic surveys. After an extensive review of measurement methods in the literature, I firstly employ and describe two selected methods, which are layer stripping method and damped least squares solution. Noise amplifying from layer stripping method is treated by injecting a standard regularization term in damped least squares method that helps to smooth the solution. After this, a new method based on a Gaussian mixture model (GMM) is developed. $\Delta V/V$ is rewritten from a number of pre-set Gaussian grid and hence the time-shifts, Δt, can be represented through an analytic form which makes the inversion become robust and stable. This chapter limits itself in the post-stack domain where the source and receiver are assumed to be coincident at zero-offset. Thus, here we are looking at the vertical seismic rays and do not target a complete 100% solution, but a simple, quick yet stable outcome. All the methods are working in time domain.

2.1 On the post-stack time-shift inversion

As introduced in the previous chapter, time-shifts come from the time-lapse changes in thickness and velocity. Therefore, it is essential to find the ways to recover these changes from time-shift data. This has been an active topic and the existing methods are divided into two main following groups. This chapter limits itself to the post-stack domain, in which only the vertical direction of wave propagation is considered.

2.1.1 Differentiation group

Time-shift is an accumulative quantity, in which the measurement at a particular position is the summation of the time-shifts of all layers above. It is created by interval changes in layer thickness and/or velocity. Differentiation can be used as a way of backing out these interval variations. Rickett et al. (2007) introduced a new terminology in time-lapse seismic, called *time-strain*, $\Delta t/t$. This can be obtained by differentiating the time-shift function over a certain time window. Assuming small changes in time-lapse amplitude, the time-shift function, $\tau(t)$, is related to the monitor and baseline traces by:

$$m(t) \approx b(t + \tau(t)). \tag{2.1}$$

Considering two geological events E and F at the corresponding traveltime t_E and t_F, the differentiation of the time-shift function, $\tau(t)$, over this time period yields the fractional change in traveltime between these two events as:

$$\frac{\Delta t_{EF}}{t_{EF}} = \frac{\tau(t_F) - \tau(t_E)}{t_F - t_E}. \tag{2.2}$$

Given a relative small time window, this equation returns to a differential form as

$$\frac{\Delta t}{t} = \frac{d\tau}{dt} \tag{2.3}$$

Earlier, Landrø and Stammeijer (2004) also derived this quantity of $\Delta t/t$ from the time-lapse thickness and velocity changes, but referred to it as *normalized time-shift* (Equation 1.3). From here, a common fast-track approach to estimate the velocity

changes from the measured time-shift is to drop out the $\Delta z/z$ term in Equation (1.3) as:

$$\frac{\Delta V}{V} \approx -\frac{\Delta t}{t}. \tag{2.4}$$

The velocity changes are now derivative of time-shift Δt over a small time window t. In Figure 2.1, I show a field example at Genesis field of time-strain $\Delta t/t$ obtained from differentiating the time-shift function $\tau(t)$. The velocity changes $\Delta V/V$ are hence just opposite polarity of Figure 2.1 (right).

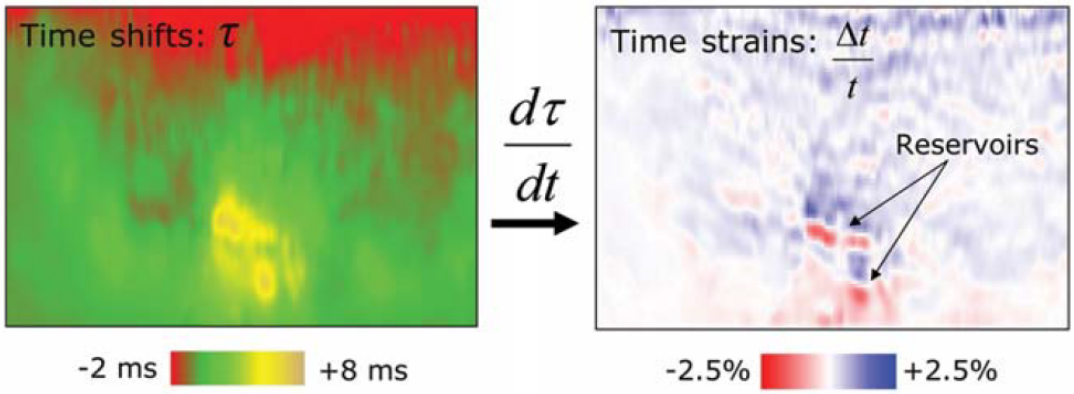

Figure 2.1: A turbidite sandstone Genesis field example: The left is time-shift function $\tau(t)$ and the right is time-strain $\Delta t/t$ obtained by differentiating the time-shift function. According to Equation 2.4, the velocity changes $\Delta V/V$ are opposite to $\Delta t/t$. An increase in $\Delta t/t$ indicates a decrease of $\Delta V/V$, which is assciated to extension in the overburdern due to reservoir depletion. After Rickett et al. (2007).

This differentiation method of estimating velocity changes has been widely applied in many studies such as Aarre (2006); Rickett et al. (2007); Chu et al. (2012), to name a few, when considering the saturation and/or pressure changes at a stiff rock reservoir (which means $\Delta z/z \approx 0$). However, this is an unstable operator that is sensitive to noise hence less reliable and hard to interpret. We can obviously observe these noise in the background of inverted time-strain in Figure 2.1 (right). Chu et al. (2012) combines the time-shift information from different angle-stacks and linearly fits them into a straight line as:

$$\Delta t_{center} = at + b. \tag{2.5}$$

where Δt_{center} is the time-shift at the center of the running, b is the fitting line intercept and the best fitting parameter a is time-strain $\Delta t/t$ and hence velocity changes $\Delta V/V$.

2.1.2 Trace warping group

The warping approach is one category of methods used in measuring time-shift. By aligning the monitor and baseline traces, the method returns the shift in traveltime between them. Williamson et al. (2007) applied this method in a new fashion, in which the technique warps for the time-lapse velocity perturbation instead of simply the time-shift. Dependence of time-shifts on velocity changes is explicitly expressed in the equation as:

$$m(t_i) = b\left(t_i + \sum_{k=1}^{i} -\frac{\Delta V}{V}\right) + \Delta A. \tag{2.6}$$

where i is the index of sample number, k is the current running index and ΔA indicates the change in amplitude and is expressed as a function of $\Delta V/V$. The warping problem is then posed as matching the shifted monitor trace to the amplitude-adjusted baseline trace. A common least square optimisation algorithm can be applied in Equation 2.6 to minimize the difference of the left and right hand side of the equation and return the time-lapse velocity perturbation. The time-shift is used as an optimization parameter. It should note that, according to Equation 1.3, the physical strain, $\Delta z/z$, is assumed to be negligible when substituting the velocity change quantity into the shifted monitor trace in equation 2.6.

The novelty of the Wiliamson's method is that it directly inverts for velocity changes from time-lapse seismic traces instead of using the measured time-shift data. As an outcome of this direct inversion, Williamson's method can avoid the inevitable errors in time-shift measurements. The method proves to be stable and the velocity change attributes can be estimated in broadband down to zero frequency when aiming to determine the velocity changes for each sample. Also, the method simultaneously takes account of the effects of not only time-shifts but also amplitude changes. Further analysis of this amplitude term will be discussed in Chapter 6. Baek and Keho (2015) developed this method in depth domain, in which the velocity changes are functions of depth, instead of time, with the inclusion of the amplitude term. Grandi et al. (2009a) implements Williamson's method by modifying this algorithm to invert for time-strain which carries both velocity changes $\Delta V/V$ and physical strain $\Delta z/z$, instead of velocity changes only but excluding the amplitude change term. Figure 2.2 shows the recovered $\Delta V/V$ due to a expansion overburden (blue) accommodating reservoir compaction (red) from a HPHT reservoir (a) and due to

water injection (blue) and gas injection (red) from a turbidite system. Beyond the consistency to production activities, the recovered $\Delta V/V$ seems to be smooth and stable than the example of differentiation method in Figure 2.1.

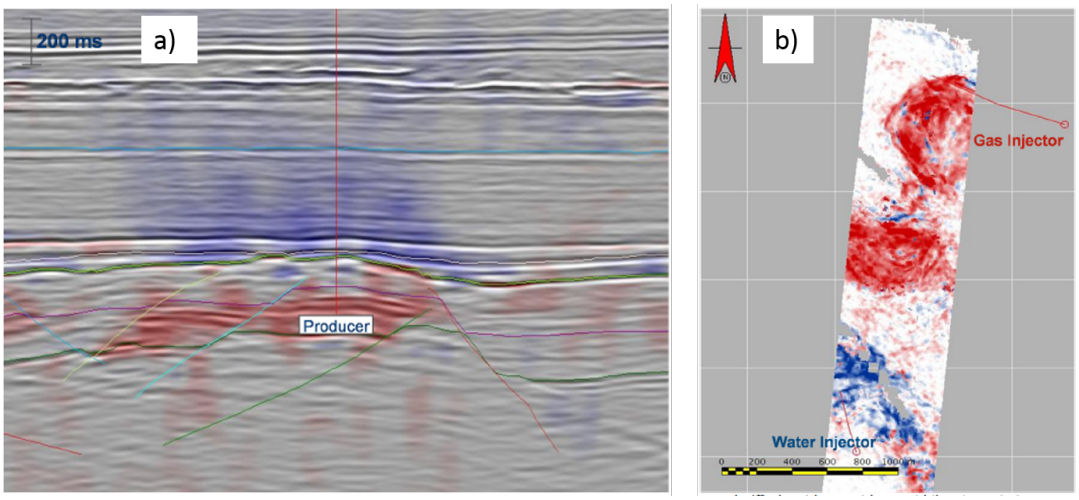

Figure 2.2: Recovered $\Delta V/V$ using Williamson's method without the amplitude change term from (a) HPHT reservoir with strong extension in the onverburden (blue - relaxtion) and compaction in the reservoir (red - compaction) and (b) turbite channel with north gas injection (red - $\Delta V/V$ decreases) and south water injection (blue - $\Delta V/V$ increases). No quantitative colour scale is available. After Grandi et al. (2009a).

2.2 Time-shifts and velocity change equation

Given:

- Baseline velocity field, $V(l)$
- Time-lapse velocity changes, $V(l) + \Delta V(l)$

Assume no change in ray-path from baseline to monitor, the time-shift, Δt, is then calculated by traveltime differences between baseline and monitor as:

$$\Delta t = \int_0^l \frac{\mathrm{d}l}{V(l) + \Delta V(lz)} - \int_0^l \frac{\mathrm{d}l}{V(l)}, \tag{2.7}$$

or

$$\Delta t = \int_0^l \left(\frac{1}{1 + \dfrac{\Delta V(l)}{V(l)}} - 1 \right) \frac{\mathrm{d}l}{V(l)}. \tag{2.8}$$

Converting the equation into the two-way traveltime domain, in which the velocities are sampled as the functions of traveltime, t:

$$\Delta t = \int_0^t \left(\frac{1}{1 + \dfrac{\Delta V(t)}{V(t)}} - 1 \right) \mathrm{d}t, \tag{2.9}$$

where

$$\mathrm{d}t = \frac{\mathrm{d}l}{V(l)}. \tag{2.10}$$

This equation collapses to:

$$\Delta t = \int_0^t \vartheta(t)\mathrm{d}t, \tag{2.11}$$

where

$$\vartheta(t) = \frac{1}{1 + \dfrac{\Delta V(t)}{V(t)}} - 1. \tag{2.12}$$

The equation 2.11 relates the time-shifts, Δt, to the relative velocity changes, $\Delta V/V$, in time domain through the quantity, ϑ. From here, the equation can be discretised and applied to the post- or angle-stack domain in my subsequent work. ϑ can be approximated as:

$$\bar{\vartheta} \approx -\frac{\Delta V}{V} \tag{2.13}$$

by using a first-order Taylor approximation, which is:

$$\frac{1}{1 + \dfrac{\Delta V}{V}} \approx 1 - \frac{\Delta V}{V}. \tag{2.14}$$

Equation 2.11 then becomes:

$$\Delta t \approx \int_0^t \bar{\vartheta}\mathrm{d}t. \tag{2.15}$$

However, in order to obtain the best degree of accuracy, this thesis tries not to use this unnecessary approximation and prefers to use the quantity, ϑ, for relative time-lapse velocity changes instead of $\Delta V/V$. Also noted that the work in this thesis is in the time-domain, hence all the quantities $V, \Delta V$ and ϑ are re-

ferred instead as $V(t), \Delta V(t)$ and $\vartheta(t)$. For easy following, Table 2.1 provides the colour convention used in this thesis, in which red indicates the velocity changes $\Delta V/V$ slowdown/extension and reversely, blue indicates the velocity changes $\Delta V/V$ speedup/compaction.

Reservoir scenarios	Δt	ϑ or $\overline{\vartheta}$	$\Delta V/V$	Color convention
Compaction	↓	↓	↑	- 0
Gas injection	↑	↑	↓	0 +
Water injection (in water pool)	↑	↑	↓	0 +
Water injection (in oil pool)	↓	↓	↑	- 0

Table 2.1: Colour convention used in this thesis for a few common reservoir scenarios.

2.3 Layer stripping method

The terminology *"layer stripping"* was literately introduced by Yagle and Levy (1985). This principle was utilized earlier by Clarke (1984) and Shiva and Mendel (1983) under the term of *"stripping off the effect of the stratification layer by layer"* or *"layer-recursive procedure"*, respectively. However, Yagle and Levy (1985) commented that these algorithms were complicated as they require an iterative solution or maximum-likelihood estimation at each step. He then simplified the method in a straightforward fashion by assuming a continuous medium, which allows differential updates of the parameters of the medium.

This is an inversion method and as its name suggests, the method produces subsurface images layer by layer following a top-down procedure. The method operates differentially and the effects of each layer is recursively computed and then stripped away so that the size of problem is reduced and the computational cost is much cheaper. It has been commonly applied in the seismic inversion problem to recover the elastic properties of the medium, such as in Lines et al. (1984) used for vertical seismic profiles. Justice (1990) extended layer stripping to two dimensions whilst Singh (1990) applied it o the seismic waveform. Recently, Hondori et al. (2013) combined the layer stripping with reflectivity inversion to develop *"a random layer*

stripping method" for reflectivity inversion, in which the reflectivity series do not follow a top-bottom procedure, but are determined from a completely random scheme. The advantage of layer stripping is direct solution to the inverse problem for each succeeding layer (Justice, 1990). The disadvantage of layer stripping is at the propagation of unavoidable data errors from all the previous layers. However, this can be constrained by optimization solutions. In time-lapse seismic application, Rickett et al. (2007) used the differentiation method and mentioned it as an effectively way to do layer stripping.

2.3.1 Implementation of layer stripping

In this section, I employ the layer stripping method to invert for time-lapse velocity change using time-shift data. The algorithm is developed under the guidance and understanding of the real field data (data-driven) and is based on the derived relation of time-shift and velocity changes. The input data is post-stack time-shifts vertically measured from post-stack time-lapse seismic data, which implies small offsets or almost vertical ray-paths. Each time-shift trace is discretised by a time sampling rate, sr, into N time samples. Figure 2.3 shows the distribution of the time-lapse perturbed velocity model, ϑ_{ij}, where $i = 1 : M$ indicates the index number of traces and $j = 1 : N$ indicates the index number of time samples. At a single trace, three near offset rays indicate to the accumulative traveltime and the whole trace system can be moved to the next traces. Discretizing Equation 2.11, the time-shifts for a single trace Δt_i can be rewritten as:

$$\Delta t_i = \sum_{j=1}^{N} t_{ij}\vartheta_{ij}. \tag{2.16}$$

where t_{ij} is the traveltime spent in each cell. In the case of vertical rays, this traveltime t_i is the time sampling rate sr. Equation 2.16 can be more simply by dividing by the time sampling rate to transfer to dimensionless domain. The time-shift Δt_i now becomes fractional time-shift ΔT and the summation operator $\sum_{j=1}^{N}$ can be written as a matrix when populating the ray system over all the traces. The

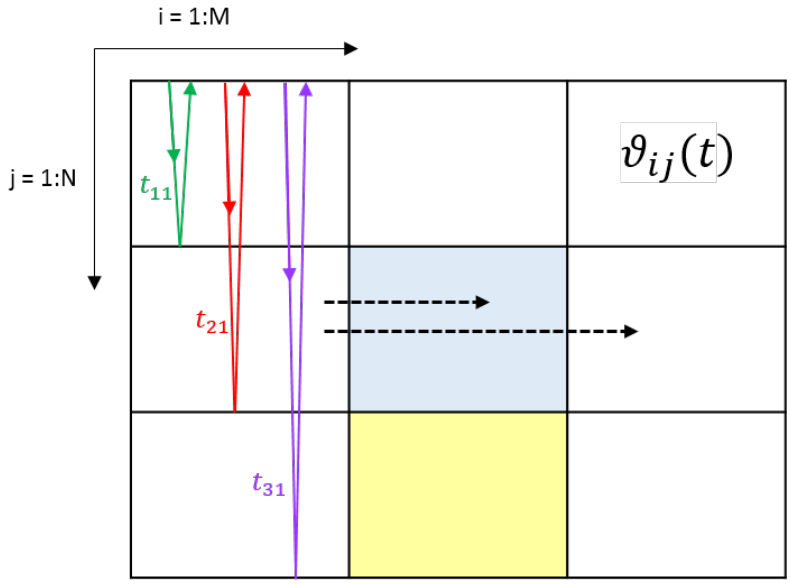

Figure 2.3: Time-lapse perturbed velocity model, ϑ_{ij}, with two non-zero ϑ_{ij} coded in blue and yellow cells. The schematic rays indicate the accumulative traveltime spent at each time sample.

resultant zero-offset equation in matrix form is:

$$\underbrace{\begin{bmatrix} 1 & 0 & 0\dots & 0 \\ 1 & 1 & 0\dots & 0 \\ 1 & 1 & 1\dots & 0 \\ \vdots & \vdots & \vdots\dots & \vdots \\ 1 & 1 & 1\dots & 1 \end{bmatrix}}_{\mathbf{D}} \underbrace{\begin{bmatrix} \vartheta_{11} & \vartheta_{12} & \vartheta_{13} & \dots & \vartheta_{1M} \\ \vartheta_{21} & \vartheta_{22} & \vartheta_{23} & \dots & \vartheta_{2M} \\ \vartheta_{31} & \vartheta_{32} & \vartheta_{33} & \dots & \vartheta_{3M} \\ \vdots & \vdots & \vdots & \dots & \vdots \\ \vartheta_{N1} & \vartheta_{N2} & \vartheta_{N3} & \dots & \vartheta_{NM} \end{bmatrix}}_{\mathbf{x}} = \underbrace{\begin{bmatrix} \Delta T_{11} & \Delta T_{12} & \Delta T_{13} & \dots & \Delta T_{1M} \\ \Delta T_{21} & \Delta T_{22} & \Delta T_{23} & \dots & \Delta T_{2M} \\ \Delta T_{31} & \Delta T_{32} & \Delta T_{33} & \dots & \Delta T_{3M} \\ \vdots & \vdots & \vdots & \dots & \vdots \\ \Delta T_{N1} & \Delta T_{N2} & \Delta T_{N3} & \dots & \Delta T_{NM} \end{bmatrix}}_{\mathrm{y+e}}$$

or

$$\mathbf{D}\mathbf{x} = y + e. \tag{2.17}$$

where x is the unknown velocity changes, y is input time-shift data with the noise e. $\mathbf{D}$ is a square and lower triangular matrix and is invertible. Furthermore, this is an even-determined system where the number of data, ΔT, equals to the number of unknowns, ϑ. Therefore, the solution is unique and is as following:

$$\hat{\mathbf{x}} = \mathbf{D}^{-1}(y + e), \tag{2.18}$$

where ˆ indicates the closest to the truth solution and

$$\mathbf{D^{-1}} = \begin{bmatrix} 1 & 0 & 0 & ... & 0 \\ -1 & 1 & 0 & ... & 0 \\ 0 & -1 & 1 & ... & 0 \\ \vdots & \vdots & \vdots & ... & \vdots \\ 0 & 0 & 0 & ... & 1 \end{bmatrix}$$

Thus, ϑ is easily solved. The inverse of the $\mathbf{D}$ operator is exactly the differential operator hence this method may also be thought of differentiation.

2.3.2 Field data example

I next apply the method above to field data for the An'Teallach field. This field is located in the West of Shetland, North Sea. It has gas injection into a sandstone aquifer, which is sufficiently large to accommodate the gas without over-pressuring the structure. Figure 2.4 shows the seismic of baseline in 1999 and monitor in 2002 after gas injection. The injected gas saturation slows down the velocity changes so that the seismic responses are push-down.

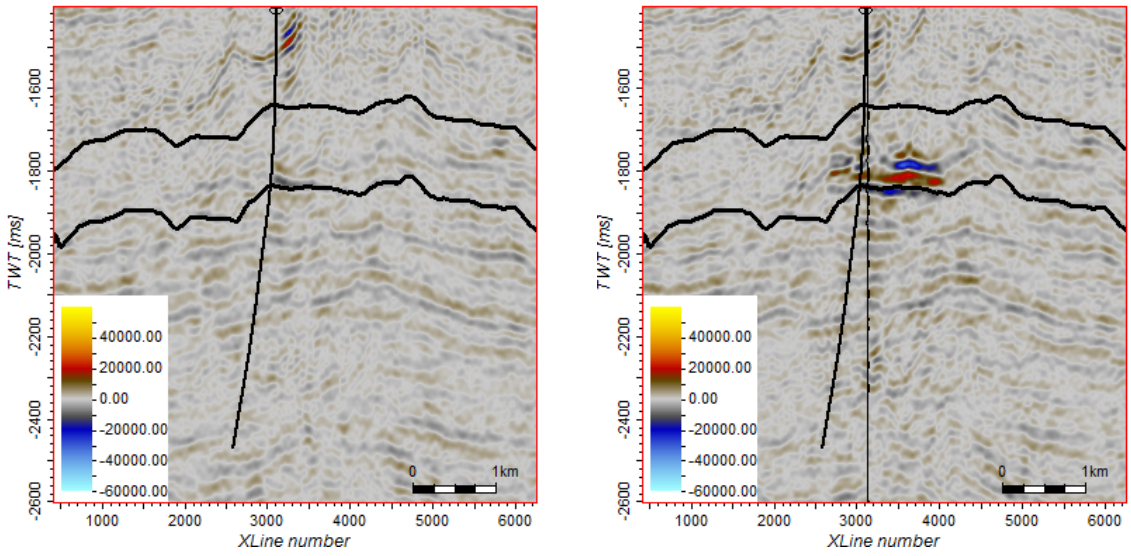

(a) (b)

Figure 2.4: An'Teallach field 4D examples of gas injection from (a) Baseline survey acquired in 1993 to (b) monitor survey acquired in 2002. The two black lines indicate the top and base of the sand volume. About 16 ms delay in traveltime observed in (b) in compared with (a) due to injected gas saturation as shown in the next Figure 2.5.

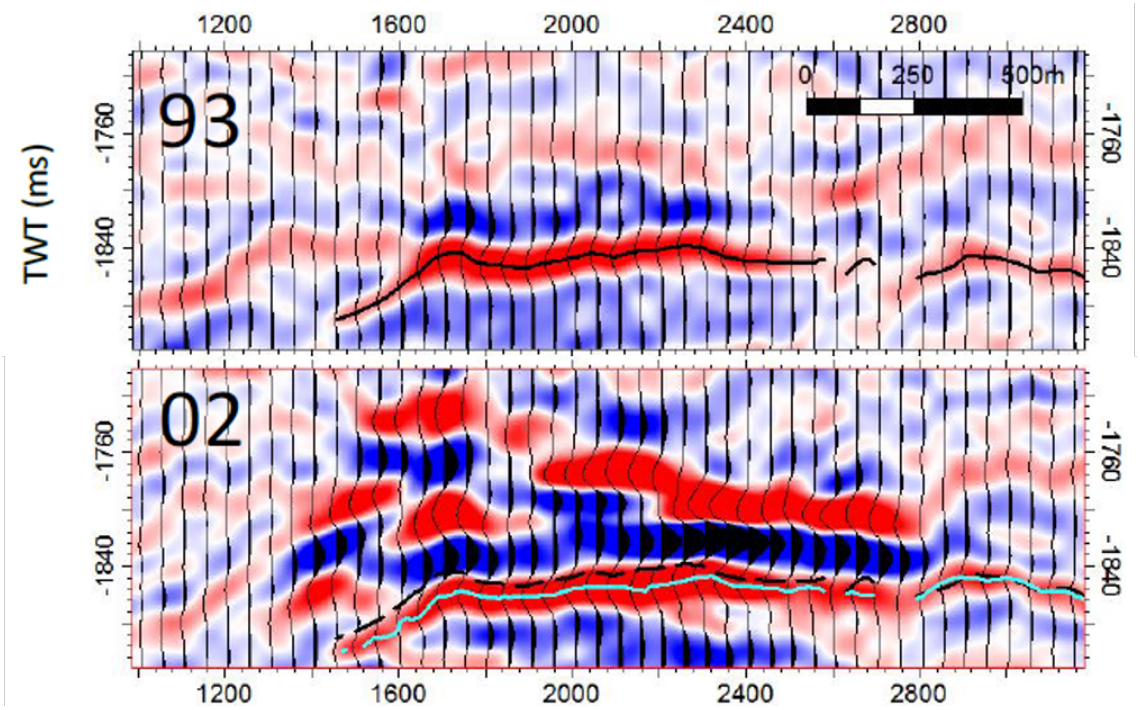

Figure 2.5: Baseline (top) and monitor (bottom) seismic sections with the interpreted horizons show about 16 ms shifted in the traveltime. The original black line in the baseline 1993 is shifted to the cyan line in the monitor 2002. Courtesy of Maren Joa.

The time-shift used for the inversion is measured by NLI method and shown in Figure 2.6a. As stated by Ji (2017), this NLI time-shift measurement method returns the most stable and smoothest time-shift thanks to its global solution and constraints (Appendix B) so that the velocity change can be recovered trustfully. After 9 years of injection, the time-shifts of up to 15 ms appear in the reservoir and underburden due to its accumulative nature. Using layer stripping, the recovered interval velocity changes ϑ are shown in Figure 2.6b. Since this is an even-determined problem and forward operator is invertible, hence there is nothing left in the residual (zero residual) so that I do not show this here purposely. Approximately 8% velocity changes are observed in the reservoir area where the gas is injected. It is interesting to observed the speed-up (blue) and slowdown (red) below the reservoir, at and below 2200 ms, correspondingly as these events do not relate to the gas injection activity. This could be due to errors in time-shift measurements.

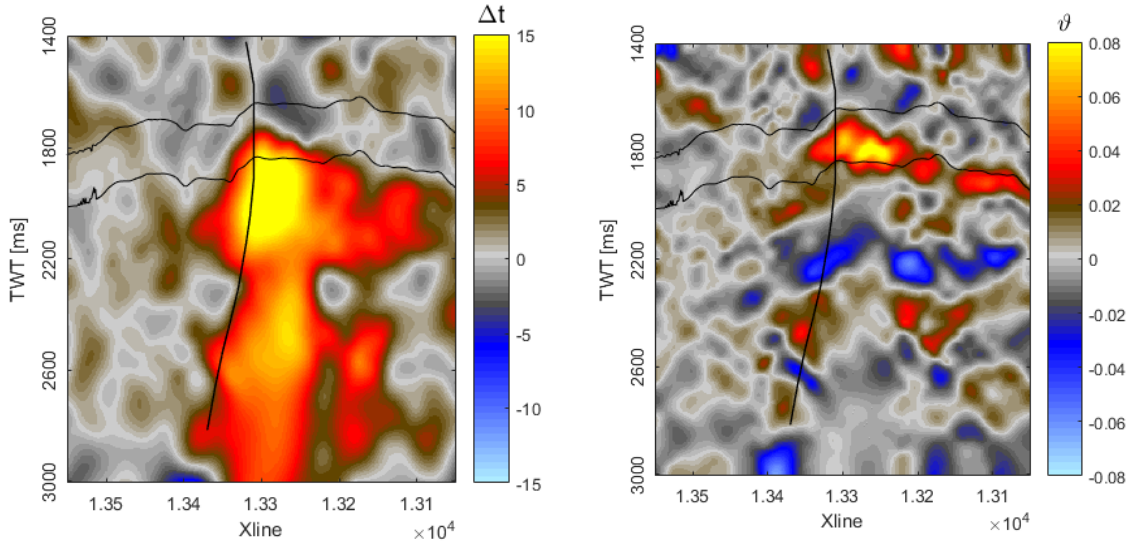

(a) (b)

Figure 2.6: (a) Time-shift measurement from baseline and monitor seismic surveys using NLI method used for the inversion. (b) Corresponding recovered interval ϑ using layer stripping. Obviously, the method amplifies the noise in the surrounding area due to the differential operator $\mathbf{D}$. According to layer stripping, gas injection over 9 year periods causes about 8% slowdown velocity changes in the reservoir. The speed-up (blue) and slow-down events below the reservoir (at and below 2200 ms) could be due to the errors in time-shift measurement.

2.4 Damped least squares solution

There is always noise inherently present in the data. Directly inverting the data will put the imprint of noise into the solutions. Therefore, it is essential to find a way to smooth either the data or regularise the solution. This section explores the available options and then explains the chosen method and its implementation with a synthetic example.

2.4.1 Implementation

There is always noise present in time-shift data so that the solution above will also perfectly fit the noise if it is inverted as it stands. Thus, I aim to provide a regularisation term to balance the solution for smoothness, however this also effects accuracy. Regarding noise in time-shift data, there are two solutions in the literature, either smooth the data or smooth the recovered model. The nature of time-shift data is quite smooth as an accumulative property and the measured time-shift data is also already quite smooth because of employing certain kind of smoothness in

time-shift measurement methods. Therefore, it seems not necessary to smooth the time-shift data rather than the inverted $\Delta V/V$. I choose to smooth the second option ($\Delta V/V$) by using well-known Tikhinov regularization theory as a standard way to stabalize the inversion. Providing a regularisation term that balances the resolution of the solution and noise contribution is necessary. The optimal damping factor is determined by the knee point curve (or L-curve) using Hansen (1994):

$$OF_{DLSQ} = \|y - \mathbf{D}\hat{x}\|_2 + \gamma \|\mathbf{\Gamma}\hat{x}\|_2 . \tag{2.19}$$

where $\mathbf{\Gamma}$ is Tikhinov matrix, γ is damping factor, y and $\hat{x}$ are defined as in Equation 2.17. The key to success in this optimization is choosing an optimal damping factor γ. I use the L-curve, which is a trade-off curve in logarithm space, between the norm of the misfit and penalty term that should be controlled (Figure 2.7). By adding regularization, we are able to damp these contributions and keep the norm of this penalty term at a reasonable size. If too much regularization or damping (more filtering) is imposed on the solution, the solution will not fit the given data hence the misfit will be large. But if too little regularization is imposed, the fit will be good but the solution will be dominated by the contributions from noise in the data.

There are also other options to solve the even-determined problem, such as using Occam's inversion as detailed in Lizarralde and Swift (1999). For determining the optimal factor, a Gaussian noise distribution assumption and statistics or Morozov's discrepancy principles are alternatives (Anzengruber and Ramlau, 2010).

2.4.2 Field data example

I use the same time-shift measured from Figure 2.6a for the An'Teallach field and apply the damped least square solution to invert for velocity changes. A range of 61 optimal damping factors from 0.1 to 1 are tested and superimposed on the L-curve with corresponding misfit norm $||y - \mathbf{D}\hat{x}|\,|_2$ and penalty norm $||\mathbf{\Gamma}\hat{x}|\,|_2$ as shown in Figure 2.7. The chosen γ from this procedure is 794.

Using this optimal damping factor, the damped-least-square solution is resolved as in Figure 2.8a and the corresponding absolute time-shift residual in Figure 2.8b is

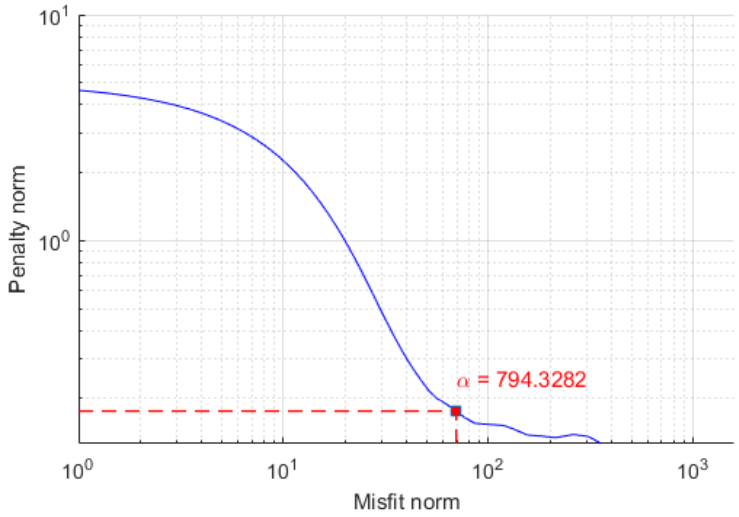

Figure 2.7: L-curve in logarithm plot and the most optimal damping factor $\alpha \approx 794$ denoted by red square box for damped least square solution at An'Teallach.

obtained. The regularization term helps to smooth the solution, ϑ, and leaves some noise in the residual as expected. Obviously, the noise is better handled in this inverted $\Delta V/V$ than the layer stripping method. The speed-up event below the reservoir (2200 ms) seems to fade away to some degree. However, in the reservoir, the body sand seems to be a little bit thicker and much narrower which makes it seem not geologically realistic.

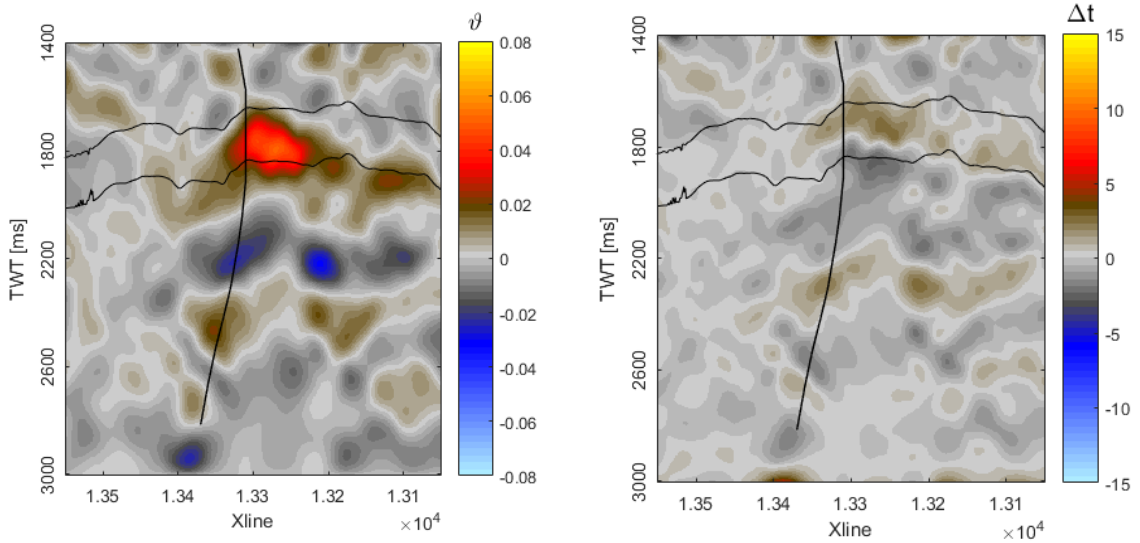

(a) (b)

Figure 2.8: (a) Inverted ϑ using Damped-Least-square and (b) absolute time-shift residual. ϑ is smoother yet maintaining the main features of slow-down and speed-up velocity changes in the reservoir and underburden, respectively. However, the scale is smaller, about 4-5% of recovered velocity changes in the reservoir. In terms of geological interpretation, the speed-up event below the reservoir seems to fade away but the sand body in the reservoir becomes a bit thicker and more narrow which makes it seem unrealistic.

2.5 Gaussian reconstruction

So far, I have described my implementation of two existing methods for inverting to velocity changes (or variable ϑ). The layer stripping inverts samples from top to the bottom so that the noise has a chance to accumulate and amplify as the number of samples are increased. Further, this method responds strongly to inherent noise in the data. The damped least squares provides a trade-off solution to balance the noise and resolution of the solution by introducing a regularization term, which is of course adding an "artificial" quantity to the solution. As an alternate approach, I develop a new algorithm of Gaussian reconstruction to invert for ϑ.

2.5.1 Why is Gaussian?

Gaussians have been applied in many scientific fields in many different ways. For example, they appears as the density function of a normal distribution in statistics and probability theory; or serve as Gaussian filters in signal processing. Here, I focus on a mixture model of many Gaussians – the fundamental quantity of the radial basis function applied in Artificial Neural Network problems. It is utilised in enhancing images of molecules in electron microscopy (Rust et al., 2006; Kapanidis, 2015). Figure 2.9 shows a success of high-precision localisation of a single molecules by using Gaussian function (right) compared with the blurred images due to diffraction (left and middle).

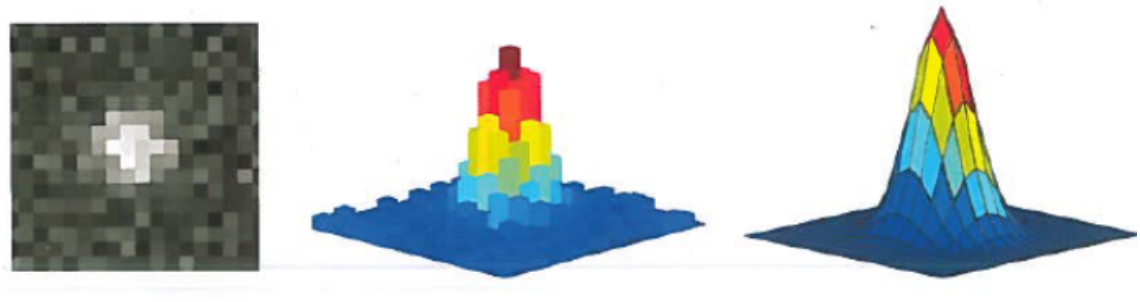

Figure 2.9: 2D diffraction-limited images (left and middle) versus high precision localisation (right) fitted by Gaussian function of single molecules. After Kapanidis (2015).

Besides the Gaussian, there are also other basis function choices, such as B-splines curves, commonly used in a range of problems in geophysics inversion. Several types

of B-splines curves family can be named as cubic, quadratic, etc as shown in Figure 2.10a and an example of data fitting using GMM is presented in Figure 2.10b.

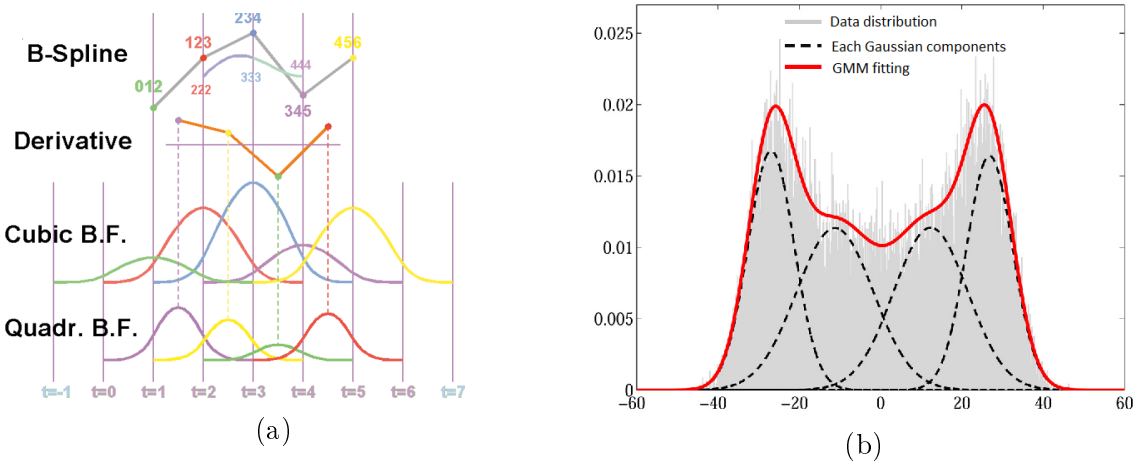

(a) (b)

Figure 2.10: (a) B-spline curve and its family. (b) An example of data fitting using GMM, after Mistry et al. (2015).

In the context of 4D seismic, Lie (2011) applied cubic B-splines basis function with variable node density for time-shift estimation. B-splines has a high level of freedom depending of the number of nodes used so that theoretically it could represent various field properties. However, for our purpose of velocity change estimation, I observe that the Gaussian function is more representative of the physical property distributions and that the inversion will be performed faster. Evensen and Landrø (2010) also uses Gaussian functions to describe the time-lapse velocity anomalies using six and nine parameters for two- and three dimensions, respectively to invert pre-stack time-shifts. I implement Gaussian basis functions differently by using a mixture of Gaussian models. I find that the Gaussian basis function is also good for analytic integration to determine time-shift fields. Therefore, I choose the Gaussian basis function in the form of a mixture of Gaussian functions.

2.5.2 Gaussian mixture model

Figure 5.11 shows the schematic of Gaussian function formed by three variables, in which μ is the mean, location or expected value, σ^2 is variance and σ itself is standard deviation, and finally ω is the Gaussian's amplitude.

In this Gaussian Mixture Model (GMM) method, $\Delta V/V$ data are represented by combining many Gaussians to form a 2D field of this property. Thus, GMM guar-

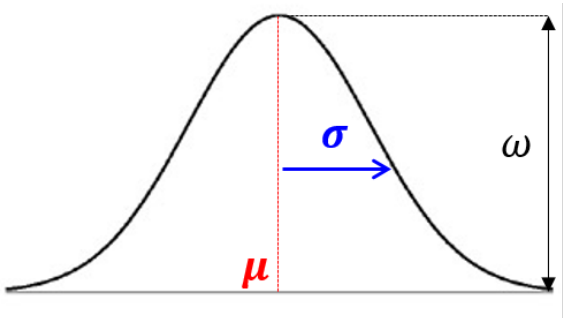

Figure 2.11: Gaussian function

antees a stable and analytic solution. The key to this GMM method is to decide on a suitable Gaussian grid with a skilful selection of number of variables. I found that for this particular problem of estimating time-lapse velocity changes, only one variable, ω, is necessary to be variable whilst the other two variables, μ and σ, can be preset. An example will be provided later on to test out this determination of using a preset Gaussian grid defined by (σ, μ) to dial into this problem. For such a chosen preset Gaussian grid, a sensitivity analysis of the grid and Gaussian dimensions with respect to computational time and mean squared error is essential. To adapt the GMM for use in the context of this study, I refer to μ, σ and w as location, width and weighting factor of the Gaussian, respectively. Given μ and σ, the quantity is rewritten as a linear mixture of Gaussians $\mathbf{G_i}$ as:

$$\vartheta(t_i) = \sum_{j=1}^{ng} \omega_j \mathbf{G_j}(t_i|\mu_j, \sigma_j). \tag{2.20}$$

where ng indicates the number of Gaussian used in GMM. The corresponding integral Δt is then:

$$\Delta t_i = \sum_{j=1}^{ng} \omega_j \left[\mathbf{E_j}(t|\mu_j, \sigma_j) - \mathbf{E_j}(0|\mu_j, \sigma_j)\right], \tag{2.21}$$

where the cumulative distribution function (CDF) $\mathbf{E}$ is:

$$\mathbf{E_j}(t_i|\mu_j, \sigma_j) = \int_{-\infty}^{t} \mathbf{G}(0|\mu, \sigma)dt \tag{2.22}$$

$$= \frac{1}{2}\left[1 + erf\left(\frac{t_i - \mu_j}{\sigma_j\sqrt{2}}\right)\right]. \tag{2.23}$$

Time-shifts are now represented as a kind of ramp function $\mathbf{E}$ as an integral of velocity changes, which are now reconstructed in the linear mixture of Gaussian function $\mathbf{G}$. . Existence of the term $\mathbf{E_j}(0|\mu_j, \sigma_j)$ in Equation 2.21 is because we are

here interested in the integral of ϑ for a finite time whereas the CDF of a Gaussian is valid from negative infinity. Hence,

$$\int_0^t \vartheta dt = \int_{-\infty}^t \vartheta dt - \int_{-\infty}^0 \vartheta dt. \tag{2.24}$$

Instead of inverting for velocity changes, this method inverts for the weighting factors ω_i and the final solution of ϑ can then be easily calculated following Equation 2.20. Figure 2.12 illustrates two examples of GMM in which each single Gaussian interferes and is separated with its corresponding integration CDF. A linear mixture of these single Gaussians physically reconstructs velocity changes ϑ and the corresponding integral of this linear mixture successfully represent the physics of time-shifts Δt.

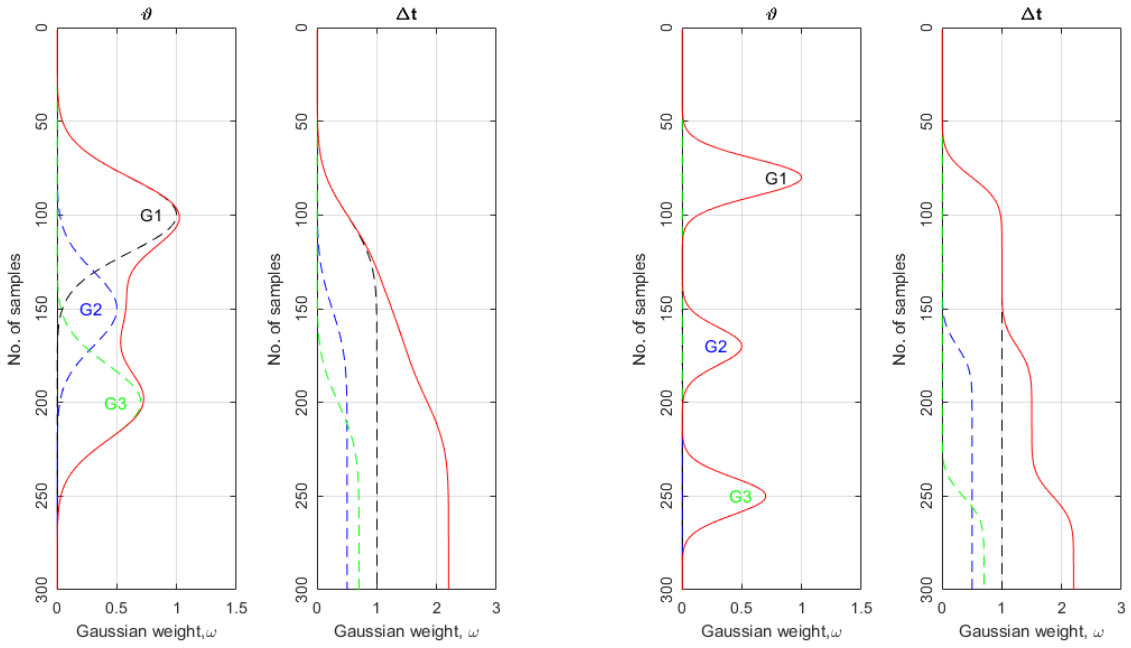

Figure 2.12: Two examples of (a) three interfered GMM and (c) three separated GMM to reconstruct ϑ and their corresponding CDFs (b) and (d) which describe Δt, respectively. These three Gaussians have the same weights where $\omega_1 = 1$, $\omega_2 = 0.5$ and $\omega_3 = 0.7$.

The corresponding time-shifts in these two simple examples do reflect the physical properties of observed time-shifts (e.g. accumulative nature). In order to verify the implementation of this preset GMM in estimating velocity changes, I then use Equation 2.21 to reconstruct an observed time-shift field, such as the above An'Teallach measured time-shifts. A range of different Gaussian grids, $(\sigma, d\mu)$, whereas σ in-

dicates width of a single Gaussian and $d\mu$ defines the space between two adjacent Gaussians, are preset from a window gate of 10 to 80 samples. It should be noted that as in layer stripping and damped least squares, the time-shifts are used in estimating ϑ in this thesis is fractional time-shift so that we are working in the sample domain. The constructed time-shifts are then generated for selected Gaussian grids as shown in Figure 2.13 together with the corresponding residual, r_{GMM}, subtracting from the observed time-shift in Figure 2.6a. Generally, the algorithm successful reconstructs the observed time-shift field with very small r_{GMM} (a, f). With other Gaussian grids, the reconstructed time-shift versions (Δt_{GMM}) are smoother yet maintaining the observed time-shift features, hence r_{GMM} is large (b, c, e, h). Another point that can be concluded here is that the smaller $d\mu$ is, the closest Δt_{GMM} is to the truth, Δt.

I also provide the comparisons between Δt_{GMM} and Δt in a trace view as in Figure 2.14. Notably, Δt_{GMM} is almost as same as Δt in (a) and (f). In cases of other Gaussian grids, Δt_{GMM} also stay closely to the truth Δt. This forward modelling gives confidence to move forward to the next step of inverting for the Gaussian weight, ω, and hence recovering ϑ.

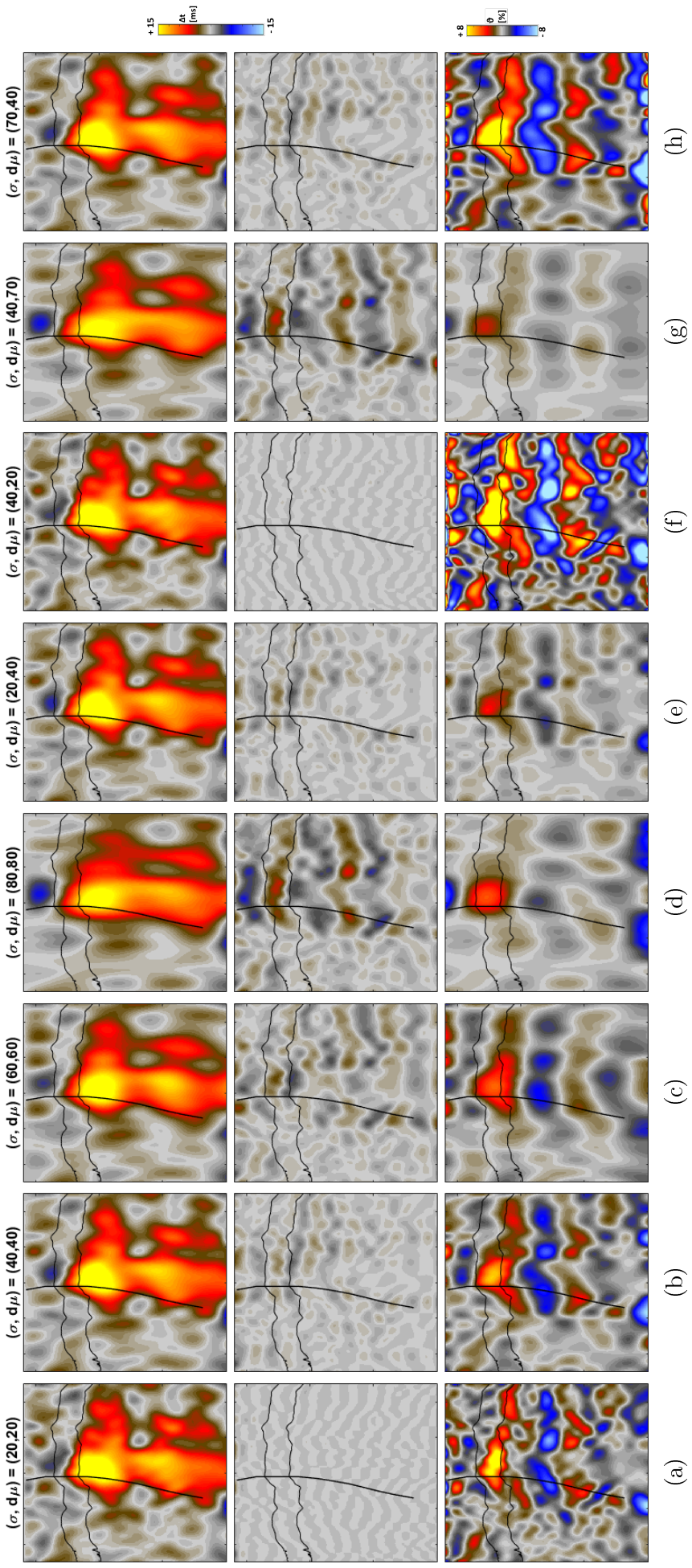

Figure 2.13: Reconstructed time-shift Δt_{GMM} (top row), corresponding residual r_{GMM} subtracting from the observed time-shifts in Figure 2.6a (middle row) and inverted $\Delta V/V$ (bottom row) over a selection of preset Gaussian grids. The algorithm can fully reconstruct the observed time-shift field with almost zero-residual in (a), (f). Comparison of (e) and (f) evidently point out that the residual gets larger when $d\mu$ increases. (b), (e) and (h) seem to smooth the observed time-shifts with a small residual yet preserve the observed time-shift's features. Inverted $\Delta V/V$ of (a), (b), (c) and (h) could possibly suggest the optimum Gaussian grids $(20, 20)$, $(40, 40)$, $(60, 60)$, and $(70, 40)$, correspondingly, where the main feathers of reconstructed time-shifts are preserved from time-shifts. Choosing an optimal grid will be discussed later on.

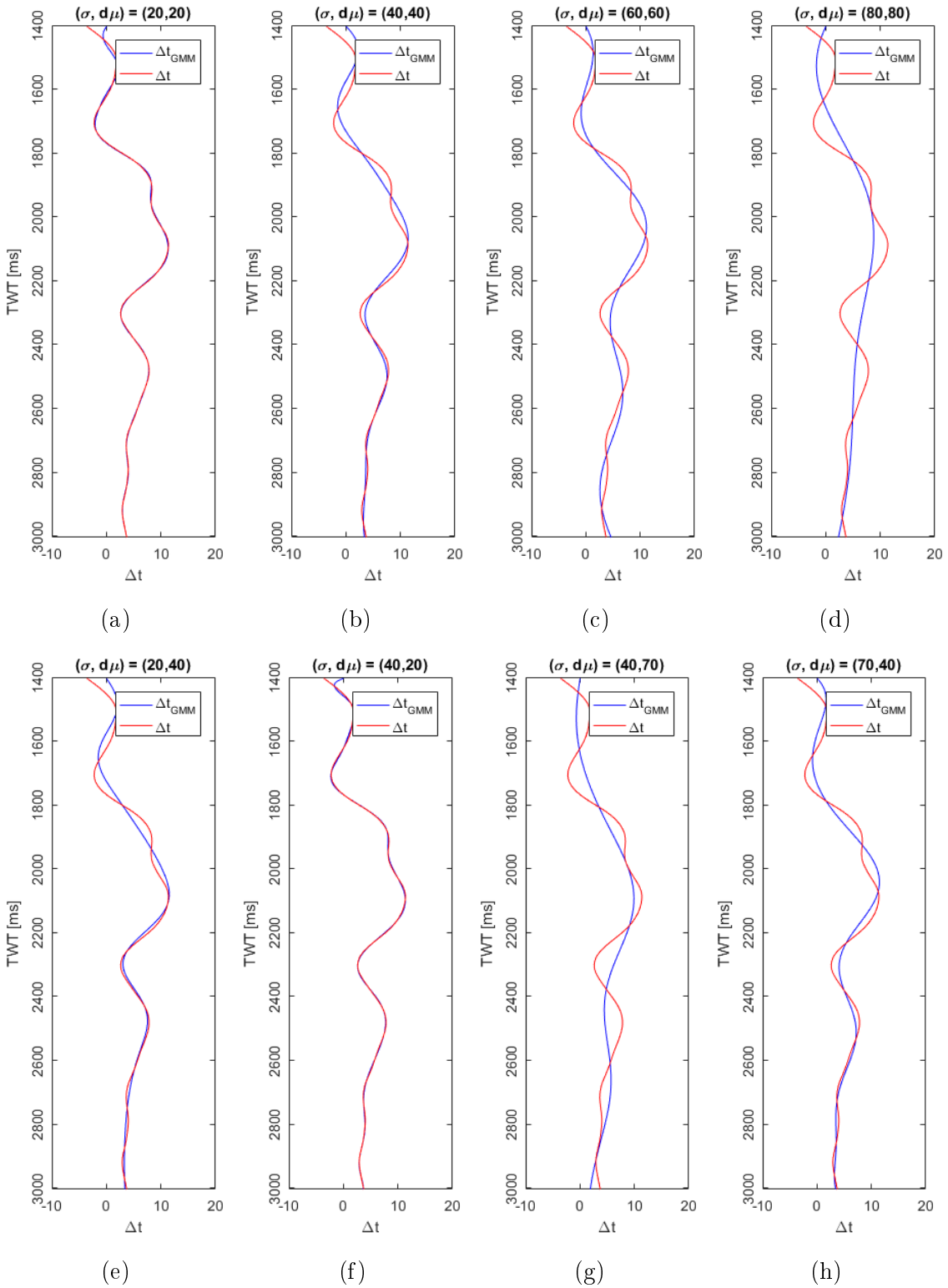

Figure 2.14: Plotting view of Δt_{GMM} versus Δt over various Gaussian grids. Similar observation as described in Figure 2.13.

2.5.3 Field data example

I here apply this new developed GMM method to the An'Teallach field mentioned above. The key of this method is about choosing a suitable Gaussian grid to a

particular dataset. Hereafter, the sensitivity analysis is carried out before doing the inversion. This task has been already partial done in the above subsection 2.5.2 with the An'Teallach field example of reconstructing time-shift. Therefore, in this subsection, I will describe the other aspects of presetting an optimal Gaussian grid.

Gaussian grid choice versus CPU time and MSE

Given the various possible Gaussian grid, choosing an optimal one is based on the computational cost (CPU time) and mean square error (MSE) of residual r_{GMM}. Figure 2.15 shows a whole range of different combinations between eight σ (filled circles) and eight $d\mu$ (X-axis) versus the two Y-axis of CPU time (left) and MSE (right). Obviously, the wider spacing ($d\mu$) is, the less CPU time costs and the larger error is. The most optimal grid that satisfies these two standards is ($\sigma, d\mu$) = (40,40).

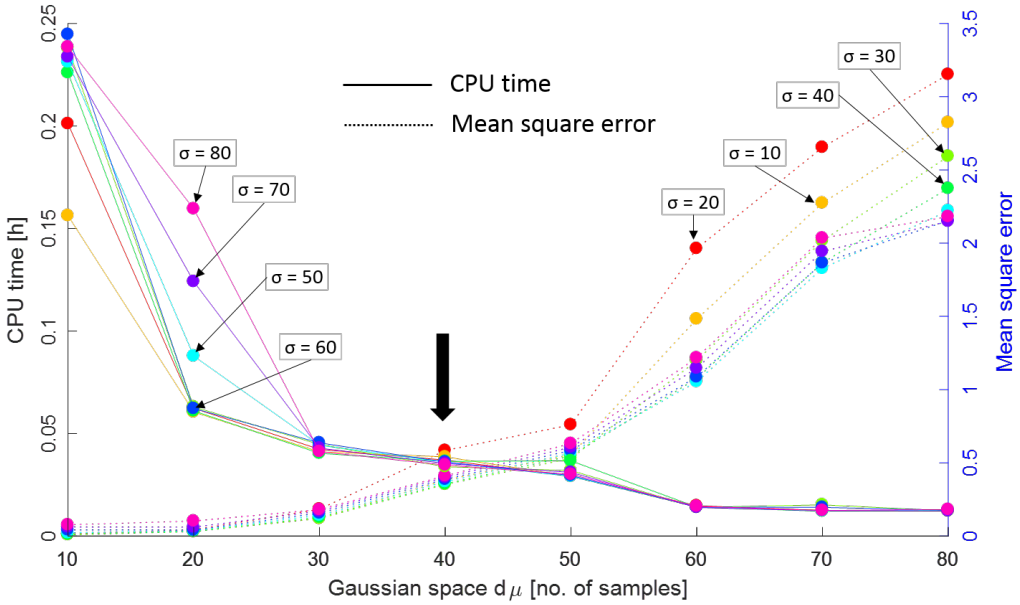

Figure 2.15: Variety of Gaussian preset grids formed by combining of σ (filled circles) and $d\mu$ (X-axis) from 10 to 80 number of samples versus both the computational time (CPU time on left Y-axis) and mean square error (right Y-axis). The grid of (σ, $d\mu$) = (40,40) with bold black down-arrow indicates the optimal grid that honours both CPU time and error estimation.

The grid choice can be extended to the neighbour $\sigma = 30, 50$ and $d\mu = 30, 50$ parameters depending on the size of data and how much accuracy we want to achieve. In this An'Teallach field example, I choose the most optimal one, (40,40).

Inversion result

Given the preset Gaussian grid selected from above, (40,40), I perform the inversion and its result is shown as in Figure 2.16. The algorithm forces the noise out of the recovered ϑ solution which is smooth and stable. A comparison of GMM with the other two velocity change estimation methods will be explored later.

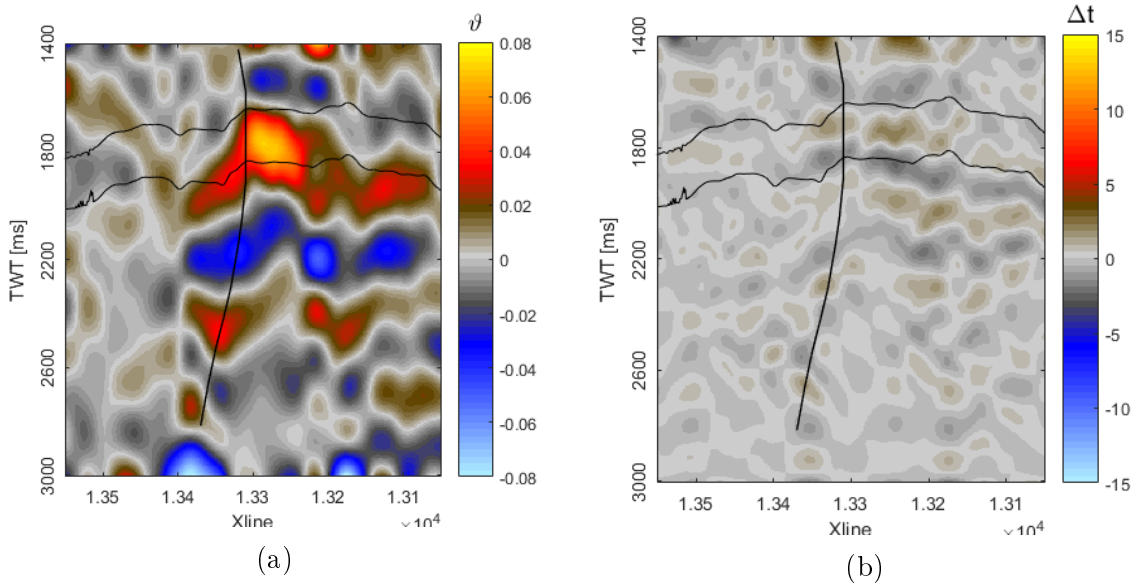

(a) (b)

Figure 2.16: (a) Inverted ϑ using GMM and (b) Absolute time-shift residual. GMM works well on this dataset by preset Gaussian grid (40,40). The noise is forced out and left a smooth and stable solution, ϑ. The recovered ϑ ranges about 4-5% in the reservoir corresponding to gas injection activities.

2.6 Comparisons of three inversion methods and Chapter summary

To conclude on the post-stack time-shift inversion methods in this Chapter, I first compare these three used methods, one novel and two selected methods from the literature before providing the summary of the chapter.

2.6.1 Comparison of three post-stack time-shift inversion methods

Comparison of GMM to the two other selected methods of layer stripping and damped least squares helps to understand the nature of GMM using Gaussian reconstruction and the benefits it may offer. Figure 2.17 shows three recovered ϑ from inverting An'Teallach post-stack time-shifts in Figure 2.6a using layer stripping, damped least squares and GMM. In terms of the magnitude, ϑ from layer stripping (a) is largest, up to 8% in the reservoir whereas ϑ from damped least squares (b) and GMM (c) are about 4-5%. As expected, layer stripping works as a differentiation operator which amplifies the noise as seen in the background of (a). Therefore, the magnitude of recovered ϑ in the reservoir might not be that reliable. Damped least squares does help to smooth out the results thanks to the regularization term in spite of relying on the choice of damping factor. Regarding GMM, even though it also relies on the choice of Gaussian grid as damped least square relies on the choice of smooth factor, γ, through the required initial sensitivity analysis, its inversion algorithm is based on a basis function that well represents the nature of velocity changes and time-shifts. Therefore, the recovered ϑ is guaranteed to be stable yet preserved the subsurface solution. Furthermore, it proves to be more robust throughout inverting for a limited number of the Gaussian weighting coefficients, ω, instead of an entire trace. These observation will be further explored in Chapter 5 where I also apply these three methods on three post-stack time-shifts with different levels of noise.

2.6.2 Chapter summary

In this Chapter, after revising on the current methods of inverting post-stack time-shift for velocity changes, I implemented two widely used methods, layer stripping and damped least squares, in the literature and developed my new own GMM using Gaussian reconstruction to invert for velocity changes due to the injected gas scenario at An'Teallach field. Detailed explanations on implementing each method are also provided to understand the nature of the method. I program these inversion algorithms in MATLAB language and the visualization is supported by Petrel software.

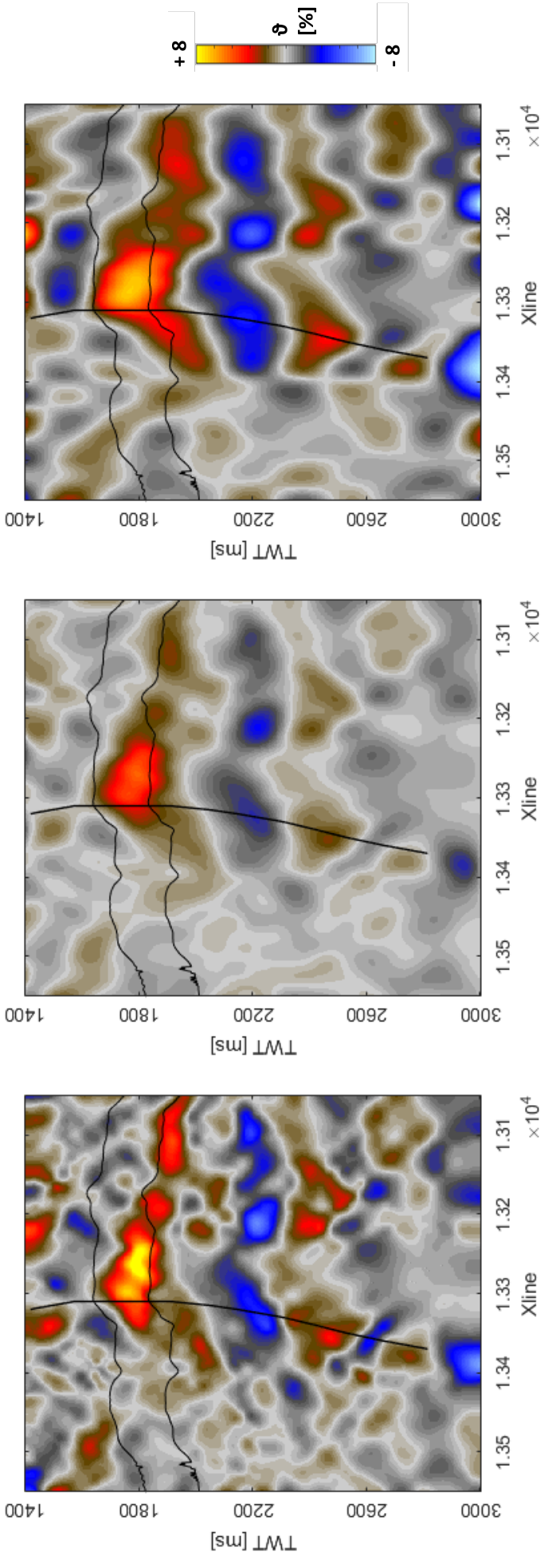

Figure 2.17: Inverted ϑ using (a) Layer stripping, (b) Damped least squares and (c) GMM. Compared to (a), (c) provides more stable result with less noise amplified in the background. Compared to (b), (c) provides similar velocity change scale (about 4-5%) yet reveals better subsurface resolution. However, in terms of interpretation, it seems that GMM introduces artefacts of a thick sand (red) and the blue event underneath due to the Gaussian grid. Meanwhile, the layer stripping result seems more practical in this example.

In the end, I also compare the inverted results from these three velocity change estimation methods. GMM stands out as providing more stable result compared with layer stripping and is better at preserving the subsurface changes with finer degree of resolution. With the analytical formulae that physically represent ϑ and Δt, GMM proves its stable and robustness as expected. I find that with the implementation of preset Gaussian grid in which Gaussian width, σ, and spacing, $d\mu$, and let the algorithm find the suitable weight that fits data, it is relatively easy to dial in to the problem and allows straightforward implementation to the seismic problem. The essence of this new GMM in estimating velocity changes is that both Δt and ϑ are re-formulated in an analytical form explicitly so that the recovered ϑ is assured to be smooth and stable. However, we should be careful to interpret the inverted velocity changes from GMM results since the usage of Gaussian grid in the algorithm might introduce artefacts as experienced in the above field example. Further field applications in Chapter 5 will bring more understanding on GMM and the other two methods.

Chapter 3

Angle-stack timeshifts

ABSTRACT

So far, I have looked at the one-dimensional earth by using post-stack data, which is standard industry practice and provides a limited solution – "80% solution" (Audebert and Agut, 2014). In this chapter, I aim to look for a more complete picture of the subsurface by using the data from another angles of incidence. Time-shifts measured from angle-stack data provide additional measurements of time-shifts from variable offset or angles. Extraction of this information can bring out other aspects for understanding the subsurface. This chapter first describes the evolution of the offset/angle dependence of time-shifts through different applications published in the literature. I then examine this dependence with a number of synthetic examples and finish the chapter with conclusions and discussions.

3.1 Time-shift versus offset (TVO)

The success of 4D seismic in understanding the dynamic properties of the subsurface characteristics for reservoir monitoring and management has pushed the limit of seismic acquisition. Starting from a very poor 4D repeatability due to the utilization of seismic vintages, 4D seismic acquisition is now mature and is able to provide the high quality 4D seismic data with an adequate offset coverage to measure the variations of the subsurface as mentioned in MacBeth et al. (2017a). This allows the 4D seismic researchers to dive into a new domain, with studies of the dependence of time-shift versus offset (TVO) being a growing topic of recent. TVO provides additional measurements so that the separation of thickness and velocity changes becomes possible. This helps to gain insight into geo-mechanic effects occurring in the surrounding areas of the reservoir. Also, it helps to understand the reservoir itself and for monitoring the CO_2 storage scenarios. This section will provide an extensive summary of the relevant studies exploring the relationship between time-shifts versus offset. These studies can be categorised based on the type of data used and the model chosen as laid out below.

3.1.1 Homogeneous model - restricted angle stack data

The very first studies on the dependence of time-shift versus offset were performed in the angle-stack domain by Landrø and Janssen (2002) and Landrø and Stammeijer (2004). They proposed a simple homogeneous one-layer model for a compaction scenario in the reservoir hence extension in the overburden as illustrated in Figure 3.1.

I recall here the analytic form of time-shift as a function of velocity changes $\Delta V/V$, thickness changes $\Delta z/z$ and incident angle θ, using the notation in this thesis from Equation C.9 in Appendix C:

$$\frac{\Delta t_0(\theta)}{t_0} = \frac{\Delta z}{z} - (1 + tan^2\theta)\frac{\Delta V}{V}. \tag{3.1}$$

where $t_0 = 2z/V$ is vertical two-way traveltime of the overburden layer. In Equation 3.1, Landrø and Stammeijer (2004) assumes small changes in thickness and velocity. Also, it is restricted to an isotropic medium, in which the P-wave velocity changes

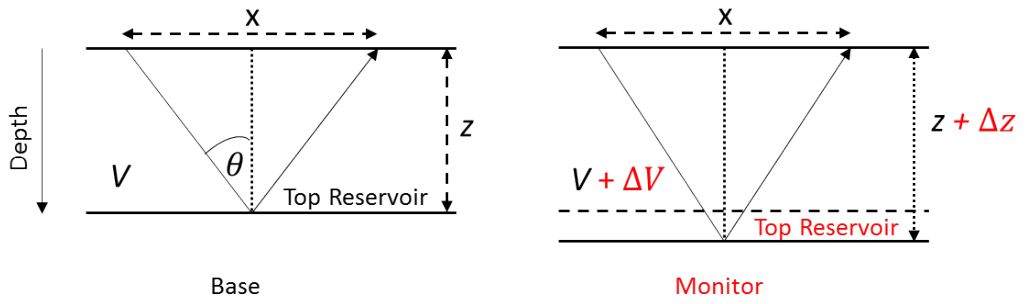

Figure 3.1: Schematic figure showing an offset ray prior to (left) and after *compaction* changes (right). x = offset, z = thickness, V = baseline velocity, θ = incident angle and symbol Δ indicates the time-lapse changes. It should be noted that the *compaction* here implies for reservoir area, hence the sketched extension overburden. Redrawn after Landrø and Stammeijer (2004).

equally in the vertical and horizontal direction, and no lateral velocity variation. Equation 3.1 is obtained after correcting for the NMO together with considering the NMO stretch affects of the baseline data. A detailed derivation can be found in Appendix C. This NMO correction will not remove the time-shift angle dependence effects if we use the same velocity model for both baseline and monitor, as will be seen in the numerical study (Figure 3.14 and 3.15). The input data are near and far angle stacks which have been corrected for NMO during the seismic processing workflow. The study expresses the dependence of time-shifts with offset through the incident angle θ in quadratic form. It is observed that in Equation 3.1, the incident angle θ presents in the velocity change, $\Delta V/V$,but not the thickness change, $\Delta z/z$. Therefore, for the NMO-corrected data, the dependence of time-shift versus offset comes from the contribution of velocity changes, $\Delta V/V$, only. I will use $rTVO_0$ to refer the dependence of relative time-shift versus offset for NMO-corrected data later on where as TVO refers to general relationship between time-shift versus offset.

However, the dependence of relative time-shift versus offset for non NMO-corrected data ($rTVO_x$) is due to the thickness changes. I recall here Equation C.2 and C.3 provided in Appendix C as following:

$$\frac{\Delta t_x}{t_x} = \frac{t_0^2}{t_x^2}\frac{\Delta z}{z} - \frac{\Delta V}{V}. \tag{3.2}$$

and

$$t_x^2 = t_0^2 + \frac{x^2}{V^2}. \tag{3.3}$$

where t_x denotes the two-way traveltime at a given offset x and Equation 3.3 is used

to apply the NMO correction for a constant-velocity case. From here, I use a simple relation between offset x and incident angle θ as:

$$x^2 = (2z)^2 tan^2\theta \tag{3.4a}$$

$$= t_0^2 V^2 tan^2\theta, \tag{3.4b}$$

to replace x^2 into Equation 3.3, after a few arrangements, we have:

$$\frac{t_x^2}{t_0^2} = 1 + tan^2\theta. \tag{3.5}$$

Finally, replacing Equation 3.5 into Equation 3.2 yields:

$$\frac{\Delta t_x}{t_x} = \frac{1}{(1 + tan^2\theta)} \frac{\Delta z}{z} - \frac{\Delta V}{V}. \tag{3.6}$$

Landrø and Stammeijer (2004) also derives the same as Equation 3.5. I walk my own way through this re-derivation because of further usage of the equation from this procedure. There is difference between the right-hand-side of the Equation 3.1 and 3.6 due to different types of data used (with NMO correction and without NMO correction). Therefore, one cannot compare the behaviour of TVO dependence between them. In next section 3.2, I will examine these equations and visualize both $rTVO_0$ and $rTVO_x$ dependence for NMO- and no NMO-corrected data, respectively over various scenarios by using different values of $\Delta z/z$ and $\Delta V/V$. In case of significant 4D velocity changes, Landrø and Stammeijer (2004) recommends to use the non NMO-corrected version (Equation 3.2).

3.1.2 Lateral gradient model - pre-stack data

Soon after, Røste et al. (2005) and Røste et al. (2006) extended this TVO relationship for a gradient change model, in which the lateral P-wave velocity variations (instead of a constant layer) are taken into account but the vertical changes are not. These lateral variations mostly appear in the scenarios of compacting reservoir or fault reactivation (Røste, 2007). These two studies also uses a one-layer model as illustrated in Figure 3.2 and is then extended to interpret the vertical variation in Røste et al. (2007).

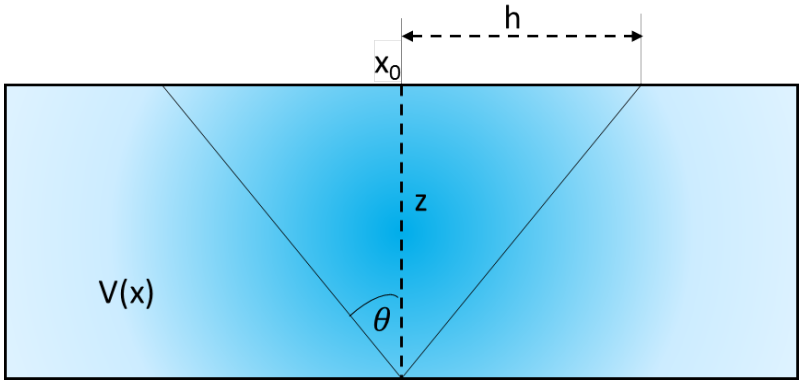

Figure 3.2: Sketch of a gradient model with lateral velocity change variations from (x_0-h) to (x_0+h), but not vertical. x_0 is a CMP position and $h = x/2$ is half-offset. Redrawn after Røste et al. (2007).

With the straight ray-path assumption, the dependence of time-shift with offset for this model is expressed analytical as following after adjusting to the notation used in this thesis:

$$\frac{\Delta t_x}{t_x} \approx \frac{z^2(x_0)}{z^2(x_0)+h^2}\left(\frac{1}{1+R}\right)\frac{\Delta t_0(x_0)}{t_0(x_0)} - \frac{1}{2h}\left(\frac{-R}{1+R}\right)\int_{x_0-h}^{x_0+h}\frac{\Delta t_0(x)}{t_0(x)}dx. \qquad (3.7)$$

where $z(x_0)$ represents the layer thickness at the CMP position x_0, t_0 is vertical two-way traveltime, Δt_0 is vertical time-shift, and R is dilation factor as mentioned in Chapter 1 ($R > 0$). Equation 3.7 describes the $rTVO_x$ dependence through the offset $2h$, relative vertical traveltime differences $\Delta t_0/t_0$ and dilation factor R. Given a position $x = 0.35(km)$, various R from 0 to +20 inserted into Equation 3.7 estimates the dependence of relative time-shifts versus offset as presented in Figure 3.3. As R decreases, the quantities $1/(1+R)$ and $-R/(1+R)$ have negligible effects, and resulting in almost unchanged the relative time-shifts $\Delta t/t$. In other words, there is the difficulty of distinguishing R for decreasing values of R. The optimal R value is +5.

Figure 3.3 shows the decrease of $rTVO_x$ for almost all the case of various chosen α values, in which the contribution of thickness and velocity changes are implicitly connected. The TVO dependence in Røste's studies expresses through α values which implicitly connects two parameters of velocity and thickness changes. In the next section 3.2, I will prove that for no lateral variation, Equation 3.7 derived by Røste et al. (2006) is as same as Equation 3.2 derived by Landrø and Stammeijer (2004).

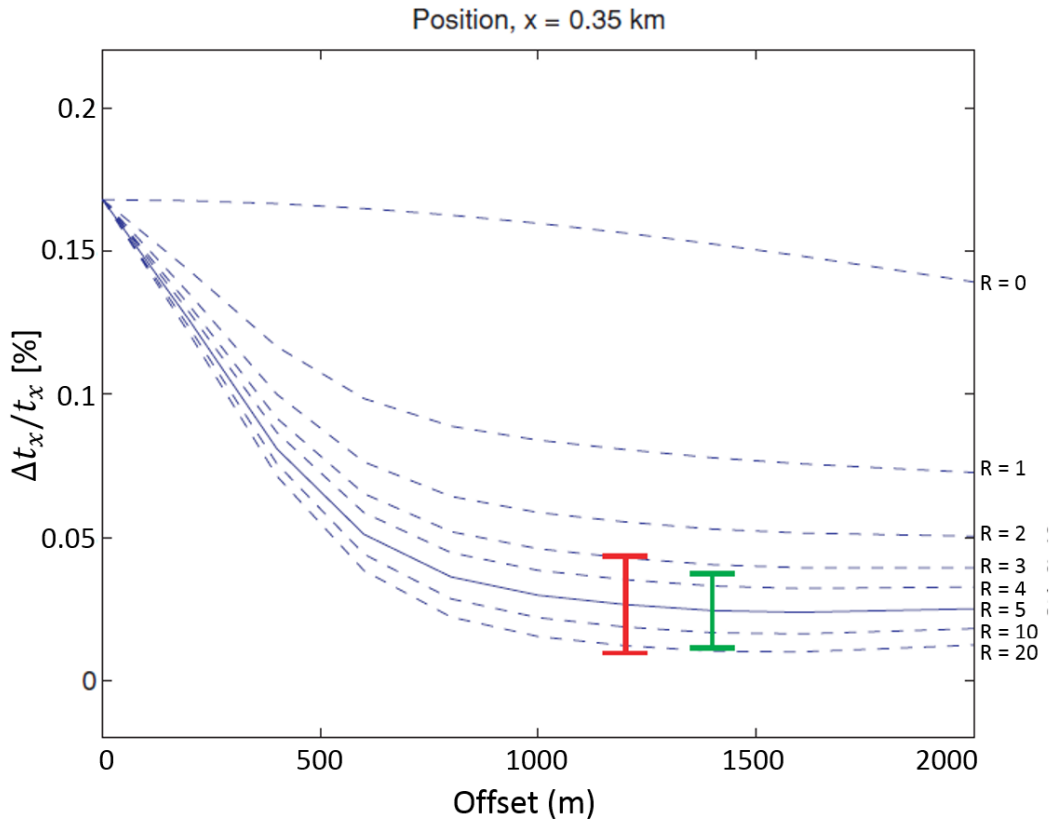

Figure 3.3: Estimated relative time-shifts (as a function of offset) for several values of R for position $x = 0.35$ km. The solid line indicates the optimal $R = +5$. Note the increased difficulty of distinguishing R values as R decreases. The red and green vertical bars indicate the standard and mean deviations (respectively) in picked relative time-shifts. Modified from Røste et al. (2007).

3.1.3 Horizontal layered model - pre-stack data

Different from Landrø and Røste's studies, Hawkins et al. (2006, 2007) disregards the assumption of straight rays, instead it uses the ray-tracing theory for all offsets and expands to multiple-layer model yet remains the horizontal layer assumption. The authors applied this method on a time-lapse synthetic data and plotted the time-shifts and normalized time-shifts versus offset as in Figure 3.4.

The synthetic model is loosely based on the Franklin and Elgin reservoir. The model has 11 layers, in which the velocity and thickness changes are derived from typical reservoir depletion with a constant R value of 5 throughout inspired by Hatchell and Bourne (2005). This R value can be translated into $\alpha = -5$ which is the optimal choice of $\alpha = -5$ in Figure 3.3 by Røste et al. (2007). It should be careful to compare these two figures as there are different quantities and they are presented in different scales before we make the comparison and draw conclusions. In Figure

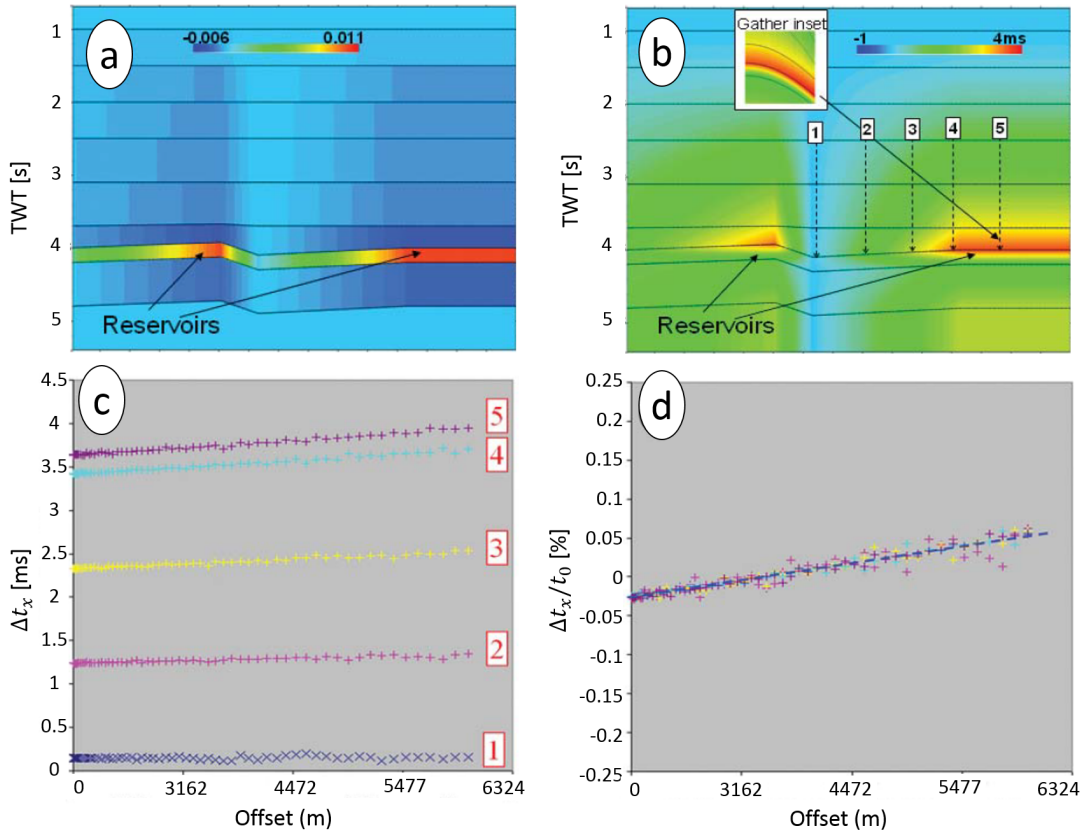

Figure 3.4: A slight increase behaviour of (c) time-shifts and (d) normalized time-shifts versus offset squared obtained from the ray-traced synthetic of a multiple-horizontal-layer model. (a) shows the relative velocity change model and (b) indicates the five traces selected correspondingly to the top reservoir event from five locations vary from completely off reservoir to centre of reservoir. After Hawkins et al. (2007).

3.4c, it is the absolute time-shifts, Δt_x, which I will refer to as $aTVO_x$ later on, and it has a slight increase. In Figure 3.4d, it is *normalized time-shifts* as stated in Hawkins et al. (2006)'s study which, following my educated guess, is divided by t_0. The $aTVO_{x-Hawkins}$ has the opposite direction to $rTVO_{x-\text{Røste}}$ and its gradient is much smaller at such a long offset (up to $6300km$). These opposite directions are due to the offset-dependent quantity t_x in $rTVO_x$ term and will be further explored in Section 3.2.

3.1.4 Anisotropic medium - pre-stack data

The story of TVO dependence becomes more complicated in an anisotropic medium. Herwanger et al. (2007) includes anisotropic velocity changes and concludes that the TVO dependence should be expected to decrease at larger incidence angles. Figure 3.5 shows the decreasing up to 50% in the overburden of measured time-

shifts from near to far angle gathers on the compacting chalk of the South Arne field. It should be noted that this is absolute time-shifts as the unit is in ms. Therefore, even it is not mentioned in the study of which types of data being used (before or after NMO correction, $aTVO_x$ or $rTVO_0$, respectively), its trend will remain the same because the NMO correction does not affect the absolute time-shift as proved in Section 3.2. However, as the study compares against Landrø's $rTVO_0$ equation (Equation 3.1), I can assume that the study measures time-shifts on NMO-corrected 4D seismic data and the observed time-shift is in ms units, hence $aTVO_0$. If this is the case, Herwanger's observation supports TVO dependences on the velocity changes rather than $\Delta z/z$ as in Equation 3.1 regardless of the opposite polarity prediction. According to Herwanger et al. (2007), for reservoir compaction scenarios, in anisotropic medium, TVO decreases whereas in homogeneous model, TVO increases following Equation 3.1.

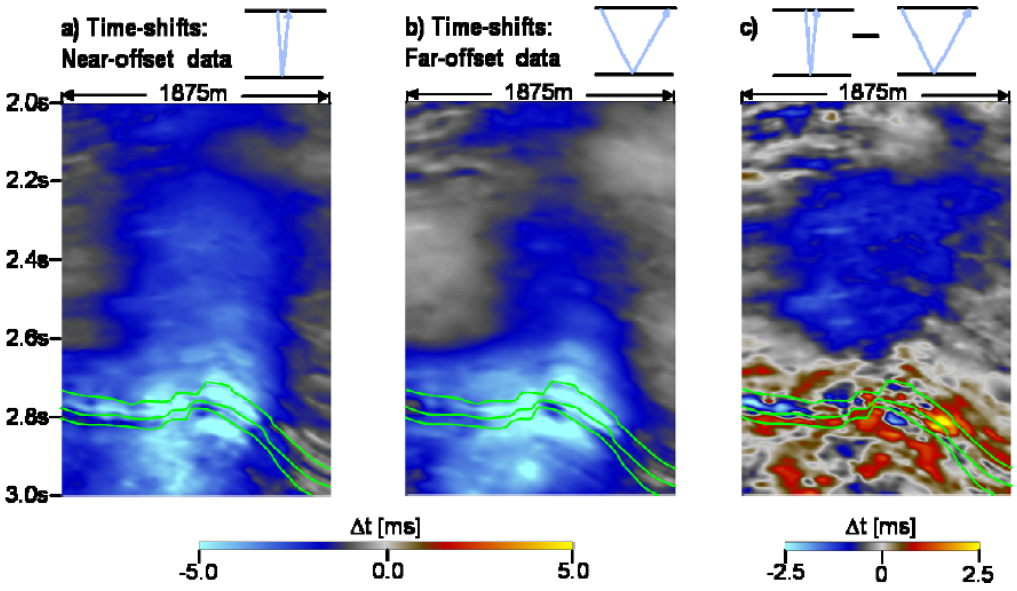

Figure 3.5: A significant decreasing of measured time-shifts $aTVO_0$ in the overburden due to reservoir compaction from(a) $5-15^0$ to (b) $25-35^0$ angle-stacks on a chalk field - South Arne. The subtraction (c) shows the decreasing up to 50% of time-shifts versus incident angle with negative time-shift (blue) in the overburden. After Herwanger et al. (2007).

However, the picture of TVO dependence is now flipped again with the study of Hawkins (2008). The measured time-shift on the HPHT Elgin Field shows that the absolute time-shifts slightly increases with offset as plotted in Figure 3.6 (b) and (c). The author compares these measured time-shifts with the synthetic ray-traced time-shifts for an isotropic medium (Figure 3.6 c and e) and finds that there is a fairly poor-match at the far angle but not the near. Again, it is not clear whether $aTVO$

($aTVO_x$ or $aTVO_0$) is mentioned here even though it does not affect the TVO's trend. I would assume $aTVO_x$ as the author works with synthetic ray-tracing.

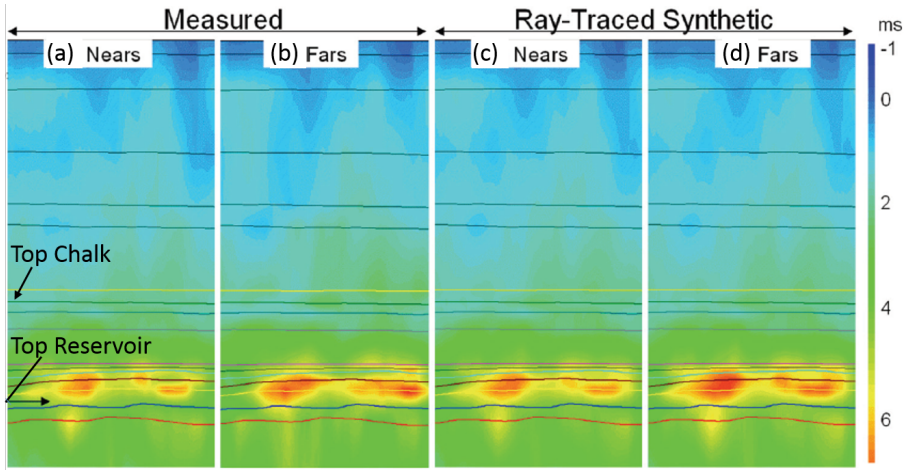

Figure 3.6: Observed increase of measured time-shifts from (a) near to (b) far angles on the HPHT Elgin Field with a strong depletion. Synthetic isotropic time-shifts for (c) near and (d) far angles are matched well in the Nears but slightly larger at Fars, possibly due to anisotropy. After Hawkins (2008).

According to Hawkins, the disparity an the far angle is due to anisotropy. Another synthetic ray-traced time-shifts for the anisotropic medium is carried out in this study (Figure 3.7) with range of different anisotropic values represented by the quantity $R2$. It is shown that at $R2 = 5$, there is a well-matched synthetic time-shift with measured time-shift at far angle.

In a similar way to Herwanger's work, Hawkins's study also points out the contribution of anisotropy to the dependence of TVO. However, the TVO behaviours are opposite. There might be field dependence, South Arne is a chalk reservoir at a normal temperature and pressure environment, with strong extension in the overburden as seen in Figure 3.5. Whereas Elgin is a HPHT reservoir and has an unusual situation with a stiff layer above the reservoir which probably causes strong observed extension below the reservoir (we will observe the stiff layer in Section 3.2 with multilayer model - layer 7 and strong extension in the underburden in Chapter 5 with a surrounding HPHT field - Shearwater). Excluding the field dependence issue and also the unavailable information relating to the data (before or after NMO correction), I find that a lack of clarity still exists with the following proposed equation which is used for the anisotropic synthetic study in Figure 3.7 above:

$$\frac{\Delta t_\theta}{t} \approx \frac{cos\theta \Delta z}{z} - \frac{\Delta V_\theta}{V_\theta cos\theta}. \tag{3.8}$$

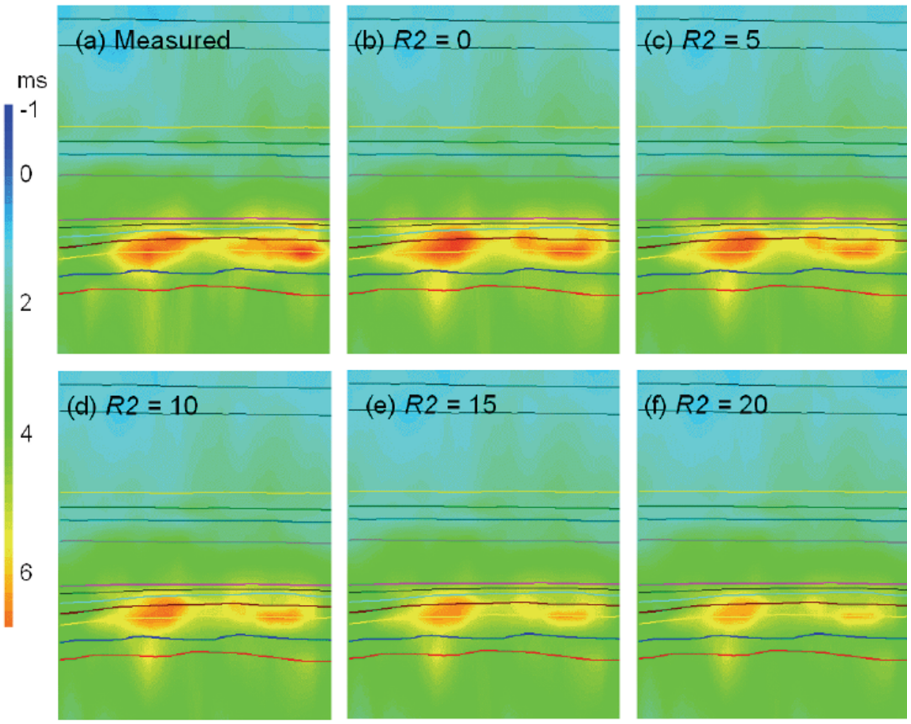

Figure 3.7: Comparison of (a) measured far angle time-shift from Figure 3.6 c to (a-d) a range of anisotropic far angle synthetic ray-traced time-shifts using $R2$ parameter. $R2 = 0$ means weakest 4D anisotropy (using the baseline anisotropy). $R2 = 5$ shows the best match at most levels with the measured time-shifts. After Hawkins (2008).

where the subscript θ indicates the angle dependent variables and the definition of t is not provided whether it is vertical traveltime t_0 or offset dependent traveltime t_x as referred in Landrø's work. This equation takes into account the anisotropic effect and predicts the dependence of TVO is now relying on both terms, $\Delta z/z$ and $\Delta V/V$, with the presence of angle θ in these two terms, which is different from either $rTVO_0$ or $rTVO_x$ as we have discussed. With Equation 3.8 for anisotropic medium, we can predict that at larger angles with increase of θ, the quantity $cos\theta$ decreases and $1/cos\theta$ increases, this leads to a decrease of $\Delta t_\theta/t$. However, this prediction of TVO behaviour remains difficult due to unknown t_0 or t_x.

3.1.5 Specific localised heterogeneities

The behaviour of TVO dependence has been so far focused on the deformation scenario in the overburden which cause the entire changes in the thickness (shifted reflector) and velocity. In this subsection, we look at localised heterogeneous scenario in which the velocity is changed at a specific area and the entire thickness of the

subsurface remains the same ($\Delta z/z = 0$). A typical example for this localised heterogeneous scenarios can be referred to is CO_2 storage. As mentioned in Sleipner field example in Chapter 1, injecting a gas volume in a homogeneous subsurface (e.g. CO_2 storage) as illustrated in Figure 3.8 can be monitored by 4D seismic via time-shift attributes.

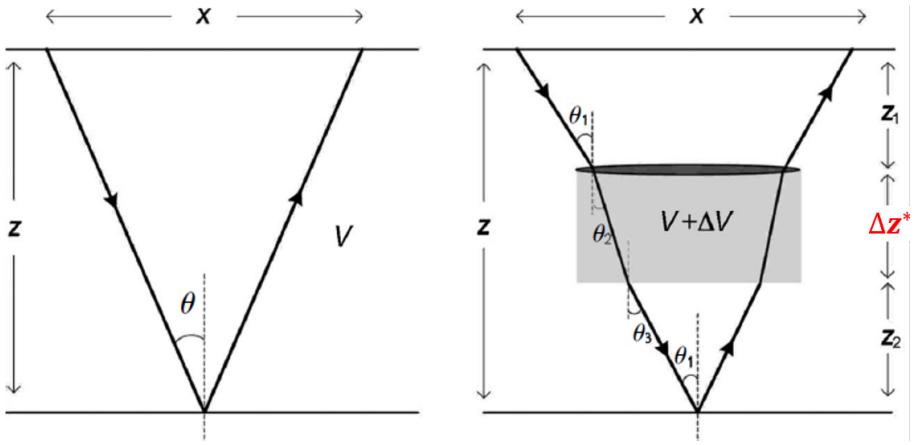

Figure 3.8: Sketch of pre-(left) and post-(right) CO_2 injection. The straight ray-path before the injection is now bent. The gas volume becomes an anomaly with thickness and different velocity property. It should be noted that the objects are not to scale and are exaggerated for clarity. It should be noted of the difference Δz^* (changes of gas volume thickness) from Δz (thickness changes in the overburden due to deformation) defined in Landrø and Stammeijer (2004)'s study. After Ghaderi and Landrø (2009).

Ghaderi and Landrø (2009) derived the changes in the ray-path for such that homogeneous localised-heterogeneous model as:

$$\frac{\Delta t_x}{t_x} = -\frac{\Delta V}{V}\frac{\Delta z^*}{z\left(1 + cos^2\theta\frac{\Delta V}{V}\right)}. \tag{3.9}$$

where θ is the incident angle of baseline and importantly, Δz^* indicates the thickness changes of gas volume after the injection, which is totally different from Δz, thickness changes due to deformation in the overburden (shifted in the reflector). Prediction of TVO behaviour is not that straightforward due to inclusion of offset dependent variable t_x on the left-hand-side of the equation. For a small value of $\Delta V/V << 1$, Equation 3.9 returns to:

$$\frac{\Delta t_x}{t_x} \approx -\frac{\Delta V}{V}\frac{\Delta z^*}{z}\left(1 - \frac{\Delta V}{V}cos^2\theta\right). \tag{3.10}$$

Another approximation at small offset $\theta \approx 0$ can be applied to Equation 3.10 yields:

$$\frac{\Delta t_0}{t_0} \approx -\frac{\Delta V}{V}\frac{\Delta z^*}{z}. \tag{3.11}$$

where Δt_x and t_x are replaced by Δt_0 and t_0, respectively due to almost vertical traveltime. One can not compare the TVO_x of this particular localised heterogeneous model (Equation 3.10) with TVO_x of a homogeneous one-layer model derived by Landrø and Stammeijer (2004) in Equation 3.6 since these two models are different at the usage of ray-path (straight versus bending rays) and at the zero thickness changes ($\Delta z/z = 0$ and the appearance of the new quantity Δz^*). However, in the previous Chapter 1 and 2, there are a few mentioned studies assuming $\Delta z = 0$ but still in the favor of using the straight-ray assumption. Therefore, a further investigation on eliminating Δz^* from Equation 3.10 will be of interest to gain deeper understanding on this TVO topic. I would prefer this issue as further researches in Chapter 7.

3.1.6 Insignificant TVO observations

In spite of published benefits of TVO dependence in the literature that I have reviewed, recently Kudarova et al. (2016a) concluded that the TVO dependence has no additional values in compacting reservoir environments. The study measures the time-shifts at a deep water field environment in Gulf of Mexico (Mars) and a shallow water field environment in the North Sea (Shearwater - HPHT field) and does not observe any significant offset dependence with time-shifts as in Figure 3.9 and Figure 3.10.

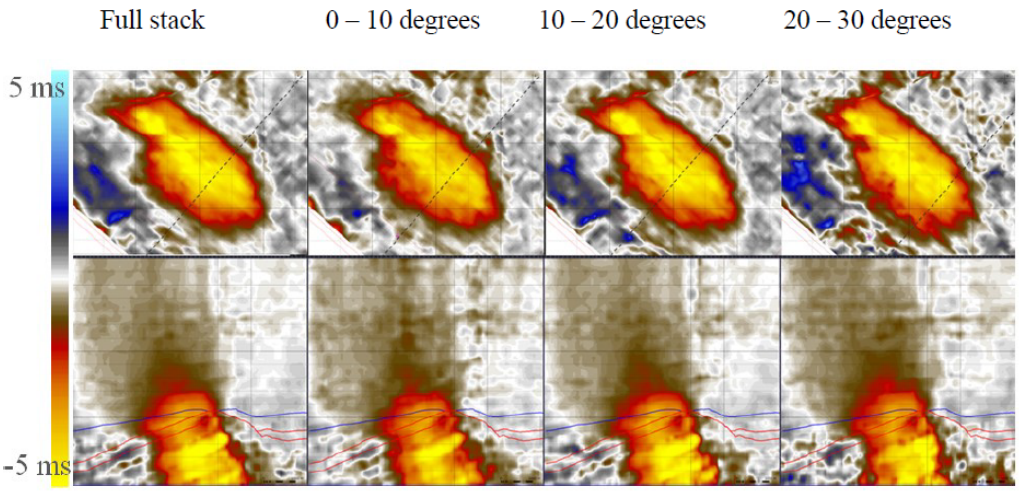

Figure 3.9: Insignificant TVO dependence observed at Shearwater field. Upper panel: maps of time-shifts for top-reservoir. Lower panel: vertical cross-section through the reservoir area. About 5 ms time-shifts observed and there is almost no variation with angles. After Kudarova et al. (2016a).

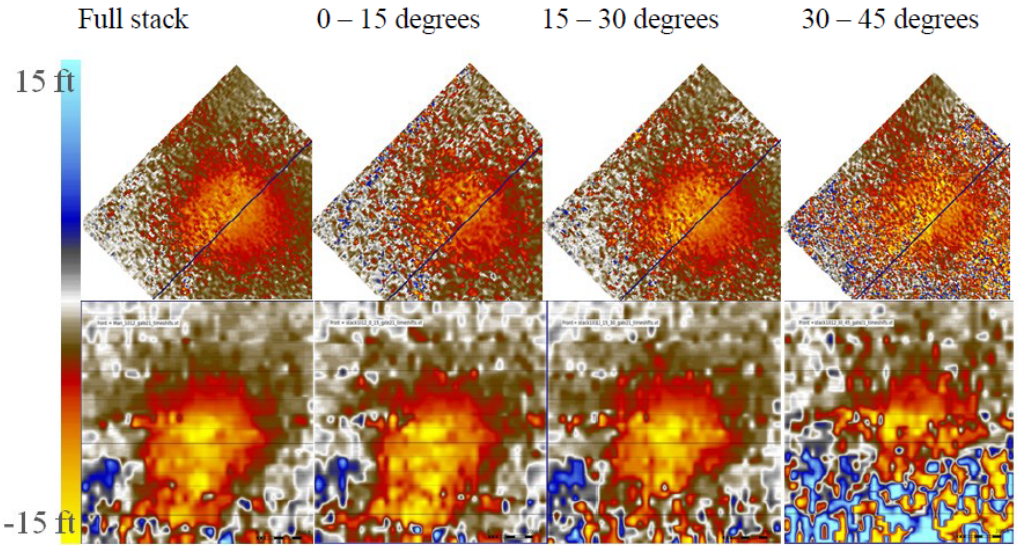

Figure 3.10: Almost no dependence of depth-shifts versus offset observed at Mars field. Upper panel: maps of time-shifts for top-reservoir. Lower panel: vertical cross-section through the reservoir area. There is undershooting observed at $30-45^0$ offsets. After Kudarova et al. (2016a).

3.1.7 Section summary

To sum up, TVO dependence has various behaviour for different varieties of field mechanisms, inclusion of anisotropy and types of data used. I here summarize all these observations with detailed information of field application in the following Table 3.1.

Field	Scenarios	TVO	Method	References
Synthetic	Overburden extension	$\Delta t_x/t_x \downarrow$, $\Delta t_0/t_0 \uparrow$	Analytic, homogeneous	Landrø and Stammeijer (2004)
Synthetic	Overburden extension	$\Delta t_x \uparrow$	Isotropic ray-tracing	Hawkins et al. (2007)
Synthetic	Overburden extension	$\Delta t_x \uparrow$	Anisotropic ray-tracing	Hawkins (2008)
Synthetic	Overburden extension	$\Delta t_x/t_x \downarrow$	Analytic, lateral variation	Røste et al. (2007)
South Arne	Overburden extension	$\downarrow$	Sections	Herwanger et al. (2007)
Shearwater	Overburden extension	Flat	Sections	Kudarova et al. (2016a)
Mars	Overburden extension	Flat	Maps	Kudarova et al. (2016a)

Table 3.1: Summary of time-shift versus offset/angle in the above revised studies.

3.2 Synthetic studies

I now set up a few synthetic examples to examine the dependence of time-shifts with offset. These models are inspired by the previous studies in my review. The values of parameters used in these models are based on my observation and understanding of real data and the suggested geo-mechanical models from the literature. For example, the velocity changes are usually about 1% meanwhile the thickness changes is much smaller ($10^{-4} to 10^{-3}$). In Hatchell et al. (2005), typical R value is approximately 5. Hawkins et al. (2007) also use an $R = 5$ value to create the synthetic model which can mimic the HPHT reservoir in the North Sea. I choose the values for the North Sea data inspired by Hawkins et al. (2007). Note that density changes are assumed to be negligible in this thesis.

In order to calculate the numerical time-shifts for each synthetic scenario, I use the ray-tracing method with individual rays to calculate the traveltime for baseline and monitor. The corresponding time-shifts (Δt_0 or Δt_x) are then calculated by subtracting them from each other and so these are $\Delta t_0/t_0$ or $\Delta t_x/t_x$.

3.2.1 One-layer model

I start with a one-layered model of Landrø and Stammeijer (2004) and Røste et al. (2006). In order to examine the TVO dependence via the same variables of thickness and velocity changes, I bring here the explicit form of Equation 3.7 derived in the appendix of Røste et al. (2006)'s study:

$$\frac{\Delta t_x}{t_x} \approx -\frac{1}{2h}\int_{x_0-h}^{x_0+h}\frac{\Delta V(x)}{V(x)}dx + \frac{z^2(x_0)}{z^2(x_0)+h^2}\frac{\Delta z(x_0)}{z(x_0)}. \tag{3.12}$$

This equation is derived for angle-stack data with all offsets. The effects of NMO correction is not considered as we are dealing with full traveltime changes. In the case of a homogeneous medium where the lateral variation is negligible, the velocity changes $\Delta V(x)/V(x)$ remains constant so that I can be put it outside the integral. Equation 3.12 then becomes:

$$\frac{\Delta t_x}{t_x} \approx -\frac{1}{2h}\frac{\Delta V(x_0,h)}{V(x_0,h)}(x_0+h-(x_0-h)) + \frac{z^2(x_0)}{z^2(x_0)+h^2}\frac{\Delta z(x_0)}{z(x_0)}. \tag{3.13}$$

Replacing h by $x/2$ and using subscript x instead of the location (x_0, h), Equation 3.13 then becomes:

$$\frac{\Delta t_x}{t_x} \approx \frac{1}{(1+tan^2\theta)}\frac{\Delta z}{z} - \frac{\Delta V}{V}. \tag{3.14}$$

where the transformation of $z^2/(z^2+h^2)$ term is done by following manipulations with taking into account Equation 3.4a:

$$\begin{aligned}\frac{z^2}{z^2+h^2} &= \frac{4z^2}{4z^2+x^2}\\ &= \frac{4z^2}{4z^2+4z^2tan^2\theta}\\ &= \frac{1}{1+tan^2\theta}.\end{aligned} \tag{3.15}$$

According to Equation 3.6, at small offset $\theta = 0$, it returns to the post-stack time-shift Equation 1.3 as a function of thickness and velocity changes only. Thus, though there are differences in the mathematical expressions and notations in Landrø and Stammeijer (2004) and Røste et al. (2006) studies, I have approved that they belong to the same family. The TVO dependence for the lateral gradient model in Røste et al. (2006)'s study (Equation 3.7) is the extension of Landrø and Stammeijer (2004)'s study (Equation 3.2 for non-NMO correction) for a homogeneous model.

I choose to only work on the homogeneous and flat one-layer model to be in keeping with the fundamental TVO dependence of both Equation 3.1 with NMO correction and Equation 3.14 or 3.2 without NMO correction. I initialise a homogeneous overburden with depth ($z = 2000m$) and velocity ($V = 2500m/s$). Figure 3.11 illustrates the numerical ray-tracing model before and after the production.

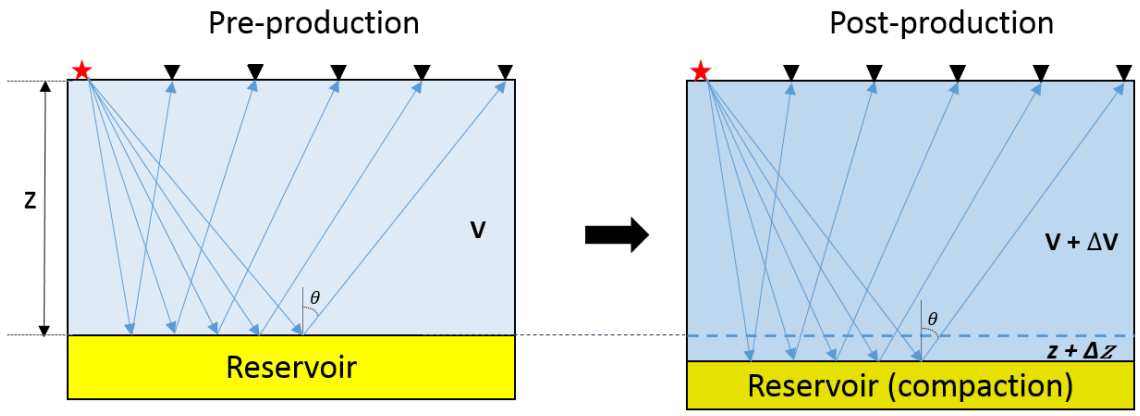

Figure 3.11: Sketch of one-layer homogeneous flat model (left) before and (right) after production. I assume no change in the ray-path from pre- to post-production hence the incident angle θ remains the same. Various scenarios of velocity changes in associated with thickness changes are presented in Table 3.2.

Both changes of thickness and velocity are taken into account in this experiment under the assumption of a simple reservoir compaction and overburden extension, and uni-axial deformation. Table 3.2 shows six post-production scenarios, where these two velocity and thickness changes are combined differently. Cases 1, 2 and 4 are designed for reservoir compaction hence there is extension ($\Delta z/z > 0$) and slowdown ($\Delta V/V < 0$) in the overburden. Case 3 is for reservoir extension hence there is speed up and compaction in the overburden. Cases 4, 5 and 6 consider the contribution of thickness changes or velocity changes, to separate these coupled effects using the TVO behaviour.

3.2.1.1 TVO dependence without NMO correction - TVO_x

It would be of interest to visualize the dependence of time-shift versus offset described in Landrø's equations for non-NMO correction, $\Delta t_x/t_x$ ($rTVO_x$), (Equation 3.6) in comparison with the numerical results. Given the variables in Table 3.2, the ray-traced time-shifts are calculated by directly taking differences between traveltime of monitor and baseline without any NMO correction. Hence, the TVO

Various over-burden scenarios		Layers	Δz - re (m)	ΔV - ob (m/s)	Δz/z - ob (%)
Case 1	Slow down + extension	2	-12.5	0.1	-0.5
Case 2	Slow down + extension (smaller magnitude)	0.8	-5	0.04	-0.2
Case 3	Speed up + Compaction	-0.8	5	-0.04	0.2
Case 4	Slow down ONLY	0	-5	0	-0.2
Case 5	Extension ONLY	0.8	0	0.04	0
Case 6	Compaction ONLY	-0.8	0	-0.04	0

Table 3.2: Different cases for changes in the overburden of a one-layer model.

dependence is expected to be close to the result from Landrø's equation. Figure 3.12 shows the results of relative time-shift versus offset ($rTVO_x$) are as anticipated.

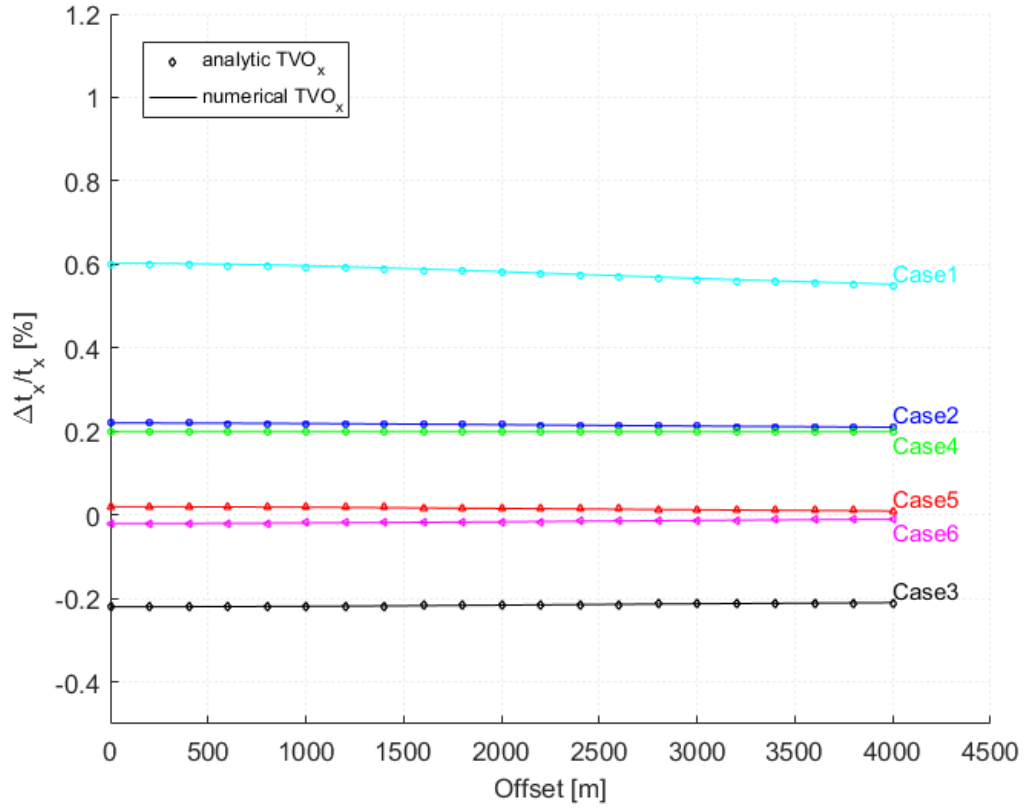

Figure 3.12: $rTVO_x$ for six various cases denoted by different colours of the one-layer model. Theoretical results by Landrø's prediction (dots) and numerical results by ray tracing (lines) produce similar $rTVO_x$ behaviour. $rTVO_x$ of cases 2 and 3 are flat due to no changes in velocities. Cases 1, 3, 4 and 6 show a slight variations from the quantity $1/(1+tan^2\theta)$.

However, it is difficult to know how much time-shift is generated from the certain amounts of thickness and velocity changes described in Table 3.2. Also there is still dependence of offset in quantity t_x in the left-hand-side of Equation 3.6 as mentioned

above. Therefore, hereafter I plot the absolute time-shifts Δt versus offset ($aTVO_x$) by multiplying with t_x as in Figure 3.13. The TVO trend is now changed due to implicit offset dependence on t_x, the results are now expanded at the end of the figure. For the compaction reservoir scenarios, cases 1, 2 and 4, it shows an increase with offset. For the extensional reservoir situation, case 3, it decreases and is of opposite polarity. A little contribution from thickness changes without consideration of velocity changes in cases 5 and 6 produces a slight variation of time-shift versus offset, in which one case is flipped by the other due to opposite magnitude. From here, we can know, for example, very large time-shifts, about over $10ms$, come from quite small changes, 0.5% and 0.1%, from velocity and thickness changes, respectively. Both theoretical and numerical results predict the same $aTVO_x$ and $rTVO_x$ behaviour.

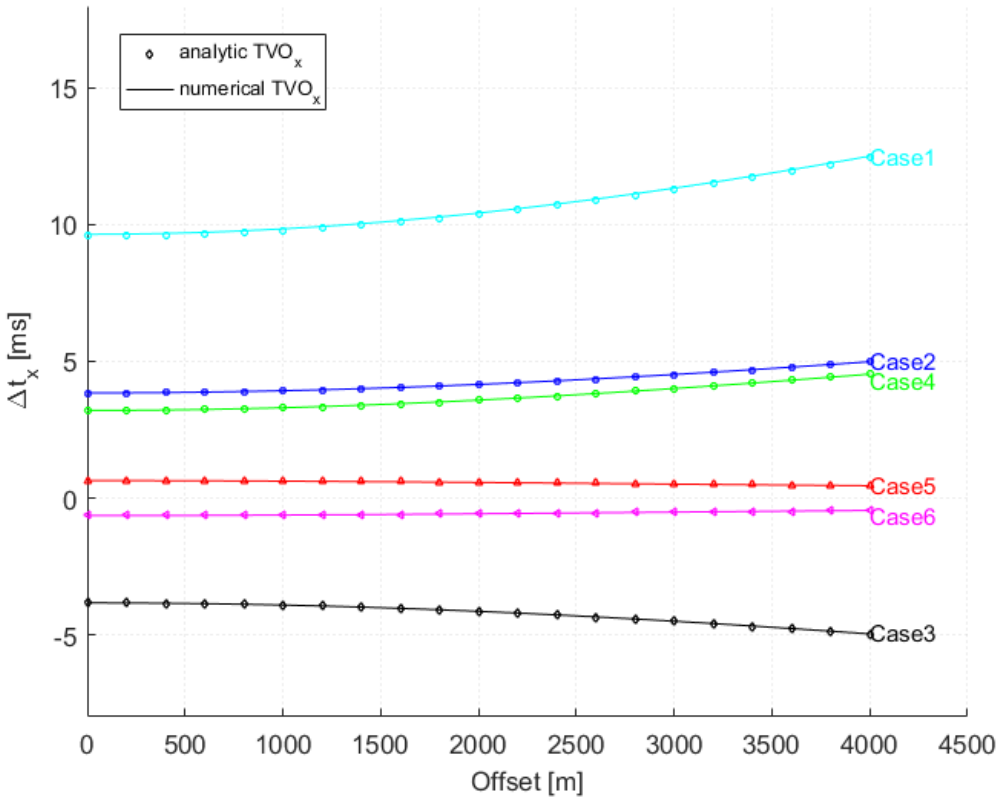

Figure 3.13: $aTVO_x$ for six cases denoted by different colours of the one-layer model over. Theoretical results by LandrØ's prediction (dots) comparing to numerical results by ray tracing (lines) produce identical $aTVO_x$ behaviour. Cases 1, 2 and 4 for reservoir compaction show an increase of $aTVO_x$. Case 3 is for reservoir extension with the same magnitude as case 2 hence the TVO behaviour has opposite polarity. Case 5 and 6 exclude the contribution of velocity changes and consider the thickness changes only, hence the TVO dependence is quite small and almost flat. They also have opposite polarities but the same magnitude.

3.2.1.2 TVO dependence with NMO correction - TVO_0

Most data for TVO work are presented as NMO corrected gathers. The NMO operator has been designed to flatten the baseline traces. Given the above traveltime for baseline and monitor, I use the NMO Equation (Equation 3.3) to apply the correction using the known baseline velocity model as follow:

$$t_{b_{NMO}} = \sqrt{t_b^2 - \frac{x^2}{V^2}}. \tag{3.16}$$

The relative time-shifts are then calculated as:

$$\frac{\Delta t_0}{t_0} = \frac{t_{m_{NMO}} - t_{b_{NMO}}}{t_{b_{NMO}}}. \tag{3.17}$$

Plotting these numerical results in the same plot as the theoretical results obtained from Landrø's equation for NMO correction (Equation 3.1) yields $rTVO_0$ as shown in Figure 3.14. As above, I also plot the dependence of $aTVO_0$ in Figure 3.15. These two figures generate similar trends principally due to the offset-independence of t_0 and interestingly, are still similar to Figure 3.13. Cases 1, 2 and 4 describe reservoir compaction with both velocity and thickness changes and give an increase of both $rTVO_0$ and $aTVO_0$. In cases 5 and 6, I exclude velocity change contribution and thus both $rTVO_0$ and $aTVO_0$ remains unchanged (see Equation 3.3). For non-zero $\Delta V/V$ (case 1, 2, 3 and 4), there are slight gaps between the numerical and theoretical results. This gap is biggest for case 1 where $\Delta V/V$ and $\Delta z/z$ are largest. I suspect that the differences between these numerical and theoretical results is due to NMO stretch effect, which is applied in Landrø's study to derive Equation 3.1 but not taken into account in the numerical calculations. For a one-layer model, the numerical calculation is fairly simple and is basically the same as the analytical derivation. Therefore, for non-NMO correction, these two results are in agreement (Equation C1, C2 and C3). However, when it comes to employ the NMO stretching effect together with the NMO correction (Equation C.6, C.7 and C8), there is the derivative step applied to time-lapse seismic data (Equation C.6 and C.7) to form the final NMO-correct TVO equation (Equation C.9). Meanwhile, the numerical study does not include the NMO stretching effect, but only NMO correction. This can cause a slight difference between the analytical and numerical results, in which

the analytical results are flattened out thanks to the derivative process to apply the NMO stretching. Meanwhile, the numerical results still maintain their curly shape, especially at the very far offsets where the effects of NMO stretching are more dominant. This NMO stretch effect can be found in Appendix C. Nevertheless, the numerical results do stay close to the trends of the theoretical solutions.

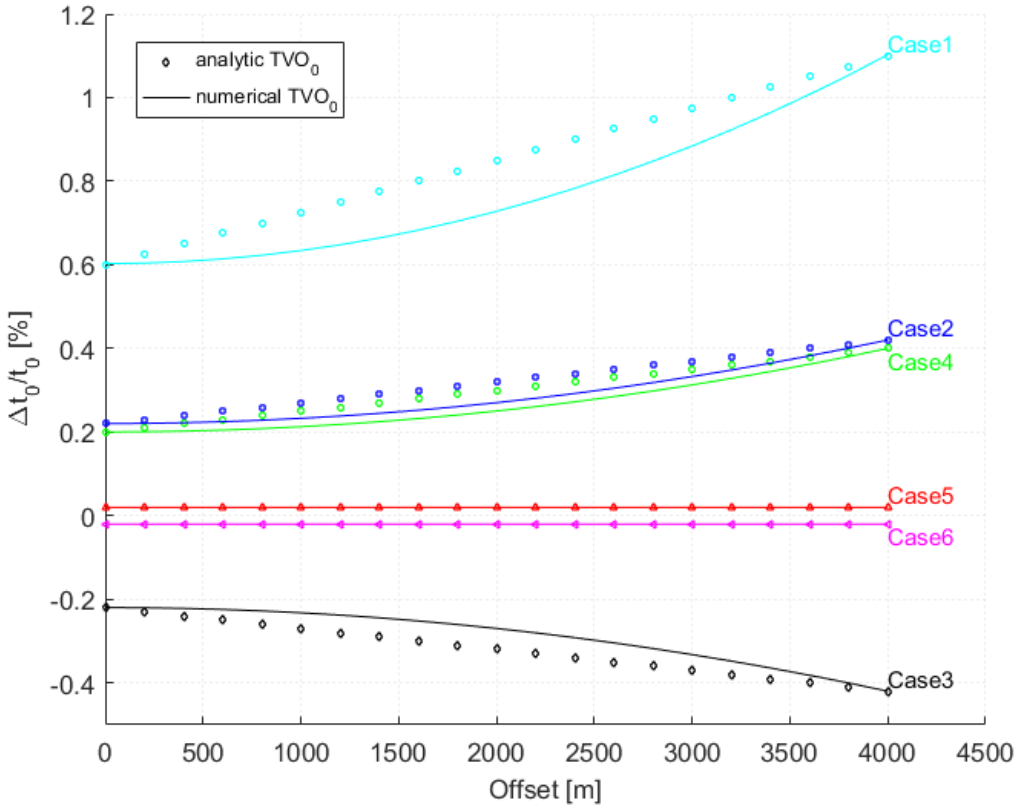

Figure 3.14: $rTVO_0$ of six cases denoted by different colours for the one-layered model. Cases 1,2 and 4 represent reservoir compaction scenarios and show an increase of $rTVO_0$ whilst the reservoir extension scenario (case 3) behaves in the opposite way. Cases 5 and 6 provide flat $rTVO_0$ due to exclusion of velocity changes. Comparison of theoretical Landrø's prediction (dots) and the numerical results (lines) show similar trends. The differences between the theoretical and numerical predictions are due to employing NMO-stretching effects in LandrØ's method but not in the ray-tracing algorithm.

Thus, in a one-layer model, for a compaction reservoir scenario, all three TVO quantities, $aTVO_x$, $rTVO_0$, and $aTVO_0$, show the increase of TVO. This proves that the type of data used, either before or after NMO correction, is not an issue when dealing with absolute time-shift $aTVO_0$ or $aTVO_x$. The trends of either increase or decrease would remain the same. However, it should be very precise when dealing with the relative time-shift quantity $rTVO_x$ due to the angle dependence quantity t_x

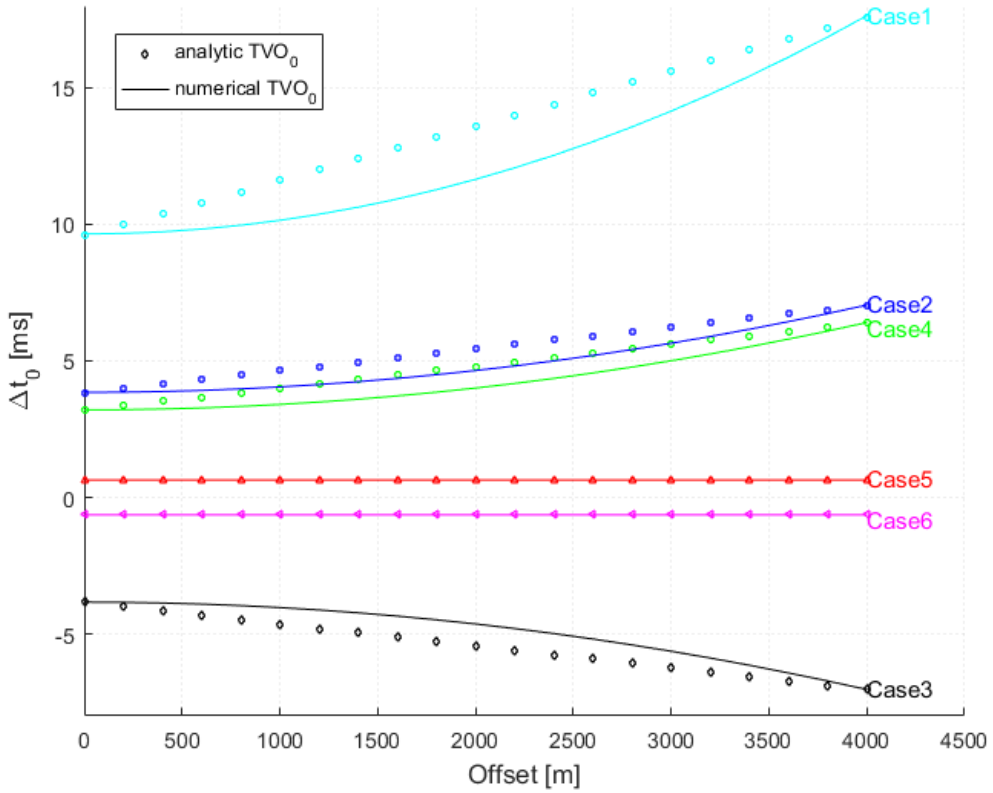

Figure 3.15: $aTVO_0$ of six cases denoted by different colours for the one-layered model. There are very similar observations as in Figure 3.14 due to offset-independence of variable t_0 on the LHS of Equation 3.3. This $aTVO_0$ is still similar gradient with $aTVO_x$ in Figure 3.13.

in the denominator on the left-hand-side of Equation 3.6. In this examples, $rTVO_x$ decreases. These four TVO quantities are now fully clarified and for the sake of simplicity, in the next numerical examples, I will only account for $aTVO_x$ which is also in line with the usage of angle-stack data in practice.

3.2.2 Two-layer model

Here I extend the TVO synthetic ray-tracing to a two-layer model of the overburden, where $V_1 = 2500m/s$, $z1 = 1000m$ and $V_2 = 2700m/s$, $z2 = 1000m$ as sketched in Figure 3.16. Different cases for possible changes in the over-burden due to production are presented in Table 3.3. I here focus on the reservoir compaction scenarios. Due to the arching effect (Staples et al., 2007b), the overburden layer closer to the top reservoir (layer 2) is expected to be stretched more than the top overburden (layer 1)($\Delta z_2 > \Delta z_1$). Six different cases are generated by combining various possibilities by considering only changes in thickness or velocities or by considering both changes of these two effects over either two layers or one layer only.

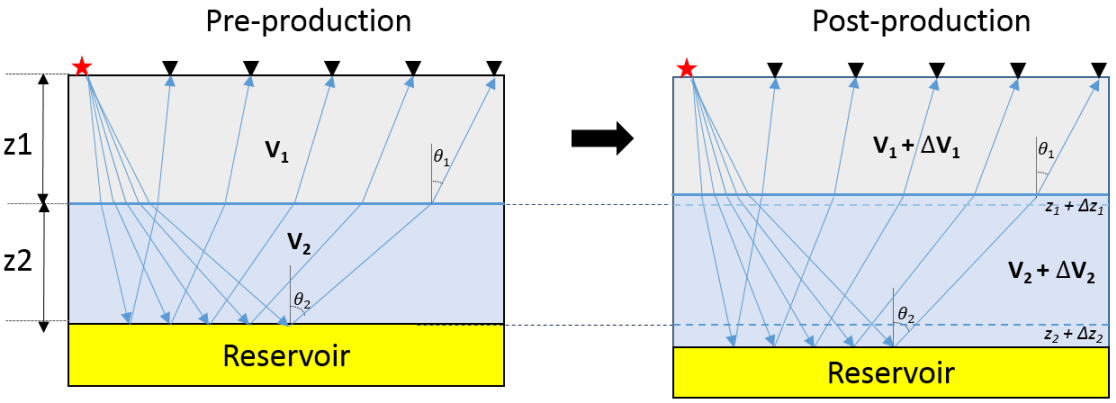

Figure 3.16: Pre- (left) and post-(right) production model for two-layer model. Subscript 1 and 2 indicate the layer number. Symbol Δ is for time-lapse changes. Variety of different scenarios for Δz and ΔV are presented in Table 3.3.

Given the horizontal reflector depths, interval velocities and offsets, optimal incident angles are found using the iterative Newton-Gaussian method for each individual ray-path. The algorithm finds the shortest ray-path that honours Fermat's principle and simultaneously satisfies the ray bending effect according to Snell's law. The ray-paths are no longer straight as in the one-layer model. The results of this two-layer model for the six different cases are presented in Figure 3.17. The numerical results for straight ray-paths are also compared for reference purposes. As expected, $aTVO_x$ shows a positive gradient for all the cases of reservoir compaction (case 1,3,5,6) and a negative gradient for reservoir extension (case 4). Case 1 and case 2 have opposite TVO trends (regardless their gradients) when considering only velocity changes ($\Delta z/z = 0$) and only thickness changes ($\Delta V/V = 0$), respectively. Case 6 taking account into the changes in only the second layer returns smaller time-

Various over-burden scenarios		Layers	Δz - re (m)	ΔV - ob (m/s)	Δz/z - ob (%)	ΔV/V -ob (%)
Case 1	Slow down ONLY	OB 1	0	-10	0	-0.4
		OB 2	0	-18	0	-0.667
Case 2	Extension ONLY	OB 1	0.3	0	0.03	0
		OB 2	0.5	0	0.05	0
Case 3	Slow down + extension	OB 1	0.3	-10	0.03	-0.4
		OB 2	0.5	-18	0.05	-0.667
Case 4	Speed up + Compaction	OB 1	-0.3	10	-0.03	0.4
		OB 2	-0.5	18	-0.05	0.6667
Case 5	Slow down + extension (smaller magnitude)	OB 1	0.1	-5	0.01	-0.172
		OB 2	0.2	-8	0.02	-0.296
Case 6	Slow down + extension (second layer ONLY)	OB 1	0	0	0	0
		OB 2	0.2	-8	0.02	-0.296

Table 3.3: Different cases for changes in the overburden of a two-layer model.

shifts over case 5. Overall, quite small changes in velocities ($< 0.7\%$) and thickness ($< 0.05\%$) cause big time-shifts ($> 9ms$) due to the accumulative nature of time-shifts over the overburden depth column. The straight ray-path seems to work well with these small time-lapse changes as the dots are in the line with the lines up $> 3800m$ and starts to breakdown afterwards. It should be noted that the offset in this two-layer example is purposely extended longer than the one-layer model above to examine the straight-ray assumption.

Thus, the trend of TVO dependence for this two-layer model is the same as the one-layer model with an increase of $aTVO_x$ for the reservoir compaction scenario. Beside bending ray tracing, I also include the calculation of straight ray assumption, which is broken down at a very far offset, over $3800m$.

3.2.3 Water variation model

In the work of Bertrand and MacBeth (2003); Ong et al. (2015), the authors pointed out the impact of seawater velocity variations for reservoir time-lapse seismic analysis and interpretation. It could significantly alter measured travel-times and hence time-lapsed time-shifts, especially on angle-stack traveltime. Therefore, as my study is moving forward to the angle-stack domain in the next chapter, it is important to have the awareness of the water velocity variations. The water column is included as the topmost layer in the one-layer model (3.18). The ray-tracing algorithm for

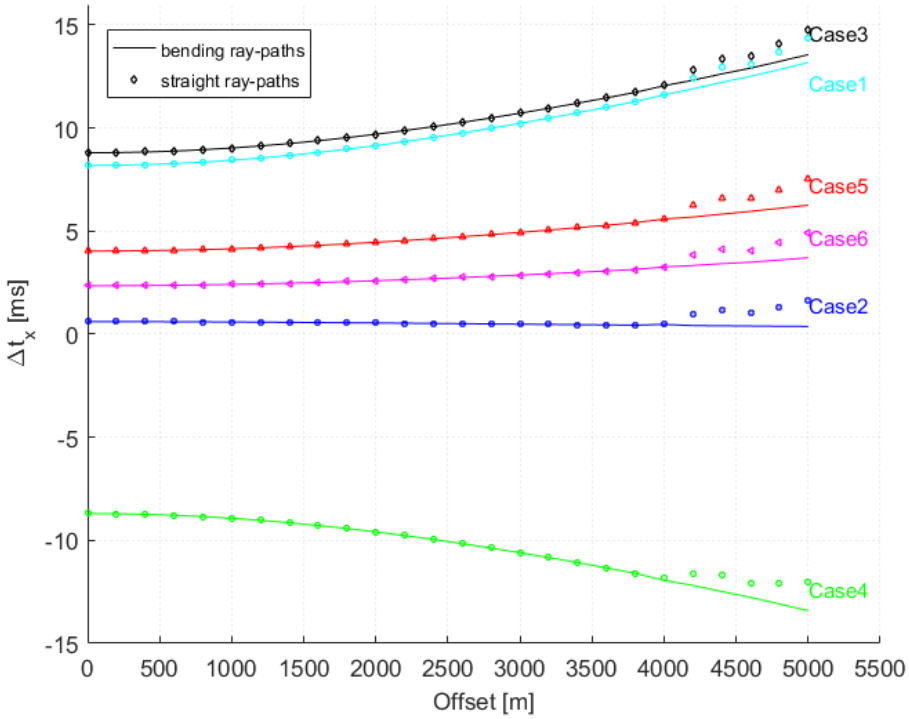

Figure 3.17: $aTVO_x$ of two-layer model for the six cases described in Table 3.3 and denoted by different colours. Time-shifts increase with offset for the reservoir compaction scenarios (cases 1, 3, 5, 6) and with opposite polarity for case 4. Small changes of time-lapse velocities ($< 0.7\%$) and thickness ($< 0.05\%$) do not break the straight ray-path estimation (solid circles) compared with the bending ray-paths (lines). However, they can induce quite big time-shifts of up to $9ms$.

bending rays is applied to the two-layer model for the various scenarios described in Table 3.4. Two scenarios of shallow water depth (90 m at the Teal South field) and deep water depth (500m at the Foinaven field) are used to examine the effects of water variations on TVO relationship. For each scenario, three different cases are generated by changing the thickness and velocity either in the water column only (case 1) or in both water and overburden layers (case 2, 3). These water variations are extracted from Bertrand and MacBeth (2003). The thickness and velocity changes in the overburden of case 2 are purposely taken from Table 3.2 (case 2) for one-layer model in order to access the effect of water column on the time-lapse attributes.

Figure 3.19 shows the TVO behaviour for this model for the Teal South and Foinaven fields as three different scenarios. Case 1 representing for the only variations in the water layer (but not overburden) show a slight decrease $aTVO_x$ in shallow water depth (3.19a) and become steeper in deeper water depth (3.19b) with larger gradient

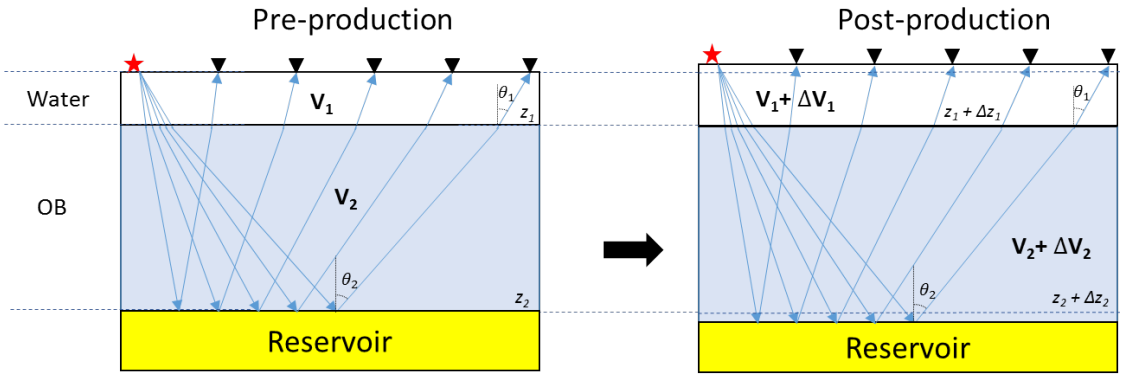

Figure 3.18: Pre- (left) and post-(right) production model for water variation model, made of the water column (white colour) over one-overburden-layer (light blue). Variety of different scenarios for Δz and ΔV are presented in Table 3.4.

Water-variation scenarios		Layers	Δz - re (m)	ΔV - ob (m/s)	Δz/z - ob (%)	ΔV/V -ob (%)
Teal South field Z1 = 90m, Z2 = 2000m V1 = 1530 m/s, V2 = 2500m/s	Case 1	Water	0.1	10	0.111	0.667
		OB	0	0	0	0
	Case 2	Water	0.1	10	0.111	0.667
		OB*	0.8	-5	0.04	-0.2
	Case 3	Water	0.1	10	0.111	0.667
		OB	-0.8	5	-0.04	0.2
Foinaven field Z1 = 500m, Z2 = 2000m V1 = 1500 m/s, V2 = 2500m/s	Case 1	Water	0.1	10	0.111	0.667
		OB	0	0	0	0
	Case 2	Water	0.1	10	0.02	0.667
		OB*	0.8	-5	0.04	-0.2
	Case 3	Water	0.1	10	0.02	0.667
		OB	-0.8	5	-0.04	0.2

Table 3.4: Different cases for changes in water and overburden for water variation model. OB stands for overburden in this table and symbol $*$ indicates case 2 in one-layer model.

in spite of the same thickness and velocity changes in both fields. $aTVO_x$ in case 2 for both changes in the water layer and overburden increases in shallow water (3.19a) but decrease in deeper water (3.19b). This can be understood easily thanks to the blue dotted lines, which stand for the one-layer model without the topmost water layer as described in subsection 3.2.1. Roughly speaking, $aTVO_x$ in case 2 is summation of $aTVO_x$ in case 1 and $aTVO_x$ in the one-layer model. In a similar way to case 2, $aTVO_x$ in case 3 can be obtained by summing case 1 and opposite values of the one-layer model, resulting a similar decreasing TVO performance.

Thus, the water variation does effect on time-shifts and hence TVO behaviour. More

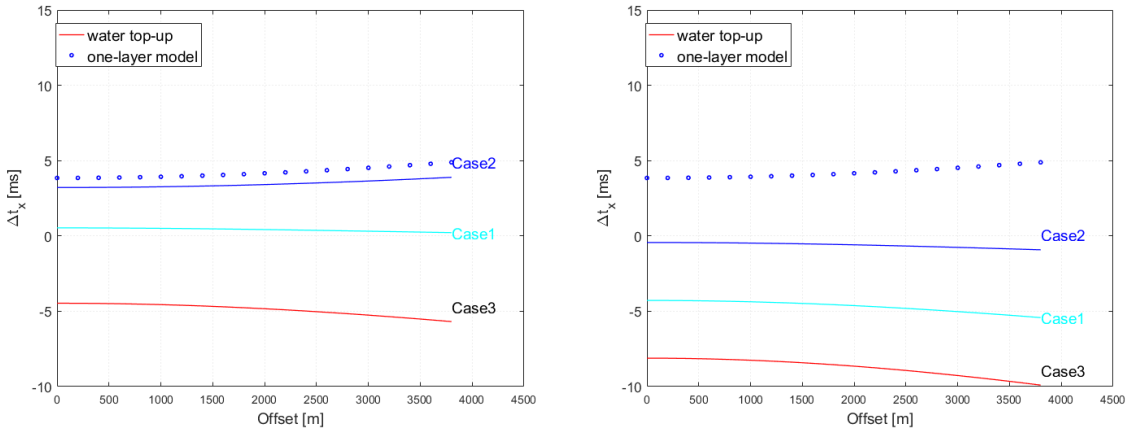

(a) (b)

Figure 3.19: $rTVO_x$ of water variation at the (a) shallow and (b) deep water depth with three different cases denoted by three different line colours. The dotted lines are $aTVO_x$ of case 2 in the one-layer-model for reference purpose since if this water-variation model is stripped of the topmost water layer, it becomes the one-layer model. It is observed that with the same variation of water column and velocity, there are differences of $aTVO_x$ in these two plots over the same plot scale. This provide the evidence of different effects of water variation on TVO for different fields.

importantly, these impacts are differently for different field with various water depth column.

3.2.4 Horizontal multilayer-model

Here I extend the models to horizontally multiple layers. The parameters are used from Hawkins et al. (2007)'s study as in Table 3.5, which loosely bases on a HPHT reservoir, Franklin and Elgin in the North Sea. It should be noted that these parameters are at a particular position (location 5 in Figure 3.4b) as explained in Hawkins's study. I use these position-particular 4D parameters to propagate for the whole lateral perturbed (hence monitor) velocity model for ray tracing. Therefore, strictly speaking, the horizontal multilayer generated in this thesis is lateral constant, which is slightly different from Hawkins's perturbed models with lateral variations as seen in Figure 3.4a. Hence, this slightly difference should be considered when it comes to any comparison later on. From a given baseline and 4D parameters with $R = 5$ from Hawkins's study here, I also try with another five selected values of R factors from 0 to 15. I keep $\Delta z/z$ the same, via R factors, I generate six corresponding $\Delta V/V$ and hence $V_{monitor}$.

For ray tracing, I use CAT3D - a tomography package provided by an Italian Insti-

Base survey parameters			4D parameters			
Layers	TWT (ms)	V (m/s)	Δz/z - ob (%)	R = 0 ΔV/V - ob (%)	R = 3 ΔV/V - ob (%)	R = 5 ΔV/V - ob (%)
1	100	1500	0	0	0	0
2	1000	2000	0	0	0	0
3	1500	2200	0.01	0	0.03	0.03
4	2000	2400	0.02	0	0.06	0.06
5	2500	2600	0.03	0	0.09	0.09
6	3100	2800	0.04	0	0.12	0.12
7	3700	4500	0.04	0	0.12	0.12
8	4000	3000	0.1	0	0.3	0.3
9	4200	3000	-0.2	0	-0.6	-0.6
10	4800	4000	0.03	0	0.09	0.09
11	6000	3500	0	0	0	0

Table 3.5: Baseline and three display-selected 4D parameters corresponding to R factors for horizontal multilayer model.

tute *Istituto Nazionale di Oceanografia e di Geofisica Sperimentale* to generate the bent-rays at given offsets. During generating the above two-layered-model, I did compare the results from my Matlab codes to results from CAT3D and they are the same. Then the TVO behaviours for this horizontal multilayer model is simply obtained by subtracting the various monitor traveltime corresponding to various R factor to baseline traveltime and being plotted as in Figure 3.20a.

For non-zero R, TVO_x slightly increases versus such a long offset (up to 7000 m). Particularly, at $R = 5$ which is used in Hawkin's study, TVO_x produces a very similar trend of slight increase at a very far offset ($> 6000m$) as in Figure 3.4c by Hawkins et al. (2007) in spite of larger Δt_x in this example (about $2.2ms$ as in Y-axis). The mis-matched Δt_x might come from the different models of between constant and lateral variation, which is important for ray-tracing. Nevertheless, the gradient of TVO_x matters, which is in line with Hawkins's observation for horizontal multilayer model. More interestingly, at $R = 0$ ($\Delta V/V = 0$), TVO_x changes its direction - decreasing. This decrease agrees with the analytical prediction of Equation 3.6 by Landrø and Stammeijer (2004) and numerical result (case 5, Figure 3.12) even though again, this comparison is not wholly compatible between a one-layer model

and a multilayer model.

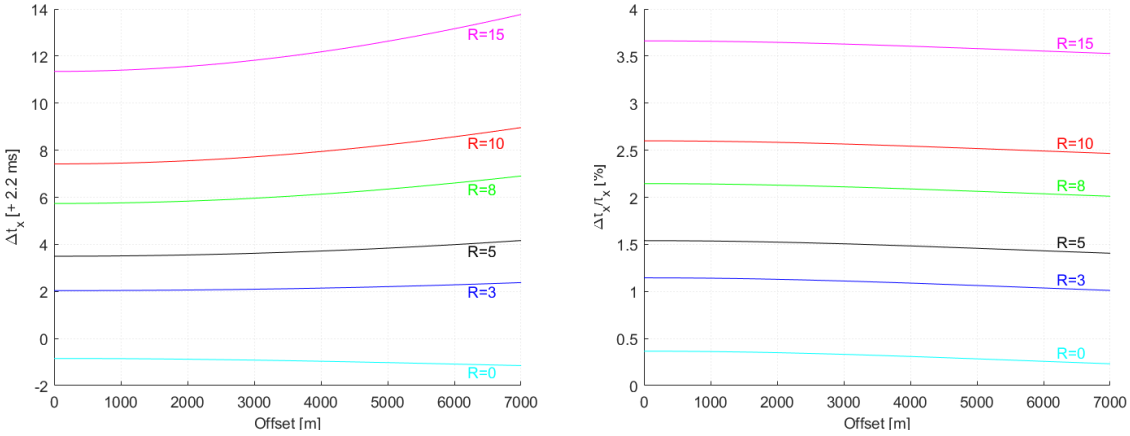

(a) (b)

Figure 3.20: (a) $aTVO_x$ and (b) $rTVO_x$ for a horizontal multilayer model over six different R factors. $aTVO_x$ increases for all non-zero R excepting $R = 0$ ($\Delta V/V = 0$), which is in line with Equation 3.6 for a homogeneous one-layer model. For $R = 0$, $aTVO_x$ in this numerical calculation for constant lateral variation is very similar to location 5 in Figure 3.4a. $rTVO_x$ decreases over all R factors, which has similar trends to $rTVO_x$ of the one-layer model and to $rTVO_x$ in Figure 3.3.

I then look at $rTVO_x$ as shown in Figure 3.20b. Different from TVO_x, $rTVO_x$ decreases with offset for all the values of R yet remains the same small gradient. In spite of constant lateral variation and multilayer model, this decrease of $rTVO_{x-Multilayer}$ is in line with $rTVO_{x-\text{Røste}}$ for a lateral variation one-layer model and with $rTVO_{x-\text{Landrø}}$ for a homogeneous one-layer model. Thus, in spite of various underlined models used in different published studies, there is consistent of TVO dependence for the compaction scenarios - TVO_x increases and $rTVO_x$ decreases. In next section 3.3, I will provide the summary table of TVO behaviour from all these numerical examples in this thesis loosely in correlation with the published studies.

3.3 Chapter conclusions

In this chapter, I provided a review and critical analysis on the dependence of timeshift versus offset over various physical models using a classification scheme of:

- Underlined physical models: a homogeneous one-layer model, a lateral variation one-layer model and multilayer.
- Methodologies: straight ray assumption, isotropic ray-tracing, anisotropic ray-

tracing.

- Type of data used: NMO correction or no NMO correction, post-stack or angle-stack.

By setting up common notation systems, re-deriving the published equations, and putting efforts to bring the reported plots and charts back to the most possible similar scale, the lacks of clarify of various reported TVO dependence over different studies in the literature are diminished. Other field observation of TVO are also included in this chapter as summarised in Table 3.1 to provide a broader spectrum of TVO dependence.

Numerical examples in this thesis		**TVO_x**	**$rTVO_x$**	**TVO_o**	**$rTVO_o$**	**Synthetic studies in the literature**	
One-layer model	Homogeneous	↑↑	↓↓	↑↑	↑↑	Homogeneous	Landrø
			↓			Lateral variation	Røste
Two-layer model		*↑					
Water variation*		↓				Ong et al. (2015)	
Multi-layer model	Constant lateral	↑	↓				Hawkins
		↑				Lateral variation	

Table 3.6: Summarised TVO observation from the numerical examples in this thesis and the reported synthetic studies in the literature. The blue * indicates case-dependence.

I also include the numerical examples for a chain of various synthetic models designed from a simple one- and two-layer model to more complicated levels of multilayer model as described in Table 3.6 on the left (blue area). The synthetic studies in the literature are put on the the right of the table (red area). The blue and red arrows indicate the increase (↑) and decrease (↓) of each TVO variables (TVO_x, $rTVO_x$, TVO_0 and $rTVO_0$) observed from the numerical calculations and reported studies, respectively. Overall, for compaction reservoir scenarios, disregarding the number of layer taken into account and constant or lateral variation, TVO_x increases but $rTVO_x$ decreases. For the water variation scenario, the TVO direction is variable (described by curved blue arrow) for each field example. Thus, it seems that there is a certain degree of dependence of time-shift versus offset even though they are quite small. This might be the reason why most of the published studies focus on

examining this TVO dependence for the compaction reservoirs, in which the time-shifts are usually largest (Figure 1.7). Therefore, this type of geomechanical scenario might benefit the inversion of partial-stack time-shifts while this TVO topic is still growing.

Chapter 4

Time-lapse traveltime tomography

ABSTRACT

The previous chapter introduced the concept of offset or angle dependent time-shifts. Finding a way to invert angle-stack time-lapse seismic to best recover changes in the subsurface becomes an essential task. This chapter concentrates on time-lapse tomography (or 4D seismic tomography) which is one of the key methodologies to tackle this problem. The evolution of 4D seismic has started from 3D seismic tomography, in which the baseline and monitor are separately inverted and the 4D changes of the subsurface are estimated by taking the differences. Then the *sequential 4D tomography* was introduced leading to the most recent innovations in *4D perturbed tomography*. This chapter first explains in detail this evolution. Consequently, I present my developed *angle-stack 4D perturbed tomographic inversion* using straight-ray assumption from time-shift measurement with a synthetic example. At the end, I investigate a *the small ray-bending solution* to examine the validity of straight-ray assumption and I close the chapter with some discussions.

4.1 Evolution of time-lapse seismic tomography

Together with the extension of time-lapse seismic studies to pre-stack domain (e.g. TVO), time-lapse tomography topic has gain more interest recently. At the early stage, most of the time-lapse tomographic studies are still relying on the fundamental static (2D or 3D) tomography, such as Vesnaver et al. (2001), Guilbot and Smith (2002), Vesnaver et al. (2003) to name a few. Recently, with the development of 4D seismic, there is more focus on directly extracting the 4D seismic attribute (time-shifts and amplitude changes) (Shragge et al., 2013; Yang et al., 2014; Edgar and Blanchard, 2015; Edgar and Mastio, 2017). Therefore, in this section, I will briefly revise static tomography before getting directly into the time-lapse tomography and its differences and advantages.

4.1.1 3D seismic tomography

"Tomography" means slices (*tomos*) of the images. It has been applied in many different areas of sciences, most commonly in medical Computed Tomography scanning with the images of various parts of the body. In seismic application, the technique images the subsurface medium using the seismic waves produced by earthquakes, explosion or acquisition for oil and gas exploration and production. This is an inversion method so that it also has some key aspects of model paremeterization (e.g layers, rectangular blocks), forward calculation, inversion and analysis of solution's robustness. The heart of tomography is the forward operator, which has three main categories - ray tracing, shortest path ray tracing or wavefront tracking. Ray tracing finds the path between a source and receiver, either by shooting or bending methods. Shortest path ray tracing uses Fermat's principle directly. Finally, wavefront tracking aims to follow the propagation path of the entire wavefront by solving the eikonal equation and using different tools such as finite difference scheme or fast marching (Jones, 2010; Rawlinson, 1996; Červený and Pšenčík, 2011). Once the forward modelling operator is set up from the pre-set velocities and interfaces of the initial subsurface model, the inversion process is carried out either on backprojection method, gradient methods or global optimization. From here, we can see the complexity of tomography at each step, from parameterization to making the decision of ray-tracing method and then inversion algorithm. The scope of this thesis is to

investigate a simple and robust time-lapse tomography algorithm as a short-cut for more complex tomographic techniques mentioned above.

3D straight ray tomography

Since this thesis uses the shooting ray tracing method with straight ray assumption, it is useful to provide more details on the usage of the straight ray assumption in 3D seismic tomography. Seismic energy is described as wavefronts from source to the receivers. The perpendicular line to the wave-front is called the ray, which points the local direction of the waves' propagation. These seismic propagations can be modelled in the fashion of either ray tracing or wavefront tracing. This depends on the choice of three following basic theories that are often applied in reflection traveltime tomography.

The first theory is Snell's law. It predicts the orientationof ray as it crosses an interface. Secondly, Fermat's principle finds the minimum travel path between two points. Lastly, Hughen's principle describes the expansion of a wavefront from a source point, in which every single point of a wavefront can be the source of secondary wavelets that spread out in all directions with the same speed as the wave's propagation. For tracing rays, there are two methods: shooting or two-point perturbation. Shooting method requires the sources' positions and take-off angles for the rays arriving at the receivers. The two-points method, as it is named, finds the raypath between two known points. These two methods can be used separately (Cassell, 1982) or combined (Langan et al., 1985) depending on the scale of the problem and available computation. For tracing the wavefronts, Moser (1991) presented graph methods; however solving the eikonal equation seems to be more preferable in studies using characteristics methods (Červený and Pšenčík, 2011) (p106), finite different methods (Vidale, 1988) and finite element methods (Smith, 1975).

The use of straight ray has been analysed in the past by the work of Schuster (1988) and Schuster et al. (1988). They derived an analytical form to generalize the inverse matrix associated with the common-depth-point and vertical-seismic-profile traveltime equation. The comparison of using straight ray and bending ray (which honors Snell's law) pointed out that the straight ray algorithm can *predict roughly*

the actual values (rays honoring Snell's law) for offset-to-depth ratios of less than 1 (Schuster et al., 1988).

4.1.2 4D seismic tomography

4D seismic study assumes the changes of static properties of the subsurface are negligible during the production activities - only fluid-related changes are taken into account. Therefore, time-lapse seismic tomography aims to recover the dynamic changes of the velocity model due to the production based on the provided information of a 3D velocity model. This recovery process can be done in the fashion of *"separate"*, *"coupled"* or *"direct"* inversion as mention in Figure (1.12) by Sarkar et al. (2003). In this tomographic inversion context, I refer to the terminology of *"sequential"* for both separate and coupled inversion and *"perturbed"* for direct inversion.

4.1.2.1 Sequential time-lapse seismic tomography

Sequential 4D seismic tomography is a transitional methodology from 3D to 4D tomography. The term "sequential" implies that the tomographic inversion that are carried out sequentially, one by one at different production stages and the time-lapse changes are derived by taking the differences. For example, in Broto et al. (2011), the author used the 3D traveltime tomography of blocky parameterization and bending ray-tracing in iterative fashion to seperately recover the baseline and monitor velocity models. Vesnaver et al. (2001) orientated to time-lapse velocity analysis by using both AVO and tomographic inversion inherited from 3D tomography. In their studies, seismic vintages are inverted separately without any constraint or averaging procedures so that the seasonal changes in the seawater layer and production-related changes at the target are present in the data. The authors remarked that differences among the corresponding interfaces were small and there is a decrease of velocities at the target in the central area as indicated by the white arrows in Figure 4.1. In the work of Guilbot and Smith (2002), they instead used the term *"4D constrained tomography"* to estimate the interval monitor velocity model in depth domain for a compaction reservoir in the North Sea. The input is baseline velocity model, time-shifts map together with other prior knowledge available from reservoir simulation

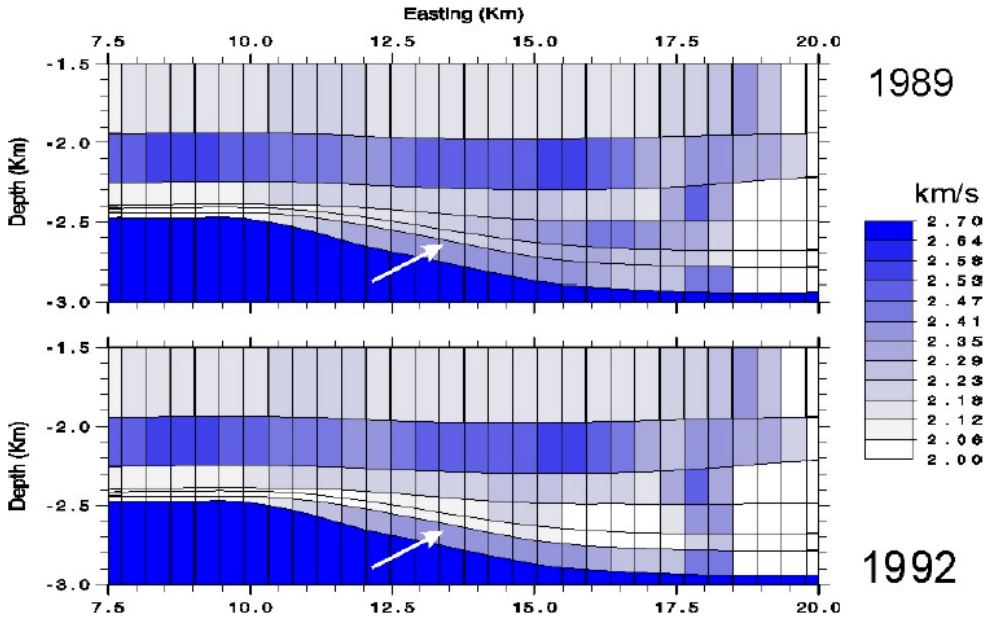

Figure 4.1: Velocity field at the target (white arrow) seperatedly estimated by the baseline (top) and monitor data (bottom) using 3D tomography. From here, a decrease of velocities at the target is revealed. After Vesnaver et al. (2001).

(Figure 4.2) to constrain the monitor tomographic inversion. Though this posed inversion problem has an analytical solution and is solved directly without an optimization method, the method heavily relies on the known baseline velocity model of layers and depth of interfaces.

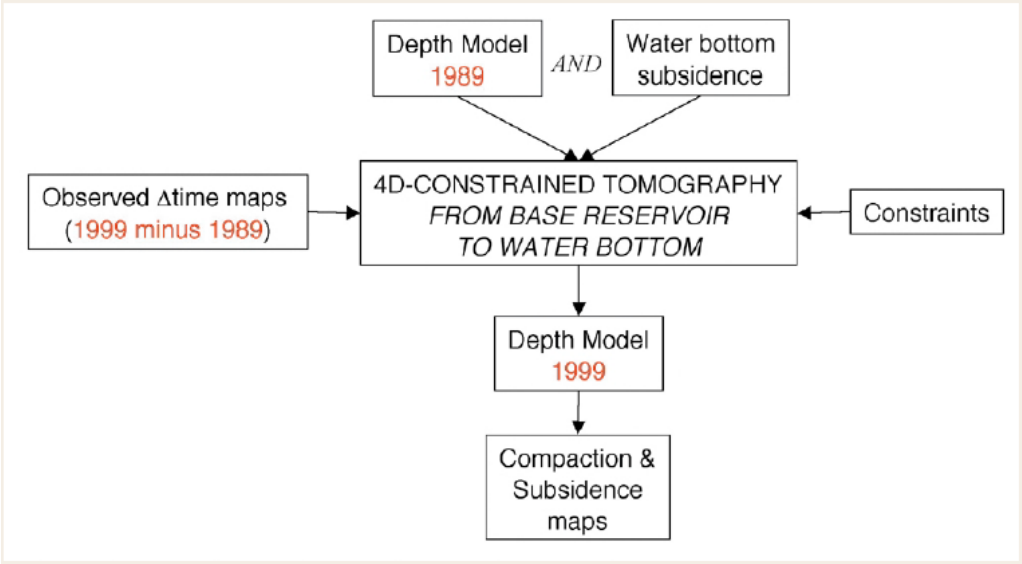

Figure 4.2: Workflow of "4D constraint tomography" by Guilbot and Smith (2002). The prior information, such as time-shift map, baseline velocity depth model in 1989 obtained from tomographic inversion and other constraints, are coupled into the tomographic inversion for monitor seismic data in 1999.

Similarly, Shragge et al. (2013) also proposed time-lapse image-domain tomography

using the adjoint-state method to invert for time-lapse velocity changes ΔV in the *"absolute"* and *"relative"* fashion. In the context of Sarkar et al. (2003) mentioned in Chapter 1, *"absolute"* here means "separate inversion", which inverts the baseline and monitor separately. Meanwhile, the *"relative"* equals "coupled inversion", which uses the baseline as prior information to incorporate into the monitor inversion. Either of these two fashions consumes time and efforts to perform the inversion for each time-lapse seismic surveys yet takes a good consideration of the geological structures.

4.1.2.2 Perturbed time-lapse seismic tomography

In this section, I focus on the studies that directly use 4D seismic differences, such as the 4D time-shift attribute or amplitude changes. Yet we know doing 3D study is important in 4D seismic study, inverting each seismic vintage costs much more time and effort than inverting on the time-lapse differences.In Landrø and Stammeijer (2004)'s work along with others mentioned in Chapter 3 of the TVO dependence, there is no notion for a prior 3D model. Therefore, it is a natural process to perform 4D seismic tomography directly on 4D seismic differences.

There are not many published studies focusing on this direction so far. Evensen and Landrø (2010) proposed a direct time-lapse tomographic inversion using Gaussian parameterisation for a CO_2 injection project in the overburden of a field in the North Sea. Time-lapse velocity changes, ΔV, are expressed into six and ten parameters for two and three dimensions, respectively. The method uses the input of pre-stack time-shift attributes from time-lapse seismic and also relies on the choice of background or baseline model. By using Gaussian parameterisation, the method analytically describes ΔV and limits the amount of parameters used over a large area covered by pre-stack seismic data. Also using pre-stack time-shift, recently Edgar and Blanchard (2015) developed 4D linear pre-stack tomography to invert for time-lapse relative velocity changes $\Delta V/V$ instead of ΔV. The studies elegantly set up the link of offset-dependent time-shift Δt with the model parameter $\Delta V/V$ as:

$$\Delta t = \mathbf{A_t} \frac{-\Delta V}{V}. \tag{4.1}$$

where $\mathbf{A_t}$ is the tomographic matrix, which contains the travel time per cell of each

ray. It is constructed only once, via ray-tracing of a known baseline velocity model. Using Equation 4.1, the perturbed velocity changes $\Delta V/V$ is robustly updated from time-shift measurement. With this setting, the underlined assumption is that the ray-path from baseline to monitor remains the same. The derivation of this matrix equation is shown in detail in Section 4.2.1. Edgar and Blanchard (2015)'s study solves Equation 4.1 for the velocity changes $\Delta V/V$ by an iterative fashion using an objective function with geological and geo-mechanical constraints for time-strain inversion. The study was then extended to the image domain in Edgar and Mastio (2017). The inverted velocity changes are remarkably close to the synthetic truth as in Figure 4.3.

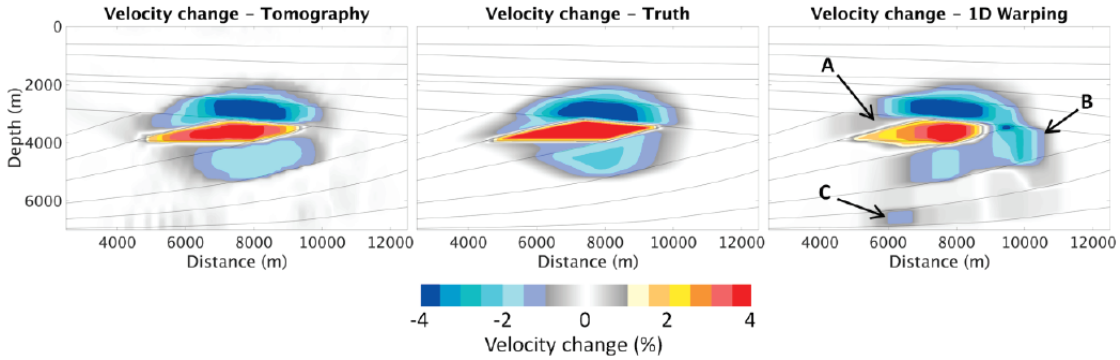

Figure 4.3: Synthetic data example: Comparison of time-lapse velocity changes estimated by Tomography (left), 1D Warping (right) with the Truth (middle). Arrows A, B and C highlight the most significant errors in the 1D Warping result. These are due to the invalid 1D assumption: that post-stack time shifts are caused by velocity changes vertically above. Tomography does not suffer these errors because prestack time shifts are correctly attributed to velocity changes along traced ray paths. Horizons are overlain on the images, for reference. After Edgar and Mastio (2017).

4.2 New approach – Angle-stack 4D perturbed straight ray tomography

The above studies have proved the value of 4D tomography. Further, as stated by Edgar and Mastio (2017), 1D approximation in post-stack domain conflicts with how seismic propagation is in reality. Therefore, finding a way to invert pre-stack time-lapse seismic to best recover changes in the subsurface is essential. Edgar and Blanchard (2015); Edgar and Mastio (2017) introduced such a notable way

to write the pre-stack time-shift as a function of velocity changes $\Delta V/V$ and the tomographic matrix $\mathbf{A_t}$, as mentioned above in Equation 4.1. The $\mathbf{A_t}$ matrix is created for a given baseline velocity model by using the method of characteristics to solve the 2D Eikonal equation from Červený and Pšenčík (2011) (p106, Equation 3.1.19) (personal communication with John Edgar). My tomographic work in this section stems from Edgar's 4D tomography equation 4.1. The form of A matrix will be further revealed in next subsection. Even though there is a need of a given 2D or 3D velocity model to set up the solution of Equation 4.1, $\mathbf{A_t}$ matrix is not very sensitive to the accuracy of a good baseline velocity model to begin with. Because we are here looking at the differences so that the changes between monitor and baseline traveltime can be reasonably negligible (personal discussion with John Edgar).

In the scheme of seeking for a simple, robust yet efficient method as in the aim of this thesis, in the next section, I introduce a new and simplified angle-stack tomography at a constant angle. The method uses the individual rays and employs a straight ray-path assumption. The study aims to include the effect of offset dependence but also keep the same level of simplicity and fast track, hence the angle sub-stack seismic data of Near, Mid and Far are used instead of the whole different ranges of raw angle-stack data. To map the changes in ray-path imaging among different angles in seismic data, re-gridding is applied meanwhile the algorithm remains the same. The inversion is done through a direct inversion of the modelling operator, which makes this method very robust. Note that, similar to Edgar's study, this method excludes the effect of thickness changes.

In 4D time-lapse seismic, there are several studies using the straight-ray assumption such as Vesnaver et al. (2003), Landrø and Stammeijer (2004), Røste et al. (2007), Kudarova et al. (2016b). The velocity changes in time-lapse seismic is small, 1 - 5%, hence the changes in travel path-length can be negligible. This straight ray assumption makes the method easier to access and has yet proved its robustness in the case of insignificant contrast of velocity changes between two adjacent layers (Røste et al., 2006). In the work of this thesis, the main motivation behind using straight assumption is in translation to a linear relationship between the model parameters and data, thereby allowing a fast implementation of inversion.

4.2.1 Straight ray tracing equation

We recall the relationship of time-shifts and relative velocity changes from Equation 2.11 for easier following:

$$\Delta t = \int_0^t \vartheta(t) dt, \tag{4.2}$$

where

$$\vartheta(t) = \frac{1}{1 + \dfrac{\Delta V}{V}} - 1. \tag{4.3}$$

Given a simple model of ϑ in $t-x$ space with individual ϑ_i for each cell, the traveltime from a source to a receiver over the reflection point is:

$$\Delta t \approx \sum_{i=1}^{P} t_i \vartheta_i. \tag{4.4}$$

where t_i is the travel time spent in each cell and i denotes the number of cells in t-x space, from 1 to M. $P = N * M$ where N is numbers of time samples and M is number of traces. This is a discretised form of equation 4.2 under the assumptions of straight image ray-path and no change in the image ray-path from baseline to monitor. Equation 4.4 can be sorted in matrix notation as:

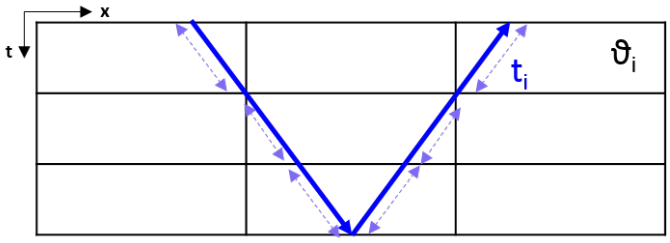

Figure 4.4: Straight ray-path assumption in this new 4D perturbed tomography at a constant incident angle. The reflection point is assigned the centre bottom of grid cell. t_i is the traveltime spending in i cell. ϑ_i is the perturb velocity changes at each cell.

$$\Delta t = \mathbf{A_t} \vartheta, \tag{4.5}$$

where $\mathbf{A_t}$ has an initial form as:

$$\mathbf{A_t} = \begin{bmatrix} t_{11} & t_{12} & t_{13} & \dots & t_{1P} \\ t_{21} & t_{22} & t_{23} & \dots & t_{2P} \\ t_{31} & t_{32} & t_{33} & \dots & t_{3P} \\ \vdots & \vdots & \vdots & \dots & \vdots \\ t_{K1} & t_{K2} & t_{K3} & \dots & t_{KP} \end{bmatrix}.$$

where t_{ij} is the traveltime spent in each cell per ray, in which $i = 1, P$ is the number of columns and $j = 1, K$ is the number of rows (also the number of rays) of $\mathbf{A_t}$ matrix. Generally in tomographic methods, $\mathbf{A_t}$ is not a square matrix because the number of rays K are usually generated more than the number of cells M so that the ray can be assured to recover the whole interest area. The problem is hence over-determined so that the solution can be found. It should be noted of a slight difference between Equation 4.5 in this thesis and Equation 4.1 in the Edgar's study which ignores of higher order terms.

4.2.2 Grid generation

The grid cell is defined by vertical and spatial length dz and dx, respectively. Given an average baseline velocity medium V, dz is now related to sampling rate dt as $dz = dt \times V$. Choosing the reflection point at centre of the base of the grid cell and $dz = dx$, the incident angle θ is:

$$\theta = arctan\left(\frac{dx/2}{dz}\right) \approx 26.5^o. \tag{4.6}$$

This grid geometry can be changed by compressing or stretching the spacing of dx while maintaining the same dz. By controlling this ratio of dx/dz, we can access into various incident angles depending on the availability of angle-stack seismic. Figure 4.5 demonstrates grid generation of three typical incident angles that represent for Far, Mid, and Near angle by compressing dx to $dx/2$ and then $dx/4$. The above incident angle θ can named θ_F for Far angle and the other incident angles of Mid

and Near angles are calculated as:

$$\theta_M = arctan\left(\frac{dx/4}{dz}\right) \approx 14^o, \tag{4.7}$$

$$\theta_N = arctan\left(\frac{dx/8}{dz}\right) \approx 7.1^o. \tag{4.8}$$

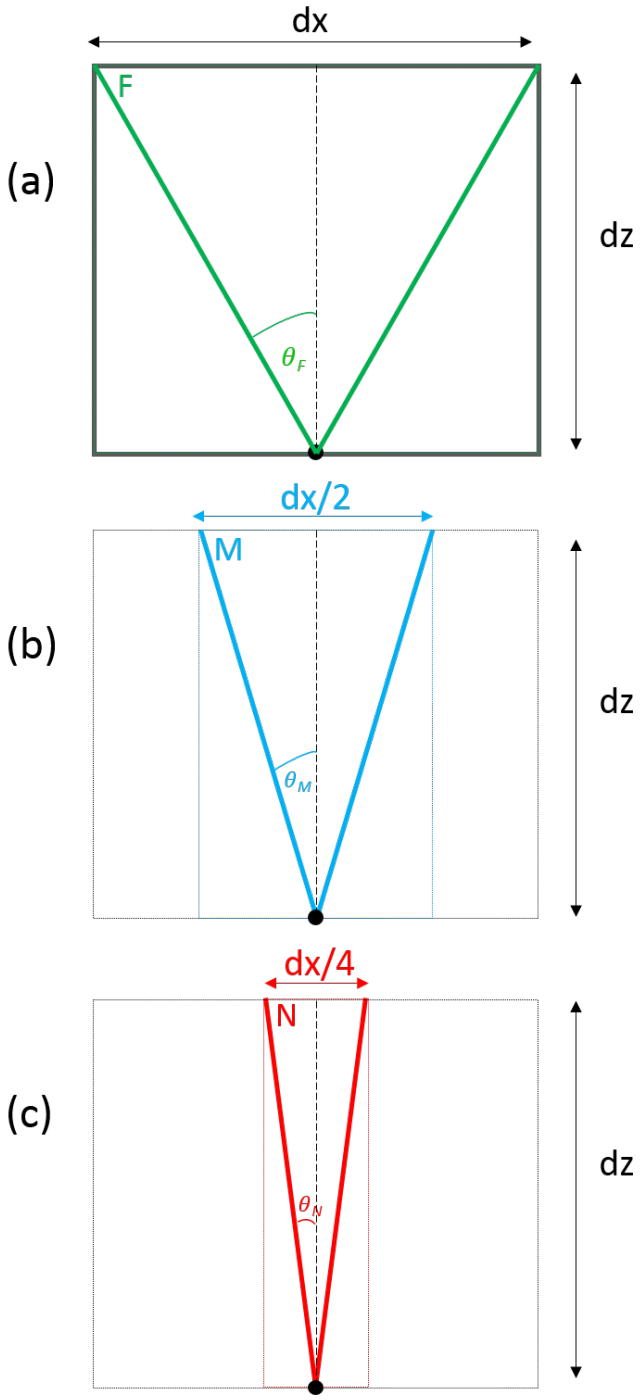

Figure 4.5: Grid generation for three typical incident angles of (a) Far, (b) Mid and (c) Near.

The more dx is compressed, the smaller the incident angle is and the closer it is to zero, which returns to the zero-offset case. By reducing the grid size, in effect we are reducing the angle of incidence while maintaining the image ray along the diagonal. Hence the algorithm is the same. The forward operator will be the same for all the incident angles but the medium is regridded to successively narrower cubes. These three Near/Mid/Far grids can allow us to easily access the angle-stack seismic data of Near, Mid and Far, in which incident angles are usually stacked from $0^0 - 10^0$, $10^0 - 20^0$ and $20^0 - 30^0$, respectively. Note that it is not necessary to always stick with the ratio of $dx/dz = 1$ (where $dx = dz$). Depending on the data sampling rate dt and its conversion into dz, this ratio can be different and then the incident angles are adjusted accordingly. Given these incident angles, the traveltime spent in each grid cell is:

$$t_i = \frac{dt}{cos(\theta_i)}. \tag{4.9}$$

where $i = Near, Mid, Far$

This t_i quantity for Near/Mid/Far grids imply that vertical path-lengths remain the same, but horizontal path lengths do not in the $t - x$ space. It can be named as as the *"angle weighting factor"*. In order to get rid of adjusting the path length in $t - x$ space for each grid of Near/Mid/Far, I divide the time-shift Δt by this factor, the equation 4.5 now becomes:

$$\Delta T = \mathbf{A}\vartheta, \tag{4.10}$$

where

$$\Delta T = \frac{\Delta t}{t_i}. \tag{4.11}$$

indicates dimensionless time-shift, $\mathbf{A}$ is a dimensionless tomographic matrix and the tomographic system now works with samples.

4.2.3 Tomographic forward modelling example

The nature of tomography requires the number of spatial cells to be at least two times larger than the number of vertical cells. I use here a simple model of ϑ which has 3 time samples and 7 traces. For sake of communication, I number the model from 1 to 21 which represents 21 values of ϑ. The anomalies of 5% velocity changes are chosen at positions 8, 11 and 14.

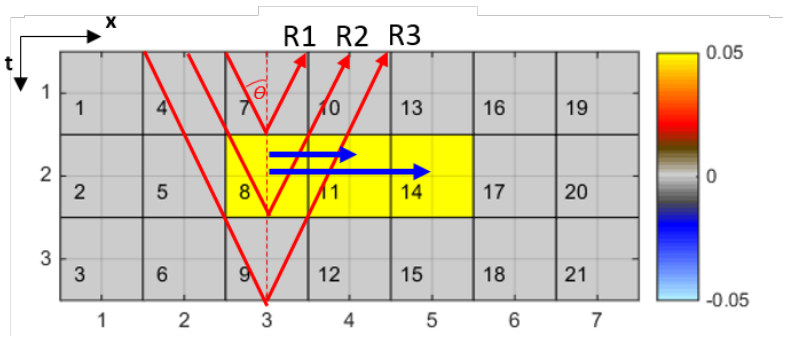

Figure 4.6: An example of straight ray forward modelling for a perturbed velocity changes ϑ. Three rays are shoot at the constant incident angle θ from three reflectors 7, 8, 9 and this three ray geometry is moved to the next two columns following the blue arrows.

Assigning the reflection point at the center of the base of the grid cell, I start to shoot rays R1, R2 and R3 at a certain angle θ as in Figure 4.6. Every single ray through a grid cell can be counted as 1 due to the above mentioned normalization. A matrix in this case has the size of 3×21 because the number of rays is 3 and the number of grid cells is 21. ϑ has 21×1 size and the forward modelling time-shifts can be calculated as:

$$\begin{matrix} c1 & c2 & c3 & c4 & c5 & c6 & c7 & c8 & c9 & c10 & c11 & c12 & \dots & c21 \end{matrix}$$
$$\begin{bmatrix} 0 & 0 & 0 & 0 & 0 & 0 & 2 & 0 & 0 & 0 & 0 & 0 & \dots & 0 \\ 0 & 0 & 0 & 1 & 0 & 0 & 0 & 2 & 0 & 1 & 0 & 0 & \dots & 0 \\ 0 & 0 & 0 & 1 & 1 & 0 & 0 & 0 & 2 & 1 & 1 & 0 & \dots & 0 \end{bmatrix} \begin{bmatrix} \vartheta_1 \\ \vdots \\ \vartheta_{21} \end{bmatrix} = \begin{bmatrix} \Delta T_7 \\ \Delta T_8 \\ \Delta T_9 \end{bmatrix}$$

Shifting this three ray system to the fourth and fifth column, the corresponding time-shifts are shown as in Figure 4.7.

This simple example aims to demonstrate the form of the forward operator and tomographic equation. A proper tomography requires the ray shoot over the whole area and this matrix becomes much bigger. In this example, I describe for the far incident angle grid. Its matrix has the form as below, disregarding the 0 elements

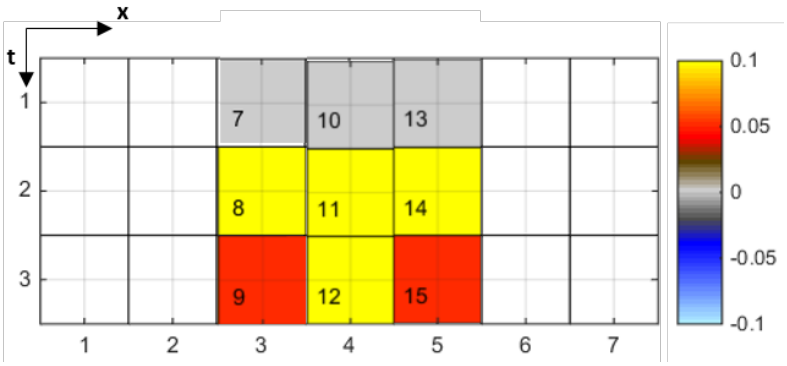

Figure 4.7: Selective modelled time-shifts are generated from the ray geometry as described in Figure 4.6.

in each row:

$$\mathbf{A_F} = \begin{bmatrix} & & & 2 & & & \\ & & 1 & 2 & 1 & & \\ & 1 & 1 & 2 & 1 & 1 & \\ 1 & 1 & 1 & 2 & 1 & 1 & 1 \end{bmatrix} \tag{4.12}$$

Figure 4.8 shows the ray propagation from layer to layer for far, mid and near in which the cells are coded by gradient colours to indicate their propagations from different layers. For mid incident angle where dx is now divided by 2 while remaining the same global grid, which is $dx \times dz$ and is represented by bold black boundaries with number of cell indexes (Figure 4.8 left), there is now two rays passing through cell 2 which propagate from the assigned reflection points (at the center of the base of the grid cell) of cell 2 and 5 (Figure 4.8 middle). Therefore, in the first two rows of tomographic matrix for Mid, $\mathbf{A_M}$, as in Equation 4.13, there are 2 and 2. In a similar way to mid incident angle grid, for near offset, the global grid is now divided by 4 which means there are four rays fitted into four cells 2, 5, 8 and 11, hence the first four rows of tomographic matrix for near, $\mathbf{A_N}$, has only elements 2. Their matrix forms are then:

$$\mathbf{A_M} = \begin{bmatrix} & & & 2 & & & \\ & & & 2 & 2 & & \\ & & 1 & 2 & 2 & 1 & \\ & 1 & 1 & 2 & 2 & 1 & 1 \\ 1 & 1 & 1 & 2 & 2 & 1 & 1 & 1 \end{bmatrix} \tag{4.13}$$

$$\mathbf{A_N} = \begin{bmatrix} & & 2 & & & \\ & & 2 & 2 & & \\ & & 2 & 2 & 2 & \\ & & 2 & 2 & 2 & 2 \\ & 1 & 2 & 2 & 2 & 1 \end{bmatrix} \tag{4.14}$$

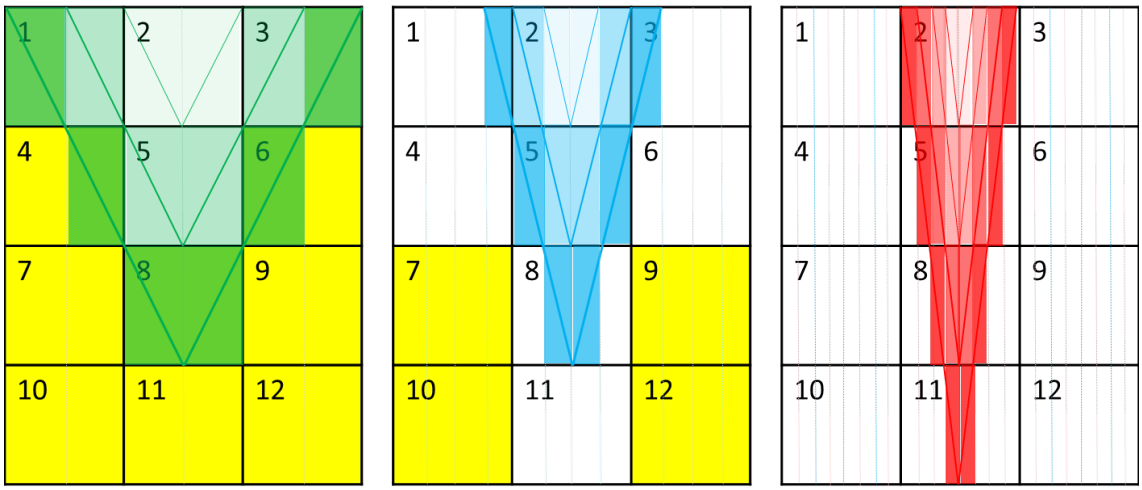

Figure 4.8: Ray propagation for Far (left), Mid (middle) and Near (right). The global grids are defined in the bold black boundaries with corresponding to the number of cell indexes. Gradient colours for each incident angles - Far, Mid, Near - indicate the ray propagations from different layers. Yellow cells denote inactive areas where the rays can not access into.

Understanding how the rays propagate for Mid and Near, we can now insert the 0 elements into the original tomographic matrix. Figure 4.9 shows a complete **A** matrix for this example at near and far incident angles. It is essential to clarify that **A** is a square matrix. Apart from the element 1 and 2 coded by red and yellow colour, respectively, there are a few other light blue elements which have negative values. These elements belong to inactive areas where the rays can not reach at a certain angle θ (Figure 4.8 - yellow cells). By simultaneously assigning a certain value for these cells in the model and corresponding position in the data, the **A** matrix formed has a very high possibility to be invertible. The best chosen value is 1 in both model and data domain. In this example, I use -2 instead for the display purpose only, avoid repeating number 1 in case one ray is presented in a grid cell.

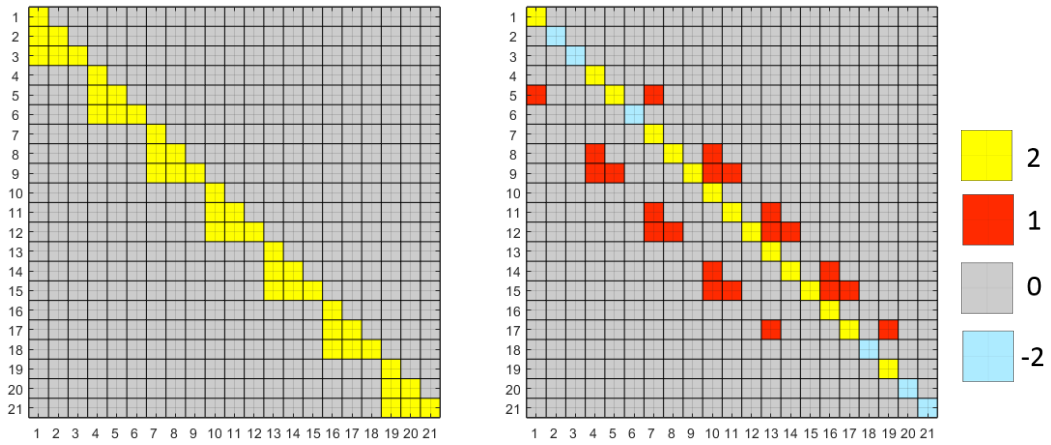

(a) (b)

Figure 4.9: Tomographic matrix **A** for (a) Near and (b) Far with the elements of $0, 1, 2$. A value of -2 indicates an inactive area to avoid repeating with elements of value 1 (active areas) for the purpose of presentation only.

4.2.4 Tomographic inversion example

Given a time-shift model as in Figure 4.10a, the inversion for θ is done layer by layer from the top to bottom. Shooting the ray over the first layer, it is obvious to recover the ϑ in these positions. Keeping the same angle and shooting the rays over the second layer, we get ϑ in the layer with known ϑ from the first row. Repeating this process until the final layer, the whole ϑ area is solved recursively. Note that there might be a decrease in the number of rays as the ray systems are shifting down because of the inactive cells, as explained above. Therefore, it is always useful to cover a larger area than our interested area in any tomographic study.

Generally, the tomographic method needs a high ray density, in which the numbers of rays must be greater than the numbers of cells. This leads to an over-determined system which is almost always inconsistent. In this study, by means of assigning time-shifts to individual cells, and eliminating the inactive areas, A is a square matrix ($K = P$). In spite of sparseness, the inversion is achievable via *mldivide* Matlab function. The inverted ϑ is:

$$\vartheta = \mathbf{A^{-1}} \Delta T. \tag{4.15}$$

However, this direct inversion is also inverting the noise inherited in measured time-shifts. Depending on the noise level, there might be a need to add constraints to smooth the solution using the regularization tool or other equivalent methods.

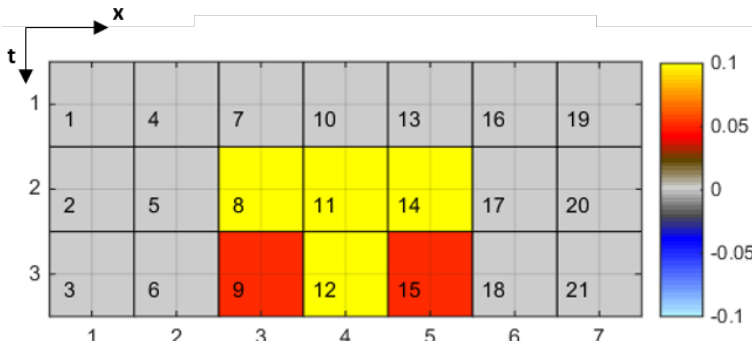

(a)

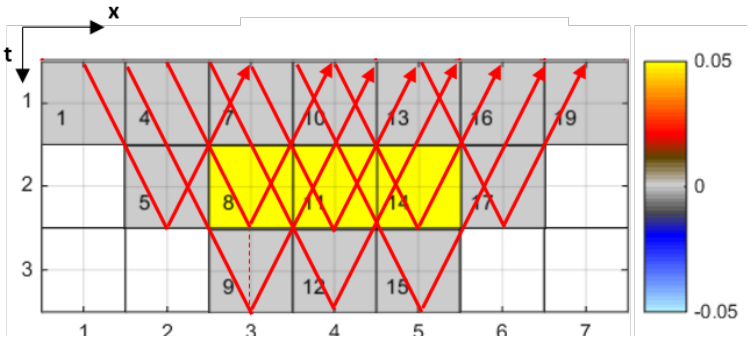

(b)

Figure 4.10: An example for tomographic inversion with (a) the input of dimensionless time-shifts, ΔT, and (b) the inversion results of ϑ. The white cells indicate the inactive areas.

Figure 4.11 shows how the inversion of the $\mathbf{A}$ matrix looks like for Near and Far. At Near, the inversion of tomographic matrix $\mathbf{A^{-1}}$ appears to be more stable than Far.

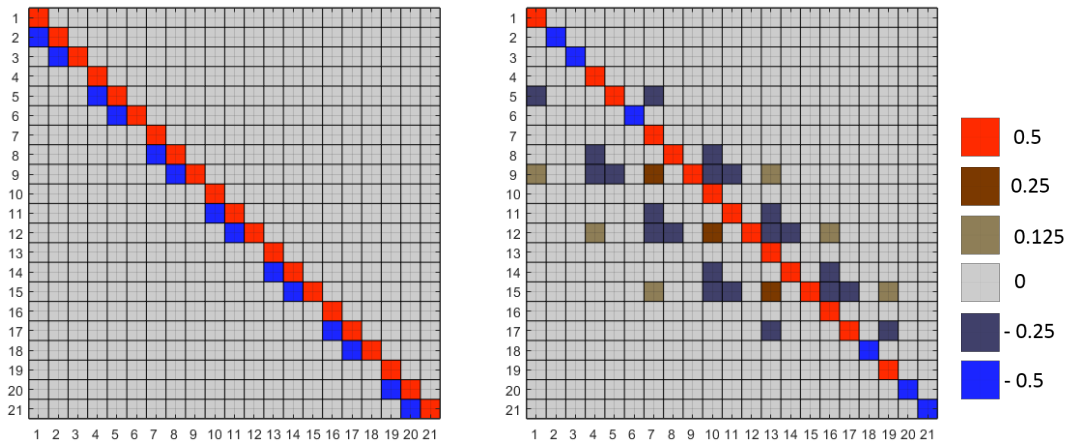

(a) (b)

Figure 4.11: Inversion of tomographic matrix $\mathbf{A^{-1}}$ for (a) Near and (b) Far. In spite of the sparsity of $\mathbf{A^{-1}}_F$ than $\mathbf{A^{-1}}_N$, the inversion is achievable.

Assuming straight ray-path imaging, I develop a new and simplified angle-stack tomography for constant angle data. This determines changes in ray-path imaging

for differently angled seismic data, re-grids whilst keeping the algorithm the same. The inversion is achieved through a modelling operator, which makes this method very robust. In this example, I explained the method in the sample domain. In chapter 5, I will further describe the procedure of tailoring the method with specific data parameters, in a field application.

4.3 Chapter summary

In this chapter, after briefly revising on the static (3D) tomography methods, I explored the (dynamic) time-lapse tomography methods including the sequential and perturbed strategies. I found that the perturbed time-lapse tomography strategy is well-fitted into the scope of this thesis which aims to directly extract the 4D seismic attributes. From the proposed time-lapse tomography equation by Edgar's work (Equation 4.1), which links the pre-stack time-shifts and perturbed velocity changes via the tomographic matrix, I developed the straight ray time-lapse tomography for constant angle-stacked time-shifts. The motivation behind this straight ray assumption is to set up a linear connection between the model parameters, ϑ, and data, Δt. The key of this straight ray time-lapse tomography is at re-gridding technique which allows us to access into different incident angle yet keeps the algorithm the same throughout. The modelling operator is simplified as a square tomographic matrix so that in spite of spareness, the inversion is achievable. In order to measure the sensitivity of straight ray assumption, I analytically derived a analytically small ray-bending solution and applied to Shearwater field as presented in Appendix D.

Chapter 5

Field application – Shearwater

In Chapter 2 and 4, I described the different methods of estimating the velocity changes for both post- and angle-stack time-shifts, respectively. In this chapter, these methods are applied to a field dataset. The chosen field is a HPHT reservoir located in the North Sea and has dominant geo-mechanical effects in the overburden, reservoir and underburden. I first underline the reasons for choosing this field and the field application workflow and describe a few key facts of the field together with the general generation of the post- and partial angle-stack seismic. Then I will implement various methods of recovering the velocity changes from both post- and angle-stack time-shifts measured from three different methods as explained in Chapter 1. Even though there is only one field application, the varying availabilities of different monitors of the field and also of different noise levels of the measured time-shifts from three different methods help to reveal the nature of each algorithm and to bring different perspectives to interpret and analyse the changes in the field's subsurface.

5.1 The case study: introduction and description

Shearwater is known by its strong geo-mechanical effects over the whole subsurface area as studied by Rangel (2016) and Ji (2017). The main production mechanism is depletion resulting in a large pressure change between the initial conditions and the dew point pressure. As a result, it causes a strong geo-mechanical imprint on the subsurface's elastic properties, giving rise to time-lapse velocity changes. Therefore, this is a good case study to implement the new algorithms to recover the time-lapse velocity changes from time-shift data.

Furthermore, both post-stack and partial angle-stack seismic are available so that I can examine the inversion methods for both domains and the recovered ϑ can be interpreted and analysed from various angles. Additionally, the full-stack seismic dataset has good time-lapse repeatability with NRMS $< 10\%$ (less than 10% of non-repeatability) calculated by Ji (2017) and the partial angle stacked data was reprocessed recently with a range of available angle stacks from 0^0 to 40^0. Figure 7.1 describes the inversion workflow applied to the Shearwater fieldwith two domains: post-stack in blue area and angle-stack in pink area. In post-stack domain (1), three different methods are used to measure time-shifts from baseline (2001) and monitor (2004), NLI, CLM and DHF, and then they are all inverted for $\Delta V/V$ using also three different methods (1a, 1b, 1c), one novel (GMM) and two selected from the literature (layer stripping and damped-least squares). In angle-stack domain (2), only the NLI time-shift measurement method described in Chapter 1 is used to measure the partial angle-stack seismic data and the resulting time-shifts are the input for two new tomographic methods (2a and 2b) to recover $\Delta V/V$. In the next subsections, I will explain in more detail about the field geological settings and production history before employing these inversion methods.

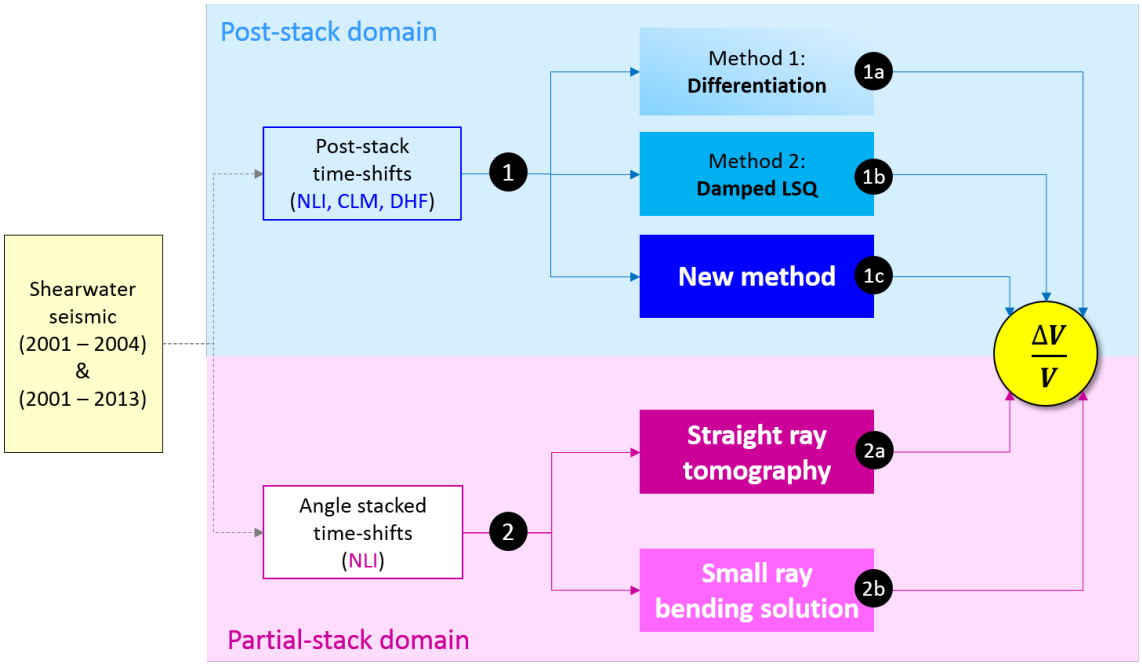

Figure 5.1: The workflow of Shearwater field application in this chapter for both (1) post-stack and (2) angle-stack domains to recover $\Delta V/V$. In (1), three different inversion methods (1a, 2b, 1c) are applied for three different measured time-shifts from NLI, CLM and DHF methods. In (2), only NLI method is used to measure the angle stacked time-shifts, which are then inverted by using the new tomographic methods (2a and 2b).

5.1.1 General field description

Ji (2017), Rangel (2016) and many other researchers (Staples et al., 2007a,b; Gilham et al., 2005; Jones et al., 2018) have intensively investigated both the static and dynamic characterisation of the Shearwater field. Therefore, I will not repeat this work here, instead I summarize few key facts of this field in the view of understanding the results from the velocity change estimation methods. The field is located in the central graben of the Central North Sea, UK Block 22/30b, and is operated by Shell with other partners including Arco British, Esso and Mobil. The field was discovered in 1988 at the water column of $90m$, the first well drilled in 1991 and was initially produced in September 2000. This is a gas condensate reservoir which was produced under a pressure drive mechanism. There are two main separate reservoirs in Fulmar formation at late Jurassic, which are the Upper Fulmar with high porosity sandstones (24%) and the Lower Fulmar sandstone formations with low to moderate porosity (Figure 5.2).

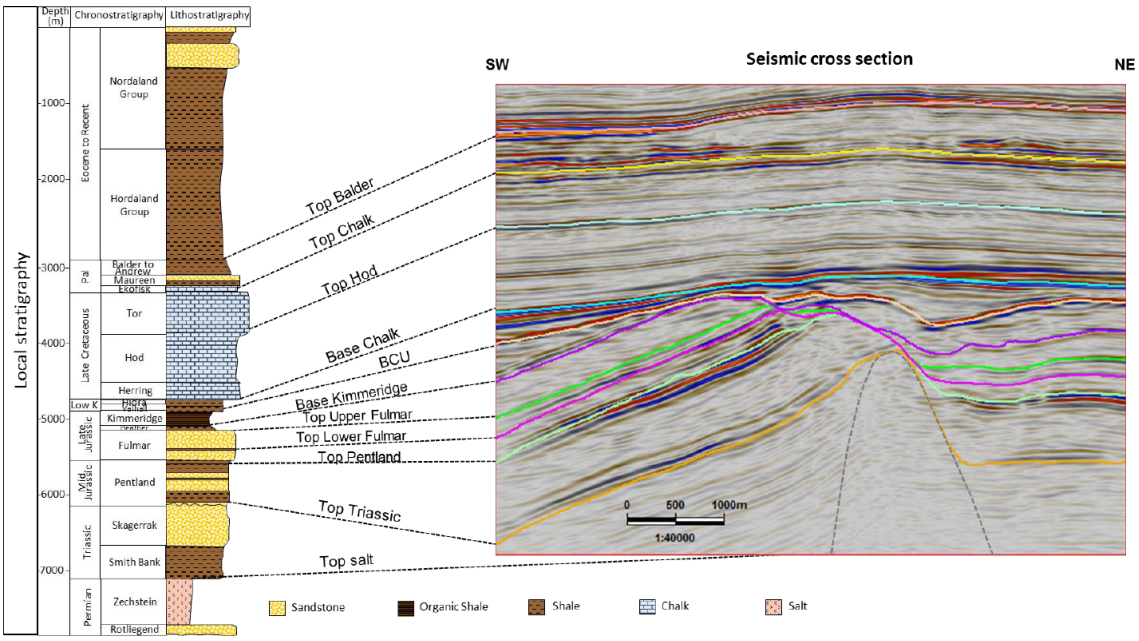

Figure 5.2: Shearwater stratigraphic column (left) corresponding to the crossline section from the baseline seismic survey in 2001. After Ji (2017).

The baseline seismic survey was acquired in 2001 about a half year after the first production, and the pressure still remained close to the initial reservoir pressure (about $15,400psi$). The monitors were then acquired in 2002 and 2004 after the pressure depletion of $2000psi$ and $8000psi$, respectively, (Figure 5.3). This caused velocity changes that are associated with potential geo-mechanical hazards.

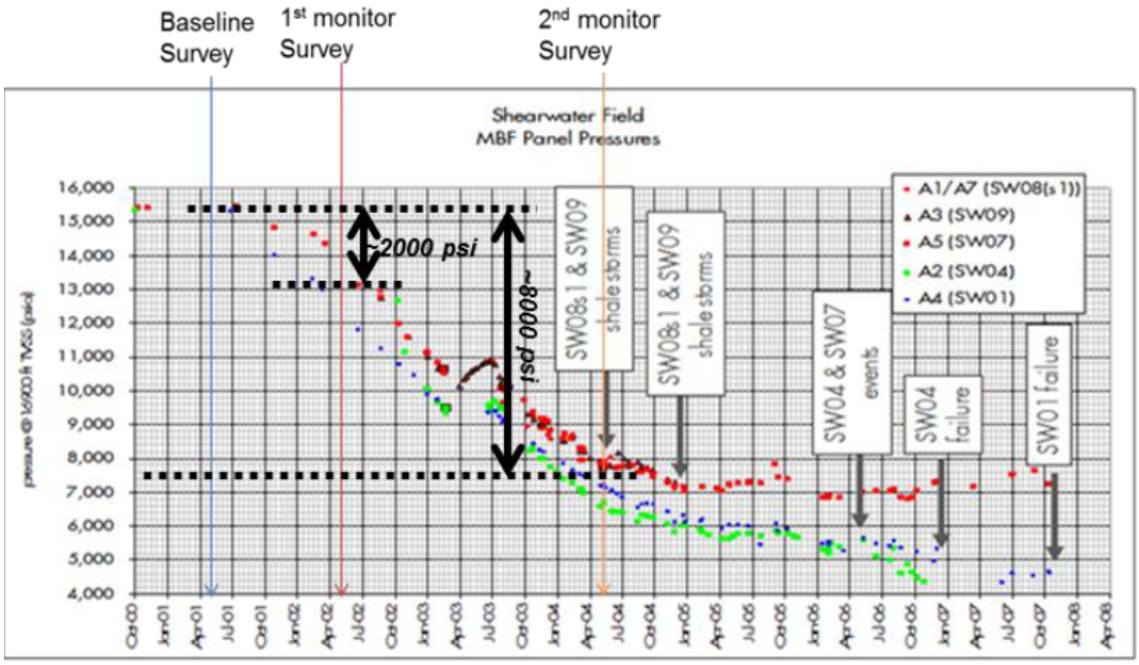

Figure 5.3: Shearwater resevoir pressure history over the time-lapse seismic surveys at five different wells. After Ji (2017).

5.2 Post-stack time-shift inversion

Firstly, I measure the time-shifts from two post-stack seismic vintages of baseline (2001) and monitor (2004). Three typical methods are used: correlated leakage method (CLM) by Whitcombe et al. (2010), fast cross correlation (DHF) by Hale (2009) and non-linear inversion (NLI) by Rickett et al. (2007) as described in Chapter 1. The measured time-shifts are presented in Figure 5.4 for an extracted crossline. The general features of these three measured time-shifts are quite similar to each other, with slowdown areas shown in yellow and red over the whole subsurface area, from overburden, to reservoir to underburden. These time-shifts are loosely separated into two blobs of maximum time-shifts ($5ms$). The dark and light blue line markers indicate the top and base reservoir, respectively, whilst other black lines mark key reflectors in the overburden and underburden. Time-shifts diminish when entering the surrounding reservoir areas (less yellow) and then build up again at the last underburden reflector before diminishing again. Due to cumulative property of time-shifts, it is challenging to provide an intuitive interpretation. The following inversions for interval properties of velocity changes will enable better understanding. Different noise levels from various methods of time-shift measurement will help to reveal the nature of each inversion method.

5.2.1 Layer stripping results

I apply layer stripping on the above time-shift crossline section (XL 1840) which contains 1000 time samples per trace (with sampling rate $dt = 4ms$) and 350 traces each. The time-shifts are then converted into sample domain (dimensionless) and the layer stripping forward operator $\mathbf{D}$ is tailored for 1000×1000. In spite of different noise levels of each measured time-shift, layer stripping inverts both signals and noise, hence all the time-shifts are completely reconstructed and there is no residual left in the three different time-shifts (Figure 5.5). However, the inverted velocity changes, ϑ, in Figure 5.6 are pointing out how sensitive the method is to the input data. For the most noisy CLM-time-shift (Figure 5.6b), the method returns very noisy inverted ϑ which is hardly interpretable. On the other hand the most smooth NLI-time-shift (Figure 5.6a) can produce very clear features of the velocity changes ϑ along the geological horizons. The reduction in velocity (in red) in the

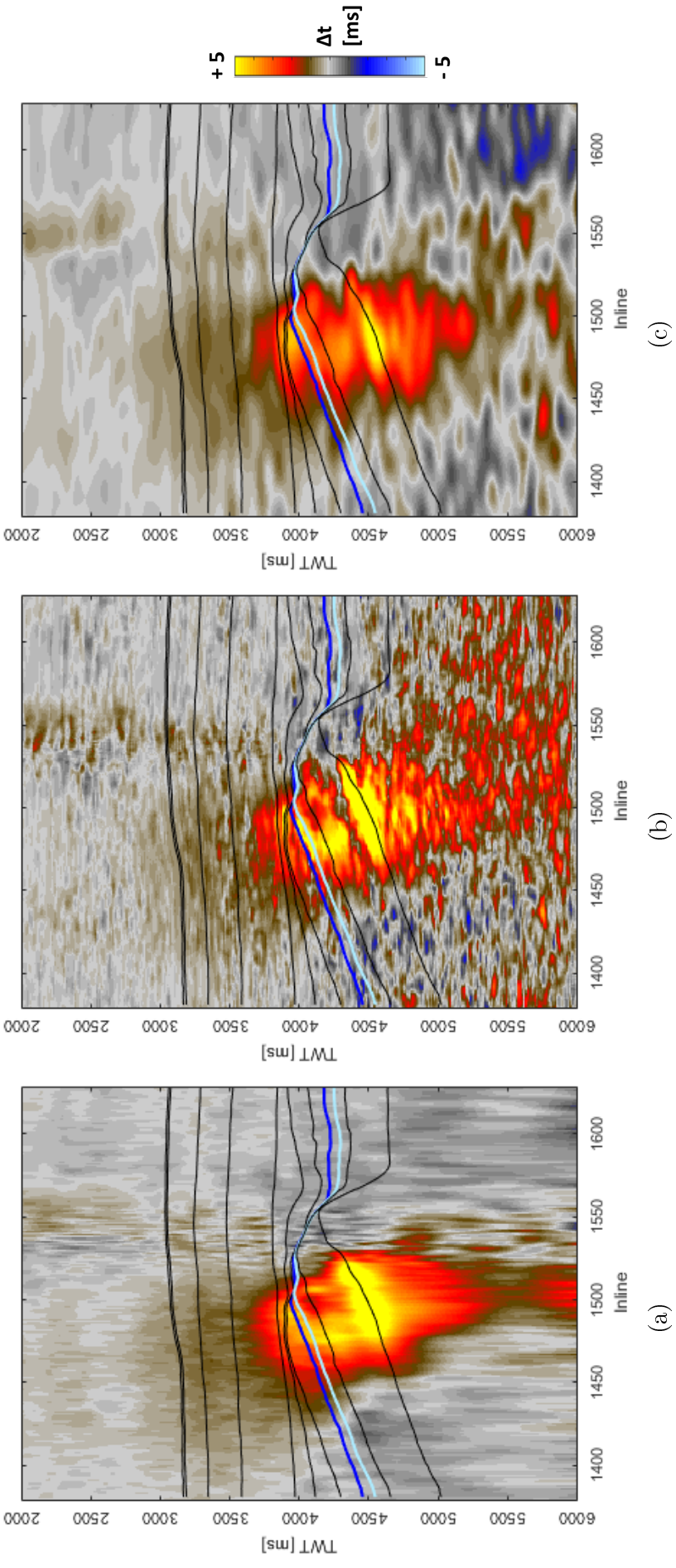

Figure 5.4: Shearwater post-stack time-shift measurement between baseline 2001 and monitor 2004 using three different methods: (a) NLI; (b) CLM and (c) DHF. The dark and light blue lines are top (Top Upper Fulmar) and bottom (Top Upper Fulmar) reservoir, respectively. The NLI and DHF results are quite smooth whereas CLM has higher resolution at the risk of being more noisy. Different levels of noise in these three time-shift data are the best examples for implementing the post-stack time-shift inversion methods.

overburden builds up and reaches maximum magnitude close to the top reservoir (blue). Corresponding to the large time-shift feature in the underburden, recovered ϑ from NLI time-shifts also shows large anomalies in this area. Interestingly, DHF-time-shifts seem to have quite similar resolution as NLI-time-shifts, even though its inverted ϑ (Figure 5.6c) is very different, especially in the underburden area.

5.2.2 Damped least squares solution

In order to avoid problems arising from layer stripping as mentioned in Chapter 2, here I use a damped least squares solution to constrain the noise and bring out smoother solutions using the same measured time-shifts in Figure 5.4. In this method, choosing the damping or smooth factor α is a critical step. A range of various α is tested and the L_2 norm plot of the data misfit and penalty term are carried out and plotted as in Figure 5.7 with the chosen optimal α following L-curve method.

Passing these optimal damping factors into Equation 2.19, the reconstructed time-shifts in comparison with the input time-shifts and the residuals between them are carried out and shown in Figure 5.8. Even though the reconstructed time-shifts (middle column) turn out quite similar to the input time-shifts (left column), the residuals (right column) show the differences between them due to the penalty (smoothing) term introduced in this method to balance the solution resolution and noise in the input data. The obtained velocity changes ϑ in Figure 5.9 shows that the CLM- and NLI-inverted ϑ becomes smoother whilst the DHF-inverted ϑ is a bit more noisy compared with those inverted from layer stripping method.

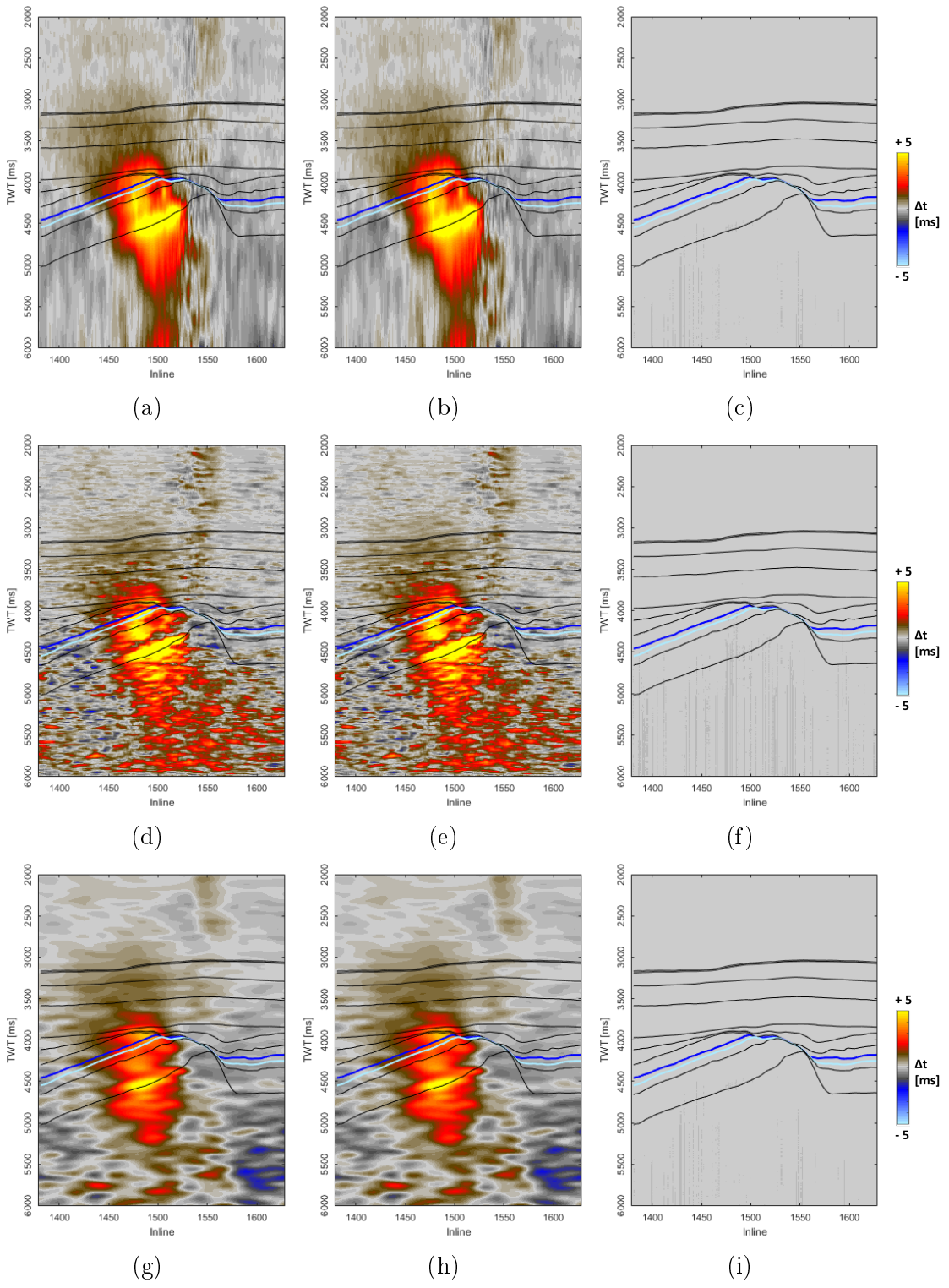

Figure 5.5: Reconstructed time-shifts (middle column) using layer stripping in comparison with the input time-shifts (left column) and their differences of residual time-shifts (right column) for NLI-(first row), CLM-(second row) and DHF-(third row) time-shifts. Nothing left in the residuals show the method inverting for both signals and noise.

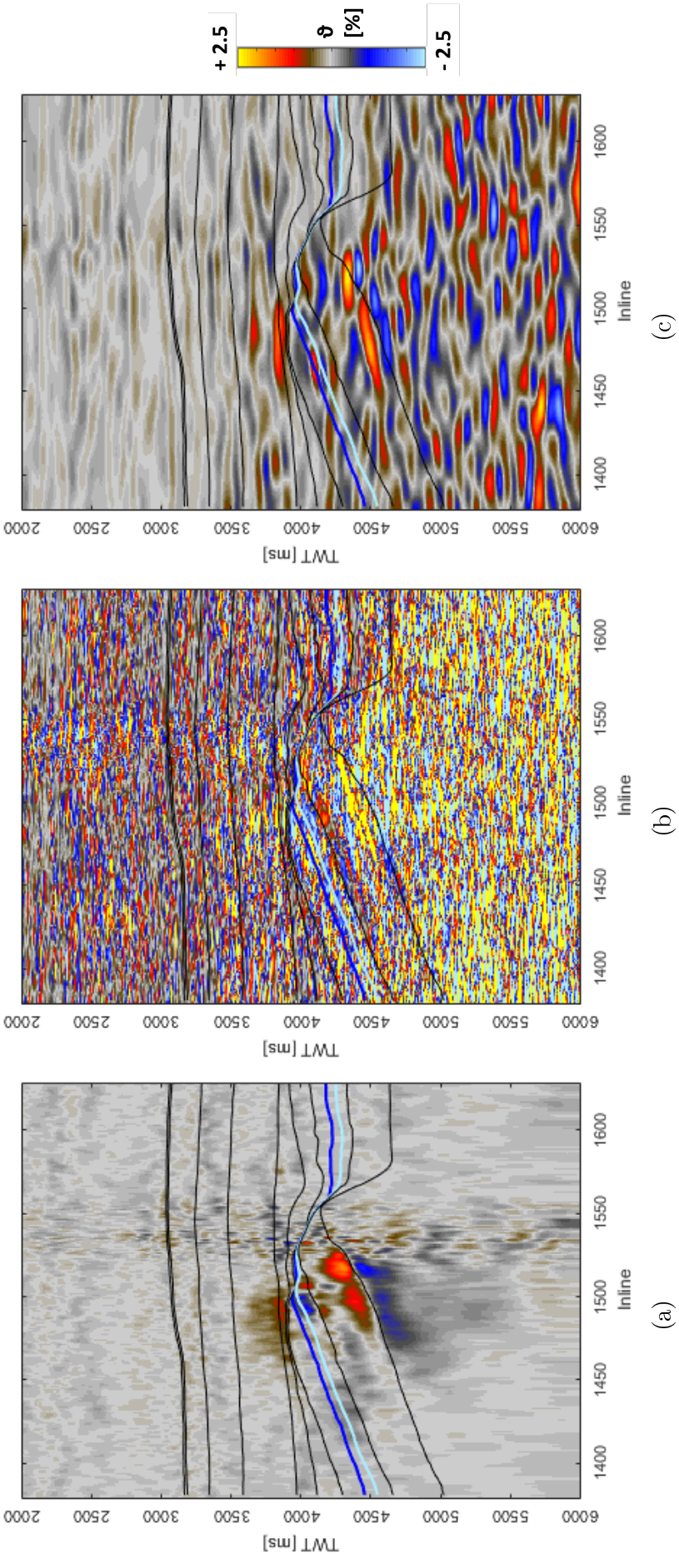

Figure 5.6: (a) NLI, (b) CLM and (c) DHF inverted ϑ results from the corresponding measured time-shifts in Figure 5.4 using layer stripping. Different noise levels of the input data reveal the nature of the method. Good NLI-time-shift resolution provides very good recovery of ϑ. CLM-time-shifts are too noisy for this method to invert directly hence the resultant inverted ϑ is impossible to interpret. Inverted ϑ from DHF-time-shifts behaves like a trade-off between NLI and CLM, it seems to be interpretable but still too noisy.

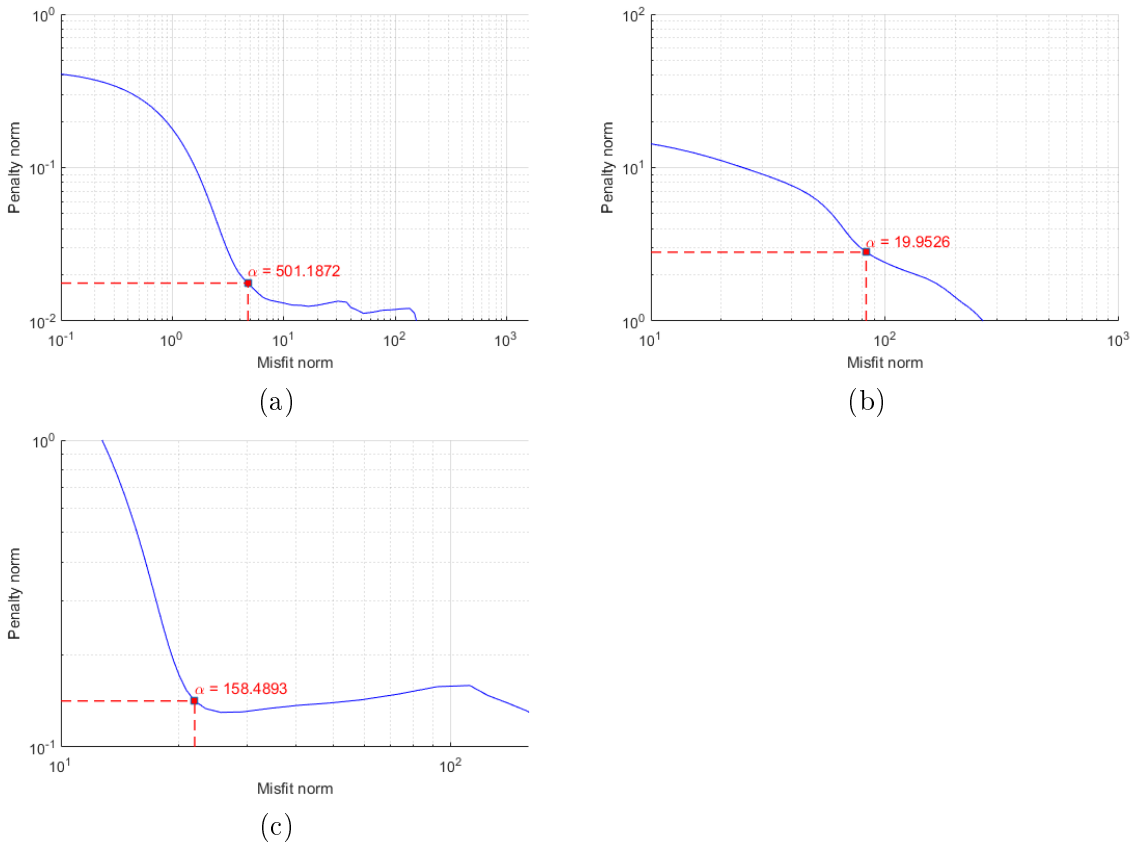

Figure 5.7: The choice of the optimal α for (a) NLI-, (b) CLM- and (c) DHF-time-shifts using L-curve method.

5.2.3 Gaussian reconstruction

So far, we have observed that directly inverting from layer stripping suffers from noise amplification. Having a noise treatment method by using the damped least square solution relies on the choice of the smoothing factor in spite of obeying the L-curve. These two methods work well on the NLI-time-shifts but not on CLM- and DHF-time-shifts. Therefore, here I apply Gaussian reconstruction using GMM with a better analytical expression, as explained in Chapter 2, on these three measured time-shifts to recover ϑ. For this method, choosing a suitable Gaussian grid for each dataset is critical. Hence, before doing the inversion, a sensitivity analysis is carried out to search for the best Gaussian grid for Shearwater time-shift data, which is $(30, 30)$ for NLI and DHF time-shift measurements and $(40, 40)$ for CLM time-shift measurement. This procedure was already explained in Chapter 2. Given the most optimal Gaussian grid of $(30, 30)$ and $(40, 40)$, the reconstructed time-shifts and residuals for three different time-shifts (NLI, CLM and DHF) are presented in Figure 5.10 and the recovered velocity changes, ϑ, are shown in Figure 5.11.

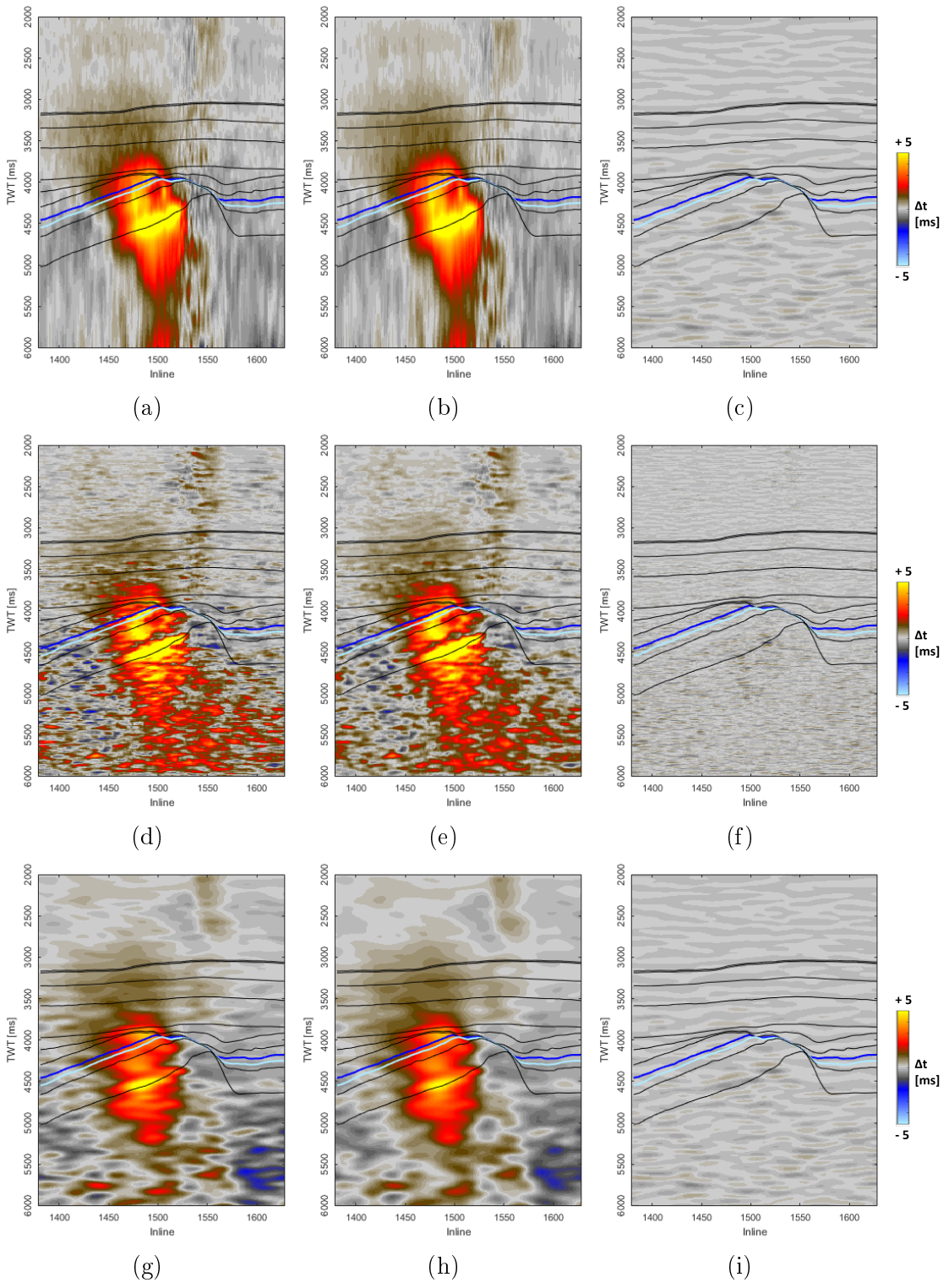

Figure 5.8: Reconstructed time-shifts (middle column) using damped least squares solution in comparison with the input time-shifts (left column) and their differences of residual time-shifts (right column) for NLI-(first row), CLM-(second row) and DHF-(third row) time-shifts. Including the regularization term induces small residuals.

Gaussian reconstruction is able to push the noise out of the solution yet still keep a similarly smooth solution. It works well on different levels of noise from three measure time-shift datasets successfully.

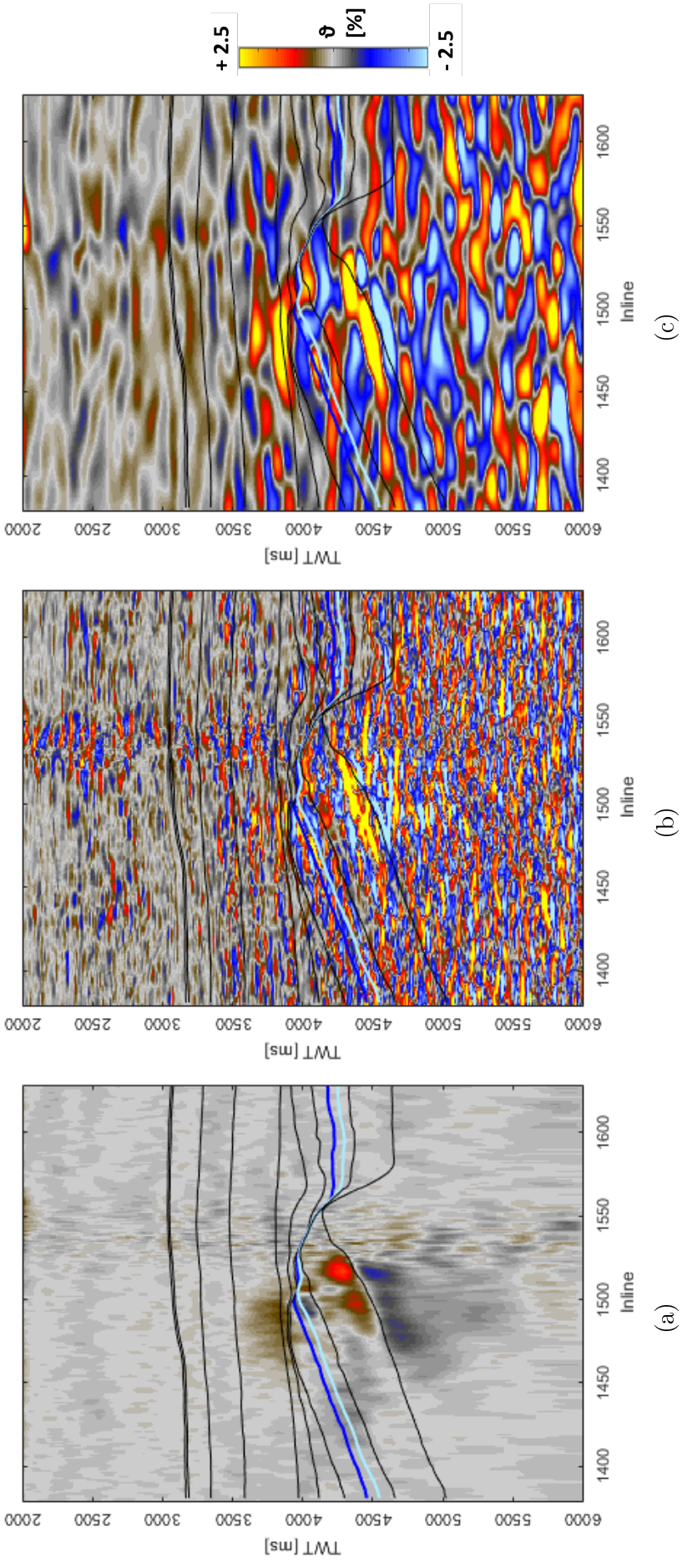

Figure 5.9: (a) NLI, (b) CLM and (c) DHF inverted ϑ results from the corresponding measured time-shifts in Figure 5.4 using damped least squares solution. Different noise levels of the input data reveal the nature of the method. The regularization term does help to smooth the solution for CLM-time-shifts but not for DHF (compared with Figure 5.6b and c, respectively) due to the sensitivity of the method to the chosen damping factor according to L-curve. For NLI case, the method is not effected much by the damped least square solution because of very good smoothness and resolution of NLI time-shifts.

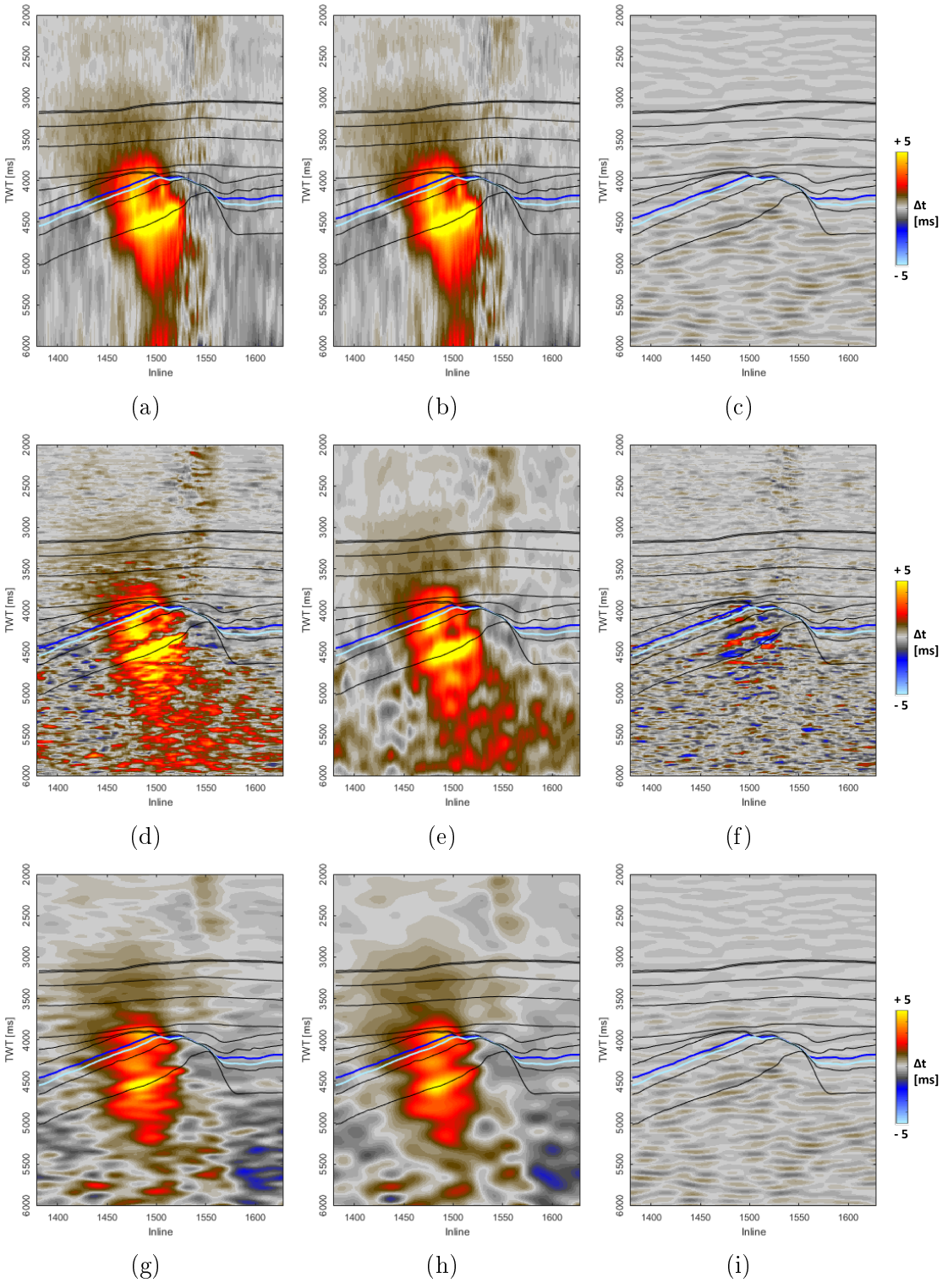

Figure 5.10: Reconstructed time-shifts (middle column) using Gaussian reconstruction method in comparison with the input time-shifts (left column) and their differences of residual time-shifts (right column) for NLI-(first row), CLM-(second row) and DHF-(third row) time-shifts. Given preset Gaussian grid, the method can recover all the important features of the input time-shifts whilst forcing the noise out to the residual.

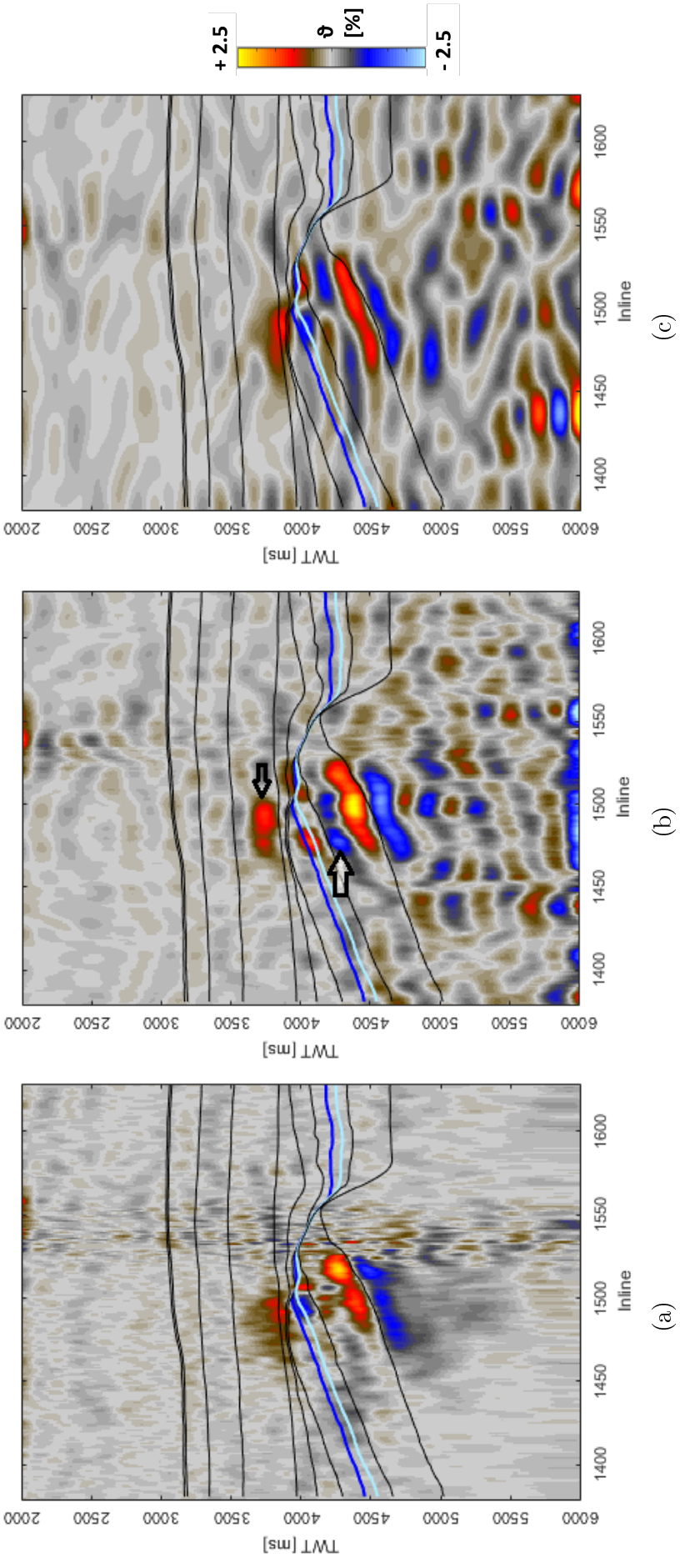

Figure 5.11: (a) NLI, (b) CLM and (c) DHF recovered ϑ results from the corresponding measured time-shifts in Figure 5.4 with Gaussian reconstruction using the Gaussian grid of $(30, 30)$ for NLI and DHF time-shifts and $(40, 40)$ for CLM time-shifts. The method successfully inverts for all three different input time-shifts with different levels of noise with agreements of the velocity change features from the overburden, to the reservoir to underburden.

5.2.4 Comparison of three inversion methods

Figure 5.12 summaries the inverted ϑ obtained from three different methods for three various input time-shifts. The proposed Gaussian reconstruction (bottom row) is observed to remain stable over different levels of noise in the input data in comparison with the other two existing methods of layer stripping and damped least squares solution. All three methods work well on NLI-time-shifts and return quite similar ϑ. Compared with layer stripping, the Gaussian reconstruction produces a smooth, stable image with less smearing in the background. Compared with damped least squares solution, the Gaussian seems to preserve better the subsurface variability and resolution. These conclusions are clearly validated with the other two input time-shift data of CLM and DHF.

Notably, regardless of the various input time-shifts, the Gaussian reconstruction inversion method recovers the velocity changes, ϑ, of Shearwater field's subsurface quite similarly to each other and well in line with the geological horizons, with the clear slowdown (red) in the overburden, small speedup (blue) in the reservoir and the opposite slowdown and speedup over the last underburden horizon. However, when we look closer at the three inverted velocity changes from CLM time-shift (Figure 5.12 h), the speedup in the reservoir seems to be faded compared with the results from NLI and DHF time-shifts ((Figure 5.12 g and i). Instead, there is a new speedup blue event below at the right arrow mark, which is similar to (i) but not to (g). The slowdown in the overburden marked by the left arrow in (h) is also higher than (g) and (i). From all of these observations, it seems that the Gaussian grids do help to smooth out the noise in time-shift data (CLM and DHF), but it might also introduce some artefacts. Therefore, adapting these Gaussian grids to the geology might be a good direction in further research. Nevertheless, this simplified Gaussian mixture model has proved its robustness for these three different noise levels of Shearwater time-shifts.

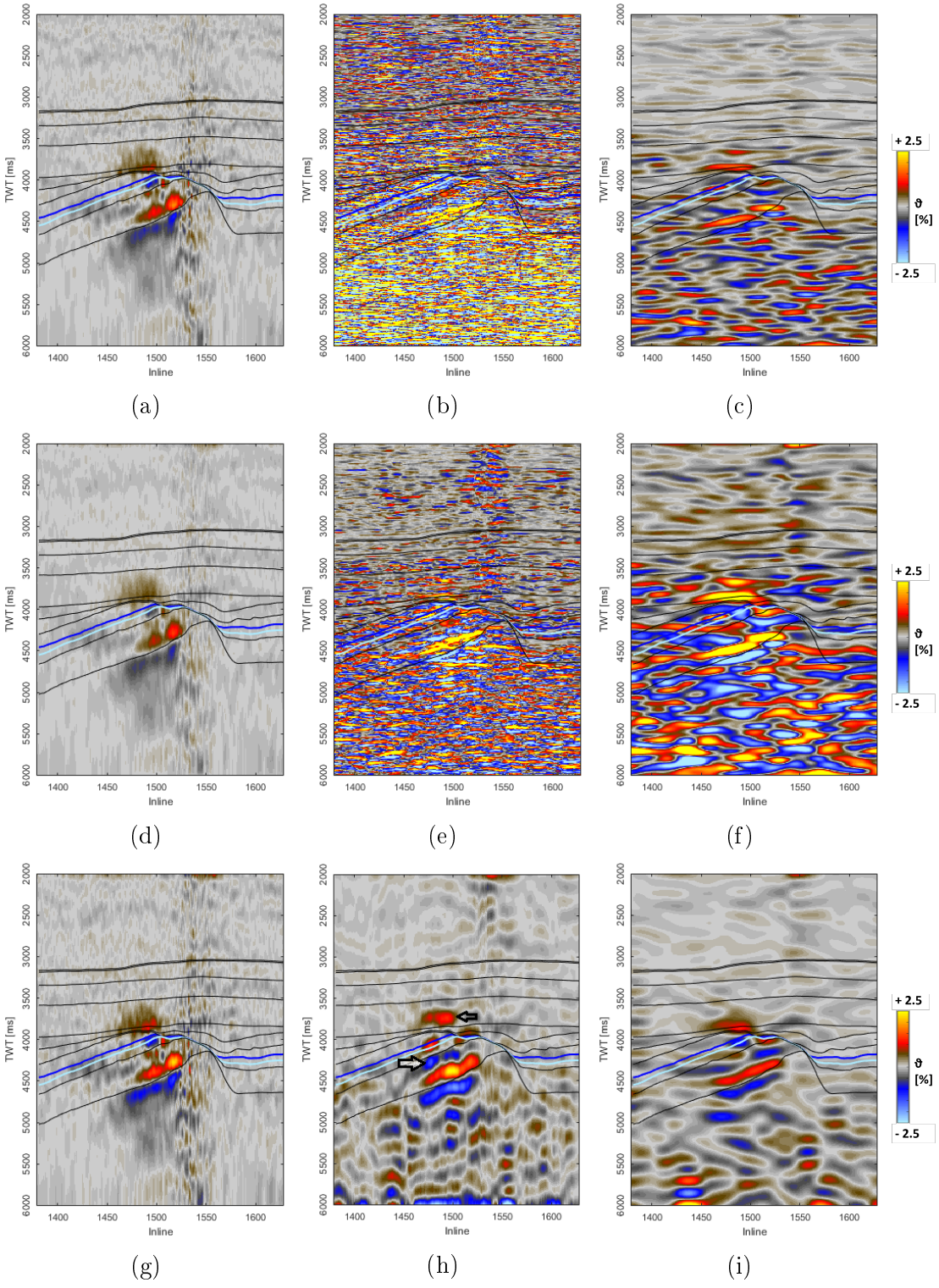

Figure 5.12: Recovered ϑ using (top row) layer stripping method, (middle row) dampled least squares solution and (bottom row) the newly developed Gaussian reconstruction method for (left column) NLI-, (middle column) CLM- and (right column) DHF-time-shifts. The Gaussian reconstruction stands out as the best method that works well on the different input data with different noise levels thanks to its stable analytical formulae. Meanwhile, the two existing methods of layer stripping and damped least squares solutions depend on the noise levels in the input data and the choice of damping factor α. However, for the very noisy input (CLM time-shift), applying Gaussian grid might introduce some artefacts as marked right and left arrows.

5.3 Time-shift inversion – angle dependence

In 2013, Shearwater seismic data were re-processed with the outcome of additional partial angle stacks for baseline 2001, monitor 2004 and monitor 2013. There are 4 partial angle stacks for each vintage, which are A0010, A1020, A2030 and A3040. A0010 means the seismic data stacked from a range of incident angle from 0 to 10 degrees. However, there are important missing areas in the 2004 data and the angle-stack A3040 of 2013 data. Therefore, I decide to use the baseline 2001 and monitor 2013 instead of 2004 despite the larger gap in time. Only three angle stacks, A0010, A1020 and A2030, are used for this tomographic implementation and are referred as Near, Mid and Far, respectively, in the rest of this thesis.

5.3.1 Angle-stack time-shift measurements

Before carrying out the tomographic inversion, I measure the angle-stacked time-shifts between 2001 and 2013 using only one method for the sake of simplicity. As mentioned in Chapter 2 on the different nature of three time-shift measurement methods, NLI provides the best behaved time-shifts with an adequate good resolution. Furthermore, from the above post-stack time-shift inversion, the input NLI time-shifts proved to be well fitted for Shearwater data since the recovered velocity changes remain stable throughout three different inversion methods compared with CLM and DHF. Therefore, for this tomographic inversion, I use the NLI time-shift measurement method. A quick quality check on seismic data was done to remove the low quality area before the measurement. Figure 5.13 shows the measured time-shifts at Near, Mid and Far extracted for an Inline. The extracted horizons from seismic interpretation are overlaid on the top, for reference. The yellow and green lines indicate top and bottom reservoir, respectively. Similarly to post-stack time-shift in Figure 5.4, they are increasing from the overburden to the top reservoir, and then decreasing through the reservoir before getting larger in the underburden with the largest time-shifts on the last horizon. Approximately, the time-shift is about 6ms in the overburden and reservoir and 8ms in the underburden. Overall, these three angle time-shifts have similar features in the overburden and reservoir. However, in the underburden, as the incident angles increase, the time-shift gets bigger and expands in width; and notably at the bottom of Far time-shifts (Figure

5.13c), there is separation into two directions.

In order to better visualize the behaviour of time-shifts over traveltime and three different angles, Figure 5.14 plots three selected time-shift traces. Obviously, they get more separated in the underburden. Especially, time-shifts are decreasing below 4500ms which seems to be geologically unreasonable. Again, this can be due to errors in the time-shift measurement method as mentioned in Chapter 2.

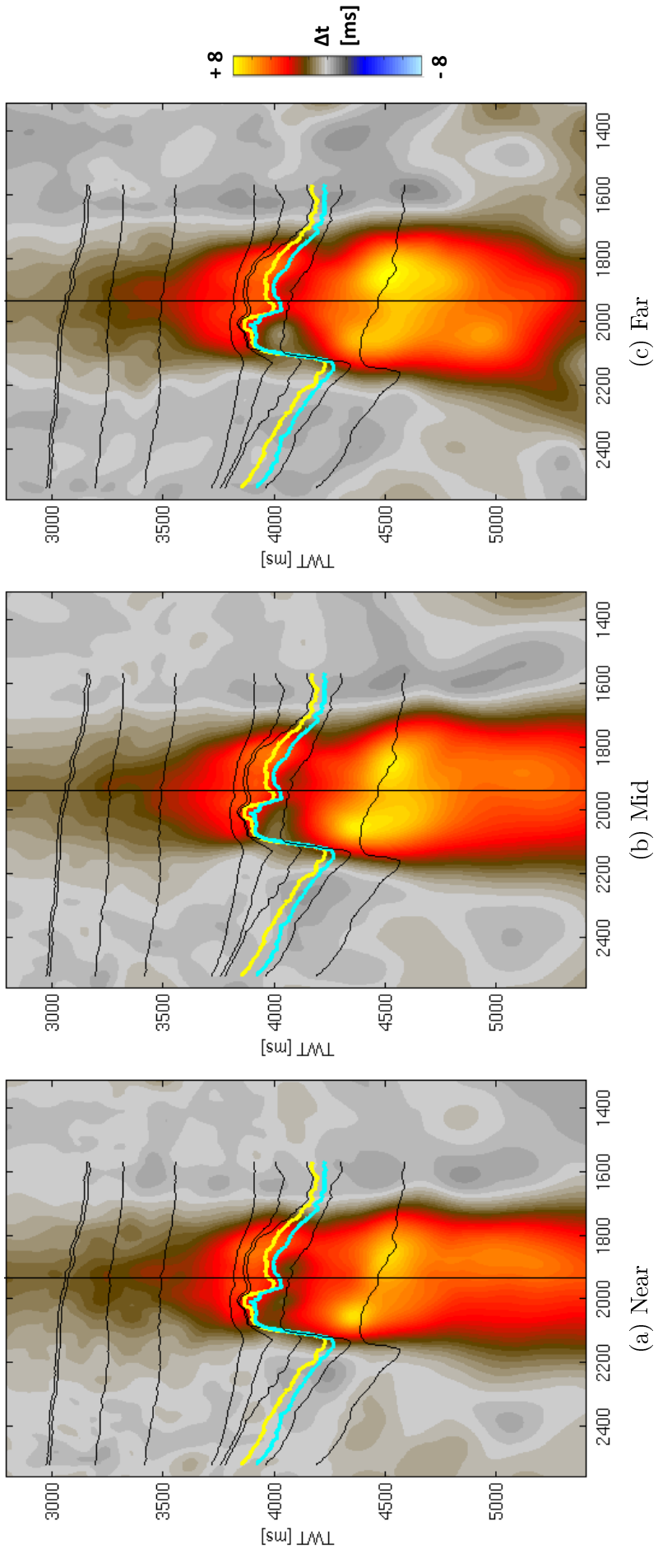

(a) Near (b) Mid (c) Far

Figure 5.13: Measured time-shift from angle-stack between 2001 and 2013 in Shearwater. The yellow and green lines indicate top and bottom reservoir, respectively. As the angles increase, the time-shifts in the overburden and reservoir are quite similar with about 6ms, whilst they get bigger and extend more widely in the underburden. At the bottom of Far time-shift, it is observed that time-shift is spread into two directions. The vertical lines show the positions of extracted traces in the next Figure 5.14.

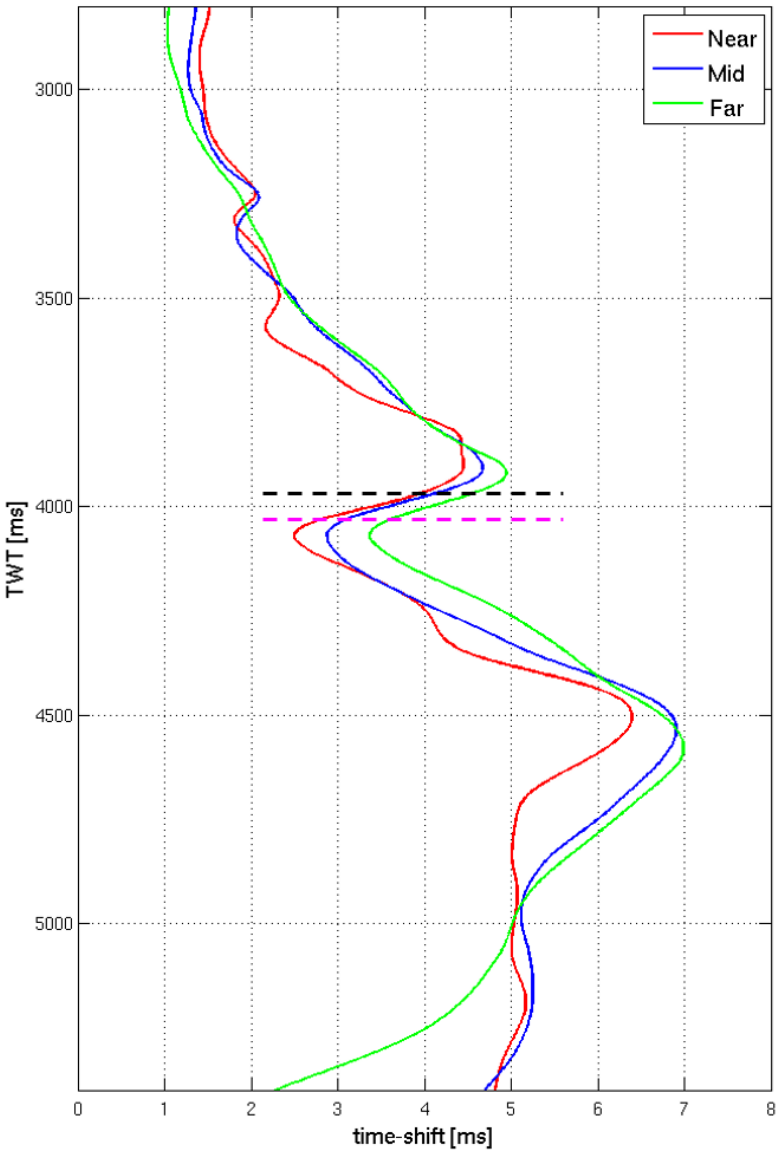

Figure 5.14: Three time-shift traces selected from three corresponding angle-stacked time-shift sections in Figure 5.13. The black and pink dash lines roughly indicates the top and bottom reservoir. In the overburden and reservoir, they are close to each other but then become more separated in the underburden. It should be noted that the top and bottom reservoir are not inline with the peak and trough of the measured time-shifts due to possible time-shift calculation errors (Ji, 2017). The decreasing of time-shifts below 4500ms could also be due to these measurement errors.

5.3.2 Straight ray tomographic inversion

In Chapter 4, I described straight ray tomographic inversion in sample (dimensionless) domain. In this section, I implement the technique for a field application of Shearwater angle time-shifts measured above, which has the cube geometry as in Table 5.1.

The original *"data grid"* is $50m \times 50m \times 4ms$. Before setting up the straight ray trac-

	Numbers of	Sampling rate
Inline	367	50 m
Crossline	623	50 m
Time samples	651	4 ms

Table 5.1: Geometry of the Shearwater input time-shift cube.

ing operator matrix, the data needs to be re-gridded to an appropriate *"tomographic grid"* that maps the time-shift data at a certain incident angle. This is the most critical step of this method and it requires a background velocity model to convert the vertical time into depth. This background velocity model can be simply made by taking the mean of pre-stack depth migration interval baseline velocity (V_{BL}) of the Shearwater field, which is $3500m/s$. The vertical grid can now be translated into depth, which is $dz0 = V_{BL} \times dt0 = 3500m/s \times 4ms = 14m$. For simplicity, I here consider a section rather than a cube. In either Inline or Xline direction, the lateral grid remains the same, $dx0 = 50m$.

Thus, the original grid cell size in depth is now $50m \times 14m$, which equals 60^0 since the method assigns the reflector point at the centre bottom of the grid. However, this incident angle is out of the range of our data. I then need to reduce this angle down to the range of Far partial stack angle in this field $(20 - 30^0)$, by either compressing the grid cell's lateral distance or stretching the vertical distance. The compression requires interpolation to add more data points in the lateral direction meanwhile the stretching can be done by averaging the next data points in the vertical direction. I choose to preserve the data points in the lateral direction as much as possible, which is suitable to the natural purpose of any tomography method. Therefore, this $50m \times 14m$ rectangular grid cell is converted into a square grid cell $50m \times 50m$, where the new time sampling rate, dt_1, is $14,3ms$ corresponding to $50m$ vertical distance, dz_1, and $50m$ lateral distance, $dx0$. The ratio of lateral to vertical grid, dx/dz, is 1 and, as mentioned in Chapter 4, the corresponding incident angle is $\approx 26.5^0$, which lies within the range of incident angles in the far angle stacked time-shift A2030 of the Shearwater field maps. Having the new time sampling rate $dt1$, the data can be easily regridded and normalized to convert into the sample domain as described in Chapter 4, where the number of vertical samples (nz) is 183 and the number of later samples remains the same, either 623 or 367.

However, for any tomographic study it is important to note that the lateral coverage must be large enough for the angle ray-path to reach the desired reflector depth. For example, given a far incident angle of 45^0, the ratio dx/dz approximately equals to 2, calculating from the straight ray-path assumption. Thus, the lateral coverage must be a minimum of $2 \times 183 = 396$ samples. Therefore, I set up the tomographic matrix along the Inline direction, which has the dimensions of 623×183 samples. Given the $dx/dz = 1$ of far angle stacked time-shift, it is easy to access into the mid and near tomographic grids for the mid and near angle stacked time-shift A1020 and A0010 by keeping dz the same whilst compressing the dx to twice and four times smaller than the far angle stacked time-shift, respectively as explained in Chapter 4. Figure 5.15 summarises these regridding steps to tailor the suitable grid for this field data application.

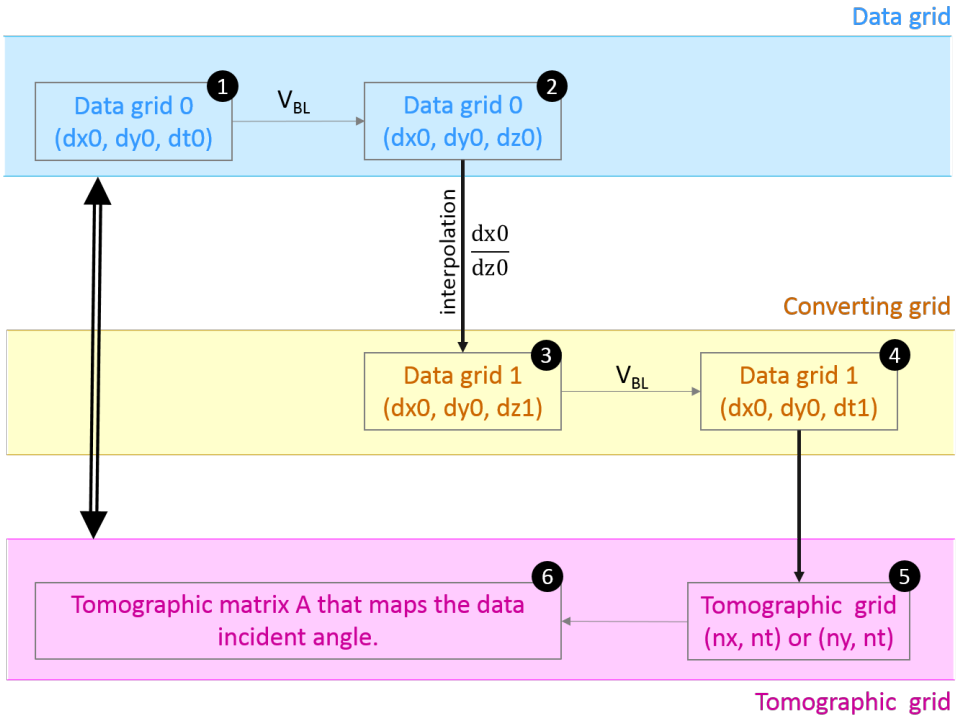

Figure 5.15: Summarized procedure of converting from *"data grid"* into *"tomographic grid"* that maps the incident angle of the data. V_{BL} is the background baseline velocity model that is used to convert from vertical time $dt0, dt1$ (1 and 3) to vertical depth $dz0, dz1$ (2 and 4), respectively. The interpolation step from 2 to 3 requires the ratio $dx0/dz0$ to adjust the suitable angle that the data maps. 4 is then normalized to 5 with the consideration of the ratio of the maximum lateral to the maximum vertical coverage. Given tomographic grid 5, the tomographic matrix in 6 can be set up, which correlates to the data grid 1.

5.3.2.1 Forward modelling

To test out the forward modelling operator **A** for this implication, there is a need for a reasonable and realistic input model ϑ to start with. With the success of implementing the layer stripping method in post-stack domain to invert for ϑ from time-shifts measured by NLI, I reapply the method here, using the full-stack time-shifts measured from baseline 2001 and monitor 2013 (Figure 5.16a). The recovered velocity changes ϑ are shown in Figure 5.16b. In the overburden, the extension is quite small while in the underburden, it becomes much stronger. The compaction in the reservoir is strong as well and corresponds to the yellow interpreted top reservoir horizon. This realistic ϑ model will be a good input example into the tomographic modelling to reveal the features of time-shifts at different angles.

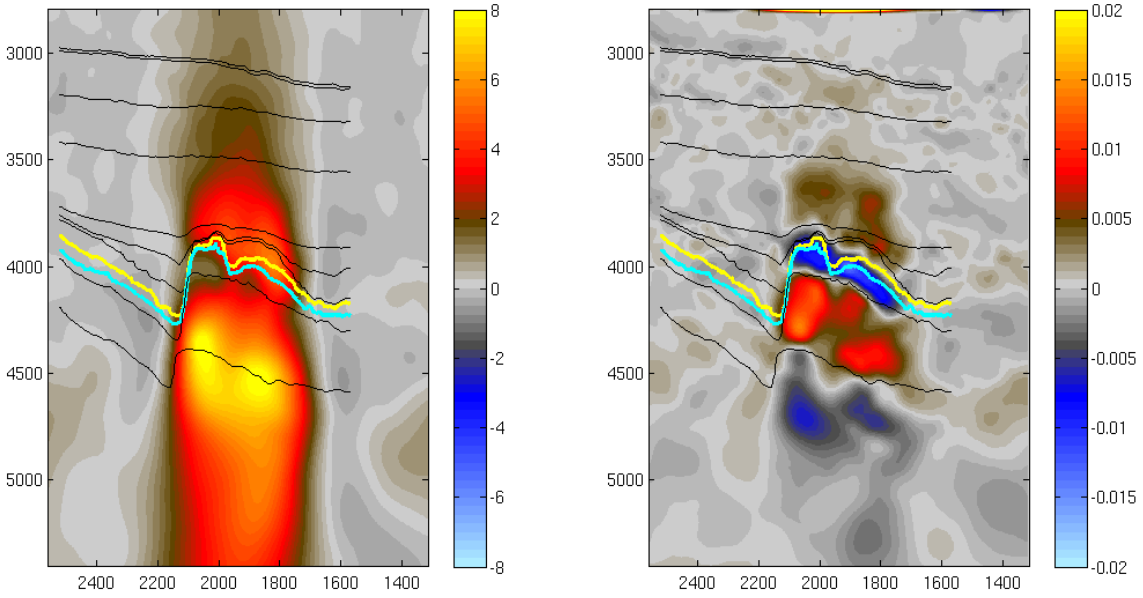

(a) (b)

Figure 5.16: (a) Full-stack time-shifts measured from baseline 2002 and monitor 2013 using NLI and (b) inverted ϑ using layer stripping inversion method for post-stack time-shift. The extracted interpreted horizons are overlaid on the top for reference. The yellow and green lines imply top and bottom reservoir, respectively. About $5ms$ time-shifts are being built up from the overburden to reservoir due to geomechanical effects from depletion. In the underburden, time-shifts become larger, up to $8ms$, and more complicated. The recovered interval ϑ provides more intuitive interpretation with the small slowdown in the overburden, large speedup and slowdown in the reservoir and underburden, respectively. Notably, this inverted result is well-correlated to the interpreted top reservoir and is a good input example for the following tomographic modelling.

Given the tomographic matrix A and ϑ, the tomographic modelling of near (7.1^0), mid (14^0) and far (26.5^0) time-shifts are presented in Figure 5.17. It should be

noted that at these modelled time-shifts are multiplied with new time sampling rate $dt1$ to convert from dimensionless (sample) domain to time domain. The yellow areas at the edges of the figure imply the inactive areas where the ray can not reach. Obviously, as the angle increases, the larger the inactive area is. Further, the time-shift features from near to far incident angles tend to be expanded in the underburden and separated into two different directions at the bottom. These observed features are similar to the measured time-shifts in Figure 5.13. Especially at near, the modelled time-shift (Figure 5.17a) is very close to the observed time-shifts (Figure 5.13a). In spite of not perfect matching between the modelled and observed time-shifts at mid and far, due to the same input of ϑ (Figure 5.16 b), this test of the forward modelling gives confidence in carrying out the inversion below.

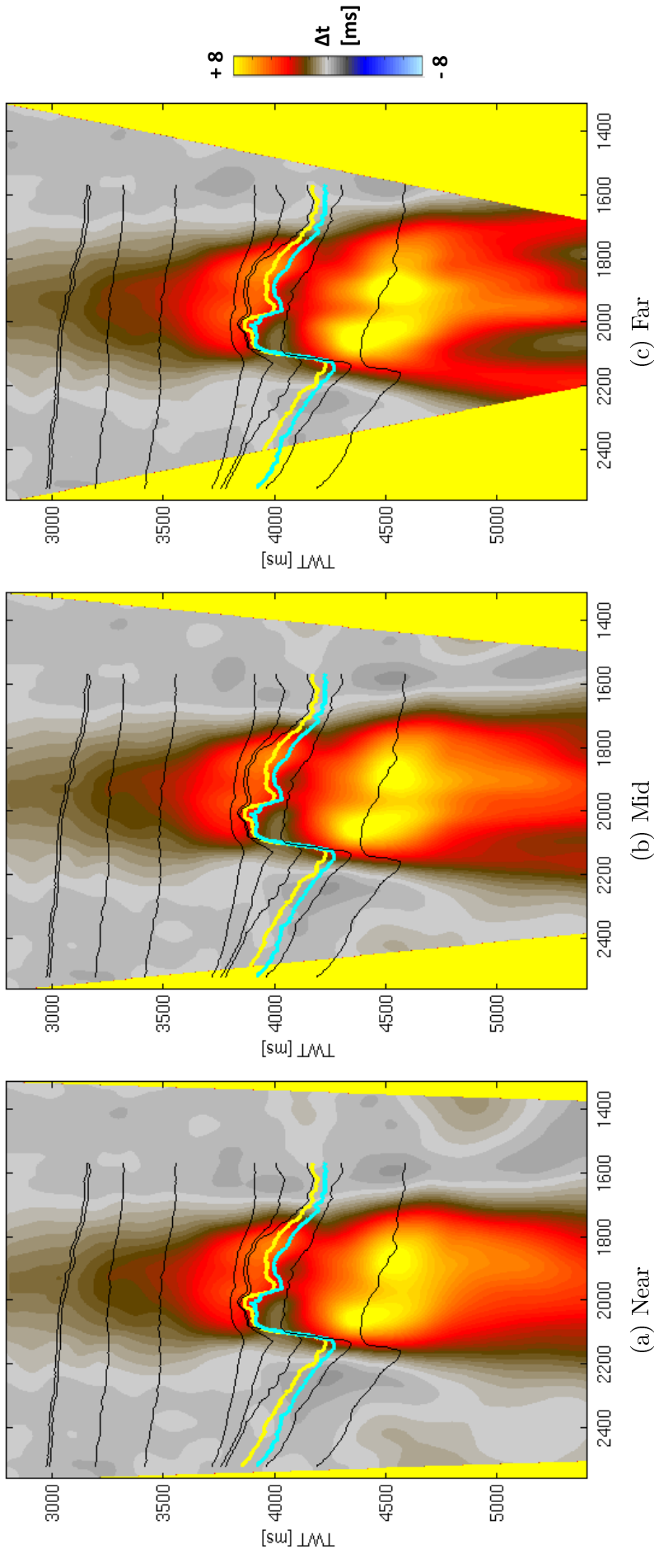

(a) Near (b) Mid (c) Far

Figure 5.17: Forward estimated time-shifts using the recovered ϑ from inverting (post-stack) time-shifts and straight rays at (a) Near, (b) Mid and (c) Far using the ϑ input model in Figure 5.16b. The yellow areas on the edges denote the inactive cells. The larger the angle is, the bigger the inactive areas are and the more the modelled time-shifts expand, especially in the underburden. It is observed that at the bottom underburden, the modelled time-shifts tend to separate into different directions.

5.3.2.2 Inverted results

Using the tomographic forward operator A in subsection 5.3.2.1, I do the inversion for three angle-stacked time-shifts. Because the inversion is carried out in sample domain, these inversion results of recovered ϑ are divided by t_i (= *near, mid, far*) corresponding to each incident angle as mentioned in Chapter 4 and are shown in Figure 5.18. Similarly to the modelled time-shift results, there is a presence of inactive yellow areas at the edges and yet the results still recover the information at the main areas of interest. Figure 5.19 provides a closer look into these meaningful areas. Note that these are unique solutions because the forward modelling operator is completely invertible. It means that these solutions also invert for the noise presented in the data. Some distortion starts to appear in the Mid and then the Far, observed in Figure 5.19b and c, respectively. A regularization method can be applied to avoid the possible noise amplification. However, this step seems to be unnecessary because of the stable NLI-time-shift concluded from the above post-stack time-shift inversion using three different methods (Section 5.2.4). Further, these inverted results are obviously good enough for further interpretation and analysis in the next subsection. Overall, the recovered velocity changes are good correlations with the interpreted horizons. The velocity changes decrease with angles in the overburden. However, in the reservoir and underburden, the recovered ϑ variations with angles are not clear.

These inverted results show the differences at all levels of the overburden, reservoir and underburden. Three traces are selected from these three recovered ϑ sections and plotted in Figure 5.20. As expected, it shows larger changes of ϑ in the reservoir (1%) than in the overburden (0.5%). The changes in underburden are complicated, with larger changes than in the overburden, which can not be explained by the arching effect (Ji, 2017). However, once the overburden and reservoir are corrected, the changes in the underburden are made clearer (personal discussion from John Brain).

5.3.2.3 Result analyses and conclusions

In order to have a better analysis of the inverted ϑ features with angle, I produce the differences of (Mid - Near) and (Far - Near) as shown in Figure 5.21, together with

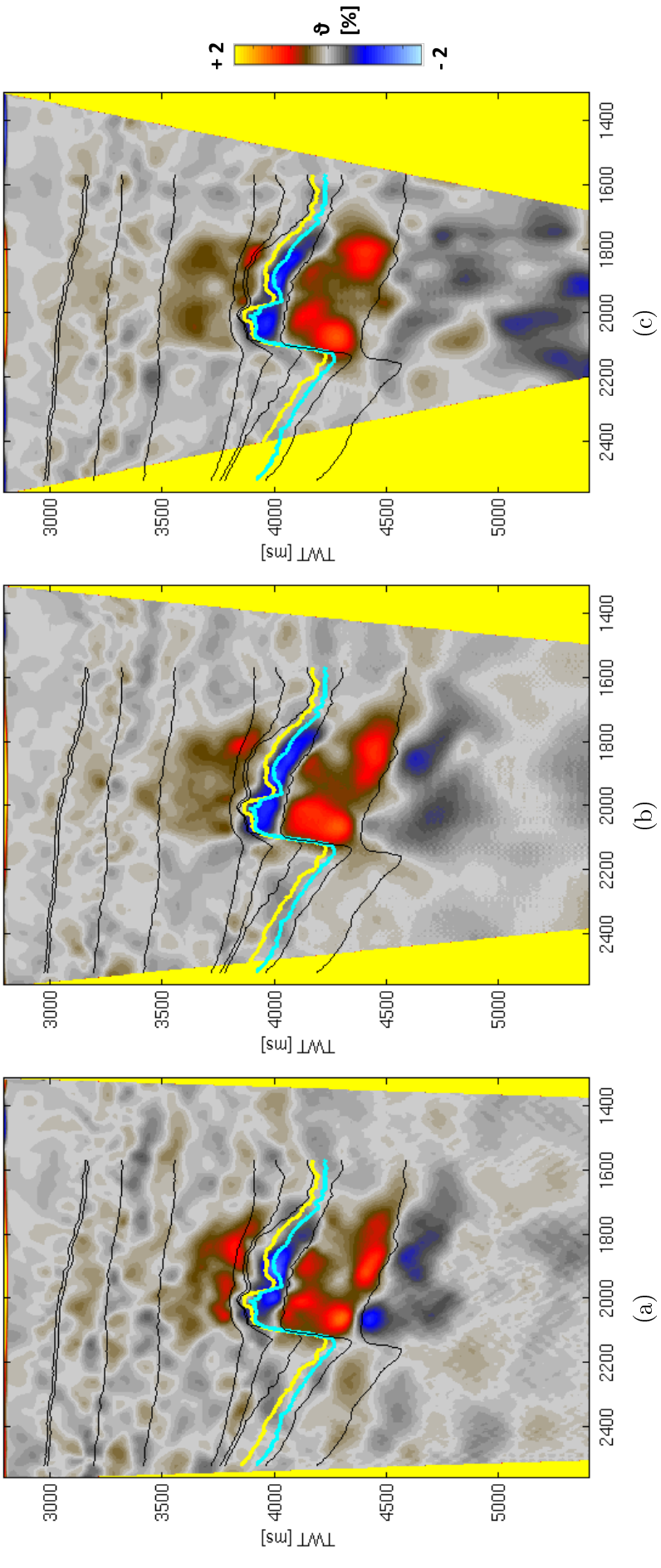

Figure 5.18: Shearwater tomographic inversion for (a) Near, (b) Mid and (c) Far angle stacked time-shift measured by NLI method. The yellow edges imply the inactive areas. The method works well on these dataset and the tomographic design is able to cover enough of the interested areas, of which I will zoom in closer in the next Figure 5.19 for further analysis.

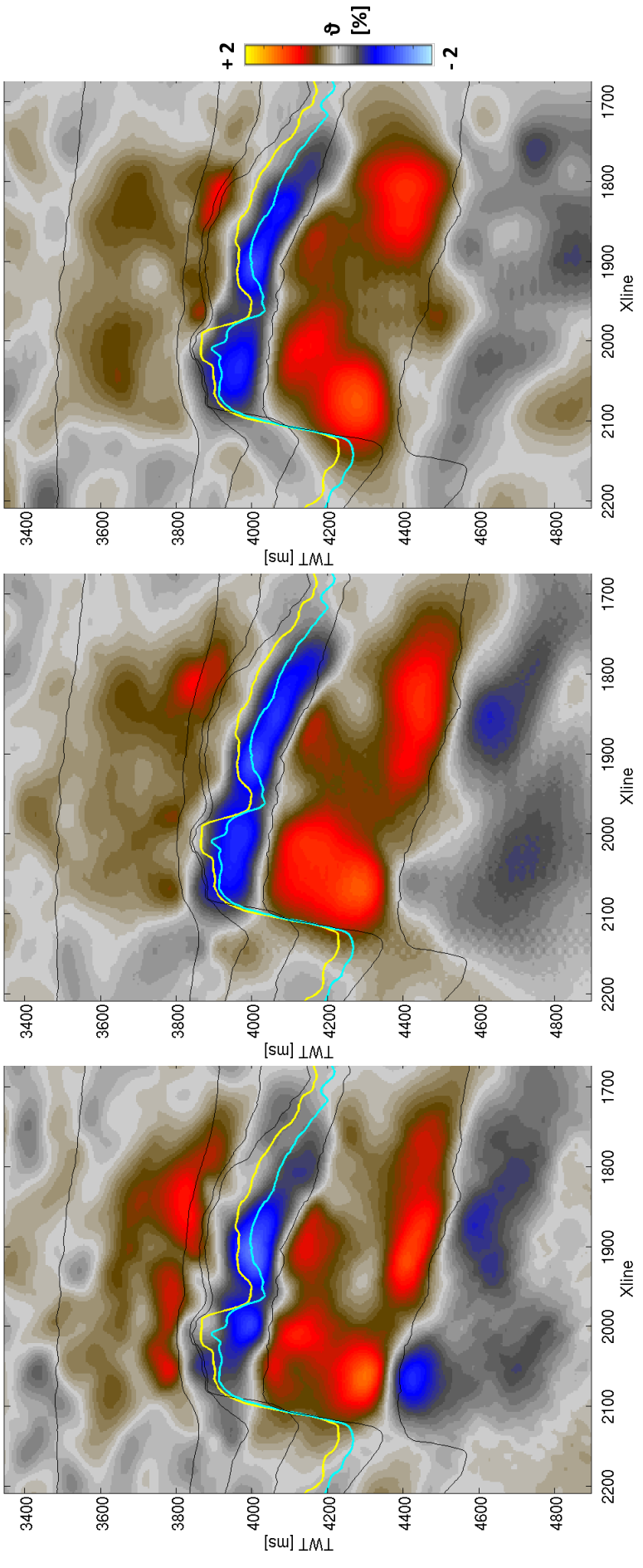

Figure 5.19: Detailed recovered ϑ of the areas of interest zoomed in from Figure 5.18 for (a) Near, (b) Mid and (c) Far angle stacked time-shifts. ϑ is obviously decreasing with angles in the overburden whilst in the reservoir and underburden, the velocity change variations with angles are unclear. The compaction in reservoir areas are well-correlated with the interpreted top reservoir horizon.

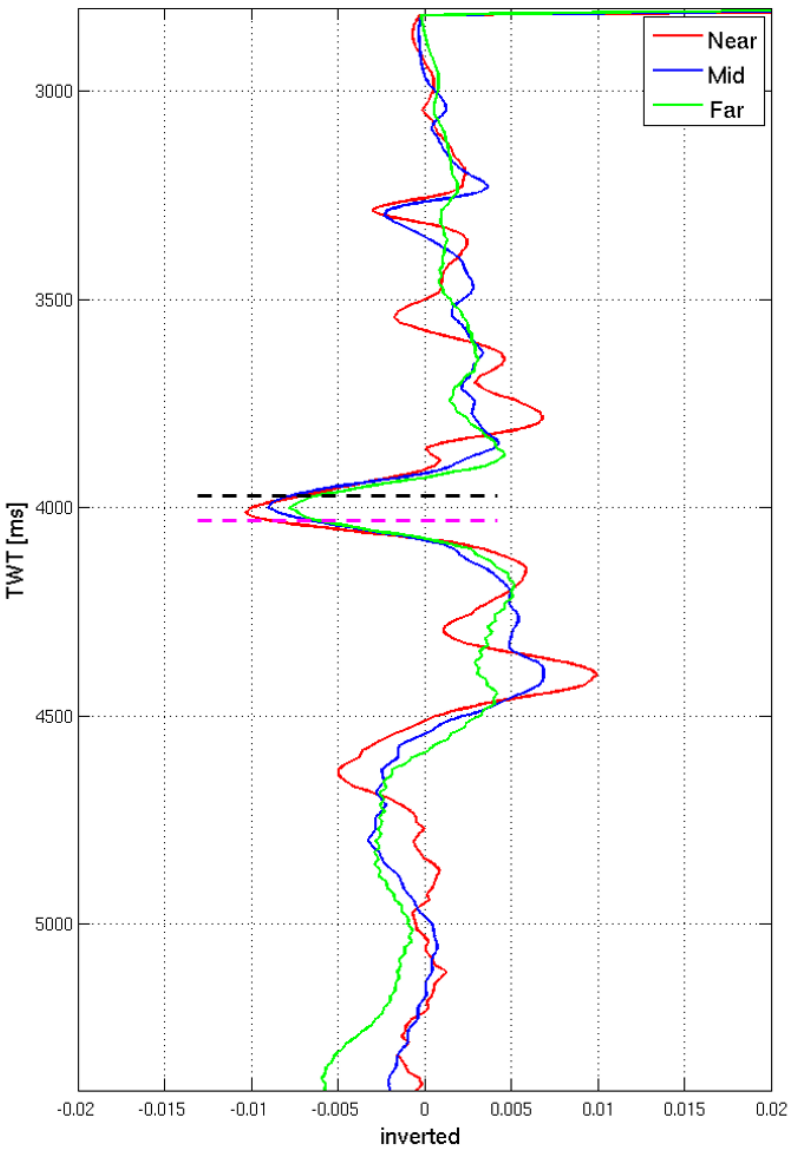

Figure 5.20: Recovered ϑ traces at 3 different partial angle-stack. Black and pink dash lines roughly imply the top and bottom reservoir. About 1% changes of ϑ observed in the reservoir and smaller changes of 0.5% in the overburden. The responses in the underburden remain complex with larger extensions than in the overburden.

the labels of selected main horizons. The differences of (Far - Near) are larger than (Mid - Near) indicating speedup or slowdown effects, these variations are generally decreasing with the angle (or offset).

I then take the mean of ϑ among the labelled horizons which roughly represents for the overburden, reservoir and underburden, and plot these mean values with Near, Mid and Far as in Figure 5.22. It is observed that the extension in the overburden (from Hod_Top to Chalk_Base and Chalk_base to Kimmeridge) is decreasing with the angle, with a maximum magnitude of 11.6% changes. For the compaction effect in the reservoir (Fulmar_Top to Pentland), the velocity changes get a bit stronger

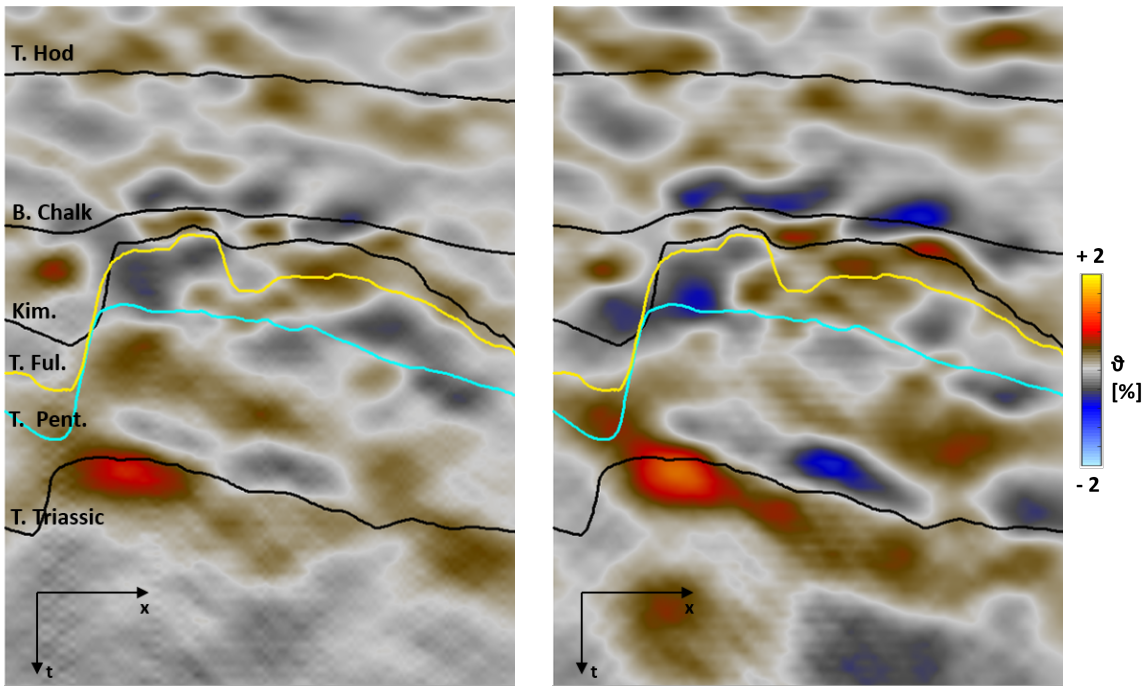

(a) (b)

Figure 5.21: Differences of inverted ϑ between (a) (Mid - Near) and (b) (Far - Near). Generally, these changes seem decreasing with the angle due to the presence of stronger blue and red in (b) than (a).

with offset, with 11.9%, which is similar to the increasing changes in the underburden (Pentland to Triassic) in spite of the underburden's opposite effect (extension).

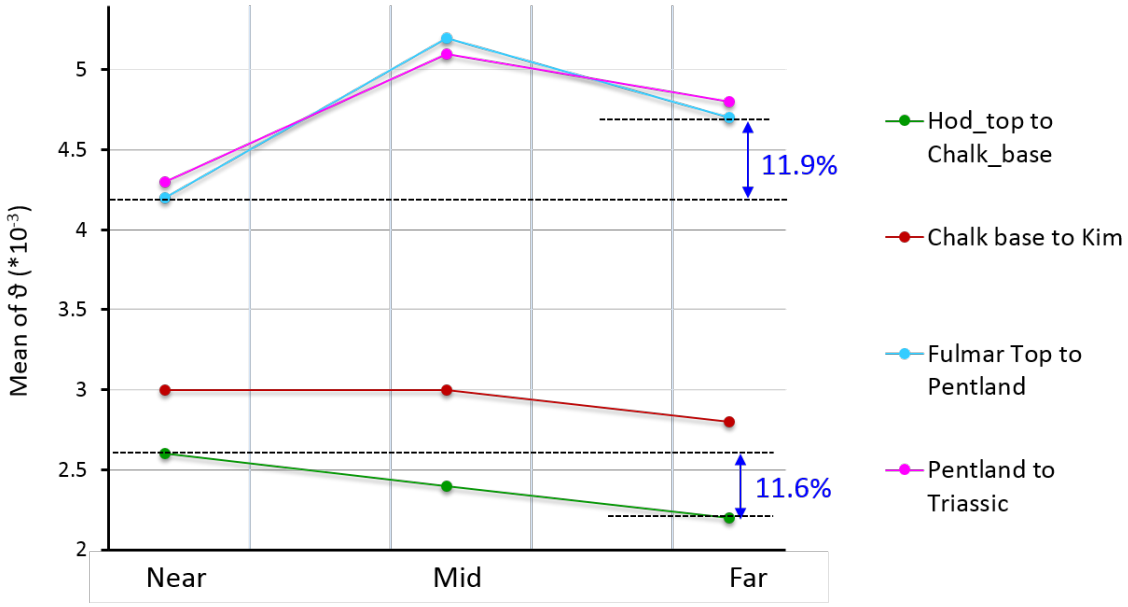

Figure 5.22: Graph of the inverted ϑ mean from different zones of the overburden, reservoir and underburden over three different angles. It is observed that the overburden decreases by 11.6% and the reservoir and underburden similarly increase by 11.9%.

It is of interest to look at the time-lapse velocity change distribution over the whole field. I therefore perform the tomographic inversion for the whole cube by populating the inversion for every Inline. Having the recovered ϑ cube, I generate the three maps of mean ϑ for the top reservoir and of vertical mean ϑ over the overburden and underburden as shown in Figure 5.23, 5.24 and 5.25, respectively. At the top reservoir (Figure 5.23), there is not only the presence of the compaction coded by blue color but also the presence of the extension at some degree. The compaction is decreasing over the whole area, but in the blue rectangular area, they are getting stronger. The extension seems to be weaker from Near to Far (pink curves) but this is not always true for some local areas (dashed pink curves). In the overburden and underburden (Figure 5.24 and 5.25), there is only extension with a smaller magnitude in the overburden than the underburden. Note that the color bar scale in overburden map is half the size of the top reservoir and the underburden. There are larger changes in the reservoir (1.4%) than in the overburden (0.8%) whilst the underburden maintains the largest velocity changes. These observations highlight the presence of the geomechanical effects in both overburden and underburden due to the reservoir depletion. Notably, all these compaction and extension features show the agreement with well locations. A clear variation of velocity changes with offset suggests the possible anisotropic contribution.

Thus, a robust tomographic inversion using the straight ray assumption has been developed and applied on angle stacked time-shifts. The method works very well on the Shearwater dataset with NLI time-shift measurement. It provides a direct, quick yet efficient and stable solution of the recovered interval velocity changes ϑ for the whole time-shift cube so that a quick and intuitive interpretation and decision can be made during the reservoir management and development procedure. The straight ray assumption may be a weak point of this method as it does not follow the physics. The magnitude of recovered ϑ can be trusted but not their exact locations due to the assumed homogeneous background baseline velocity model (in spite of the agreement of these recovered ϑ with well locations as mentioned above). In the next subsection, I will apply a small analytical bending solution, expecting to reflect more possible potentials of this straight ray tomography method.

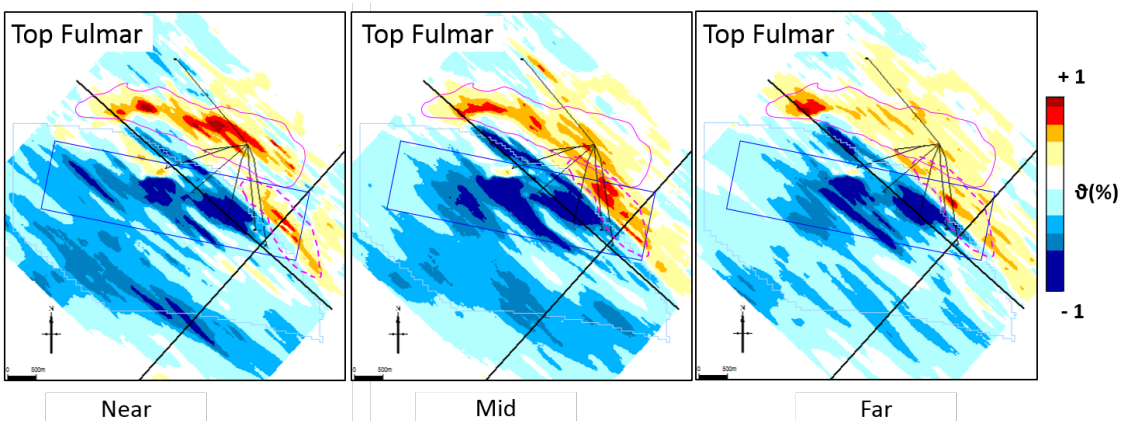

Figure 5.23: Mean of the recovered ϑ at top reservoir (Top Fulmar) with about 1% changes. Generally, these velocity changes correspond well to the well locations. The extension (red) seems to get smaller with the angles (pink curves) except the local areas (dashed pick curves) meanwhile the compaction at the interested areas (blue rectangular boxes) is increasing.

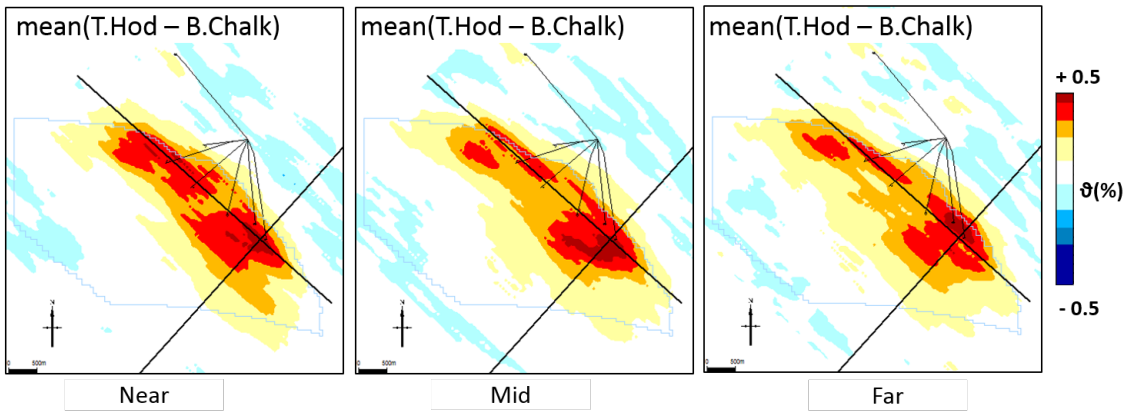

Figure 5.24: Vertical mean of the recovered ϑ for the overburden from Top-Hod to Base Chalk. Only extension in ϑ is observed here with about 0.5% changes, half smaller than the reservoir (1%). Notably, these small changes are in agreement with the well locations. These extension effects are clearly decreasing with angles.

5.4 Chapter conclusions

I have presented a Shearwater field application for the new development methods described in Chapter 2 and 4. For post-stack time-shift inversion, the GMM method provides a quick and stable solution with an analytical expression in comparison with other two selected methods of layer stripping and damped least squares. In order to choose a suitable Gaussian grid to the dataset, I did the sensitivity analysis based on the cost of computational time and residual errors. Apart from forming the analytical expression of ϑ and Δt, the novelty of this GMM method is also the skilful implementation of GMM by changing only one parameter while pre-setting the other two location, μ, and width, σ. Looking at angle-stack time-shift

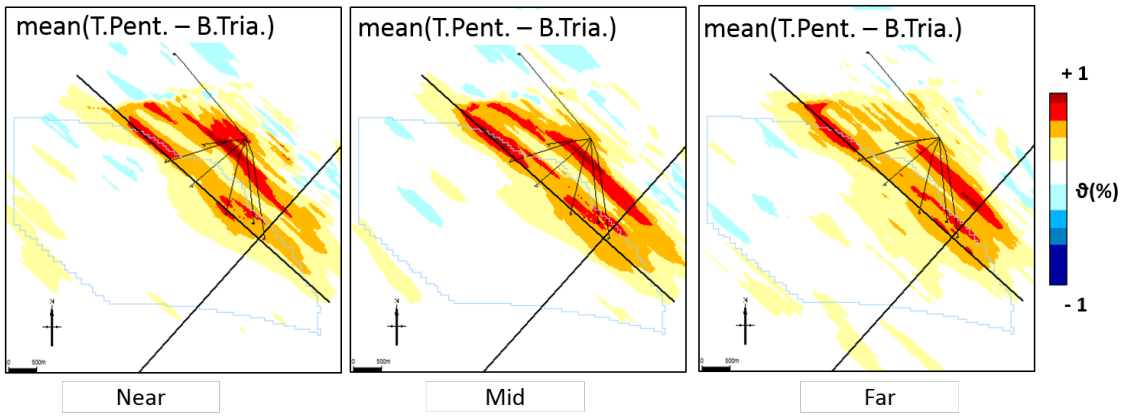

Figure 5.25: Vertical mean of the recovered ϑ for the underburden from Top-Pentland to Top-Triassic. As in the overburden, only extension is observed in the underburden but with the magnitude of two times larger (1%). The velocity changes are increasing at Mid but then reducing at Far.

inversion using straight ray tomography with the constant incident angles, I found that, in spite of a larger amount of input data with three different angles, the method provides a robust and direct solution. Innovation using a constant incident angle and re-gridding technique makes the tough and heavy tomography method in general become straightforward and quickly applicable. Both these new methods work well on Shearwater dataset and NLI time-shift measurement method. The recovered ϑ, either from post-stack or angle-stack domain, can be quickly produced to help the time-lapse interpretation and analysis.

In Shearwater, the velocity changes are about 1% speedup in the top reservoir and 0.5% extension in the overburden. Corresponding to the biggest time-shifts in the underburden, the velocity changes here also remain large by about 1%. These results help to reveal the strong geo-mechanical effects happening in the overburden and especially in the underburden, due to the reservoir depletion. Regardless of the straight assumption, these angle recovered ϑ are in agreement with the well locations, similar to the vertical ϑ recovered from post-stack time-shifts. Separated inversion of $\Delta V/V$ from each time-shift partial-stacks helps to understand distribution of velocity changes from different angles. In this application, it is observed that there is a clear variation of $\Delta V/V$ with offsets. This suggests the possible anisotropic contribution in Shearwater. Furtheremore, inverted $\Delta V/V$ from partial-stack also helps to distinguish the contribution of thickness and velocity changes to time-shifts as mentioned in Landrø and Stammeijer (2004).

Chapter 6

Beyond timeshift inversion - Waveform inversion

ABSTRACT

Changes in velocity do not just induce changes in traveltime but also the reflectivity. The previous chapters limited themselves to only the time-shift aspect of time-lapse seismic effects. This chapter explores another important attribute of time-lapse seismic - amplitude changes. After laying the foundation for general 4D amplitude and revising the time-lapse waveform inversion methods, this chapter studies the implementation of a robust trace warping scheme, incorporating the GMM method introduced in Chapter 2. The inversion is carried out in the post-stack domain using a non-linear inversion method, that takes account of the amplitude effects.

6.1 On the time-lapse waveform seismic inversion

So far, we have recovered the velocity changes ϑ from time-shifts which are measured from the time-lapse seismic data under the assumption of negligible amplitude changes. The changes of time-lapse velocity induce not only the changes of traveltime (time-shifts) but also the change of amplitude. These are two key and equally important attributes of 4D seismic. Taking into account the effect of amplitude together with time-shifts reveals a more accurate representation of time-lapse seismic data. Recovering the velocity changes, ϑ, directly from the time-lapse waveform is hence better at reflecting the subsurface variation due to the production and also helps to avoid the inevitable error from time-shift measurement methods.

Therefore, this chapter will describe a new robust and stable method to estimate the velocity changes from time-lapse waveform data. Before that, I will first explore the amplitude aspect of the time-lapse seismic attribute and will revise similar methods in the literature.

6.1.1 Time-lapse amplitude changes

When compared with time-shifts, the amplitude change attribute is more challenging in 4D seismic. Time-shifts are an accumulative property so that they are smoother and more stable. In contrast, the changes of amplitude is an interval attribute which reflects the changes of the interval velocity and density so that incorporation of the amplitude change in the inversion scheme becomes more difficult. However, their benefits are applied in many different ways of the field's production and recovery, such as detecting the variation of pore pressure and fluid saturation (Varela et al., 2006), and assessing reservoir compartmentalization (He et al., 2015). It should be noted that these benefits are usually highlighted after time-shift correction is applied to remove the possible shifts in traveltime between the baseline and monitor surveys.

6.1.2 Time-lapse waveform inversion

I categorize the methods of estimating the time-lapse velocity changes from time-lapse seismic data into two main following groups.

6.1.2.1 Full waveform inversion

Full waveform inversion (FWI) has drawn attention of 4D seismic geophysical researchers recently, due to its high resolution in building the velocity model. Routh et al. (2012) and Asnaashari et al. (2012) introduced three general time-lapse FWI schemes – parallel difference, sequential difference and double difference. These three schemes are similar to the categories of Sarkar et al. (2003) in which the parallel and sequential difference methods use the baseline and monitor surveys while the double difference method aims to minimize the 4D differences. It can be viewed as an optimization process which either minimizes (e.g. L2 norm) or maximises (e.g. cross-correlation) the objective function to find the most optimal model (Routh et al., 2012). However, at the same time, FWI aims to match *"wiggle for wiggle"* in such a way that the synthetic wiggle aims to capture the entire seismic wave types and their properties based on the physics of wave propagation theory. These seismic wave properties include not only the kinematic information as the tomography methods do, but also the amplitude and phase of seismic waveform. As a result, the recovered velocity models are achieved at a high resolution which imagines best-to-date the subsurface. Hicks et al. (2016) shows a FWI application for the Grane Field in the Norwegian North Sea to recover the velocity changes from PRM data (Figure 6.1). This is a heavy oil reservoir with no initial gas cap. The results are in line with the injected gas locations.

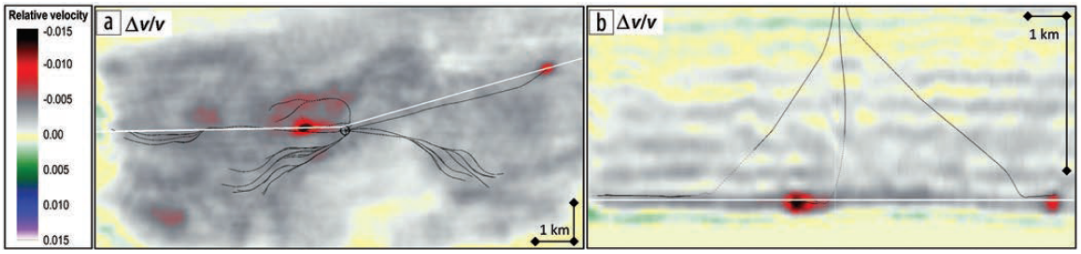

Figure 6.1: High resolution recovered velocity changes from the Grane Field using FWI for (a) a depth slice at the reservoir level and for (b) a vertical section through two main reservoir injected gas anomalies. The recovered velocity changes of 1.5% are associated with the injected gas location as there is no initial gas cap at this heavy oil field.

However, FWI is always heavy in terms of computational cost and complexity, which are not suitable to the scope of this thesis. Therefore, I will focus more on the next category.

6.1.2.2 Trace-warping methods

Originally, the warping technique comes from correcting image distortion (Beier and Neely, 1992). The method has then been applied in 4D seismic processing in the cross-equalization toolbox to remove the 4D seismic artifacts related to acquisition and processing so that the genuine production-related changes can be highlighted (Rickett and Lumley, 1998; Eastwood et al., 1999; Hall et al., 2005). Nowadays, *warping* has become quite a generic term which covers a collection of techniques, including correlation-based methods, time-shift non-linear inversion (as mentioned above) and relative velocity non-linear inversion.

Williamson et al. (2007) recast this warping method as a non-linear problem to recover the time-lapse velocity changes and named it as *trace-warping*. In this method, the monitor traces are rewritten as a function of time-shifted baseline traces and amplitude change term. The equation is adjusted to the notations used in this thesis as follows:

$$m(t_i)_{(Williamson)} = b(t_i + \Delta t_i) + \psi * \Delta R_i. \tag{6.1}$$

where ψ is the wavelet, ΔR is the reflectivity changes and symbol $*$ denotes the convolution. Δt and ΔR are then replaced by a function of $\Delta V/V$ as:

$$\Delta t_{i(Williamson)} = \sum_{k=1}^{i} \bar{\vartheta}_k, \tag{6.2}$$

where $\bar{\vartheta}$ is recalled from Equation (2.13) as:

$$\bar{\vartheta}_k \approx -\frac{\Delta V_k}{V_k}, \tag{6.3}$$

and

$$\Delta R_{i(Williamson)} = \bar{\vartheta}_i{}'. \tag{6.4}$$

where the supperscript $'$ denotes the derivative operator of the quantity $\bar{\vartheta}$. Williamson et al. (2007)'s method assumes negligible thickness changes, $\Delta z/z$, small offsets and dipping reservoir. Its novelty is of the explicit dependence of the data $m(t)$ and $b(t)$ on the variable $\Delta V/V$ so that both effects of time-shifts and amplitude changes are taken into account simultaneously, not separately as in the previous most common approaches (Thore and Hubans, 2011). Also, all the quantities are in time-domain

so that the method is not limited by the vertical resolution of seismic data and hence can access into zero bandwidth. Given Equation 6.1, the objective function for 4D trace warping can be written as in Equation 6.5 and any standard inversion can be applied to resolve for $\Delta V/V$:

$$OF_{trace-warp} = \left|\left|m(t)_{(Williamson)} - b(t+\Delta t)_{(Williamson)} - \psi * \Delta R_{(Williamson)}\right|\right|_2 . \tag{6.5}$$

Thanks to these advantages, Williamson's method are then extended and employed in different ways. In the following, I will provide a chronological summary of these extensions and employments, and will refer to them as Williamson's family methods later on.

- In Thore (2011) and Thore and Hubans (2012), in stead of using data driven, the study proposed *"a layered definition of the model"* (model driven method) in which the benefits of the prior information are utilized (e.g. well logs). The changes of density are included in the impedance changes and can be separately recovered from velocity changes without using:

$$\frac{\Delta I_P}{I_P} = (1+\beta)\frac{\Delta V_P}{V_P}. \tag{6.6}$$

  where I_P is baseline P-impedance, ΔI_P is 4D P-impedance changes and coefficient β represents the relation between relative velocity changes and impedance changes. This proposed method helps to better link the dynamic connectivities with the 4D geo-bodies. However, it is limited in the vertical seismic resolution due to the layer definition.

- Thore et al. (2012) extended Williamson et al. (2007)'s method to parallel dipping layers in depth by introducing a transformation space in which the dipping reflectors are flattened in the pseudo vertical space. The Williamson's method is then performed before transforming back to the real dipping geometrical space. In Audebert and Agut (2014), the authors also applied Williamson's method in depth imaging domain based on the basic ideas from Thore et al. (2012) with more general implementation. Audebert and Agut (2014)'s method can be applied to a non-parallel dipping reservoir with less computational cost and is an alternative to the FWI method. Similarly, Baek and Keho (2015) also employed Williamson's

warping method in depth domain. However, in this study, the velocity changes are used *in depth*, not *in time*.

Apart from Williamson's family, Baek et al. (2014) also introduced a warping method which incorporates both time-shifts and amplitude changes by using piecewise cubic polynomial basis function together with a least square regularization. Similar to GMM methods developed in Chapter 2 of this thesis, the usage of the basis function helps to eliminate the *"unphysical warping solution and impose continuity of warping function naturally"* (Baek et al., 2014).

6.1.2.3 Wavelet dependence

In the Williamson's family methods, the wavelet plays an explicitly important effect as a scaling factor to the amplitude change term ($\psi * \Delta R$, Equation 6.1). Apart from this, there is another implicit effect of the wavelet when the baseline and monitor traces are warped directly as pointed out in Griffiths et al. (2015). Figure 6.2b sketches out how the wavelet is affected by non-zero time-shift below reservoir when the warping is carried out in the trace domain but not in the impedance domain (Figure 6.2a).

Instead of directly warping on the traces, Griffiths et al. (2015) proposed *impedance warping* using the following equation:

$$OF_{imp-warp} = ||m(t) - \psi * R(t + \Delta t) - \psi * \Delta R||_2 \,, \tag{6.7}$$

where R is baseline reflectivity and is calculated as:

$$R(t) = \frac{1}{2}\frac{\partial ln(I_P(t))}{\partial t}. \tag{6.8}$$

However, this impedance warping requires a priori information of the base impedance trace as seen in Equation 6.7 ($R(t + \Delta t)$. Furthermore, its difference from trace warping (Equation 6.5) is subtle (Griffiths et al., 2015). The same as for trace warping, this impedance warping also needs wavelet estimation. There are a few common approaches for wavelet estimation developed for 3D seismic data by using either seismic data, well logs or a combination of both (well-tie to seismic), which can be straightforwardly applied to 4D seismic data (Thore and Blanchard, 2014).

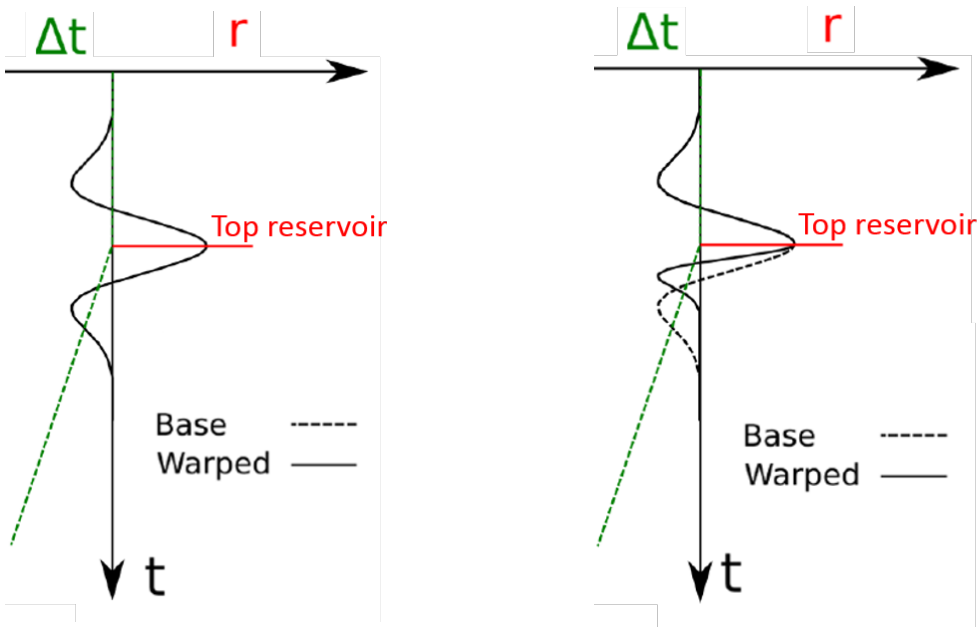

(a) (b)

Figure 6.2: Comparison sketch of (a) impedance warping and (b) trace warping. r is the reflectivity spike, which is not affected by time-shift (Δt) when warping the impedance. The resulting trace (a) is then unaffected whilst (b) is distorted when warping the trace. *"Warping the trace directly squeezes the part of the wavelet affected by the non-zero time-shift below the top reservoir" (Griffiths et al., 2015).* Redrawn after Griffiths et al. (2015).

6.2 Shearwater field application – waveform inversion

Among the various waveform inversion methods as revised above, Williamson trace warping method (Williamson et al., 2007) stands out as the most suitable waveform inversion method for the scope of this thesis. It works on traces so the algorithm is much lighter than FWI. It also does not require any prior information as does the impedance warping. Due to the challenges of incorporating the time-lapse amplitude change attribute as discussed above, I will employ Gaussian reconstruction using GMM (Chapter 2 and 5) into Williamson method to make the inversion more stable, robust and efficient. This waveform inversion's method will be applied to Shearwater field, using the post-stack baseline 2001 and monitor 2004. Before that, I will re-derive Williamson's equation and will explain the implementation of the Gaussian reconstruction method for waveform inversion. The 4D changes of density in this study is assumed negligible so that the impedance changes in the amplitude change term are now equally to velocity changes.

6.2.1 Re-derivation of Williamson's method

Williamson's formulae has been referred to differently in different studies, which cause confusion to some extent. For example, the equation in Thore and Hubans (2012) is:

$$OF_{Thore(2012)} = ||b(t) - m\,(t + \Delta t) - \psi' * \Delta R||_2\,, \tag{6.9}$$

where

$$\Delta R_{Thore(2012)} = \frac{\Delta V}{V} + \frac{\Delta \rho}{\rho}. \tag{6.10}$$

Regardless, in the inclusion of the density term $\Delta\rho/\rho$ in the reflectivity change term ΔR (Equation 6.10), in the objective function $OF_{Thore(2012)}$ (Equation 6.9), the derivative is on the wavelet ψ but not on the reflectivity term as in the original formulae Equation 6.5 from Williamson et al. (2007). In fact, the reflectivity term $\Delta R_{Thore(2012)}$ also has a slight difference with the presence of $1/2$ term to the following $\Delta R_{Thore(2014)}$ from Thore and Blanchard (2014):

$$\Delta R_{Thore(2014)} \approx \frac{1}{2}\left(\frac{\Delta V}{V} + \frac{\Delta \rho}{\rho}\right). \tag{6.11}$$

Therefore, it is necessary to re-derive Williamson's equation before employing and incorporating with Gaussian reconstruction. The re-derivation is split into two steps as following:

- **Time-shift term**

  This thesis defines time-shift Δt as the traveltime difference between monitor and baseline, so that the monitor trace $m(t)$ can be related to the baseline trace $b(t)$ for any time sample i as:

  $$m(t_i) = b(t_i + \Delta t_i), \tag{6.12}$$

  where Δt can be discretized from Equation (2.15) with time sampling rate dt as:

  $$\Delta t_i \approx dt \sum_{k=1}^{i} \bar{\vartheta_k}. \tag{6.13}$$

- **Amplitude changes term**

  Starting from the basic definition of reflectivity coefficients R between 2 adjacent layers V_1 and V_2 for the baseline velocity and the corresponding perturbed velocity

changes ΔV_1 and ΔV_2, the reflectivity changes are:

$$\Delta R_{12} = \frac{(V_2 + \Delta V_2) - (V_1 + \Delta V_1)}{(V_2 + \Delta V_2) + (V_1 + \Delta V_1)} - \left(\frac{V_2 - V_1}{V_2 + V_1}\right). \tag{6.14}$$

After several manipulations, the equation can be sorted as:

$$\Delta R_{12} = \frac{2(\Delta V_2 V_1 - \Delta V_1 V_2)}{[(V_2 + \Delta V_2) + (V_1 + \Delta V_1)](V_2 + V_1)}. \tag{6.15}$$

Divide both numerator and denominator by $V_1 V_2$, the equation then becomes:

$$\Delta R_{12} = \left(\frac{\Delta V_2 V_1 - \Delta V_1 V_2}{V_1 V_2}\right)\left(\frac{2V_1 V_2}{(V_2 + V_1)^2 + (\Delta V_2 + \Delta V_1)(V_2 + V_1)}\right). \tag{6.16}$$

Divide both numerator and denominator again by $(V_2 + V_1)^2$, we have:

$$\Delta R_{12} = \left(\frac{\Delta V_2}{V_2} - \frac{\Delta V_1}{V_1}\right)\left(\frac{2V_1 V_2}{(V_1 + V_2)^2}\right)\left(\frac{1}{1 + \dfrac{\Delta V_2 + \Delta V_1}{V_2 + V_1}}\right). \tag{6.17}$$

In a general form, we can rewrite the reflectivity changes in a time series form with time sample index i as:

$$\Delta R_i = \left(\frac{\Delta V_{i+1}}{V_{i+1}} - \frac{\Delta V_i}{V_i}\right) P_i H_i, \tag{6.18}$$

where

$$\begin{aligned} H_i &= \frac{1}{1 + \left(\dfrac{\Delta V_{i+1} + \Delta V_i}{V_{i+1} + V_i}\right)} \\ &\approx 1 - \left(\frac{\Delta V_{i+1} + \Delta V_i}{V_{i+1} + V_i}\right), \end{aligned} \tag{6.19}$$

due to the small perturbed velocity changes ΔV and

$$\begin{aligned} P_i &= \frac{2V_iV_{i+1}}{(V_i+V_{i+1})^2} \\ &\approx \frac{1}{2}. \end{aligned} \tag{6.20}$$

if there is small vertical variation of baseline velocity in time domain.

Replacing Equation 6.19 and 6.20 into Equation 6.18, the time-lapse reflectivity changes are then:

$$\begin{aligned} \Delta R_i &\approx \frac{1}{2}\left(\frac{\Delta V_{i+1}}{V_{i+1}} - \frac{\Delta V_i}{V_i}\right)\left(1 - \left(\frac{\Delta V_{i+1}+\Delta V_i}{V_{i+1}+V_i}\right)\right) \\ &\approx \frac{1}{2}\left(\frac{\Delta V_i}{V_i}\right)' \\ &\approx \frac{1}{2}\bar{\vartheta_i}'. \end{aligned} \tag{6.21}$$

- **Both effects of time-shifts and amplitude change terms**

  Adding the reflectivity changes from Equation 6.21 into Equation 6.12, the baseline trace $b(t)$ can be finally rewritten as a function of velocity changes ${}^{\Delta V}/_{V}$ as:

$$\begin{aligned} m(t_i) &\approx b\left(t_i + \Delta t_i\right) + \frac{1}{2}\psi * (\Delta R_i)' \\ &\approx b\left(t_i + dt\sum_{k=1}^{i}\bar{\vartheta_k}\right) + \frac{1}{2}\psi * \left(\bar{\vartheta_i}\right)'. \end{aligned} \tag{6.22}$$

Equation 6.22 is similar to Equation 6.1 except for the dt in the time-shift term and 1/2 in the amplitude change term. In order to examine Equation 6.22, I generate a numerical test workflow as described in Figure 7.1. I use the Shearwater interval velocity model to make the baseline velocity model, V. The perturbed velocity changes are made to mimic the field scenario with a gradual extension from the top overburden to top reservoir (up to 1%, Figure 6.4a). Having baseline and monitor velocity models (V and V_M, respectively), I use a 1D-convolution method with a Ricker wavelet at 18Hz frequency to generate the numerical baseline $b(t)$, monitor $m(t)$ (Figure 6.4b) and their differences (Figure 6.4c). This numerical $m(t)$ is then compared with the analytical $m1(t)$ using Williamson's method with the

new derivation (Equation 6.22) and their difference is shown in Figure 6.4d. The color bar scale is purposely set 20 times smaller than the numerical monitor (Figure 6.4b), but the difference is still very small, especially compared with the numerical 4D seismic in Figure 6.4c.

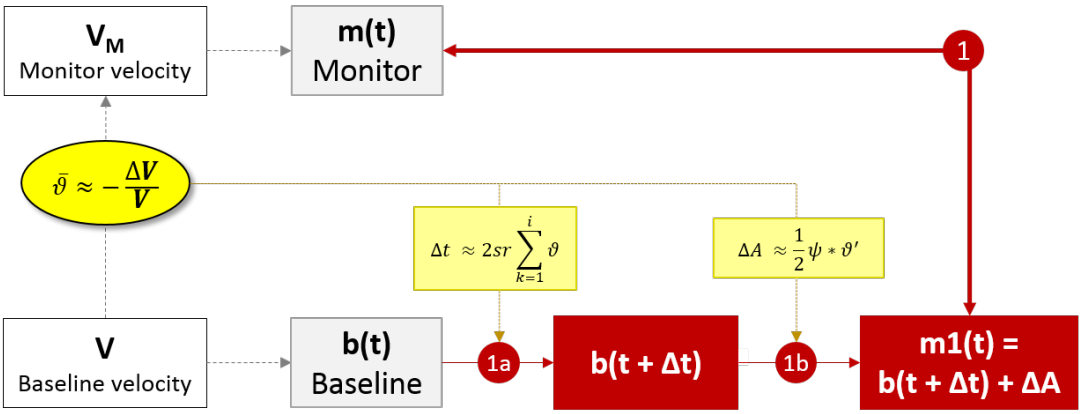

Figure 6.3: Workflow of the numerical test against the analytical Equation 6.22). Given the baseline velocity model V and velocity changes $\bar{\vartheta}$, I produce monitor velocity V_M and numerically generate synthetic baseline and monitor seismic, $b(t)$ and $m(t)$ respectively using convolution method with a Ricker wavelet with 18Hz frequency. Having $b(t)$ and $\Delta V/V$, I use Williamson method to generate $b1(t)$ by (1a) shifting the monitor and (1b) adding the amplitude term ΔA. This analytical monitor trace $m1(t)$ is compared with the numerical $m(t)$ (1).

Thus, Equation 6.22 successfully reconstructs a new analytical monitor $m(t)$ using $b(t)$ and velocity changes $\bar{\vartheta}$. We can now use it for the field application in the next section. For the inversion purpose in which the monitor traces usually carry the time-shifts and amplitude changes from a constant baseline, I rewrite Equation 6.22 as:

$$b(t_i) \approx m\left(t_i - \Delta t_i\right) - \frac{1}{2}\psi * \left(\Delta R_i\right)'. \tag{6.23}$$

6.2.2 Shearwater wavelet extraction

The wavelet needs to be known before carrying out the waveform inversion. The procedure of extracting the wavelet is described in detail in Rangel (2016)'s study with the availability of the extracted wavelet for Sheawater field over the an interested interval from the top overburden (Top-Hod) to base underburden (Top-Triassic) based on both seismic and well information (Figure 6.6). After satisfactory analysis, I will use the extracted wavelet from Rangel's study. The dominant frequency of Shearwater wavelet is about 18Hz and is displayed in Figure 6.5.

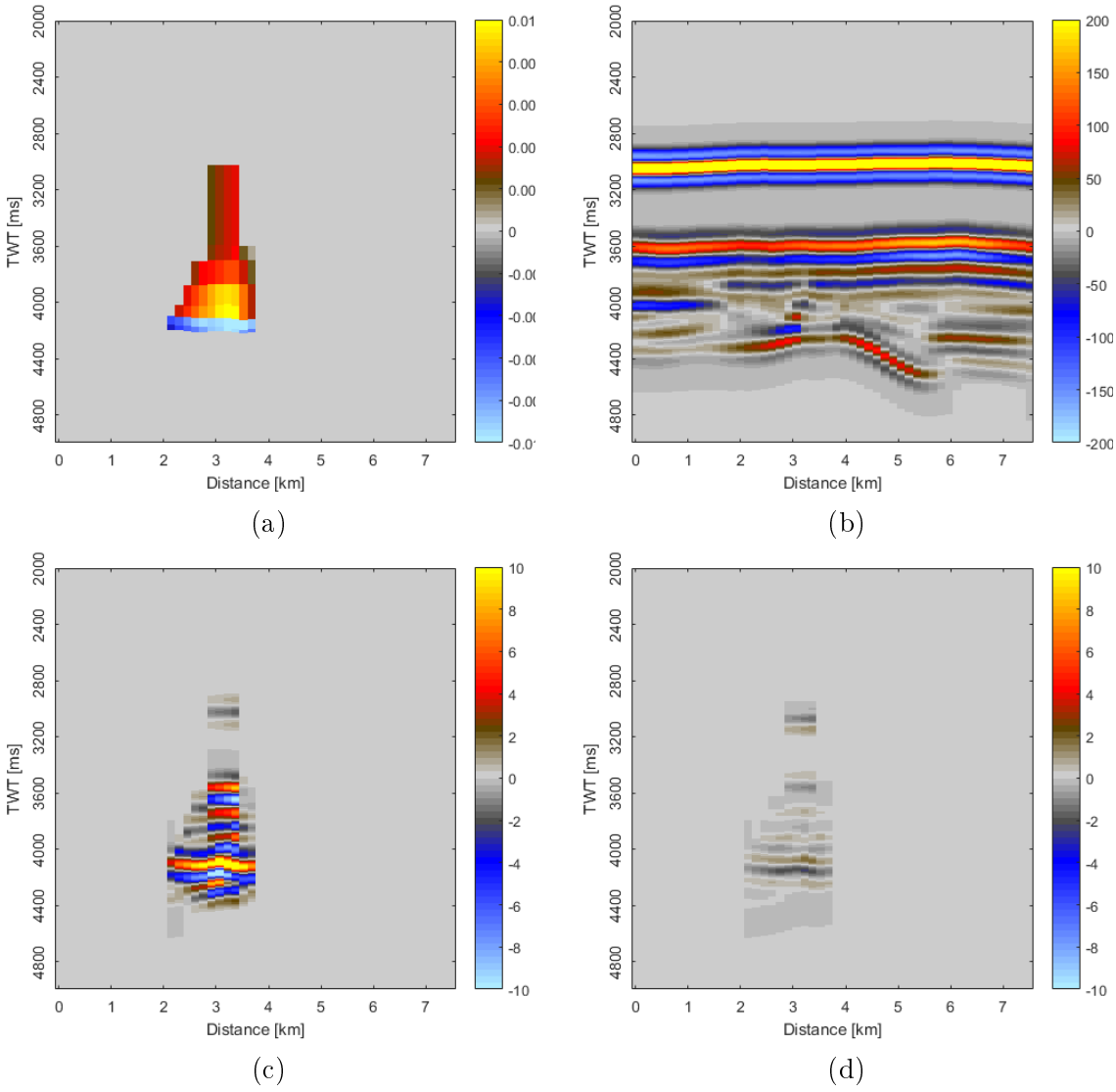

Figure 6.4: Comparison of the numerical test with analytical Equations 6.22. (a) Given velocity changes, I generate (b) synthetic monitor $m(t)$ and (c) is the 4D synthetic difference seismic. Following the workflow in Figure 7.1, reconstructing $m1(t)$ using the re-derived Williamson Equation 6.22, (d) shows the residual between the numerical $m(t)$ and analytical $m1(t)$. The residual is very small compared to the input 4D seismic (at the same color bar scale) and almost negligible compared to (b). Note that the color bar in (d) is shown 20 times smaller than in (b).

6.2.3 Incorporation of GMM into Williamson waveform inversion

Here, I develop Williamson's method by implementing the GMM introduced in Chapter 2 to represent $\bar{\vartheta}$ so that the inversion will be more stable and robust. Substituting Equation (2.20) and (2.21), which are respectively:

$$\vartheta(\bar{t}_i) = \sum_{j=1}^{ng} w_j \mathbf{G_j}, \tag{6.24}$$

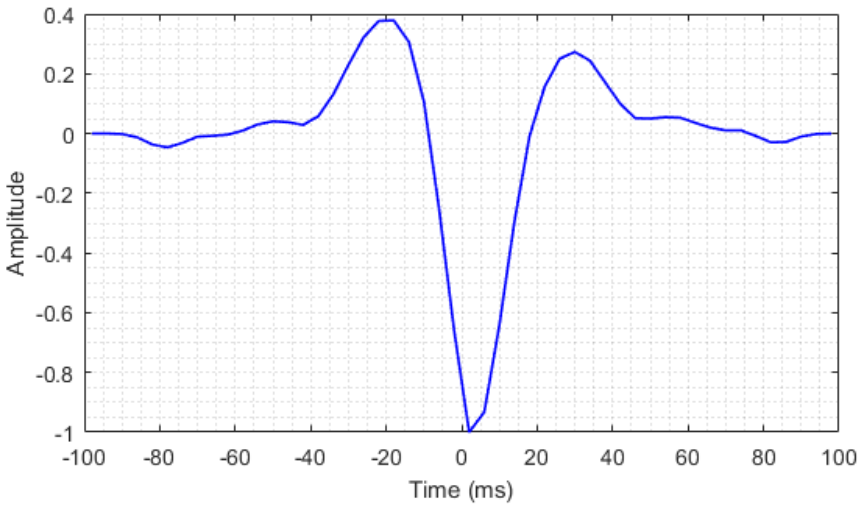

Figure 6.5: Shearwater extracted wavelet from Rangel (2016) with the dominant frequency of 18Hz.

and

$$\Delta t_i = \sum_{j=1}^{ng} w_j \mathbf{E_j}, \tag{6.25}$$

into Equation 6.23, we have:

$$b(t_i) = m\left(t_i - \sum_{j=1}^{ng} w_j \mathbf{E}_j\right) - \frac{1}{2}\psi * \left(\sum_{j=1}^{ng} w_j \mathbf{G_j}\right)'. \tag{6.26}$$

The optimization equation is then:

$$\min \left\| m\left(t_i - \sum_{j=1}^{ng} w_j \mathbf{E}_j\right) - \frac{1}{2}\psi * \left(\sum_{j=1}^{ng} w_j \mathbf{G}_j\right)' - b(t_i) \right\|_2. \tag{6.27}$$

Having Equation 6.27, an optimization method can be applied to seek to minimise the differences between the left-hand-side and right-hand-side of the equation and solve for coefficients, w_i, instead of the $\bar{\vartheta}$ directly as in Williamson's objective function (Equation 6.5). The $\bar{\vartheta}$ can be recovered following Equation 6.24. This is a non-linear inversion and I here use the iterative Gauss-Newton optimization algorithm, which is the same as NLI time-shift estimation (Rickett et al., 2007) (Appendix A). Hodgson (2009) programmed this NLI algorithm for time-shift estimation in Matlab. I develop this NLI time-shift estimation Matlab script to simultaneously incorporate the GMM implementation and amplitude change term. Thus, both time-shifts and amplitude changes are taken into account in this waveform inversion to invert for the coefficients, w_i, via GMM implementation.

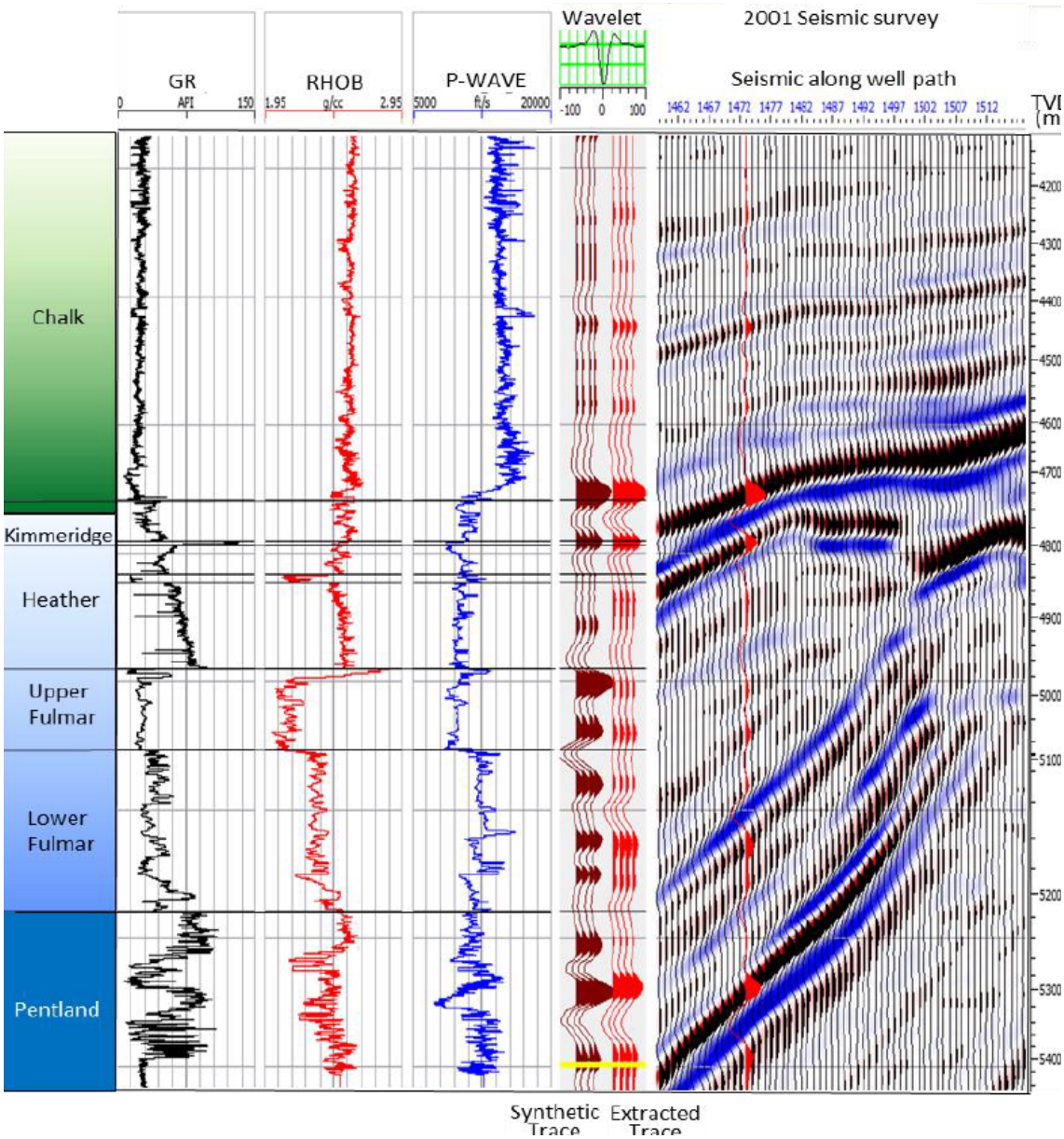

Figure 6.6: Well tie showing part of Shearwater architecture. After Rangel (2016).

As mentioned in Chapter 2 for post-stack time-shift inversion, choosing an appropriate Gaussian grid is the critical step in this GMM method. Here, I use the same Gaussian grid $(30, 30)$. The algorithm quickly converges after 3 or 4 iterations. Figure 6.7 shows the final results of velocity changes, $\bar{\vartheta}$, from integrating Gaussian reconstruction into a non-linear inversion scheme (b) and from Williamson's method (c) in compared with the inverted velocity changes from NLI time-shift data (a). Overall, these two $\bar{\vartheta}$ solutions (b and c) are able to preserve the subsurface velocity changes. The recovered $\bar{\vartheta}$ from (b) is more stable and reliable than (c), especially in the overburden area with the speedup blob in red. The nature of amplitude attribute is to reflect the differences between the reflectivity in two adjacent interfaces (Evensen and Landrø, 2010). Compared with (c), (b) seems to provide sharper

local changes between the interfaces. Comparing with (a), even though the algorithm in (b) inverts directly from the baseline and monitor traces which include the amplitude changes, (b) does not seems to add more value in interpreting the velocity changes of the Shearwater field. This might suggest that the contribution of amplitude changes is quite small here compared with the time-shifts due to the strong geo-mechanical activity. Nevertheless, by using the waveform inversion, one can extract the velocity changes directly from the baseline and monitor seismic data without the need of measuring the time-shifts. Further, employing GMM into this scheme of Williamson's waveform inversion could help to stabilize the waveform inversion. This can be a robust alternative tool to FWI.

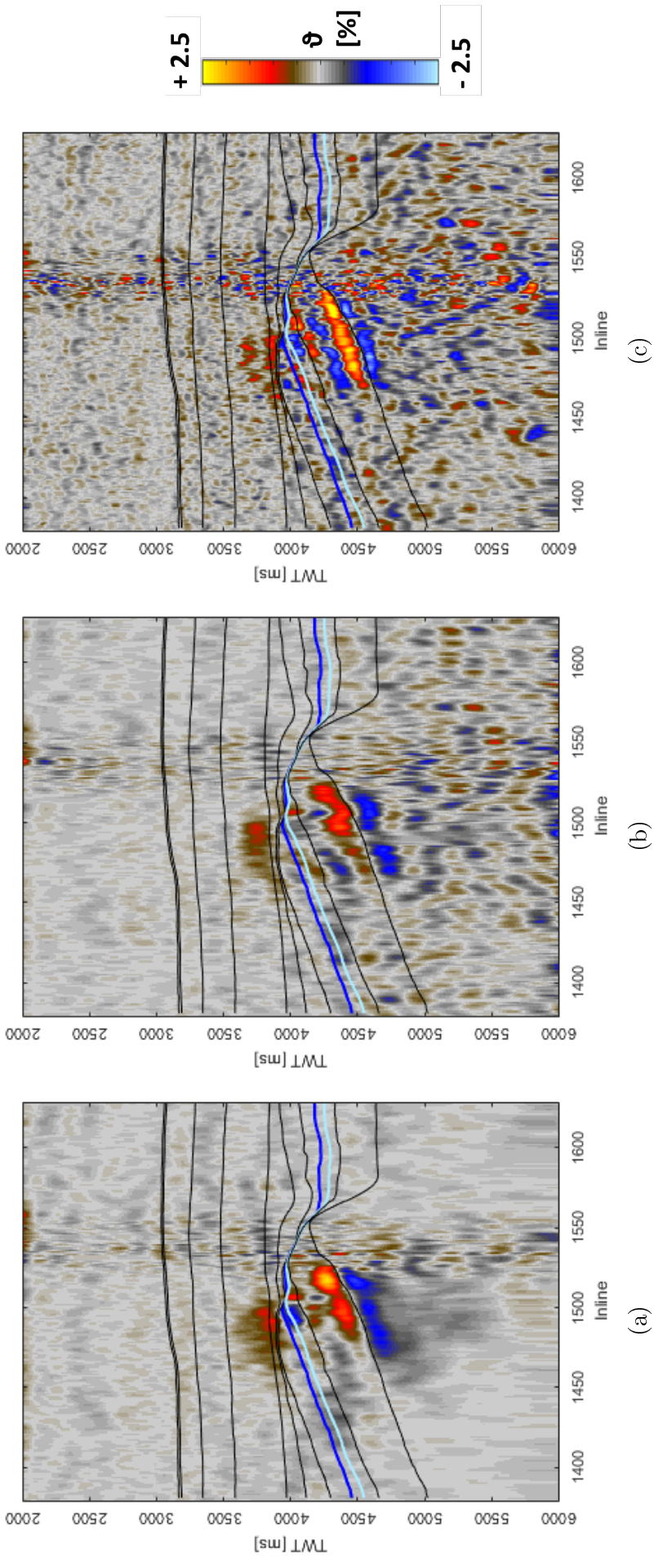

Figure 6.7: Recovered (a) ϑ from NLI time-shift inversion, (b) $\bar{\vartheta}$ from NLI waveform inversion incorporating GMM method and (c) $\bar{\vartheta}$ from Williamson's method using baseline 2002 and monitor 2004 of the Shearwater field. (b) and (c) invert for velocity changes using baseline and monitor seismic data directly meanwhile (a) uses time-shift data. In comparison with (c), (b) provides more stable and reliable recovered velocity changes thanks to incorporating the GMM, especially in the overburden area. In comparison with (a), (b) seems not to add more information even though the algorithm takes the amplitude changes into account.

6.3 Chapter conclusions

The role of the amplitude change attribute in time-lapse seismic studies is as important as the time-shifts. After pointing out the various applications of amplitude changes reported in the literature, I introduced a new and robust waveform inversion by integrating the GMM into Williamson's trace warping method. A revision, purposely focusing on the implementations of Williamson's warping method which were found to be cited differently in different studies, was provided together with my new derivation of Williamson's formulae (Equation 6.23). This helps to remove the unnecessary confusion and easily access into Williamson's warping method. I also performed the numerical modelling to verify the newly derived Williamson's equation before moving to the inversion step.

The recovered velocity changes $\bar{\vartheta}$ from the inversion method that incorporates the GMM shows that it is more stable and reliable compared with the original Williamson's method. With a new version of the Williamson trace warping merged with GMM, this waveform inversion can be a robust alternative to the complex and heavy FWI. Both time-shifts and amplitude change effects can be now simultaneously inverted to recover the subsurface changes during production. Even though for this field application, the contribution of the amplitude changes to the inverted velocity changes is not that trivial, the algorithm still does contribute a robust additional workflow in 4D seismic quantitative interpretation and analysis as mentioned in the first opening Chapter 1.

Chapter 7

Conclusions and future research

ABSTRACT

The three data-driven inversion methods for extracting time-lapse velocity changes performed robustly on the field data applications thanks to the simplicity of their analytical physical expressions and computational efficiency. This chapter summarises and reveals their properties and contributions to the topic of time-lapse velocity change estimation. However, there are limitations and weakness in their lack of geometrical constraints. These weaknesses are discussed in the further research and recommendations. The chapter then closes with final remarks about the research in this thesis.

7.1 Conclusions

The central theme of this thesis was the focus on developing a robust algorithm for estimating the time-lapse velocity change. This means not only in terms of a fast speed of computational time but also in term of light yet stable and efficient solutions. Exploring this theme, the works in this thesis have provided the potential solutions to overcome the four main challenges in 4D seismic described in Chapter 1. They are computational time, extending the solution of post-stack domain into angle-stack domain, overcoming the complexity of angle-stack domain and incorporating amplitude change as a local attribute in addition to time-shifts which are smooth due to their accumulative property.

In the world of estimating time-lapse velocity change methods that are accomplished by two themes – post-stack time-shifts and angle-stack time-shifts – the development through this work involves consideration of different inversion algorithms cast onto time-shift data or directly to seismic traces. These algorithms are expressed via analytical formulae (Gaussian-mixture-model, straight ray tomography, small ray-bending solution) with inversions that produce stable solutions and are computationally achievable as a means to overcome the more complex tomography problem. Figure 7.1 summaries the algorithms developed in this thesis and its application as well as contributions.

7.1.1 Post-stack time-shift inversion

The two selected methods, layer stripping and damped-least squares, are implemented and compared with a newly developed method of Gaussian reconstruction using a mixture of various Gaussian models. GMM is implemented by pre-setting the Gaussian grid defined by Gaussian width, σ, and spacing between two adjacent Gaussian, $d\mu$, and letting the algorithm search for only one variable of Gaussian weight, ω, that fits the data. Such implementation allows us to easily dial into this particular seismic problem yet provide efficient solutions. Among these three methods, GMM provides the most stable solutions of velocity changes regardless of which type of measured time-shifts used. Therefore, GMM is independent of time-shift measurement methods.

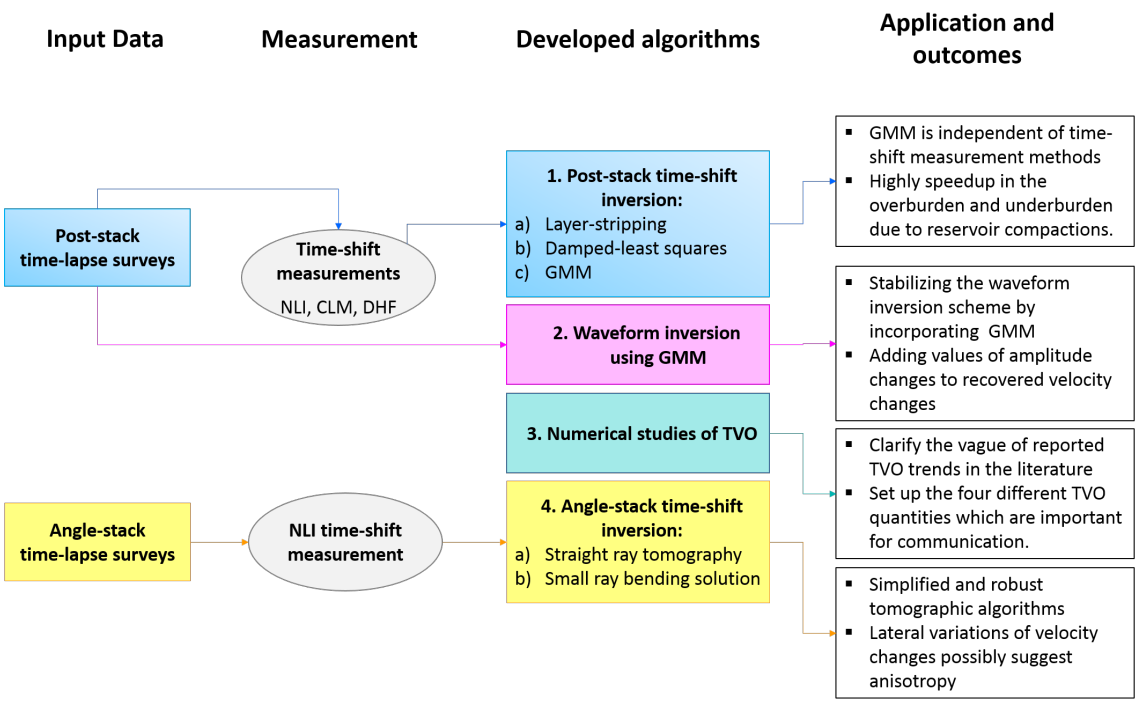

Figure 7.1: A summary of the work in this thesis and its application and contributions

Application of these three methods to recover the velocity changes from post-stack time-shift at Shearwater field indicates geo-mechanical effects in the overburden and underburden with speedup in the velocity changes about $0.5-1\%$ and $1.0-1.5\%$, respectively. Slowdown velocity changes is also observed in the reservoir due to depletion. Regarding the application in An'Teallach field, a slowdown of velocity changes is observed in the reservoir area which are in associated to the injected gas volume. It should be noted that when it comes to interpretation, it is important to be aware of the filter of Gaussian grids. In other words, the GMM method eliminates the noise and smooths the velocity changes' solutions depending on the chosen Gaussian grid. We can observe this effect in the small field example in Chapter 2 for An'Teallach case study. Besides that, it is also necessary to be aware of the possible errors in time-shift measurement methods and the affects of time-lapse seismic processing as discussed in Chapter 1.

7.1.2 Angle-stack time-shift inversion

In terms of angle-stack time-shift inversion, the straight ray tomography method is developed at a constant incident angle by implementing the re-gridding technique, which allows us to access into various incident angles yet keep the same algorithm

throughout. Additionally, an analytical derivation of a small ray bending solution is also provided to examine the sensitivity of the straight ray assumption.

7.1.3 Post-stack waveform inversion

Sensible time-lapse amplitude change attributes are treated by incorporating a mixture of Gaussian basis functions which helps to stabilize the waveform inversion. Simultaneous inversion of both time-lapse seismic attributes, time-shifts and amplitude changes, provides a fast track to recover time-lapse velocity changes and helps to avoid inevitable time-shift measurement methods when these two attributes are treated separately.

7.1.4 Time-shift versus offset

Beside the work of implementing and developing the time-lapse velocity change estimation methods, in Chapter 3, a critical revision of TVO helps to clear out the vagueness of reported TVO behaviours thanks to our classification scheme. The underlined physical model and which type of data is used (before or after NMO correction) are carefully considered while doing the analysis on the proposed analytical formulae in the literature. Further, by setting up the four quantities of $rTVO_x$, $aTVO_x$, $rTVO_0$ and $aTVO_0$, the common observations among these studies arose. For the reservoir compaction scenario, $rTVO_0$, $aTVO_0$ and $aTVO_x$ increased whilst $rTVO_x$ decreased for most of the cases. The exceptions fall into the observed TVO such as a decrease $aTVO_{0-presumably}$ reported at the South Arne - chalk field or insignificant $aTVO_{0-presumably}$ in the Shearwater and Mars fields.

Numerical examples of TVO over different models are also presented in the TVO study in this thesis. The numerical results are in line with the proposed analytical calculations by Landrø and Stammeijer (2004), Røste et al. (2007) and Hawkins et al. (2007). Small velocity and thickness changes, 0.5% and 0.1%, respectively, lead to quite large time-shifts, $10ms$. Additionally, the straight ray assumption is also examined in comparison with bending rays for a two-layer model before implementing into the time-lapse straight ray tomography. The examination indicates that the straight ray assumption breaks down at very large offset, over $3800m$. In

Chapter 5, the modelling angle-stack time-shift using straight ray tomographic forward operator shows small TVO among Near, Mid and Far. This small TVO is in line with the observed time-shifts of the same field dataset - Shearwater.

To sum up, here are general advantages of all the developed inversion methods in this thesis.

- Data-driven, no need of a prior model to train the inversion.
- Direct inversion with only one unique solution (Layer stripping method in Chapter 2, straight-ray tomography in Chapter 5). Or the inversion is quickly converged after about 3-5 iterations (waveform inversion method in Chapter 6).
- Regarding the Gaussian reconstruction method using GMM, pre-setting the Gaussian grid is simple with only one variable parameter yet efficient enough. This allows for the sensitivity analysis to be carried quickly.
- Inversion algorithms can be adapted to various domain, either post-stack time-shifts, post-stack seismic (time-shifts and amplitude changes) or pre-stack time-shifts (angle-stack).

7.2 Limitations and recommendations for further researches

The limitation of these developed methods are addressed as follows:

- Not taken into account the benefits of available prior information (e.g. well data).
- The methods are not constrained by the geology. As we experienced in An'Teallach field application, even though GMM provides more stable results, it is not necessarily the best solution when interpreting in a geological context. Therefore, a better criteria can be further developed so that the Gaussian grid can be tailored satisfactorily to a geological context, and hence the dominant wavelength can be taken into account.

- The direct inversion of developed time-lapse straight tomography might bring errors, especially at Far angle-stack.
- While comparing different methods to invert for the velocity changes helps to bring the insight of each method, it is useful to bring more information to better understanding the application field, for example the geomechanical modelling. The modelled time-strain from this modelling will further help to interpret the inverted velocity changes.

In terms of further directions of the work in this thesis, the world of pre-stack time-lapse seismic will be the only direction. While the seismic survey are acquired from vary distances between sources and receivers, moving to pre-stack seismic is a nature process which helps to reveal the subsurface at a more complete picture from the 80% solution of post-stack time-lapse seismic. Figure 7.2 suggests the work-flow of extracting the time-lapse velocity changes and their contributions to time-lapse seismic analysis and interpretation.

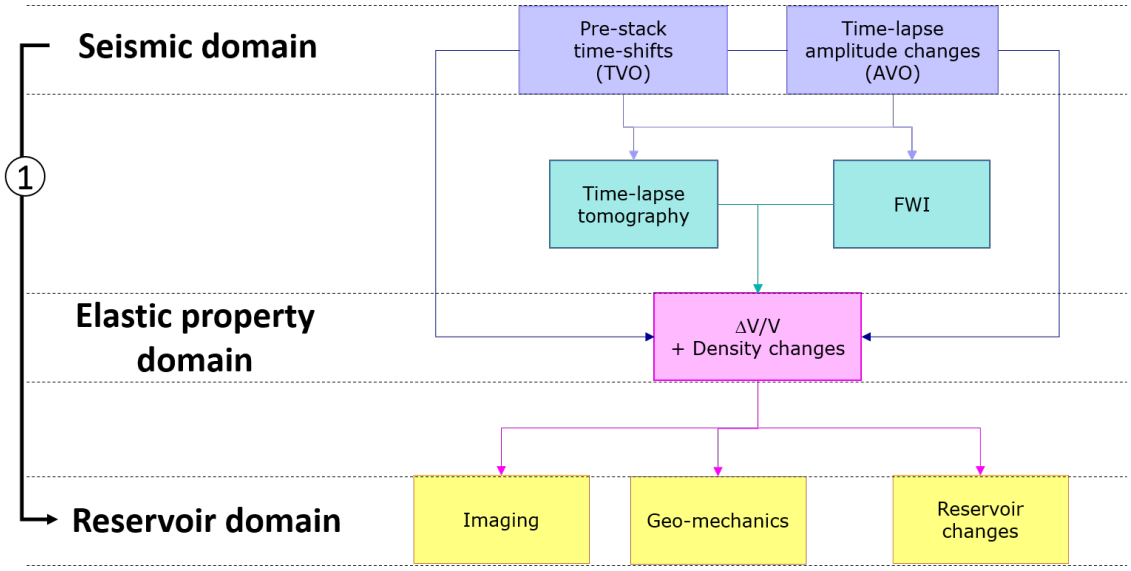

Figure 7.2: The workflow of inverting the time-lapse seismic attribute for the elastic (velocity) changes and reservoir parameters.

- From pre-stack time-shift, time-lapse reflection tomography still continues to be a trend as it provides a cheap choice of low resolution. Beyond that, time-lapse FWI with higher resolution.
- Imaging consistency which takes into account the ray bending and seismic waves could be also a possible option.
- Time-lapse density changes can be also integrated into recovering time-lapse

velocity changes.

- Further than that, the time-lapse velocity changes can be directly estimated from pre-stack time-lapse seismic data in which not only time-shift versus offset, TVO, but also amplitude changes versus offset, AVO. Together with thee growth of machine learning recently, implementing of basis functions (e.g. Gaussian) to parameterize the model might be a good option to stabilize the inversion algorithm.

- Consequently, the recovered velocity changes opens the door to seismic imaging and interpretation for both reservoir (fluid saturation, pressure changes) and its surrounding areas (e.g. geo-mechanics).

- Beyond going through the elastic domain, setting a direct inversion from seismic domain to reservoir domain without going through the velocity and/or density changes could also be a future direction (Figure 7.2- route 1).

7.3 Final remarks

The work in this PhD research has arisen from the awareness of the expansion of time-lapse seismic, which has been able to provide high time-lapse quality data with the availability of various angle-stacks. The scientific questions of finding a fast track to invert these dataset for the elastic changes have been addressed and motivated in this research to explore different domains in a light, simplified yet efficiently fashion. The topic of estimating time-lapse velocity changes from time-lapse seismic data, or shortly - inversion, is indeed challenging, especially when looking at a simplified tomographic solution for angle-stack time-shifts. However, challenges always come together with the opportunities to explore, to learn, to push the boundaries of science and finally the nature of each developed methods is revealed. Even though we are still confronted with challenges ahead, I do hope that this PhD research can inspire the further studies towards better imaging yet simple and light solutions.

Appendix A

Gauss-Newton iteration

Here I describe in detail the iterative Gauss-Newton algorithm employed by Hodgson (2009) to invert for time-shift $\tau(t)$ from the baseline $b(t)$ and monitor traces $m(t)$. The objective function is written as:

$$\min ||m(t+\tau(t)) - b(t)||_2 . \tag{A.1}$$

This is an iterative algorithm. It finds the values of the variable τ which minimizes the sum of the square (or also called as L-norm $||.||_2$) of the objective function A.1. Given an initial guess, this is done by solving a linear system of equations at each iteration as:

$$(J^T J)\Delta\tau = -J^T r. \tag{A.2}$$

where J is Jacobian matrix, which linearises the above non-linear problem, symbol ^{T} denotes the matrix transpose, $\Delta\tau$ and r are the updated τ and residual vector at that iteration. The residual r is the differences between two seismic traces $m(t+\tau)-b(t)$. The Jacobian matrix is calculated by taking the derivative of the residual r with respect to the variable τ. Due to independence of function $b(t)$ to variable $\tau(t)$, the Jacobian matrix in this case is:

$$J_{ii} = \left.\frac{\partial m(t+\tau(t))}{\partial t}\right|_{t=t_i+\tau_i^{(0)}}, \tag{A.3}$$

where i is the index of the sample number. Because of the non-uniqueness of this non-linear problem, the study also regularise the problem and a final solution is

provided as:

$$\Delta\tau = (A^T A)^{-1} A^T b, \tag{A.4}$$

where

$$A = J_k^T J_k + \alpha^2 \Gamma^T \Gamma, \tag{A.5}$$

and

$$b = -J_k^T r - \alpha^2 \Gamma^T \Gamma \tau^k. \tag{A.6}$$

where k denotes the iteration step, α is a regularisation factor and Γ is second order Tikhonov operator.

Appendix B

Three selected time-shift measurement methods

B.1 Dave Hale's fast cross correlation - Hale (2009)

Cross-correlation method has been widely used in estimating time delaying between two or more received signals (Piersol (1981)). It measures the similarity of baseline $b(t)$ and monitor $m(t)$ traces, in which $m(t)$ is a function of $b(t)$ and time-shift Δt:

$$m(t) = b(t + \Delta t). \tag{B.1}$$

Hale (2009) speeded up this standard cross correlation by 'firstly computing for each image sample a local phase correlation instead of a local cross correlation'. The method calculates three displacement components simultaneously, vertical time-shift, inline and crossline lateral time-shifts. Also, the method warps the two seismic images instead of the seismic traces. Give two seismic images $f[j]$ and $g[j]$, they are related as:

$$m[j] = b(j + \tau[j]). \tag{B.2}$$

where $\tau[j] \equiv (\tau_1[j], \tau_2[j])$ represents a sampled displacement vector field with both vertical (τ_1) and horizontal (τ_2) components of displacement.

In order to estimate the displacement vectors τ, the method searches for locations

of peaks of local crosscorelations, defined for two images m and b by:

$$c_{mb}[k,l] \equiv \sum_j f[j]g[j+l] \times w[k-j], \tag{B.3}$$

where

$$w[k] \equiv e^{-k.k/2\sigma^2}. \tag{B.4}$$

is a Gaussian window for some specified radius σ, c_{mb} is a correlation image, $l = [l_1, l_2]$ (or $[l_1, l_2, l_3]$) is lag indices for each set and k is indexed sample. In other words, Equation B.3 implies that for each set of lag indices l, the equation computes a local crosscorrelation value for every image sampled indexed by k.

The Gaussian window w makes the crosscorrelation local. Therefore, there might be sensitive to local amplitude variations. To help avoiding this issue, the method normalizes the local crosscorrelation in Equation B.3 as:

$$c[kl] \equiv \frac{c_{mb}[k,l]}{\sqrt{c_{mm}[k,0]\sqrt{c_{bb}[k+l,0]}}}, \tag{B.5}$$

where

$$c_{mm}[k,0] \equiv \sum_j m^2[j]w[k-j], \tag{B.6}$$

and

$$c_{bb}[k,0] \equiv \sum_j b^2[j]w[k-j]. \tag{B.7}$$

To obtain the more accurate and stable results, the method also uses whitening (local prediction error filters) and low-pass Gaussian smoothing filters to improve the spatial resolution before the crosscorrelation in together with the iterative cyclic search until reach the minimum errors. This method provides a robust measurement for time-shifts. However it depends very much on the window size and signal to noise level. In the case of large shifts or rapid changes in space and time, Hale (2013) introduced dynamic imaging warping method which provides more robust and reliable time-shifts against other cross-correlation methods by using a global solution.

B.2 Correlated Leakage Method - Whitcombe et al. (2010)

In order to overcome the shortcomings of cross-correlation based methods in small window size, Hatchell et al. (2003) measured time-shifts using 1^{st} order Taylor expansion. Naeini et al. (2009) extended this method to Lagrange multiplier optimization and so called Lagrange-Taylor methods to find a unique time-shift and then applied for multiple vintages simultaneously. Whitcombe et al. (2010) introduced Correlated Leakage Method (CLM) by also employing Taylor series expansion and fitted to the cross-plot.

Assuming $M = f(t)$ is a shifted version of $B = f(t)$ and the amplitude and waveform changes between baseline and monitor is negligible, a Taylor series expansion on $X-$ and $Y-$axes can be approximated as:

$$\begin{aligned} Y &= M - B \\ &= f(t+a) - f(t) \\ &\approx [f(t) + af'(t)] - f(t) \\ &= af'(t). \end{aligned} \tag{B.8}$$

$$\begin{aligned} X &= \frac{1}{2}(B+M)_{i+1} + \frac{1}{2}(B+M)_i \\ &= \frac{1}{2}[f(t+\Delta t) + f(t+\Delta t+a)] - \frac{1}{2}[f(t) + f(t+a)] \\ &\approx \frac{[f(t) + \Delta t f'(t) + f(t+a) + \Delta t f'(t+a)] - [f(t) + f(t+a)]}{2} \\ &= \frac{\Delta t f'(t) + \Delta t f'(t+a)}{2} \\ &\approx \frac{\Delta t f'(t) + [\Delta t f'(t) + a\Delta t f''(t)]}{2} \\ &\approx \Delta t f'(t). \end{aligned} \tag{B.9}$$

where Δt is a user defined time-shift applied to the average, $f'(t)$ is the time derivative, $f''(t)$ is the second derivative of $f(t)$. Y is amplitude difference between baseline and monitor. $X-$axis is amplitude difference between the baseline and monitor average and a time shifted version of this average. Placing these two X and Y term

on a cross plot yields and a is the time-shift to be estimated

Having these two equations, a cross-plot (Ji, 2017) summaries the work-flow of this method as in Figure B.1.

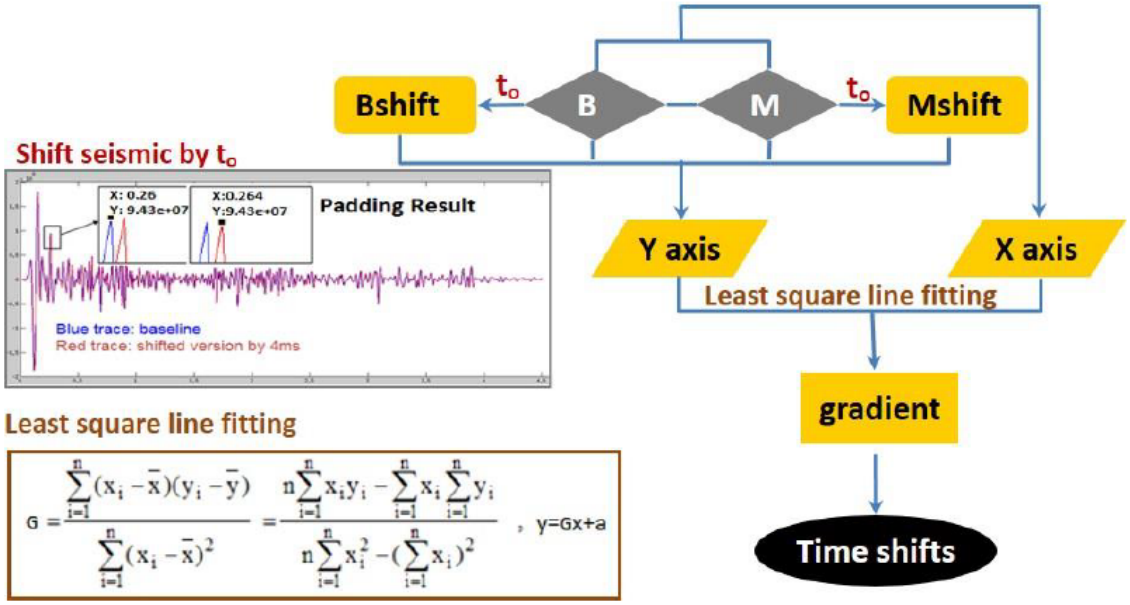

Figure B.1: The workflow of the Correlated Leakage Method. After Ji (2017).

This is also window-based method but proposed as more stable than cross-correlation. The method works well for small time-shifts and amplitude changes between the baseline and monitor survey.

B.3 Non-linear inversion - Rickett et al. (2007)

The above methods are window-based hence their solutions depend on the choice of window size. Rickett et al. (2007) introduced an objective function that matches the time-shifted baseline to monitor trace. The objective function is then minimised by least square solution in Gaussian-Newton fashion and is added smooth constraints help to stabilize the inverted time-shifts:

$$OF_{Rickett-2007} = \mid b(t) - m(t+\tau(t)) \mid^2 + \alpha \mid \bigtriangledown_x \tau(t) \mid^2 + \beta \mid \bigtriangledown_y \tau(t) \mid^2 + \gamma \mid \bigtriangledown_t \tau(t) \mid^2 \tag{B.10}$$

where $\tau(t)$ is the time-shift function, α, β, γ are smooth weights and $\bigtriangledown$ indicates Laplacian operator with the subscript x, y, t represent spatial and time constraints, respectively. Appendix A mathematically explained this algorithm.

NLI results are usually smoother than the other two methods because of the global solution where the entire trace is taken into account rather than finding a solution at a specific window and also because of the additional constraint terms.

Appendix C

Analytical derivation of time-shift versus offset

This appendix summaries the main derivation step of time-shift versus offset presented in Landrø and Stammeijer (2004). Starting the standard kinematic equation for a single horizontal layer of thickness z, velocity V at offset x:

$$t_x = \sqrt{\frac{(2z)^2}{V^2} + \frac{x^2}{V^2}}. \tag{C.1}$$

where t_x denotes the two-way traveltime at a given offset x.

Assuming small changes in thickness and velocity, where $\Delta z/z$ and $\Delta V/V << 1$, taking the differentials to the first order and rearranging, we have:

$$\frac{\Delta t_x}{t_x} = \frac{t_0^2}{t_x^2}\frac{\Delta z}{z} - \frac{\Delta V}{V} \tag{C.2}$$

where Δt_x is time-shift at offset x and t_0 is normal-incidence two-way traveltime (at zero-offset). Applying NMO correction equation for a constant-velocity case, which is:

$$t_x^2 = t_0^2 + \frac{x^2}{V^2}, \tag{C.3}$$

or

$$\frac{t_x}{t_0} = \sqrt{1 + tan^2\theta}, \tag{C.4}$$

where

$$tan\theta = \frac{x}{Vt_0}, \tag{C.5}$$

and NMO stretch effect, which is NMO derivation:

$$\frac{dt_x}{dt_0} = \frac{t_0}{t_x}, \tag{C.6}$$

we can mathematically express as:

$$\left(\frac{dt_x}{tx}\right)_{beforeNMO} = \frac{dt_x}{dt_0}\left(\frac{dt_0}{t_0}\right)_{afterNMO}\frac{t_0}{t_x}. \tag{C.7}$$

With Equation C.6, we obtain:

$$\frac{dt_x}{t_x} = \frac{t_0^2}{t_x^2}\frac{dt_0}{t_0}. \tag{C.8}$$

Approximating the change in Equation C.2 by a differential and using C.4 yields the final result of time-shift versus offset after NMO correction:

$$\frac{\Delta t_0(\theta)}{t_0} = \frac{\Delta z}{z} - (1 + tan^2\theta)\frac{\Delta V}{V}. \tag{C.9}$$

NMO stretching effect

Having the above NMO correction equation C.4, the NMO correction amount can be easily calculated by the difference between t_x and t_0 as:

$$\Delta t_{NMO} = t_x - t_0. \tag{C.10}$$

Using equation C.3, we have:

$$\Delta t_{NMO} = t_0\left(\sqrt{1 + \left(\frac{x}{t_0 V_{NMO}}\right)^2} - 1\right) \tag{C.11}$$

Obviously, the NMO correction increases with offset x and decreases with zero-offset (or vertical) traveltime t_0. Noted that the values of a single trace at a certain offset are shifted with different amounts. This leads to the stretching of the data as an

artificial increase of the wavelength as in Figure C.1.

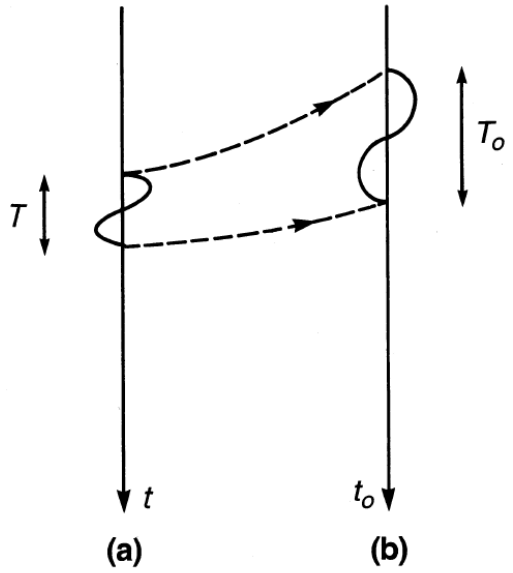

Figure C.1: A signal (a) with a period of T is stretch to a signal (b) after NMO correction (after Yilmaz (2001)).

This NMO stretch happens particularly at large offset x and shallow events (small t_0). The stretching is quantified as:

$$\frac{\Delta f}{f} = \frac{\Delta t_{NMO} t_0}{.} \tag{C.12}$$

where f is dominant frequency and Δf is the change in thee frequency. In the conventional seismic processing work-flow, this stretching effect is removed by applying the muting technique using threshold stretch limits of 50 and 100 % after the NMO correction.

Appendix D

Small ray bending solution

D.1 Analytical derivation

The fact that velocity changes from a homogeneous baseline velocity model to a perturbed velocity of monitor, the ray image is also bent from the straight path. In order to estimate how sensitive the straight assumption is, this section introduces a small ray-bending solution in analytical form. Time-shift is now re-defined for a one-layer model for the sake of simplicity as:

$$\Delta t = \frac{L + \delta L}{V + \Delta V} - \frac{L}{V}. \tag{D.1}$$

where δL represents a small change in the ray-path length and δV is the small difference between two adjacent cells. Assuming the ray travels at a certain incident angle θ and given a vertical length h, this length difference can be calculated as :

$$\delta L = \frac{h}{cos(\theta + \delta\theta)} - \frac{h}{cos\theta} \tag{D.2}$$

$$= \frac{h}{cos\theta cos\delta\theta - sin\theta sin\delta\theta} - \frac{h}{cos\theta} \tag{D.3}$$

$$= \frac{h}{cos\theta - \delta\theta sin\theta} - \frac{h}{cos\theta} \tag{D.4}$$

$$= \frac{h}{cos\theta}\left(\frac{1}{1 - \delta\theta tan\theta} - 1\right). \tag{D.5}$$

Replacing

$$L = \frac{h}{cos\theta}, \tag{D.6}$$

and apply 1st Taylor approximation for $\frac{1}{1-x} \approx 1+x$, Equation D.5 can be rewritten as:

$$\frac{\delta L}{L} \approx \delta\theta tan\theta. \tag{D.7}$$

Here I find the form for $\delta\theta$. Re-writing the Snell's law, which is:

$$\frac{sin\theta_1}{V_1} = \frac{sin\theta_2}{V_2}, \tag{D.8}$$

into this case, it becomes:

$$\frac{sin\theta}{V} = \frac{sin(\theta+\delta\theta)}{V+\delta V}. \tag{D.9}$$

where $\delta V = \Delta V_2 - \Delta V_1$. For a very small $\delta\theta$, we apply these two approximations:

$$sin(\delta\theta) = \delta\theta, \tag{D.10}$$

and

$$cos(\delta\theta) = 1, \tag{D.11}$$

into Equation D.9, we have:

$$\frac{sin\theta}{V} \approx \frac{sin\theta + \delta\theta cos\theta}{V+\delta V}, \tag{D.12}$$

$$\frac{V}{sin\theta} \approx \frac{V(1+\frac{\delta V}{V})}{sin\theta + \delta\theta cos\theta}, \tag{D.13}$$

$$1 + \frac{\delta V}{V} \approx 1 + \delta\theta cot\theta, \tag{D.14}$$

$$\delta\theta \approx \frac{\delta V}{V} tan\theta. \tag{D.15}$$

Replacing the Equation D.15 and D.7 into Equation D.1, we get:

$$\Delta t = \frac{L}{V}\left(\frac{1+\frac{\delta L}{L}}{1+\frac{\Delta V}{V}} - 1\right), \tag{D.16}$$

$$\Delta t = \frac{L}{V}\left(\frac{1+tan^2\theta\frac{\delta V}{V}}{1+\frac{\Delta V}{V}} - 1\right), \tag{D.17}$$

and using

$$t = \frac{L}{V}, \tag{D.18}$$

The final equation for time-shift estimation from a small ray-bending solution for a one-layer medium is:

$$\Delta t = \vartheta_b t, \tag{D.19}$$

where ϑ_b indicates the velocity changes for small ray-bending:

$$\vartheta_b = \frac{1 + tan^2\theta \frac{\Delta V}{V}}{1 + \frac{\delta V}{V}} - 1. \tag{D.20}$$

In this small ray-bending solution, the velocity change $\Delta V/V$ is estimated through quantity ϑ_b instead of ϑ to achieve the best accuracy. $\Delta V/V$ can be solved as:

$$\frac{\Delta V}{V} = \frac{\vartheta_b}{\vartheta_b + 1 - tan^2\theta}. \tag{D.21}$$

At zero-offset, $\theta = 0$ hence $tan^2\theta = 0$ and $\vartheta_b = \vartheta$. Extending the equation D.19 to multiple layers by taking the integral, the final equation that relates time-shift and velocity changes for small ray-bending is:

$$\Delta t = \int_0^t \vartheta_b dt. \tag{D.22}$$

Having a new analytical form for time-shifts as equation D.19, a new corresponding tomographic matrix for the small bending-ray solution $\mathbf{A_b}$ can be set up after another few more steps to find out the additional term. Figure D.1 illustrates how the ray is bent when it hits the interfaces an incident angle θ_2 from the reflection point of bottom base of the grey cell (cell 2) to the pink cell (cell 1) on the left and to the light blue cell (cell 3) on the right.

The velocity and incident angle perturbation of cell 1 to cell 2 are assigned to δV_{12} ($\delta V_{12} = \Delta V_2 - \Delta V_1$) and $\delta\theta_{12}$ quantities. Note that V_2 in this context means ($V_{baseline}$+ΔV_2) where ΔV_2 is the time-lapse velocity change. Hence, this $\delta\theta_{12}$ implies the perturbation of two monitor velocity cells, which equals to ($\Delta V_2 - \Delta V_1$). The same translation applies for δV_{32} and $\delta\theta_{32}$ quantities. Finally, the dimensionless

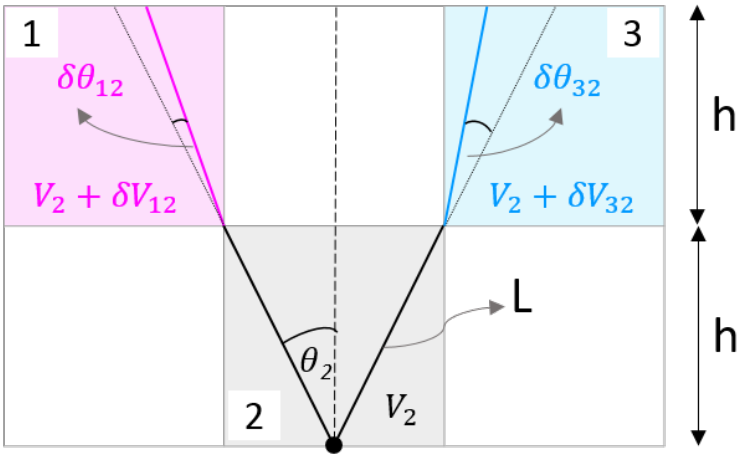

Figure D.1: Schematic of small ray-bending solution

time-shifts in this example can be then estimated from equation D.17 as:

$$\frac{\Delta t}{t} = \left(\frac{1 + tan^2\theta\frac{\delta V_{12}}{V}}{1 + \frac{\Delta V_1}{V}} - 1\right) + 2\left(-\frac{\Delta V_2}{V}\right) + \left(\frac{1 + tan^2\theta\frac{\delta V_{32}}{V}}{1 + \frac{\Delta V_3}{V}} - 1\right), \tag{D.23}$$

$$\frac{\Delta t}{t} = \left(\frac{1 + tan^2\theta\frac{\Delta V_1 - \Delta V_2}{V}}{1 + \frac{\Delta V_1}{V}} - 1\right) + 2\left(\frac{\Delta V_2}{V}\right) + \left(\frac{1 + tan^2\theta\frac{\Delta V_3 - \Delta V_2}{V}}{1 + \frac{\Delta V_3}{V}} - 1\right). \tag{D.24}$$

Rearranging and approximating this equation, it becomes:

$$\Delta t = -(1 - tan^2\theta)\frac{\Delta V_1}{V} - (2 + 2tan^2\theta)\frac{\Delta V_2}{V} - (1 - tan^2\theta)\frac{\Delta V_3}{V}. \tag{D.25}$$

From here, we can separate Equation D.25 into two terms as:

$$\Delta t = \left[-\frac{\Delta V_1}{V} - 2\frac{\Delta V_2}{V} - \frac{\Delta V_3}{V}\right] + tan^2\theta\left[\frac{\Delta V_1}{V} - 2\frac{\Delta V_2}{V} + \frac{\Delta V_3}{V}\right]. \tag{D.26}$$

where the first term is for the straight-ray and the second term is the additional term for the small ray bending solution. The ϑ_b is now approximated as $\bar{\vartheta}_b \approx -\Delta V/V$. Circulating Equation D.19 to three and four and more layers, we can see the pattern for each case of Far, Mid and Near. The additional terms for Far, Mid and Near are described respectively as follows in corresponding to the $\mathbf{A_F}$, $\mathbf{A_M}$ and $\mathbf{A_N}$ straight ray tomographic matrices for 5 first layers as presented above in Equation 4.12,

Equation 4.13 and Equation 4.14, respectively:

$$\mathbf{A_F^{add}} = tan^2\theta \begin{bmatrix} & & & & 0 & & & & \\ & & & -1 & 2 & -1 & & & \\ & & -1 & 0 & 2 & 0 & -1 & & \\ & -1 & 0 & 0 & 2 & 0 & 0 & -1 & \\ -1 & 0 & 0 & 0 & 2 & 0 & 0 & 0 & -1 \end{bmatrix} \tag{D.27}$$

$$\mathbf{A_M^{add}} = tan^2\theta \begin{bmatrix} & & & & 0 & & & \\ & & & -2 & 2 & & & \\ & & -1 & 0 & 2 & 1 & & \\ & -1 & 1 & 0 & 2 & 0 & -1 & \\ -1 & 0 & 0 & 0 & 2 & 0 & 0 & -1 \end{bmatrix} \tag{D.28}$$

$$\mathbf{A_N^{add}} = tan^2\theta \begin{bmatrix} & & 0 & & & \\ & & -2 & 2 & & \\ & & -2 & 0 & 2 & \\ & & -2 & 0 & 0 & 2 \\ & -1 & 0 & 0 & 0 & 2 & -1 \end{bmatrix} \tag{D.29}$$

The final tomographic matrices for small ray bending solutions are then:

$$\mathbf{A_b} = \mathbf{A} + \mathbf{A^{add}}. \tag{D.30}$$

where $\mathbf{A^{add}}$ ($\mathbf{A_F^{add}}$, $\mathbf{A_M^{add}}$ or $\mathbf{A_N^{add}}$) is the additional matrix to the straight ray tomographic matrix $\mathbf{A}$ for the small ray bending solution. It should be noted that this small bending solution does not strictly follow Snell's law for the entire ray-path but rather alternates around the exploded incident angle. For example, after exploding from a constant incident angle θ at the third layer and being bent at the adjacent second layer, this bent ray in the second layer is forced to get back to the same exploded incident angle as in the third layer before entering the first layer.

Thus, in this small ray bending solution, for each cells, the ray is assumed to land the interfaces at a constant incident angle θ_2. This analytical solution allows us to find out the patterns of the additional terms for corresponding incident angles of Near, Mid and Far. This small-ray bending solutions will be tested through a field

dataset in the next section.

D.2 Shearwater application

This section examines the assumption of straight ray-path on this field using the small ray-bending solution introduced in Chapter 4. The same three angle stacked time-shifts are used as above, only the straight ray tomographic matrix, A, is now replaced by the small-bending tomographic matrix, A_b, with the additional terms compensating for the bending effect of the time-lapse perturbed ϑ model. Figure D.2 shows the recovered ϑ, which is very similar to the straight-ray solution (Figure 5.19) apart from some distortions amplified with the increase of the incident angles. These distortions might come from the additional term that causes the unstable inversion of the A_b matrix compared to the inversion of A matrix. This can suggest some sort of regularization to smooth the solution. However, it might return to the straight ray tomographic solution.

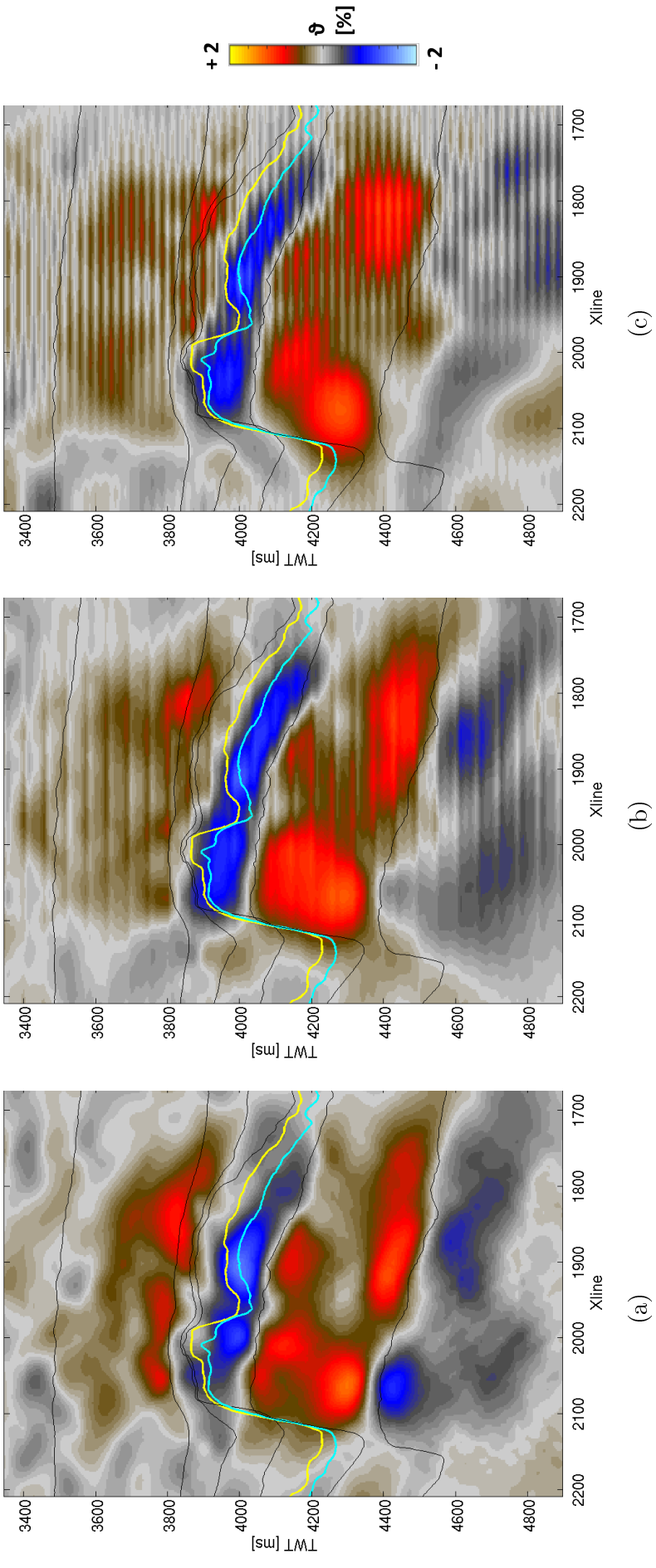

Figure D.2: Recovered ϑ from (a) Near, (b) Mid and (c) Far angle stacked time-shifts using small ray bending solutions. The distortion seems to amplify at larger angles (Mid and Far) possibly due to the unstable inversion of the additional term added into $\mathbf{A_b}$ matrix in compared with the inversion of $\mathbf{A}$ matrix itself.

Bibliography

Aarre, V. (2006). Estimating 4D velocity changes and contact movement on the Norne field. In *SEG Technical Program Expanded Abstracts 2006*, pages 3115–3119. Society of Exploration Geophysicists.

Alsos, T., Osdal, B., and Høiås, A. (2009). Improved Reservoir Imaging Using Specular Dip-angle Migration. In *71st EAGE Conference and Exhibition incorporating SPE EUROPEC 2009*.

Angus, D., He, Y.-X., Clark, R., and Hildyard, M. (2016). Analysis of time-lapse travel-time and amplitude changes to assess reservoir compartmentalization: Travel-time and amplitude changes. *Geophysical Prospecting*, 64(1):54–67.

Anzengruber, S. W. and Ramlau, R. (2010). Morozov's discrepancy principle for Tikhonov-type functionals with nonlinear operators. *Inverse Problems*, 26(2):025001.

Asnaashari, A., Brossier, R., Garambois, S., Virieux, J., Audebert, F., and Thore, P. (2012). Time-lapse imaging using regularized FWI: a robustness study. In *2012 SEG Annual Meeting*. Society of Exploration Geophysicists.

Audebert, F. and Agut, C. (2014). Making time-domain warping applicable to the retrieval of 4D perturbations in depth imaging contexts. In *SEG Technical Program Expanded Abstracts 2014*, SEG Technical Program Expanded Abstracts, pages 4873–4877. Society of Exploration Geophysicists.

Baek, H., Burnstad, R., and Keho, T. (2014). Time/Amplitude warping based on multiscale optimization. In *SEG Technical Program Expanded Abstracts 2014*, SEG Technical Program Expanded Abstracts, pages 4868–4872. Society of Exploration Geophysicists.

Baek, H. and Keho, T. (2015). A model-based warping method for 4D event characterization. In *SEG Technical Program Expanded Abstracts 2015*, SEG Technical Program Expanded Abstracts, pages 5409–5413. Society of Exploration Geophysicists.

Barclay, F., Bruun, A., Rasmussen, K. B., Alfaro, J. C., Cooke, A., Cooke, D., Salter, D., Godfrey, R., Lowden, D., and McHugo, S. (2008). Seismic inversion: Reading between the lines. *Oilfield Review*, 20(1):42–63.

Barkved, O. and Kristiansen, T. (2005). Seismic time-lapse effects and stress changes: Examples from a compacting reservoir. *The Leading Edge*, 24(12):1244–1248.

Beier, T. and Neely, S. (1992). Feature-based image metamorphosis. In *ACM SIGGRAPH Computer Graphics*, volume 26, pages 35–42. ACM.

Bertrand, A. and MacBeth, C. (2003). Seawater velocity variations and real-time reservoir monitoring. *The Leading Edge*, 22(4):351–355.

Brechet, E., Jorge, H., Turpin, P., and Maultzsch, S. (2010). 4D fast track advanced interpretation on Dalia field, block 17, angola. In *72nd EAGE Conference and Exhibition incorporating SPE EUROPEC 2010*.

Briceño, A. (2017). *Calibration and use of the Petroelastic Model for 4D Seismic interpretation*. PhD thesis, Heriot-Watt University.

Broto, K., Ricarte, P., Jurado, F., Etienne, G., and Le Bras, C. (2011). Improving seismic monitoring by 4D joint prestack traveltime tomography-application to the Sleipner CO2 storage case. In *1st EAGE Sustainable Earth Sciences (SES) Conference and Exhibition*.

Campbell, S., Lacombe, C., Brooymans, R., Hoeber, H., and White, S. (2011). Foinaven : 4d processing comes up trumps. *The Leading Edge*, 30(9):1034.

Cassell, B. R. (1982). A method for calculating synthetic seismograms in laterally varying media. *Geophysical Journal of the Royal Astronomical Society*, 69(2):339–354.

Chadwick, A., Williams, G., Delepine, N., Clochard, V., Labat, K., Sturton, S., Buddensiek, M., Dillen, M., Nickel, M., Lima, A., Arts, R., Neele, F., and Rossi,

G. (2010). Quantitative analysis of time-lapse seismic monitoring data at the Sleipner CO2 storage operation. *The Leading Edge*, 29(2):170–177.

Chamberfort, M. (2013). 4Dtime-shift interpretation for the Shearwater field. In *28th Meeting of the Edinburgh Time Lapse Project*.

Chen, G., Chu, D., Helgerud, M., Chang, D., Gorysheva, I., Palacharla, G., Zantout, S., Dewberry, S., Trantham, C., Leveque, T., Hernandez, D., Contreiras, O., Hohrath, A., Johnston, D., and Hodges, E. (2014). Improving 4D seismic imaging by modifying baseline depth migration velocity model. In *76th EAGE Conference and Exhibition 2014*.

Chu, D., Burger, J. C., and Medema, G. F. (2012). Using time strain volume for improved 4D interpretation - Methods and case studies. In *74th EAGE Conference and Exhibition incorporating EUROPEC 2012*.

Clarke, T. J. (1984). Full reconstruction of a layered elastic medium from P-SV slant-stack data. *Geophysical Journal International*, 78(3):775–793.

Cox, B. and Hatchell, P. (2008). Straightening out lateral shifts in time-lapse seismic. *First Break*, 26(5).

Eastwood, J., Johnston, D. H., Shyeh, J., Huang, X., Craft, K., Vauthrin, R., and Workman, R. (1999). Time-lapse seismic processing and analysis: Gulf of Mexico example, Lena field. In *Offshore Technology Conference*. Offshore Technology Conference.

Edgar, J. A. and Blanchard, T. D. (2015). Estimating overburden velocity changes from Pre-stack time shifts using linear tomography. In *77th EAGE Conference and Exhibition-Workshops*, pages Extended Abstract, WS02 – A04.

Edgar, J. A. and Mastio, N. (2017). Time-lapse velocity change tomography. In *79th EAGE Conference and Exhibition 2017*, pages Extended Abstract, A1 14.

Červený, V. and Pšenčík, I. (2011). Seismic ray theory. In *Encyclopedia of Solid Earth Geophysics*, Encyclopedia of Earth Sciences Series, pages 1244–1258. Springer Netherlands.

Evensen, A. and Landrø, M. (2010). Time-lapse tomographic inversion using a Gaussian parameterization of the velocity changes. *Geophysics*, 75(4):U29–U38.

Floricich, M., Jenkins, G., and McCormick, D. (2012). Probabilistic inversion of multiple 4D seismic as applied on Schiehallion field. In *74th EAGE Conference and Exhibition incorporating EUROPEC 2012*.

Gassmann, F. (1951). Über die Elastizität poröser Medien. *Vier. der Natur. Gesellschaft in Zürich*, 96:1–23.

Ghaderi, A. and Landrø, M. (2009). Estimation of thickness and velocity changes of injected carbon dioxide layers from prestack time-lapse seismic data. *Geophysics*, 74(2):O17–O28.

Gilham, R., Hercus, C., Evans, A., and Haas, W. D. (2005). Shearwater (UK Block 22/30b): managing changing uncertainties through field life. *Geological Society, London, Petroleum Geology Conference series*, 6(1):663–673.

Grandi, A., Wauquier, S., Cumming, H., Deplanté, C., and Hubans, C. (2009a). Quantitative 4D time lapse characterisation: Three examples. In *SEG Technical Program Expanded Abstracts 2009*, SEG Technical Program Expanded Abstracts, pages 3815–3819. Society of Exploration Geophysicists.

Grandi, A., Wauquier, S., Cumming, H., Deplanté, C., and Hubans, C. (2009b). Quantitative 4D warping inversion. In *International Petroleum Technology Conference*. International Petroleum Technology Conference.

Griffiths, L., Blanchard, T. D., Edgar, J. A., and Shahraeeni, M. S. (2015). Trace Warping vs. Impedance Warping in 4D Seismic Inversion. In *77th EAGE Conference and Exhibition 2015*.

Guilbot, J. and Smith, B. (2002). 4-D constrained depth conversion for reservoir compaction estimation: Application to Ekofisk Field. *The Leading Edge*, 21(3):302–308.

Hale, D. (2009). A method for estimating apparent displacement vectors from time-lapse seismic images. *Geophysics*, 74(5):V99–V107.

Hale, D. (2013). Dynamic warping of seismic images. *GEOPHYSICS*, 78(2):S105–S115.

Hale, D., Cox, B., and Hatchell, P. (2008). Apparent horizontal displacements in time-lapse seismic images. In *SEG Technical Program Expanded Abstracts 2008*,

SEG Technical Program Expanded Abstracts, pages 3169–3173. Society of Exploration Geophysicists.

Hall, S. A., MacBeth, C., Barkved, O. I., and Wild, P. (2005). Cross-matching with interpreted warping of 3D streamer and 3D ocean-bottom-cable data at Valhall for time-lapse assessment. *Geophysical Prospecting*, 53(2):283–297.

Hansen, P. C. (1994). Regularization tools: A Matlab package for analysis and solution of discrete ill-posed problems. *Numerical algorithms*, 6(1):1–35.

Hatchell, P., van den Beukel, A., Molenaar, M., Maron, K., Kenter, C., Stammeijer, J., van der Velde, J., and Sayers, C. (2003). Whole earth 4D: Reservoir monitoring geomechanics. In *SEG Technical Program Expanded Abstracts 2003*, SEG Technical Program Expanded Abstracts, pages 1330–1333. Society of Exploration Geophysicists.

Hatchell, P. J. and Bourne, S. J. (2005). Measuring reservoir compaction using time-lapse timeshifts. pages 2500–2503. Society of Exploration Geophysicists.

Hatchell, P. J., Kawar, R. S., and Savitski, A. A. (2005). Integrating 4D seismic, geomechanics and reservoir simulation in the Valhall oil field. In *67th EAGE Conference & Exhibition*.

Hawkins, K. (2008). Estimation of 4D anisotropy above the Elgin Reservoir from 4D seismic time shifts and compaction considerations. In *70th EAGE Conference and Exhibition incorporating SPE EUROPEC 2008*.

Hawkins, K., Conroy, G., and Harris, P. (2006). Estimation of production induced stress changes from 4D finite offset timeshifts. In *SEG Technical Program Expanded Abstracts 2006*, pages 1615–1619. Society of Exploration Geophysicists.

Hawkins, K., Howe, S., Hollingworth, S., Conroy, G., Ben-Brahim, L., Tindle, C., Taylor, N., Joffroy, G., and Onaisi, A. (2007). Production-induced stresses from time-lapse time shifts: A geomechanics case study from Franklin and Elgin fields. *The Leading Edge*, 26(5):655–662.

He, Y.-X., Angus D.A., R.A., C., and Hildyard M.W. (2015). Analysis of time-lapse travel-time and amplitude changes to assess reservoir compartmentalization. *Geophysical Prospecting*, 64(1):54–67.

Herwanger, J., Palmer, E., and Schiøtt, C. R. (2007). Anisotropic velocity changes in seismic time-lapse data. In *2007 SEG Annual Meeting*. Society of Exploration Geophysicists.

Hicks, E., Hoeber, H., Houbiers, M., Lescoffit, S. P., Ratcliffe, A., and Vinje, V. (2016). Time-lapse full-waveform inversion as a reservoir-monitoring tool—A North Sea case study. *The Leading Edge*, 35(10):850–858.

Hodgson, N. (2009). *Inversion for reservoir pressure change using overburden strain measurements determined from 4D seismic*. Thesis, Heriot-Watt University.

Hodgson, N., MacBeth, C., Duranti, L., Rickett, J., and Nihei, K. (2007). Inverting for reservoir pressure change using time-lapse time strain: Application to Genesis Field, Gulf of Mexico. *The Leading Edge*, 26(5):649–652.

Hondori, E., Mikada, H., Goto, T., and Takekawa, J. (2013). A random layer-stripping method for seismic reflectivity inversion. *Exploration Geophysics*, 44(2):70–76.

JafarGandomi, A., Richardson, J., Hoeber, H., Galyga, M., Smith, P., and Irving, A. (2018). Improved Reservoir Imaging Using Specular Dip-angle Migration. In *80th EAGE Conference and Exhibition 2017*.

Ji, L. (2017). *Integrating 4D seismic data into dynamic characterisation of an HPHT reservoir*. Thesis, Heriot-Watt University.

Johnston, D. (2013). *Practical applications of time-lapse seismic data*. Distinguished Instructor Series. Society of Exploration Geophysicists.

Jones, D., Taylor, B., Gill, C., Bevaart, M., van Bergen, P., Watson, J., De Gennaro, S., and Hodzic, M. (2018). The shearwater field–understanding the overburden above a geologically complex and pressure-depleted high-pressure and high-temperature field. *Geological Society, London, Petroleum Geology Conference series*, 8(1):429–443.

Jones, I. F. (2010). Tutorial: Velocity estimation via ray-based tomography. *First Break*, 28(2):45–52.

Justice, J. H. (1990). Layer-Stripping direct traveltime inversion for seismic data. *International Journal of Imaging Systems and Technology*, 2(2):134–143.

Kanu, C., Toomey, A., Hodgson, L., Gherasim, M., L'Heureux, E., Du, B., and Zhang, Q. (2016). Evaluation of time-shift extraction methods on a synthetic model with 4D geomechanical changes. *The Leading Edge*, 35(10):888–893.

Kapanidis, A. N. (2015). Physics Newsletter Autumn 2015 | University of Oxford Department of Physics. University of Oxford(7):4–5.

Kenter, C. J., Van den Beukel, A. C., Hatchell, A. C., Maron, P. J., Molenaar, K. P., Molenaar, M. M., and Stammeijer, J. G. F. (2004). Geomechanics and 4d: Evaluation of reservoir characteristics from timeshifts in the overburden. In *Gulf Rocks 2004, the 6th North America Rock Mechanics Symposium (NARMS)*. American Rock Mechanics Association, American Rock Mechanics Association.

Khalil, A. and Hoeber, H. (2016). Wave-equation-based image warping. *Geophysics*, 81(1):V1–V6.

Kragh, E. D. and Christie, P. (2002). Seismic repeatability, normalized RMS, and predictability. *The Leading Edge*, 21(7):640–647.

Kudarova, A., Hatchell, P., Brain, J., and Macbeth, C. (2016a). Offset-dependence of production-related 4D time shifts: Real data examples and modeling. In *SEG Technical Program Expanded Abstracts 2016*, pages 5395–5399. Society of Exploration Geophysicists.

Kudarova, A., van Dalen, K., and Drijkoningen, G. (2016b). An effective anisotropic poroelastic model for elastic wave propagation in finely layered media. *Geophysics*, 81(4):T175–T188.

Landrø, M. and Janssen, R. (2002). Estimating Compaction and Velocity Changes from Time-Lapse near and far Offset Stacks.

Landrø, M. and Stammeijer, J. (2004). Quantitative estimation of compaction and velocity changes using 4D impedance and traveltime changes. *Geophysics*, 69(4):949–957.

Langan, R., Lerche, I., and Cutler, R. (1985). Tracing of rays through heterogeneous media: An accurate and efficient procedure. *Geophysics*, 50(9):1456–1465.

Leguijt, J. (2009). Seismically constrained probabilistic reservoir modeling. *The Leading Edge*, 28(12):1478–1484.

Lie, E. O. (2011). Constrained timeshift estimation. In *73rd EAGE Conference and Exhibition incorporating SPE EUROPEC 2011*.

Lines, L., Bourgeois, A., and Covey, J. (1984). Traveltime inversion of offset vertical seismic profiles—A feasibility study. *Geophysics*, 49(3):250–264.

Lizarralde, D. and Swift, S. (1999). Smooth inversion of VSP traveltime data. *Geophysics*, 64(3):659–661.

MacBeth, C., Kudarova, A., Hatchell, P. J., and Brain, J. (2017a). A semi-empirical model for interpreting rock strain sensitivity in 4d seismic data. In *79th EAGE Conference and Exhibition 2017*, pages Extended Abstract, A105.

MacBeth, C., Mangriotis, M. D., and Amini, H. (2017b). Post-stack 4D seismic time-shifts: Interpretation and evaluation. *Submitted to Geophysical Prospecting*.

MacBeth, C., Mangriotis, M. D., and Hatchell, P. (2016). Evaluation of the spurious time-shift problem. In *SEG Technical Program Expanded Abstracts 2016*, SEG Technical Program Expanded Abstracts, pages 5457–5462. Society of Exploration Geophysicists.

Mistry, D., Joshi, S., and Agrawal, N. K. (2015). A novel jitter separation method based on gaussian mixture model. *2015 International Conference on Pervasive Computing (ICPC)*, pages 1–4.

Moser, T. (1991). Shortest path calculation of seismic rays. *Geophysics*, 56(1):59–67.

Naeini, E. Z., Hoeber, H., Poole, G., and Siahkoohi, H. R. (2009). Simultaneous multivintage time-shift estimation. *Geophysics*, 74(5):V109–V121.

Nguyen, P. K. T. and Nam, M. J. (2011). A review on methods for constructing rock physics model of saturated reservoir rock for time-lapse seismic. *Geosystem Engineering*, 14(2):95–107.

Nur, A., Tosaya, C., and Vo Thanh, D. (1984). Seismic monitoring of thermal enhanced oil recovery processes. In *SEG Technical Program Expanded Abstracts 1984*, SEG Technical Program Expanded Abstracts, pages 337–340. Society of Exploration Geophysicists.

Nur, A. M. (1982). Seismic imaging in enhanced recovery. In *SPE Enhanced Oil Recovery Symposium*. Society of Petroleum Engineers.

Nur, A. M. and Wang, Z. (1987). In-situ seismic monitoring eor: The petrophysical basis. In *SPE Annual Technical Conference and Exhibition*. Society of Petroleum Engineers.

Ong, B. S., Hembd, J., Srinivasan, A., Chu, D., and Johnston, D. H. (2015). Estimation of water layer correction in shallow time-lapse streamer data sets. In *2015 SEG Annual Meeting*. Society of Exploration Geophysicists.

Piersol, A. (1981). Time delay estimation using phase data. *IEEE Transactions on Acoustics, Speech, and Signal Processing*, 29(3):471–477.

Rangel, R. (2016). *The impact of shale pressure diffusion on 4D seismic interpretation*. Thesis, Heriot-Watt University.

Rawlinson, N. (1996). *Methods and Codes Used in Seismic Tomography*. Australian Geological Survey Organisation.

Rickett, J., Duranti, L., Hudson, T., and Hodgson, N. (2006). Compaction and 4D time strain at the Genesis Field. In *SEG Technical Program Expanded Abstracts 2006*, SEG Technical Program Expanded Abstracts, pages 3215–3219. Society of Exploration Geophysicists.

Rickett, J., Duranti, L., Hudson, T., Regel, B., and Hodgson, N. (2007). 4D time strain and the seismic signature of geomechanical compaction at Genesis. *The Leading Edge*, 26(5):644–647.

Rickett, J. and Lumley, D. E. (1998). A cross-equalization processing flow for off-the-shelf 4-D seismic data. In *SEG Technical Program Expanded Abstracts*, volume 17, pages 16–19.

Routh, P., Palacharla, G., Chikichev, I., and Lazaratos, S. (2012). Full Wavefield Inversion of Time-Lapse Data for Improved Imaging and Reservoir Characterization. Society of Exploration Geophysicists.

Røste, T. (2007). *Monitoring Overburden and Reservoir Changes from Prestack Time-Lapse Seismic Data: Applications to Chalk Fields*. PhD thesis, Fakultet for ingeniørvitenskap og teknologi.

Røste, T., Dybvik, O., and Søreide, O. (2015). Overburden 4D time shifts induced by reservoir compaction at Snorre field. *The Leading Edge*, 34(11):1366–1374.

Røste, T. and Ke, G. (2017). Overburden 4D time shifts - Indicating undrained areas and fault transmissibility in the reservoir. *The Leading Edge*, 36(5):423–430.

Røste, T., Landrø, M., and Hatchell, P. (2007). Monitoring overburden layer changes and fault movements from time-lapse seismic data on the Valhall Field. *Geophysical Journal International*, 170(3):1100–1118.

Røste, T., Stovas, A., and Landrø, M. (2005). Estimation of Layer Thickness and Velocity Changes Using 4D Prestack Sesimic Data.

Røste, T., Stovas, A., and Landrø, M. (2006). Estimation of layer thickness and velocity changes using 4D prestack seismic data. *Geophysics*, 71(6):S219–S234.

Russell, B. (1988). *Introduction to Seismic Inversion Methods*. Course Notes Series. Society of Exploration Geophysicists.

Rust, M. J., Bates, M., and Zhuang, X. (2006). Sub-diffraction-limit imaging by stochastic optical reconstruction microscopy (STORM). *Nature Methods*, 3(10):793–796.

Sarkar, S., Gouveia, W., and Johnston, D. (2003). On the inversion of time-lapse seismic data. In *SEG Technical Program Expanded Abstracts 2003*, SEG Technical Program Expanded Abstracts, pages 1489–1492. Society of Exploration Geophysicists.

Schuster, G. (1988). An analytic generalized inverse for common-depth-point and vertical seismic profile traveltime equations. *Geophysics*, 53(3):314–325.

Schuster, G., Johnson, D., and Trentman, D. (1988). Numerical verification and extension of an analytic generalized inverse for common-depth-point and vertical-seismic-profile traveltime equations. *Geophysics*, 53(3):326–333.

Shiva, M. and Mendel, J. M. (1983). Non-Normal Incidence Inversion: Existence of Solution*. *Geophysical Prospecting*, 31(6):888–914.

Shragge, J., Yang, T., and Sava, P. (2013). Time-lapse image-domain tomography using adjoint-state methods. *Geophysics*, 78(4):A29–A33.

Singh, S. C. (1990). Seismic waveform inversion using a layer-stripping method. In *Inverse Methods in Action*, Inverse Problems and Theoretical Imaging, pages 468–469. Springer, Berlin, Heidelberg.

Smith, W. D. (1975). The Application of Finite Element Analysis to Body Wave Propagation Problems. *Geophysical Journal of the Royal Astronomical Society*, 42(2):747–768.

Staples, R., Ita, J., Burrell, R., and Nash, R. (2007a). Monitoring pressure depletion and improving geomechanical models of the Shearwater Field using 4D seismic. *The Leading Edge*, 26(5):636–642.

Staples, R., Ita, J., Nash, R., Hague, P., and Burrell, R. (2007b). Using 4d seismic data and geomechanical modelling to understand pressure depletion in hpht fields of the central n sea. In *69th EAGE Conference and Exhibition incorporating SPE EUROPEC 2007*.

Thore, P. (2011). Application of a grid-consistent inversion to a 4D reservoir model. *The Leading Edge*, 30(11):1262–1269.

Thore, P. and Blanchard, T. (2014). 4D wavelet estimation. In *SEG Technical Program Expanded Abstracts 2014*, SEG Technical Program Expanded Abstracts, pages 4878–4882. Society of Exploration Geophysicists.

Thore, P., de Verdiere, C., and McManus, E. (2012). Estimation of 4d signal in complex media: A Fast Track approach. In *SEG Technical Program Expanded Abstracts 2012*, SEG Technical Program Expanded Abstracts, pages 1–5. Society of Exploration Geophysicists.

Thore, P. and Hubans, C. (2011). Reservoir Grid Consistent 4D Inversion.

Thore, P. and Hubans, C. (2012). 4D seismic-to-well tying, a key step towards 4D inversion. *Geophysics*, 77(6):R227–R238.

Tian, S. S. (2014). *Closing the loop by engineering consistent 4D seismic to simulator inversion*. Thesis, Heriot-Watt University.

Varela, O. J., Torres-Verdín, C., Sen, M. K., and Roy, I. G. (2006). Using time-lapse seismic amplitude data to detect variations of pore pressure and fluid saturation due to oil displacement by water: a numerical study based on one-dimensional prestack inversion. *Journal of Geophysics and Engineering*, 3(2):177.

Vedanti, N., Pathak, A., Srivastava, R. P., and Dimri, V. P. (2009). Time lapse (4D) seismic: some case studies. *Earth Science India*, 2:230–248.

Vesnaver, A., Accaino, F., Bohm, G., Madrussani, G., Pajchel, J., Rossi, G., and Moro, G. (2003). Time-lapse tomography. *Geophysics*, 68(3):815–823.

Vesnaver, A., Janex, G., Madrussani, G., Mazzotti, A., Pajchel, J., Stucchi, E., and Williamson, P. (2001). Target-oriented time-lapse analysis by AVO and tomographic inversion. In *SEG Technical Program Expanded Abstracts 2001*, pages 730–733. Society of Exploration Geophysicists.

Vidale, J. (1988). Finite-difference calculation of travel times. *Bulletin of the Seismological Society of America*, 78(6):2062–2076.

Waal, H. d. and Calvert, R. (2003). Overview of global 4D seismic implementation strategy. *Petroleum Geoscience*, 9(1):1–6.

Whitcombe, D., Paramo, P., Philip, N., Toomey, A., Redshaw, T., and Linn, S. (2010). The correlated leakage method–it's application to better quantify timing shifts on 4d data. In *72nd EAGE Conference and Exhibition incorporating SPE EUROPEC 2010*.

Williamson, P. R., Cherrett, A. J., and Sexton, P. A. (2007). A new approach to warping for quantitative time–lapse characterisation. In *69th EAGE Conference and Exhibition incorporating SPE EUROPEC 2007*.

Yagle, A. and Levy, B. (1985). A layer-stripping solution of the inverse problem for a one-dimensional elastic medium. *Geophysics*, 50(3):425–433.

Yang, D., Malcolm, A., and Fehler, M. (2014). Using image warping for time-lapse image domain wavefield tomography. *Geophysics*, 79(3):WA141–WA151.

Yilmaz, . (2001). *Seismic Data Analysis*. Investigations in Geophysics. Society of Exploration Geophysicists.